

DISSERTATION

SIMULATION OF SPACE-BASED RADAR OBSERVATIONS OF
PRECIPITATIONS

Submitted by

Direk Khajonrat

Department of Electrical and Computer Engineering

In partial fulfillment of the requirements

for the Degree of Doctor of Philosophy

Colorado State University

Fort Collins, Colorado

Summer, 2008

UMI Number: 3332750

INFORMATION TO USERS

The quality of this reproduction is dependent upon the quality of the copy submitted. Broken or indistinct print, colored or poor quality illustrations and photographs, print bleed-through, substandard margins, and improper alignment can adversely affect reproduction.

In the unlikely event that the author did not send a complete manuscript and there are missing pages, these will be noted. Also, if unauthorized copyright material had to be removed, a note will indicate the deletion.

UMI[®]

UMI Microform 3332750

Copyright 2008 by ProQuest LLC.

All rights reserved. This microform edition is protected against unauthorized copying under Title 17, United States Code.

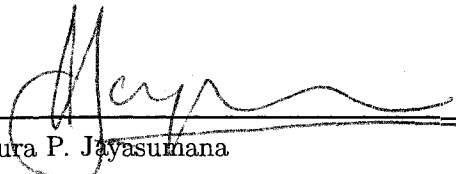
ProQuest LLC
789 E. Eisenhower Parkway
PO Box 1346
Ann Arbor, MI 48106-1346

COLORADO STATE UNIVERSITY

June 23, 2008

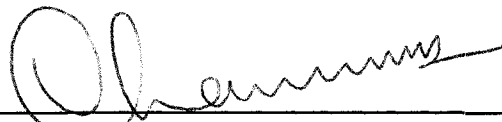
WE HEREBY RECOMMEND THAT THE DISSERTATION PREPARED UNDER OUR SUPERVISION BY DIREK KHAJONRAT ENTITLED SIMULATION OF SPACE-BASED RADAR OBSERVATIONS OF PRECIPITATION BE ACCEPTED AS FULFILLING IN PART REQUIREMENTS FOR THE DEGREE OF DOCTOR OF PHILOSOPHY.

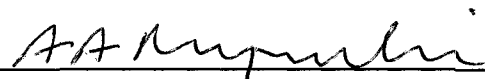
Committee


Anura P. Jayasumana


Paul W. Mielke


Branislav Notaros


Advisor: Chandrasekar V. Chandra


Department Head: Anthony A. Maciejewski

ABSTRACT OF DISSERTATION

SIMULATION OF SPACE-BASED RADAR OBSERVATIONS OF
PRECIPITATIONS

The Tropical Rainfall Measurement Mission (TRMM) will soon be followed on by the Global Precipitation Measurement (GPM). The GPM satellite will be the next generation observation of precipitation from space. The GPM will carry a dual-frequency precipitation radar (DPR) operating at 13.6 GHz (Ku-band) and 35.6 GHz (Ka-band), as opposed to a single-frequency 13.8 GHz (Ku-band) precipitation radar (PR) in TRMM. A greater degree of accuracy of precipitation measurements can be achieved by a dual-frequency radar using measurements from the two channels.

The DPR on the GPM will be the first space-based dual-frequency precipitation radar. Since spaceborne precipitation observations have never been done in Ka-band before, extensive research on dual-frequency radar, including electromagnetic wave propagation characteristics from space and retrieval algorithms are essential for system development and system evaluations. Because the DPR is the first of its kind, a simulation-based study can provide significant assessment of the GPM system which is presented here. The research reported here focuses on developing methodologies for simulating the precipitation characteristics that would be observed from space by DPR using current space-based radar observations and earth-based radar measurements.

The underlying microphysics of precipitation structures are important for developing a simulation model and a realistic model of precipitation is desired for representative simulation results. In this research, a microphysical model of precipitation

is developed based on airborne radar measurements. The simulation of precipitation observations in Ku- and Ka-band are performed using both TRMM-PR observations and ground-based radar measurements. The simulation of a wide variety of precipitation regimes reveals the characteristics of the precipitation observed in Ku- and Ka-band, and allows testing of different retrieval algorithms—either the single-frequency (TRMM-like algorithm) or dual-frequency techniques. A significant degradation of signal in the Ka-band channel in intense precipitation such as an intense convective storm and tropical storms directly affect the retrieval algorithms that can be used. Vertical reflectivity profiles classification and drop size distribution parameters estimation of tropical storms are studied and results are presented here.

Direk Khajonrat
Department of Electrical and Computer Engineering
Colorado State University
Fort Collins, Colorado 80523
Summer, 2008

ACKNOWLEDGEMENTS

First of all, I am grateful to the Royal Thai Navy for giving me a great opportunity for a once-in-a-lifetime learning experience. I am grateful to my advisor, Dr. V. Chandrasekar, for his kindness, support, guidance, and encouragement during my graduate study. Also, I would like to express my gratitude to Dr. Anura P. Jayasumana, Dr. Paul W. Mielke, and Dr. Branislav Notaros for serving as my committee members, and to Dr. V. N. Bringi for his guidance and suggestion.

During my research, I received much assistance from the members of our Radar and Communication Group at Colorado State University. Here, I would like to express my appreciation to N. Bharadwaj, Dr. Gwo-Jong Huang, Dr. Y. Wang, Dr. S. Lim, Jim George, and Minda Le for their assistance and kindness during the course of my research. Also, I would like to thank Andy Crane, our computer system administrator, for his technical support, and Karen Ungerer for her administrative support.

Finally, I am grateful to my parents, sister, and brother for their love, support and enthusiasm. I also would like to thank Sainatee Champirat for her love and inspiration.

TABLE OF CONTENTS

Abstract of Dissertation	iii
Acknowledgements	iv
Table of Contents	v
List of Figures	x
List of Tables	xxv
1 Introduction	1
1.1 Introduction	1
1.2 Literature Review	3
1.2.1 Analysis of single-frequency TRMM-PR Observations	3
1.2.2 Convective/stratiform rain type	4
1.2.3 Dual-polarization ground-based radar measurements	5
1.2.4 Satellite-based radio-wave propagation at high frequencies	6
1.2.5 Dual-frequency space-based precipitation radar	6
1.3 Statement of Problem	8
1.4 Objectives of Research	10
2 Theoretical background of Space and Earth-based radar observations : Electromagnetics and Microphysics	12
2.1 introduction	12

2.2	Microphysical Model of Precipitation: Particle Size Distribution (PSD)	13
2.3	Computation of Attenuation and Radar Reflectivity	14
2.3.1	Extinction cross-section and specific attenuation	14
2.3.2	Backscatter cross-section and radar reflectivity	15
2.4	Variability of Reflectivity with Frequency and Specific Attenuation and Reflectivity Relation	16
2.5	The Concept of Vertical Profile of Reflectivity (VPR) Simulation . . .	27
2.6	Summary and Conclusion	27
3	TRMM-PR global observation analysis and ground measurements	28
3.1	Introduction	28
3.2	TRMM-PR Overview	28
3.2.1	TRMM-PR system descriptions	29
3.2.2	TRMM-PR attenuation correction algorithm	32
3.3	Vertical Profile of Reflectivity (VPR) Analysis	37
3.3.1	Characterization of VPR for convective rain	38
3.3.2	Characterization of VPR for stratiform rain	42
3.4	Drop Size Distribution (DSD) Parameters Estimation	48
3.5	Comparison of Estimated DSD parameters between TRMM-PR and Dual-polarization Ground-based Radar	56
3.6	Summary and Conclusion	61
4	GPM-DPR : System and Retrieval methods	63
4.1	Introduction	63
4.2	GPM-DPR Overview	63
4.3	Dual-frequency Retrieval Methods	65
4.3.1	Integral Equations for the Dual-frequency Method	68
4.3.2	Standard Dual-frequency Method	71
4.4	Summary and Conclusions	88

5	Development of A Microphysical Model for Simulation of Precipitation Observations	91
5.1	Introduction	91
5.2	Development of a Microphysical Model for Simulation Based on Airborne Radar Observations	92
5.2.1	Airborne radar observations	92
5.2.2	Generation of particle size distribution parameters along the vertical profile	98
5.3	Summary and Conclusions	111
6	Simulation of Spaceborne Precipitation Radar observations : Application to GPM-DPR	114
6.1	Introduction	114
6.2	The Simulation of Ka-band Radar Observations Based on Ku-band Radar Observations	115
6.2.1	Case Study: The simulation of Ka-band radar observations based on TRMM-PR observations	115
6.3	Simulation of Ku- and Ka-band Radar Observations Based on Ground Radar Measurements	126
6.3.1	Case Study: A simulation using ground-based NEXRAD radar measurements	126
6.3.2	Case Study: A simulation using dual-polarization ground-based radar measurements	140
6.4	Summary and Conclusions	145
7	Tropical Storms	147
7.1	Introduction	147
7.2	Result of VPR Classification of Storms	148
7.2.1	Comparison of storms between years	148

7.2.2	Same-year storms comparison study	154
7.3	Study of Bright Band (BB) Properties	156
7.4	Drop Size Distribution Study	158
7.4.1	Result of D_o and N_w estimate	159
7.5	Simulation of Ka-band Radar Observations of Tropical Storms	169
7.6	Summary and Conclusion	175
8	Summary, Conclusions, and Recommendations for Future Work	177
8.1	Summary and Conclusions	177
8.2	Suggestion for Future Work	182
A	Scattering of electromagnetic wave by dielectric sphere	183
A.1	Vector scattering amplitude and Scattering matrix	183
A.2	Scattering matrix for dielectric sphere	187
A.2.1	Rayleigh Scattering	187
A.2.2	Mie Scattering	190
A.3	Extinction Cross-section and Backscatter Cross-section	191
A.3.1	Extinction Cross-section	191
A.3.2	Backscatter Cross-section	192
B	Coefficients of the k-Z_e Relation and Variability of Z_e with Frequency for Simulations	194
C	Dual-Polarization Radar Measurements	208
C.1	Polarimetric Radar Measurements	208
C.1.1	Reflectivity (Z_h)	208
C.1.2	Differential Reflectivity (Z_{dr})	208
C.1.3	Specific Differential Phase (K_{dp})	209
C.1.4	Linear Depolarization Ratio (LDR)	209
C.1.5	Correlation Coefficient (ρ_{hv})	210

LIST OF FIGURES

2.1	Scatter plots and the best fits of variability of reflectivity with frequency and k - Z_e relations for dry snow with density of 0.2 g cm^{-3} : (a) $Z_e(\text{S})$ vs. $Z_e(\text{Ku})$, (b) $Z_e(\text{S})$ vs. $Z_e(\text{Ka})$, (c) $Z_e(\text{Ku})$ vs. $Z_e(\text{Ka})$, (d) $Z_e(\text{Ku})$ vs. $k(\text{Ku})$ and (d) $Z_e(\text{Ka})$ vs. $k(\text{Ka})$	19
2.2	Scatter plots and the best fits of variability of reflectivity with frequency and k - Z_e relations for dry graupel with density of 0.4 g cm^{-3} : (a) $Z_e(\text{S})$ vs. $Z_e(\text{Ku})$, (b) $Z_e(\text{S})$ vs. $Z_e(\text{Ka})$, (c) $Z_e(\text{Ku})$ vs. $Z_e(\text{Ka})$, (d) $Z_e(\text{Ku})$ vs. $k(\text{Ku})$ and (d) $Z_e(\text{Ka})$ vs. $k(\text{Ka})$	20
2.3	Scatter plots and the best fits of variability of reflectivity with frequency and k - Z_e relations for melted graupel with water fraction of 0.2: (a) $Z_e(\text{S})$ vs. $Z_e(\text{Ku})$, (b) $Z_e(\text{S})$ vs. $Z_e(\text{Ka})$, (c) $Z_e(\text{Ku})$ vs. $Z_e(\text{Ka})$, (d) $Z_e(\text{Ku})$ vs. $k(\text{Ku})$ and (d) $Z_e(\text{Ka})$ vs. $k(\text{Ka})$	21
2.4	Scatter plots and the best fits of variability of reflectivity with frequency and k - Z_e relations for melted graupel with water fraction of 0.6: (a) $Z_e(\text{S})$ vs. $Z_e(\text{Ku})$, (b) $Z_e(\text{S})$ vs. $Z_e(\text{Ka})$, (c) $Z_e(\text{Ku})$ vs. $Z_e(\text{Ka})$, (d) $Z_e(\text{Ku})$ vs. $k(\text{Ku})$ and (d) $Z_e(\text{Ka})$ vs. $k(\text{Ka})$	22
2.5	Scatter plots and the best fits of variability of reflectivity with frequency and k - Z_e relations for rain: (a) $Z_e(\text{S})$ vs. $Z_e(\text{Ku})$, (b) $Z_e(\text{S})$ vs. $Z_e(\text{Ka})$, (c) $Z_e(\text{Ku})$ vs. $Z_e(\text{Ka})$, (d) $Z_e(\text{KY})$ vs. $k(\text{Ku})$ and (d) $Z_e(\text{Ka})$ vs. $k(\text{Ka})$	23
3.1	An example of 3-dimensional reflectivity of precipitation structure observed by TRMM-PR.	29

3.2	The ground track of TRMM orbit over one day (adopted from (TRMM, 2001)).	30
3.3	The observation geometry of the PR before the altitude boost (adopted from TRMM (2001)).	31
3.4	(a) a horizontal cross-section of the measured reflectivity (Z_m) of a hurricane observed by PR; (b) corresponding attenuation-corrected reflectivity (Z_e) of (a); (c) a vertical cross-section of (a), as indicated by the dashed line; (d) a vertical cross-section of (b), as indicated by the dashed line; (e) a vertical profile for convective rain, as indicated by A in (c) and (d); and (f) a vertical profile for stratiform rain, as indicated by B in (c) and (d).	36
3.5	The characteristic VPRs of convective rain for $\epsilon = 1$ (a) over ocean, (b) over land for year 2000. The 12 plots in each subfigure represent 12 different months.	39
3.6	Comparison of the characteristic VPRs of convective rain for $\epsilon = 1$ over ocean and over land.	40
3.7	The characteristic VPRs of convective rain for $\epsilon \neq 1$ (a) over ocean, (b) over land for year 2000. The 12 plots in each subfigure represent 12 different months.	41
3.8	Comparison of the characteristic VPRs of convective rain for $\epsilon \neq 1$ over ocean and over land for the year 2000.	42
3.9	The mean vertical reflectivity profiles of stratiform rain for $\epsilon = 1$ (a) over ocean, and (b) over land for sixteen different heights of bright band peak from sea level for year 2000.	44
3.10	The mean vertical reflectivity profiles of stratiform rain for $\epsilon \neq 1$ (a) over ocean, and (b) over land for sixteen different heights of bright band peak from sea level for year 2000.	45

3.11 Comparison of the mean profiles of stratiform rain over ocean and over land for (a) $\epsilon = 1$, and (b) $\epsilon \neq 1$	46
3.12 Comparison of the mean profiles of stratiform rain between $\epsilon = 1$ and $\epsilon \neq 1$ for (a) over ocean, and (b) over land.	47
3.13 Scatter plot Z/N_w vs. k/N_w	49
3.14 (a) Distribution of D_o , (b) N_w for $\epsilon = 1$ over land and over ocean. . .	50
3.15 (a) Distribution of D_o , (b) N_w for $\epsilon > 1$ over land and over ocean. . .	51
3.16 (a) Distribution of D_o , (b) N_w for $\epsilon < 1$ over land and over ocean. . .	51
3.17 (a) Distribution of D_o , (b) N_w for $\epsilon < 0.8$ over land and over ocean. . .	53
3.18 (a) Distribution of D_o , (b) N_w for $\epsilon < 0.6$ over land and over ocean. . .	53
3.19 Percentage occurrence of (a) $\epsilon = 1$ and mean D_o , (b) $\epsilon > 1$ and mean D_o over land (L) and over ocean (O). Percentage occurrence of convective (C) and stratiform (S) rain type over land and ocean is shown over the bars.	54
3.20 Percentage occurrence of (a) $\epsilon \leq 1$ and mean D_o , (b) $\epsilon \leq 0.8$ and mean D_o over land (L) and over ocean (O). Percentage occurrence of convective (C) and stratiform (S) rain type over land and ocean is shown over the bars.	54
3.21 Percentage occurrence of $\epsilon < 0.6$ and mean D_o over land (L) and over ocean (O). Percentage occurrence of convective (C) and stratiform (S) rain type over land and ocean is shown over the bars.	55
3.22 Worldwide locations of the TRMM ground validation sites (adopted from TRMM ground validation website).	56
3.23 Illustration of location of NCAR S-Pol radar of Large scale Biosphere-Atmosphere (LBA) experiment and TRMM-PR overpass at area of LBA experiment Green circle indicates 200 km. radius from S-Pol within the area where TRMM-PR data was analyzed for DSD comparison.	58

3.24	Comparison of distributions of retrieved D_o from TRMM-PR and S-pol data in easterly regime for (a) all rain type, and (b) convective rain type	59
3.25	Comparison of distributions of retrieved D_o from TRMM-PR and S-pol data in westerly regime for (a) all rain type, and (b) convective rain type	59
3.26	Comparison of four characteristic reflectivity profiles between the westerly and easterly regimes based on the classification of TRMM-PR data.	60
4.1	Graphical illustration of GPM system.	64
4.2	(a) Dual-frequency precipitation radar (DPR), (b) Scan geometry of DPR (adopted from Senbokuya et al. (2004)).	65
4.3	Concept of the dual-frequency measurement of precipitation (adopted from Senbokuya et al. (2004)).	66
4.4	Schematic illustration of dual-frequency radar observation along vertical profile of precipitation (adapted from Rose 2004).	68
4.5	Schematic illustration of storm profile for difference of attenuation difference (DAD).	73
4.6	Plot of $I_{b1}(D_o)/I_{b2}(D_o)$ versus D_o . Note that subscripts 1 and 2 refer to Ka-band and Ku-band channel, respectively.	75
4.7	Scattering plot and power law fit (red) of k - R relation: (a) 35.5 GHz, (b) 13.6 GHz. The associated coefficients for each frequency are also shown.	76
4.8	Comparison of path-averaged rainfall rate over range r_1 and r_2 computed using (4.20) for different values of μ .	78
4.9	“Measured” reflectivity of 35.5 and 13.6 GHz as a function of altitude. D_o at 3.25 km. is 1.4 and 0.5 km. is 1.6 and N_w at 3.25 km. and 0.5 km. are 8000 and 4400, respectively.	79

4.10	(a), (c), and (e) show the comparison of three path-averaged rainfall rate (PAR) estimates as a function of D_o . The “true” PAR is approximately 5 mm hr ⁻¹ . In (a), $D_o(r_1) = 1.0$ mm, and $D_o(r_2)$ varies from 1.0 to 1.2 mm, giving the maximum $\delta D_o = 0.2$ mm; (b) shows Δ PAR as a function of δD_o . (c), (d), (e), and (f) are similar to (a), (b), except $D_o(r_1) = 1.2$ mm in (c) and 1.4 mm in (e), respectively.	82
4.11	Similar to Fig. 4.10 except $D_o(r_1)$ are 1.2, 1.4 and 1.6 mm and “true” PAR is about 10 mm hr ⁻¹	84
4.12	Similar to Fig. 4.10, except $D_o(r_1)$ are 1.2, 1.4, and 1.6 mm and “true” PAR is about 15 mm hr ⁻¹	85
4.13	Similar to Fig. 4.10, except $D_o(r_1)$ are 1.2, 1.4, and 1.6 mm and “true” PAR is about 20 mm hr ⁻¹	86
4.14	Scatter plot between PIA(Ku) and DAD, along with the best fit in the power law form.	88
4.15	Scatter plot between PIA(Ka) and DAD, along with the best fit in the power law form.	89
5.1	APR-2 scanning geometry on the NASA DC-8 aircraft. Antenna is scanned in cross-track plane (adopted from Im et al. (2002)).	93
5.2	NAMMA experiment area.	94
5.3	Along-track observations at nadir of the APR-2 radar in the NAMMA experiment. The (a) panel is reflectivity at Ku-band, the (b) panel is reflectivity in Ka-band, the (c) panel is LDR at Ku-band, and the (d) panel is velocity at Ku-band.	95
5.4	Convective rain profiles at location A in Fig. 5.3. (a) Reflectivity profile of the two channels, (b) the difference of reflectivity between the two channels, (c) linear depolarized ratio (LDR) in Ku-band, and (d) fall velocity in Ku-band. The dashed lines indicate the melting layer boundary.	96

5.5	Same as in Fig. 5.4 for location B.	96
5.6	Stratiform rain profile with bright band at location C in Fig. 5.3. (a) Reflectivity profile of the two channels, (b) the difference of reflectivity between the two channels, (c) linear depolarized ratio (LDR) in Ku-band, and (d) fall velocity in Ku-band. The dashed lines indicate the melting layer boundary.	97
5.7	Same as in Fig. 5.6 for location D.	97
5.8	DFR vs D_o for snow densities of 0.05, 0.1, 0.2, and 0.4 g cm ⁻³ when $\mu = 0$ (implying exponential size distribution).	99
5.9	Distribution of the retrieved (a) D_o , and (b) N_w along the height of dry snow using a density of 0.1 g cm ⁻³ . The solid line is the best fit. The y-axis is the height above the bright band.	100
5.10	Distributions of the retrieved (a) D_o , and (b) N_w for four different height levels, namely, 0.5, 1, 1.5 and 2 km above the bright band (BB), with a snow density of 0.1 g cm ⁻³	100
5.11	DFR vs D_o for wet snow with water fraction (wf) of 0.1, 0.2, 0.3, and 0.4.	101
5.12	Distributions of the retrieved (a) D_o and (b) N_w of wet snow along the height. The positive and negative values represent the above and below the bright band peak, respectively. The bright band peak is indicated by 0 km. The solid line is the best fit.	102
5.13	Distributions of the retrieved (a) D_o , and (b) N_w of wet snow for four different height levels, namely, 0.1 and 0.3 km above (+) and below (-) the bright band (BB) peak.	102
5.14	DFR vs D_o for raindrops for 4 different μ values, 0, 1, 2 and 4.	103
5.15	Distributions of the retrieved (a) D_o and (b) N_w of raindrops along the height. The solid line is the best fit.	103

5.16	Distributions of the retrieved (a) D_o and (b) N_w of raindrops for four different height levels, namely, 0, 0.5, 1, and 2 km below the bright band.	104
5.17	DFR vs D_o for snow densities of 0.05, 0.1, 0.2, and 0.4 g cm ⁻³ . when $\mu = 0$ (implying exponential size distribution).	105
5.18	Distributions of the retrieved (a) D_o and (b) N_w of dry graupel along the height in convective rain. The solid line is the best fit.	105
5.19	Distributions of the retrieved (a) D_o and (b) N_w of dry graupel in convective rain at 4 different height levels, namely, 0.5, 1, 1.5, and 2 km above the melting layer.	106
5.20	DFR vs D_o for wet graupel for water fraction (wf) of 0.05, 0.1, 0.2, and 0.4 g cm ⁻³ .	107
5.21	Distributions of the retrieved (a) D_o and (b) N_w of wet graupel along the height within the melting layer for convective rain. The positive and negative values represent the above and below the center of the melting layer, respectively. The center of the melting layer is indicated by 0 km. The solid line is the best fit.	108
5.22	Distributions of the retrieved (a) D_o and (b) N_w of wet graupel in convective rain at four different height levels, namely, 0.1 and 0.3 km above (+) and below (-) the center of the melting layer (ML).	108
5.23	Distributions of the retrieved (a) D_o and (b) N_w of raindrops along the height below the melting layer. The solid line is the best fit.	109
5.24	Distributions of the retrieved (a) D_o and (b) N_w of raindrops in convective rain at four different height levels, namely, 0, 0.5, 1, and 2 km below the melting layer.	109
5.25	Microphysical rain model (a) stratiform rain, and (b) convective rain.	110
6.1	An overpassing orbit of the TRMM-PR over the area of the NAMMA experiment. The precipitation in the rectangle is used in the simulation.	115

6.2	The attenuation-corrected reflectivity at Ku-band ($Z_e(\text{Ku})$): (a) a horizontal cross-section at 2 km; (b) a vertical cross-section across PR ground track, as indicated by the dashed line in (a); (c) and (d) vertical profiles at the locations A and B, as indicated in (b), respectively.	116
6.3	A simple diagram of the simulation procedure based on TRMM-PR observations.	117
6.4	A horizontal cross-section of $Z_e(\text{Ku})$, separated based on the rain-type information of the precipitation observed by the TRMM-PR in this case study: (a) all rain types; (b) stratiform rain with a bright band; (c) convective rain, and (d) stratiform rain without a bright band.	118
6.5	$Z_e(\text{Ku})$ and simulated $Z_e(\text{Ka})$ at three different horizontal cross-section heights above the surface: (a) and (b) for the rain region at 2 km, (c) and (d) for the melted particle (snow/graupel) region at 4.5 km, and (e) and (f) for the dry snow/graupel region at 6 km.	119
6.6	$Z_e(\text{Ka})$ and simulated $Z_m(\text{Ka})$ at 3 different horizontal cross-section heights above the surface. The (a) and (b) for the rain region at 2 km, (c) and (d) for the melted particles (snow/graupel) region at 4.5 km, and (e) and (f) for the dry snow/graupel region at 6 km.	120
6.7	Simulated path-integrated attenuation: (a) Ku-band; (b) Ka-band.	121
6.8	Location of vertical cross-section across TRMM ground track. Location A is stratiform rain and B is convective.	122
6.9	A vertical cross-section of stratiform rain, as indicated by the dashed line at A in Fig. 6.8: (a) $Z_e(\text{Ku})$; (b) the simulated $Z_m(\text{Ku})$; (c) the simulated $Z_e(\text{Ka})$; and (d) the simulated $Z_m(\text{Ka})$.	122
6.10	The difference between a vertical cross-section of $Z_e(\text{Ku})$ (Fig. 7.30 (a)) and the simulated $Z_e(\text{Ka})$ (Fig. 7.30 (c)) in stratiform rain.	123

6.11	Two vertical profiles of reflectivity in stratiform rain with a bright band, as indicated by two dashed lines in Fig. 7.30 (a). The dashed lines represent $Z_e(\text{Ku})$ and the simulated $Z_e(\text{Ka})$, while the solid lines represent the simulated $Z_m(\text{Ku})$ and $Z_m(\text{Ka})$	123
6.12	A vertical cross-section of: (a) $Z_e(\text{Ku})$; (b) simulated $Z_m(\text{Ku})$; (c) simulated $Z_e(\text{Ka})$, and (d) simulated $Z_m(\text{Ka})$, as indicated by the dashed line at B in Fig. 6.8 in the convective rain.	124
6.13	Two vertical profiles of reflectivity in convective rain, as indicated by the two dashed lines in Fig. 6.12 (a). The dashed lines represent $Z_e(\text{Ku})$ and the simulated $Z_e(\text{Ka})$, while the solid lines represent the simulated $Z_m(\text{Ku})$ and $Z_m(\text{Ka})$	125
6.14	A simple schematic diagram of the simulation procedure based TRMM-PR observations.	126
6.15	The simulation of $Z_e(\text{Ku})$ using KMLB measurements ($Z_e(\text{S})$) for three different height levels above the surface. In (a) and (b) the $Z_e(\text{S})$ and $Z_e(\text{Ku})$ at 2 km, (c) and (d) the $Z_e(\text{S})$ and $Z_e(\text{Ku})$ at 4.5 km, and (e) and (f) the $Z_e(\text{S})$ and $Z_e(\text{Ku})$ at 6 km.	128
6.16	The same as Fig. 6.15 for Ka-band	129
6.17	The horizontal cross-section of reflectivity at altitude of 1 km above the surface: (a) the $Z_e(\text{S})$ measurement from KMLB radar; (b) and (c) the simulated $Z_e(\text{Ku})$, and $Z_m(\text{Ku})$, respectively; (d) and (e) the simulated $Z_e(\text{Ka})$, and $Z_m(\text{Ka})$, respectively.	130
6.18	The vertical cross-section of reflectivity: (a) and (b) the horizontal and vertical cross-section of the $Z_e(\text{S})$ measurement from KMLB radar, respectively; (c) and (d) the vertical cross-section of the simulated $Z_e(\text{Ku})$ and $Z_m(\text{Ku})$, as indicated by the dashed line in (a), respectively; (e) and (f) the vertical cross-section of the simulated $Z_e(\text{Ka})$ and $Z_m(\text{Ka})$, as indicated by the dashed line in (a), respectively. . .	132

6.19	The vertical profiles of reflectivity: (a) a vertical cross-section of $Z_e(S)$ measurement from KMLB radar; (b) a vertical profile of the $Z_e(S)$, the simulated $Z_e(Ku)$, $Z_m(Ku)$, $Z_e(Ka)$, and $Z_m(Ka)$ for stratiform rain with a bright band, as indicated by the dashed line to the left of (a); (c) similar to (b) for the convective rain, as indicated by the dashed line to the right of (a).	133
6.20	The simulation of $Z_e(Ku)$ using KTBW measurements ($Z_e(S)$) for three different height levels above the surface. In (a) and (b) $Z_e(S)$ and $Z_e(Ku)$ at 2 km, (c) and (d) $Z_e(S)$ and $Z_e(Ku)$ at 4.5 km, and (e) and (f) $Z_e(S)$ and $Z_e(Ku)$ at 6 km.	135
6.21	The same as Fig. 6.20 for Ka-band.	136
6.22	The horizontal cross-section of reflectivity at an altitude of 1 km above the surface: (a) the $Z_e(S)$ measurement from KTBW radar; (b) and (c) the simulated $Z_e(Ku)$ and $Z_m(Ku)$, respectively; (d) and (e) the simulated $Z_e(Ka)$ and $Z_m(Ka)$, respectively.	137
6.23	The vertical cross-section of reflectivity: (a) and (b) the horizontal and vertical cross-section of $Z_e(S)$ measurement from KTBW radar, respectively; (b) and (c) the vertical cross-section of the simulated $Z_e(Ku)$ and $Z_m(Ku)$, as indicated by the dashed line in (a), respectively; (d) and (e) the vertical cross-section the simulated $Z_e(Ka)$ and $Z_m(Ka)$, respectively, as indicated by the dashed line in (a), respectively.	138
6.24	The vertical profiles of reflectivity: (a) a vertical cross-section of $Z_e(S)$ measurement from KTBW radar; (b) a vertical profile of the $Z_e(S)$, the simulated $Z_e(Ku)$, $Z_m(Ku)$, $Z_e(Ka)$, and $Z_m(Ka)$ for a stratiform rain with a bright band, as indicated by the dash line to the left of (a); (c) similar to (b) for the convective rain, as indicated by the dashed line to the right of (a).	139

6.25	The horizontal cross-section of the five dual-polarimetric radar measurements: (a) horizontal reflectivity (Z_h); (b) differential reflectivity (Z_{dr}); (c) correlation coefficient (ρ_{hv}); (d) specific differential phase (K_{dp}), and (e) linear depolarization ratio (LDR).	141
6.26	The vertical cross-section of the five dual-polarimetric radar measurements: (a) horizontal reflectivity (Z_h); (b) differential reflectivity (Z_{dr}); (c) correlation coefficient (ρ_{hv}); (d) specific differential phase (K_{dp}), and (e) linear depolarization ratio (LDR).	142
6.27	(a) The horizontal cross-section of reflectivity, (b) the horizontal cross-section of reflectivity particle type from fuzzy classification results, (c) the vertical cross-section of reflectivity, as indicated by the dashed line in (a), and (d) the vertical cross-section of particle type from fuzzy classification results, as indicated by the dashed line in (b).	143
6.28	(a) The vertical cross-section of hydrometeor type, (b) the vertical profiles of three polarimetric measurements, namely, LDR , ρ_{hv} , and Z_{dr} , (c) the vertical profile of $Z_e(S)$, the simulated $Z_e(Ku)$, and $Z_e(Ka)$, as indicated by the dashed line in (a), and (d) the vertical profile of the simulated $Z_e(Ku)$, $Z_m(Ku)$, $Z_e(Ka)$, and $Z_m(Ka)$, as indicated by the dashed line in (a).	144
7.1	Illustrating the regions (North Atlantic, Northwestern Pacific, and South Indian Ocean) where vertical structure profiles of hurricanes, typhoons and cyclones, respectively, were collected.	149
7.2	SOM (2x2) classification result of hurricanes. In each subfigure the solid line, dashed line, and dash-dot line represent the years 2000, 2002, and 2003, respectively. Percentage of occurrence for each class is also presented.	149
7.3	Same as Fig. 7.2 for typhoons.	150

7.4	Same as Fig. 7.2 for cyclones.	150
7.5	SOM (2x2) classification results of convective rain type of hurricanes. In each subfigure the solid line, dashed line, and dash-dot line represent the years 2000, 2002, and 2003, respectively. The percentage of occurrence for each class is also presented.	151
7.6	Same as Fig. 7.5 for typhoons.	152
7.7	Same as Fig. 7.5 for cyclones.	152
7.8	SOM (2x2) classification results of the stratiform rain type of hurricanes. In each subfigure the solid line, dashed-line and dash-dot line represent the years 2000, 2002 and 2003, respectively. The percentage of occurrence for each class is also presented.	153
7.9	Same as Fig. 7.8 for typhoons.	153
7.10	Same as Fig. 7.8 for cyclones.	154
7.11	SOM (2x2) classification result without rain-type separation in year 2000. In each subfigure, the solid line, dashed line, and dash-dot line represent hurricanes (H), typhoons (T), and cyclones (C), respectively. H, T and C indicate percentage of occurrence in each class.	155
7.12	Same as Fig. 7.11 for year 2002.	155
7.13	Same as Fig. 7.11 for year 2003.	156
7.14	Distribution and averaged value of height of BB peak from sea level of hurricane (H), typhoon (T), cyclone (C) and generic oceanic storm (O).	157
7.15	Distribution and averaged value of BB thickness of hurricane (H), typhoon (T), cyclone (C), and generic oceanic storm (O).	157
7.16	Distribution and averaged value of the reflectivity of BB peak of hurricane (H), typhoon (T), cyclone (C), and generic oceanic storm (O).	158
7.17	Distribution of (a) D_o and (b) $\log_{10}(N_w)$ for various rain rate intervals of cyclones in year 2002.	159
7.18	Same as Fig. 7.17 for typhoons.	160

7.19	Same as Fig. 7.17 for hurricanes.	161
7.20	Illustration of scatter plots of D_o vs. R, and N_w vs. R, the best fit of the mean D_o vs. mean R, the best fit of the mean N_w vs. mean R, averaged over two mm hr ⁻¹ rain rate interval, and D_o -R and N_w -R relations by SS and WT for convective rain of cyclones in year 2002. The panels (a), (c), and (e) are for D_o vs. R at 0.5, 2, and 3 km altitude, respectively. The panels (b), (d), and (f) are for N_w vs. R for 0.5, 2, and 3 km altitude, respectively.	163
7.21	Same as Fig. 7.20 for stratiform rain.	164
7.22	Illustration of scatter plots of D_o vs. R, and N_w vs. R, the best fit of the mean D_o vs. mean R, the best fit of the mean N_w vs. mean R, averaged over two mm hr ⁻¹ rain rate interval, and D_o -R and N_w -R relations by SS and WT for convective rain of typhoons in year 2002. The panels (a), (c), and (e) are for D_o vs. R at 0.5, 2, and 3 km altitude, respectively. The panels (b), (d), and (f) are for N_w vs. R for 0.5, 2, and 3 km altitude, respectively.	165
7.23	Same as Fig. 7.22 for stratiform rain.	166
7.24	Illustration of scatter plots of D_o vs. R, and N_w vs. R, the best fit of the mean D_o vs. mean R, the best fit of the mean N_w vs. mean R, averaged over two mm hr ⁻¹ rain rate interval, and D_o -R and N_w -R relations by SS and WT for convective rain of hurricanes in year 2002. The panels (a), (c), and (e) are for D_o vs. R at 0.5, 2, and 3 km altitude, respectively. The panels (b), (d), and (f) are for N_w vs. R for 0.5, 2, and 3 km altitude, respectively.	167
7.25	Same as Fig. 7.24 for stratiform rain.	168

7.26	A horizontal cross-section of $Z_e(\text{Ku})$, separated based on the rain-type information of Cyclone Nargis, observed by the TRMM-PR in this case study: (a) all rain types (b) stratiform rain with bright band (c) convective rain, and (d) stratiform rain without bright band.	169
7.27	$Z_e(\text{Ku})$ and simulated $Z_e(\text{Ka})$ at three different horizontal cross-section heights above the surface: (a) and (b) at 2 km, (c) and (d) at 4.5 km, and (e) and (f) at 6 km.	170
7.28	$Z_e(\text{Ka})$ and simulated $Z_m(\text{Ka})$ at 3 different horizontal cross-section heights above the surface. The (a) and (b) at 2 km, (c) and (d) region at 4.5 km, and (e) and (f) at 6 km.	171
7.29	Simulated path-integrated attenuation: (a) Ku-band; (b) Ka-band. . .	172
7.30	A vertical cross-section of stratiform rain, as indicated by the dashed line at A in Fig. 6.8: (a) $Z_e(\text{Ku})$; (b) the simulated $Z_m(\text{Ku})$; (c) the simulated $Z_e(\text{Ka})$; and (d) the simulated $Z_m(\text{Ka})$	173
7.31	The difference between a vertical cross-section of $Z_e(\text{Ku})$ (Fig. 7.30 (a)) and the simulated $Z_e(\text{Ka})$ (Fig. 7.30 (c)) in stratiform rain. . . .	174
7.32	Two vertical profiles of reflectivity—one for convective rain, and the other for stratiform rain with a bright band. The dashed lines represent $Z_e(\text{Ku})$ and the simulated $Z_e(\text{Ka})$, while the solid lines represent the simulated $Z_m(\text{Ku})$ and $Z_m(\text{Ka})$	174
A.1	(a) Incident wave direction, specified by \hat{k}_i , with $\hat{k}_i = \hat{\theta}_i \times \phi_i$. ; and (b) the scattered wave direction in forward scatter alignment (FSA), specified by \hat{k}_s , with $\hat{k}_s = \hat{\theta}_s \times \phi_s$. (adopted from Bringi and Chandrasekar (2001))	185

A.2	Unit vectors $(\hat{k}_r, \hat{v}_r, \hat{h}_r)$ with $\hat{k}_r = \hat{v}_r \times \hat{h}_r$ for the back scatter alignment (BSA) convention. Note that $\hat{k}_r = -\hat{k}_s$, $\hat{v}_r = \hat{v}_s$ and $\hat{h}_r = -\hat{h}_s$. The scattered wave propagates along the \hat{k}_s direction. The scattered field is resolved as either $\vec{E}^s = E_h^s \hat{h}_s + E_v^s \hat{v}_s$ in the FSA, or as $\vec{E}^r = E_h^r \hat{h}_r + E_v^r \hat{v}_r$ in the BSA. (adopted from (Bringi and Chandrasekar, 2001))	186
A.3	Scattering direction and unit vectors of an incident plane wave in the FSA (adopted from Bringi and Chandrasekar (2001))	188

LIST OF TABLES

2.1	Size distribution parameters of various hydrometeor type	17
2.2	Densities and water fraction	17
2.3	The coefficients of $Z_e(Ku) = a + bZ_e(S)$ and $k(Ku) = \alpha Z_e(Ku)^\beta$ relations.	24
2.4	The coefficients of $Z_e(Ka) = a + bZ_e(S)$ and $k(Ku) = \alpha Z_e(Ku)^\beta$ relations.	25
2.5	The coefficients of $Z_e(Ka) = a + bZ_e(Ku)$ relations.	26
3.1	Precipitation radar (PR) specifications.	32
3.2	NCAR S-Band Polarization Radar (S-Pol) Characteristics	57
4.1	Main characteristics of DPR.	66
4.2	Coefficients a and b of the $k = aR^b$ relation based on simulation data for three different values of μ . A-U refers to resultant coefficients based on disdrometer measurement from Atlas and Ulbrich (1977).	77
5.1	APR-2 characteristics (Tanelli et al. (2004)).	93
5.2	The coefficients of $Z_e(Ka) = a + b^*Z_e(Ku)$ and $k(Ka) = \alpha^*Z_e(Ka)^\beta$ relations for dry snow as a function of height above the bright band. . .	112
B.1	The coefficients of $Z_e(Ku) = a + bZ_e(S)$ and $k(Ku) = \alpha Z_e(Ku)^\beta$ relations for dry snow as a function of height above the bright band. . .	194
B.2	The coefficients of $Z_e(Ka) = a + bZ_e(S)$ and $k(Ka) = \alpha Z_e(Ka)^\beta$ relations for dry snow as a function of height above the bright band. . .	195

B.3	The coefficients of $Z_e(Ka) = a + bZ_e(Ku)$ relations for dry snow as a function of height above the bright band.	196
B.4	The coefficients of $Z_e(Ku) = a + bZ_e(S)$ and $k(Ku) = \alpha Z_e(Ku)^\beta$ relations for wet snow as a function of height above (+) and below (-) bright band peak.	196
B.5	The coefficients of $Z_e(Ka) = a + bZ_e(S)$ and $k(Ka) = \alpha Z_e(Ka)^\beta$ relations for wet snow as a function of height above (+) and below (-) the bright band peak.	197
B.6	The coefficients of $Z_e(Ka) = a + bZ_e(Ku)$ relations for wet snow as a function of height above (+) and below (-) the bright band peak. . .	197
B.7	The coefficients of $Z_e(Ku) = a + b^*Z_e(S)$ and $k(Ku) = \alpha^*Z_e(Ku)^\beta$ relations for rain as a function of height below the bright band. . . .	198
B.8	The coefficients of $Z_e(Ka) = a + b^*Z_e(S)$ and $k(Ka) = \alpha^*Z_e(Ka)^\beta$ relations for rain as a function of height below the bright band. . . .	199
B.9	The coefficients of $Z_e(Ka) = a + b^*Z_e(Ku)$ relations for rain as a function of height below the bright band.	200
B.10	The coefficients of $Z_e(Ku) = a + bZ_e(S)$ and $k(Ku) = \alpha Z_e(Ku)^\beta$ relations for dry graupel as a function of height above the melting layer.201	
B.11	The coefficients of $Z_e(Ka) = a + bZ_e(S)$ and $k(Ka) = \alpha Z_e(Ka)^\beta$ relations for dry graupel as a function of height above the melting layer.202	
B.12	The coefficients of $Z_e(Ka) = a + bZ_e(Ku)$ relations for dry graupel as a function of height above the melting layer.	203
B.13	The coefficients of $Z_e(Ku) = a + b^*Z_e(S)$ and $k(Ku) = \alpha^*Z_e(Ku)^\beta$ relations for wet graupel as a function of height above (+) and below (-) the center of the melting layer.	203
B.14	The coefficients of $Z_e(Ka) = a + b^*Z_e(S)$ and $k(Ka) = \alpha^*Z_e(Ka)^\beta$ relations for wet graupel as a function of height above (+) and below (-) the center of the melting layer.	204

B.15	The coefficients of $Z_e(Ka) = a + b*Z_e(Ku)$ relations for wet graupel as a function of height above (+) and below (-) the center of the melting layer.	204
B.16	The coefficients of $Z_e(Ku) = a + b*Z_e(S)$ and $k(Ku) = \alpha*Z_e(Ku)^\beta$ relations for rain as a function of height below the melting layer.	205
B.17	The coefficients of $Z_e(Ka) = a + b*Z_e(S)$ and $k(Ka) = \alpha*Z_e(Ka)^\beta$ relations for rain as a function of height below the melting layer.	206
B.18	The coefficients of $Z_e(Ka) = a + b*Z_e(Ku)$ relations for rain as a function of height below the melting layer.	207

CHAPTER 1

INTRODUCTION

1.1 Introduction

Precipitation observation from space took its first step when the Tropical Rainfall Measurement Mission (TRMM) satellite was launched in November 1997. TRMM is a joint mission between the National Aeronautic and Space Administration (NASA) of USA and the Japanese Aerospace Exploration Agency (JAXA). One of the scientific objectives of TRMM is to provide quantitative measurement of rainfall in tropical and sub-tropical regions (Kummerow et al., 2000), where two-thirds of global precipitation falls (Hanado and Ihara, 1992). TRMM is considered an outstanding example of scientific success and of U.S.-Japanese collaboration in conducting Earth observations from space because it is capable of providing unprecedented global precipitation measurement that can benefit society. There are several types of sensors on board TRMM, including Precipitation Radar (PR) (Kummerow et al., 1998). PR is the first rain space-based radar (Iguchi, 2003; Kozu et al., 2001). PR operates at a single frequency of 13.8 GHz (2.17 cm wavelength) at Ku-band. The TRMM had an operating altitude of 350 km since it was launched. In August 2001, it was boosted to 402 km; that increased the horizontal resolution of the PR at nadir from 4.3 km to 5 km and swath width from 215 km to 245 km.

PR can provide three-dimensional downward-looking observations of precipitation with a high vertical resolution, and has been measuring global precipitation in the

tropics since the satellite was launched. Products from the PR help advance our understanding of precipitation on a global scale in term of storm structure and global variation as well as storm microphysics (Kummerow et al., 2000). In recent years, extensive progress on developing techniques and methodologies has been made in comprehension of the characteristics and microphysical structure of precipitation, specifically in the context of TRMM PR observations. A part of such progress was achieved through a set of independent measurements from TRMM ground validation sites, both ground-based radars and rain gages, as well as TRMM-filed experiments .

Following the success of TRMM, a next generation of space-based radar for precipitation observation has been proposed. Global precipitation measurement (GPM) has been planned to be the next space-based precipitation observation system. GPM has the following main scientific objectives: improved climate prediction, improved weather predictions, and global water cycle and hydrological predictions. Dual-frequency Precipitation Radar (DPR) operating at 13.6 GHz (Ku-band) and 35.6 GHz (Ka-band) has been planned to be on board the GPM core satellite. The Ku-band radar is virtually the same as the PR on TRMM, with some improvements (Iguchi, 2003). In addition to the core satellite, GPM will comprise up to 10 constellation satellites carrying microwave radiometers that will be used together to passively monitor precipitation structures approximately every three hours. The capabilities of the DPR are expected to exceed those of the PR on TRMM. This radar will be capable of making measurements of light rain and frozen precipitation present in higher latitudes because of high sensitivity of detection at the Ka-band channel. The DPR is also expected to provide to certain amount of hydrometeor discrimination ability (Iguchi, 2003). The overall goal of the DPR is to improve accuracy in estimation of drop size distribution (DSD) parameters of precipitation and hence potentially more accurate rainfall rate estimate. The combination of data from the two channels, in principle, can provide more accurate estimates of DSD parameters than the TRMM PR. A number of dual-frequency retrieval approaches have been proposed (Meneghini

et al., 1992, 1997; Iguchi and Meneghini, 1995; Mardiana et al., 2004; Iguchi, 2005; Rose and Chandrasekar, 2006a). Like TRMM, the GPM ground validation program will serve as a major validation source for evaluating performance of the retrieval techniques and their accuracy.

For GPM to reach its scientific objectives, all information, knowledge, and resources need to be integrated. Experience from the TRMM-PR and its validation program can be exploited to help DPR reach its ultimate goals. Long-term precipitation observation of PR provides us with statistical characteristics of precipitation for different regimes on a global scale, which is useful for designing the DPR system and retrieval algorithms. The earth-based radar measurements, including ground radars and airborne radars, can also play an important role as a great resource for developing the GPM-DPR system.

1.2 Literature Review

1.2.1 Analysis of single-frequency TRMM-PR Observations

Since launching TRMM in late 1997, a number of studies based on TRMM-PR observations have been reported in the literature, such as Bolen and Chandrasekar (2000); Shin et al. (2000); Meneghini et al. (2002); Peterson and Rutledge (2001); Fukatsu and Chandrasekar (2002); Chandrasekar et al. (2003a); L'Ecuyer et al. (2003); Schumacher and House (2003); Bolen and Chandrasekar (2003); Zafar and Chandrasekar (2004); Chandrasekar et al. (2005). Bolen and Chandrasekar (2000) developed methodologies to align the PR and polarimetric radar data on the ground to perform reflectivity profiles and geophysical cross-validation. Such methodology enables evaluation of the TRMM-PR attenuation correction algorithm. Zafar and Chandrasekar (2004) implemented a method for classification of vertical profiles of reflectivity (VPR) using self-organizing map (SOM) technique. They have used SOM to build statistics of characteristics of bright band (BB) in global scale. Based on

VPR classification using SOM, regional and seasonal comparison of VPR has been well investigated and interpreted from a number of different perspectives.

Fukatsu and Chandrasekar (2002) and Chandrasekar et al. (2003a) used the TRMM-PR data to generate global attenuation maps at several frequencies, such as Ka-band. Given TRMM-PR observations, they built monthly maps of attenuation on global scale. To be able to perform such attenuation maps, they assumed simple model of microphysical structures along the height of precipitation in both stratiform and convective rain types. They found that although the simple model may not provide an accurate description of the space-time microphysical structure of precipitation, it is sufficient for studying the bulk attenuation properties. They used TRMM-PR observation to develop monthly maps of attenuation at Ka-band (35 GHz). They showed that on the surface, the average path-integrated attenuation can be of an order of 30 dB at Ka-band, and it can be easily peak to values in excess of 50 to 60 dB. In addition, they used combination of parameterization for Ka-band reflectivity and attenuation to create maps of simulated reflectivity observations at Ka-band. Based on that simulation, they mapped percentages of observations missed at Ka-band due to the attenuation.

1.2.2 Convective/stratiform rain type

Convective rain, in general, is defined as precipitation that has a strong vertical air motion, small (1-10 km horizontal dimension), intense, horizontally inhomogeneous radar reflectivity, and typically produces a rainfall rate higher than 5 mm hr^{-1} (House, 1997; Schumacher and House, 2003). In contrast to convective rain, stratiform rain is defined as precipitation that has a weak vertical air motion and produces a widespread, homogeneous layer of radar echo. Typically, stratiform rain produces less than 5 mm hr^{-1} rainfall rate (House, 1997; Schumacher and House, 2003). Bright band (BB) is a radar signature and an indication of stratiform rain type. BB is denoted by a sharp increase of the vertical reflectivity profile caused by an increase

of dielectric constant, and hence an increase in the back-scattering cross-section of melted ice particles.

The characteristics of convective and stratiform rain rates have received significant attention since the launch of TRMM (House, 1997). Another study (Schumacher and House, 2003) across the tropics using TRMM-PR indicates that stratiform precipitation accounts for 73% of the area covered by rain and 40% of the total rain amount. The ratio of the convective rain rate to the stratiform rain rate is 4:1 on average at the horizontal resolution of the PR data. Research reported in the literature shows that the ocean environment appears more efficient in the production of stratiform precipitation than the land environment. In addition, some studies show that factors such as wind shear and the relative humidity of the large-scale environment can also affect the production of stratiform rain. The vertical structure of reflectivity between the two rain type has also been studied by several researchers. Schumacher and House (2003) found that over land and ocean, stratiform reflectivity profiles tend to be constant with height below $0^{\circ}C$ level. Over the tropical oceans, the convective reflectivity increase toward the surface while over land in the tropics, the maximum in the convective profile is somewhere between the surface and the $0^{\circ}C$ level.

1.2.3 Dual-polarization ground-based radar measurements

Polarimetric radar provides accurate rainfall rate estimation, and is capable of discriminating among phase-state and type of precipitation particles (Bringi and Chandrasekar, 2001). Discrimination among the particles is valuable not only for precipitation physics, but an important step prior to application of precipitation algorithms as well (Chandrasekar et al., 2003b). Five basic polarimetric radar measurements are horizontal reflectivity (Z_h), differential reflectivity (Z_{dr}) specific differential phase (K_{dp}), linear depolarization ratio (LDR), and correlation coefficient (ρ_{hv}). These measurements are useful for classifying hydrometeor type. For a particle of a given size, in general ice produces lower Z_h than liquid because of lower dielectric constant.

Z_{dr} is a good discriminator between oblate rain and more spherical hail. The sharp change in Z_{dr} occurs near the $0^{\circ}C$ isotherm and marks the transition between ice particles and water (Bringi and Chandrasekar, 2001). K_{dp} can be used to isolate the presence of rain from isotropic hydrometeors such as tumbling hail. Wet non-spherical particles such as melting snow and wet graupel can be identified with large LDR values, whereas drizzle, and dry ice particles are associated with low LDR values. In the case of melting particles (wet graupel or wet snow) conditions, ρ_{hv} drops lower than the high value seen in rain.

1.2.4 Satellite-based radio-wave propagation at high frequencies

Radio-wave propagation at high frequencies such as Ka-band has seen increasing interest not only in satellite-based communications, but also in space-based radar remote sensing. One of most recognized problems of the propagation of electromagnetic waves through precipitation at high frequency bands is the loss of the signal power due to attenuation. At Ka-band, rain, clouds, and even gaseous attenuation can significantly degrade the signal. Rain can easily cause 20-30 dB of attenuation at Ka-band frequencies. There has been a number of studies reported in the literature attempting to investigate, model, and eventually construct a statistical characteristics of precipitation attenuation effect such as Cox (1978); Ippolito (1981). Cherry et al. (1981) and Goddard et al. (1994) used dual-polarization ground-based radar measurements to study propagation effect along earth-satellite path. Beaver and Bringi (2003) used dual-polarization measurement from a S-band ground-based radar to predict the attenuation along the propagation path at Ka-band (20 GHz and 27 GHz).

1.2.5 Dual-frequency space-based precipitation radar

The global precipitation measurement (GPM) satellite will carry a dual-frequency precipitation radar (DPR) that operates at Ku- and Ka-band frequency. Unlike

TRMM, DPR will provide two independent measurements of precipitation from the two frequencies. With the additional information, dual-frequency techniques will be used to improve rainfall rate estimate. As mentioned earlier, there have been a number of dual-frequency methods proposed for GPM. They can be categorized into two types. One is a standard dual-frequency method based on the conversion of differential attenuation estimates to rain rate (Meneghini et al., 1989) and the other is based on reflectivity, which is corrected for attenuation, and DSD parameters are inferred by non-Rayleigh scattering. The second type can be formulated either in integral equations (Meneghini et al., 1997) or first-order differential equation (Iguchi and Meneghini, 1995).

The integral equation can be solved in either forward direction (forward method) or a backward direction (backward method). In the forward method, DSDs are calculated at each bin starting from the top bin and moving to the bottom. The backward method begins at the bottom bin and moves upward to the top, calculating the DSD parameters and attenuation along the path. The assumption with the forward method is that there is no attenuation above the top bin and that the integral equations can be solved in a single pass along the vertical profiles. Forward methods have limited application because of a tendency to diverge in regions of moderate to heavy attenuation (moderate to heavy rainfall). Backward calculation algorithms tend to be more stable than the forward types but generally require an a priori knowledge of the total path-integrated attenuation (PIA). The backward method can also be solved iteratively without SRT (Mardiana et al., 2004; Rose and Chandrasekar, 2006a,b). This technique randomly initializes the PIA at the bottom and solves recursively for DSDs along the path upward to the top. The iterations stop when retrieved DSDs can reconstruct the measured reflectivity at the bottom bin. The limitation of this technique is that it fails when the a large PIA is present (a combination of large D_o and N_w). Rose and Chandrasekar (2006a) used linear N_w model along the rain profile as a constraint to remedy this problem to some extent.

1.3 Statement of Problem

Dual-frequency precipitation radar (DPR) has been proposed for the core satellite in the GPM mission. The radar system is planned to operate at 13.6 GHz (Ku-band) and 35.6 GHz (Ka-band). The research community has experience working with Ku-band (13.6 GHz) observations from space. DPR will be the first dual-frequency spaceborne precipitation radar and the Ka-band observation in particular will be new. Since spaceborne precipitation radar observations have never been done in Ka-band before, extensive research work on dual-frequency radar, including electromagnetic wave propagation characteristics from space and retrieval algorithms are essentially required in developing and evaluating system design and instrument performance evaluations. A number of research articles on space-based dual-frequency radar have been reported in the literature in the past three decades.

Most of the research on the space-based dual-frequency radar retrieval methods were either theoretical or were based on dual-frequency observations from airborne radar experiments. Theoretical studies of dual-frequency radar observations typically were performed based on simple reflectivity profiles with assumed simple DSD parameters. Such studies often cannot represent the realistic situations and have limitations and unrealistic error evaluation. A dual-frequency airborne radar that is designed to emulate DPR, was deployed in a number of experiments and data were analyzed in several studies. Data from airborne experiments can provide information that can be used to improve the modeling of precipitation microphysics.

Data from dual-polarization ground-based radars from ground validation programs and field experiments, can also provide microphysical information about precipitation, and can be used to simulate what would be observed by DPR. During the GPM era there are going to be numerous dual-polarization radars around the globe that will be observing precipitation. If there is a way that one could use this ground-based dual-polarization radar observation to simulate spaceborne dual-frequency measurements,

we would have a globally diverse data set to use in system development, algorithm development, and validation. There are numerous assumptions in the algorithms, and the retrievals are based on our current understanding of the microphysical processes and our ability to model them accurately. One such example is the accuracy of retrieved DSD parameters using dual-frequency retrieval algorithms that rely strongly on correct identification of phase-height transition (PHT) from frozen to liquid hydrometeor along a vertical profile of reflectivity (VPR). It is important to understand how these various features manifest themselves in dual-frequency measurements.

Experiences from Ku-band TRMM-PR observations make it possible to simulate dual-frequency observations as if the observations were made by DPR on a global scale. Applying dual-frequency retrieval algorithms to simulated data will offer preliminary evaluation in feasibility, applicability, and generalization of retrieval algorithms as well as their uncertainty and errors. Since each algorithm has its strengths and weaknesses, a particular retrieval algorithm may perform well or may be completely inapplicable on a particular type of VPR or storm condition. It may be that more than one algorithm needs to be combined to achieve the most accurate estimate. In cases of intense rain where attenuation in Ka-band frequency becomes significant, loss of signal could occur. As a result, dual-frequency retrieval algorithms may not be applicable. Analyzing globally simulated DPR observations will equip us with the ability to evaluate the DPR algorithms. The surface reference technique (SRT) (Meneghini et al., 2000) provides a promising attenuation correction algorithm used in TRMM-PR. Measurement of a difference of surface cross-section between the presence and absence of rain ($\Delta\sigma^o$) in Ku-band could provide an idea of $\Delta\sigma^o$ in measurement of Ka-band, which is an important quantity for single (TRMM-like) and dual-frequency retrieval algorithms.

This research attempts to address the unique and specific problems that exist in space-based radar observations. In particular, this research focuses on developing a technique for simulating DPR observations. Extensive experimental verification in a

wide range of regions will be needed to validate the usability of the new developed technique.

The primary goal of this research is to develop methodologies to simulate global observations of precipitation that would be observed by dual-frequency (Ku and Ka-band) spaceborne precipitation radar (DPR), which is planned on board the Global Precipitation Measurement (GPM) satellite. The simulation will be conducted based on ground-based radar, dual-frequency airborne radar observations and global TRMM-PR (single-frequency spaceborne precipitation radar) observations. Micro-physical structures will be retrieved and correlated with reflectivity observations to improve the simulation model. Simulated Ku-band and Ka-band observations will be used to evaluate applicability of dual-frequency retrieval techniques.

1.4 Objectives of Research

The following are the main objectives of this research:

- To extensively analyze precipitation measurement observed by TRMM-PR. Global vertical profiles of reflectivity (VPR) and associated drop size distribution (DSD) parameters will be studied. A self-organizing map (SOM) technique will be used to characterize VPR on a global scale. To obtain seasonal and regional variation of VPR, the classification technique will be carried out over different time scales, e.g., monthly and annual base, and studying different regions of both land and ocean, and for different rain types. In the stratiform rain type, global variation of bright band structure and its properties will be studied. Tropical storms, namely, cyclones, hurricanes, and typhoons, will be studied and comparisons of their vertical structure and microphysics will be made.
- To estimate drop size distribution (DSD) parameters based on the global observation of TRMM-PR. Characteristics of VPR associated with their DSD will

be investigated. The DSD parameters estimated from the TRMM-PR observations will be compared with those estimated from a dual-polarization radar measurements for a validation purpose.

- To study the relationship of radar reflectivity (Z_e) and specific attenuation (k) between different operating radar frequencies, namely, S-band (2.7 GHz), Ku-band (13.6 GHz) and Ka-band (35.6 GHz). The radar reflectivity and specific attenuation will be computed based on theoretical model of precipitation microphysics and scattering. The relations between Z_e and k and variability of Z_e with frequency will be modeled. Coefficients of the constructed relation models for various types of hydrometeor will be calculated.
- To study the use of S-band single and dual-polarization radar measurements to simulate VPR in Ku and Ka band that would be observed by dual-frequency precipitation radar (DPR). Improved understanding of inter-connection between radar reflectivity profiles and their microphysical variation is explored.
- To analyze dual-frequency (Ku and Ka-band) airborne radar data, and generate a microphysical model for the simulation.
- To eventually integrate knowledge gained from simulation of dual-frequency downward-looking radar observations from dual-polarization S-band radar observations, dual-frequency airborne radar analysis, and TRMM-PR observations, thus improving the realistic simulation of global Ka-band radar observations, which is the key to this work.
- To evaluate feasibility and applicability the dual-frequency retrieval algorithms based on simulated Ka-band and Ku-band radar observations.

CHAPTER 2

THEORETICAL BACKGROUND OF SPACE AND EARTH-BASED RADAR OBSERVATIONS : ELECTROMAGNETICS AND MICROPHYSICS

2.1 introduction

Electromagnetic wave propagation through precipitation media and their scattering by precipitation particles is of fundamental importance in understanding the signal returns from both space and earth-based radar observations. Microphysical properties of precipitation such as size distribution are the underlying link between radar observations and meteorological properties, and are important in determining characteristics of precipitation (Meneghini and Kozu, 1990; Oguchi, 1983). Radar parameters, such as the equivalent reflectivity factor and specific attenuation, can be computed based on theoretical models of precipitation microphysics. Once radar parameters are computed, a theoretical relation between them can be constructed, such as cross-frequency reflectivity. This chapter describes a theoretical framework in interpreting scattering characteristics of electromagnetic wave by precipitation particles for space-based radar observations. The chapter starts with a discussion of scattering of electromagnetic wave by dielectric sphere. The scattering matrix components, which are the basis of radar parameters calculations, are given in both Rayleigh and Mie scattering. Extinction and back scatter cross-sections are formed as a function of scattering components. Particle size distribution (PSD) model of precipitation is

discussed. Then, specific attenuation (k) and radar reflectivity (Z_e) are expressed in the integral form of extinction and back scatter cross-sections over PSD, respectively. Model relations of k - Z_e and variability of Z_e with frequency for different types of precipitation (e.g., ice particle, raindrop) are determined and coefficients of the models are presented. The chapter ends with a description of a methodology for the simulation of vertical profile of reflectivity.

2.2 Microphysical Model of Precipitation: Particle Size Distribution (PSD)

The size distribution of precipitation particles plays an important role in generating radar parameters of precipitation. The radar reflectivity factor and specific attenuation can be computed by the integral of the radar cross-section and extinction cross-section, respectively, over size distribution of hydrometeor. One of the scientific objectives of dual-frequency precipitation radar (DPR) in the Global Precipitation Measurement (GPM) mission is to improve the accuracy of PSD retrieval.

Ulbrich (1983) has shown that a gamma distribution model can adequately describe much of the natural variability in the raindrop size distribution (DSD). The normalized form of gamma DSD model (Testud et al., 2001; Bringi et al., 2004) can be expressed as

$$N(D) = N_w f(\mu) \left(\frac{D}{D_o} \right)^\mu e^{-\Lambda D} \quad (2.1)$$

where

$$\Lambda = \frac{3.67 + \mu}{D_o} \quad (2.2a)$$

$$f(\mu) = \frac{6}{3.67^4} \frac{(3.67 + \mu)^{\mu+4}}{\Gamma(\mu + 4)} \quad (2.2b)$$

$N(D)$ ($mm^{-3}m^{-1}$) is the number of raindrops per unit volume per unit size in diameter interval D (mm) and $D+\Delta D$ (mm), N_w ($mm^{-3}m^{-1}$) is the normalized intercept parameter of an equivalent exponential DSD (which has the same water content as the gamma DSD), μ is the shape factor, and Λ (mm^{-1}) is the slope parameter. D_o

(mm) is the median volume diameter in (mm), and $\Gamma()$ represents gamma function. D_o is defined such that precipitation particles up to size D_o contribute to half the rainwater content.

Three critical parameters of the hydrometeor size distribution, namely μ , D_o , and N_w , control the hydrometeor size distribution, and varying them over a wide range of naturally observed values yields a physically realistic simulation of derived parameters such as radar reflectivity and attenuation.

2.3 Computation of Attenuation and Radar Reflectivity

2.3.1 Extinction cross-section and specific attenuation

Attenuation caused by precipitation is determined by the extinction cross-section (σ_{ext}) of particles. σ_{ext} represents the loss of power when electromagnetic waves propagate through precipitation. The two components comprising extinction cross-sections are absorption and scattering of incident wave by the particles. In Rayleigh scattering, where the radar wavelength is much larger than the particle size the absorption cross-section of a spherical drop is proportional to its volume and it dominates the extinction cross-section.

The extinction cross-section is given as,

$$\sigma_{ext} = \frac{-4\pi}{k_o} \text{Im} \vec{f}(\hat{i}, \hat{i}) \cdot \hat{e}_i \quad (2.3)$$

where Im denotes imagine part, \vec{f} is the scattering amplitude, k_o is the size parameter. A complete discussion and expressions of σ_{ext} in term of \vec{f} and scattering matrix components for Rayleigh and Mie scattering are given in the Appendix A. The specific attenuation of a propagating wave through a volume of precipitation particles can be expressed in an integral form of the extinction cross-section over PSD as,

$$k = 4.343 \times 10^3 \int_D \sigma_{ext}(D) N(D) dD \quad dBkm^{-1} \quad (2.4)$$

2.3.2 Backscatter cross-section and radar reflectivity

The backscatter or radar cross-section is defined as,

$$\sigma_b(-\hat{i}, \hat{i}) = 4\pi |\vec{f}(-\hat{i}, \hat{i})|^2 \quad (2.5)$$

A complete discussion and expressions of σ_b in term of \vec{f} and scattering matrix components for Rayleigh and Mie scattering are given in the Appendix A.

The reflectivity factor Z is defined as:

$$Z = \frac{\lambda^4}{\pi^5 |K|^2} \int_D \sigma_b(D) N(D) dD \quad (2.6)$$

In Rayleigh scattering, (2.6) simplifies to

$$Z = \int_D N(D) D^6 dD \quad (2.7)$$

This means that, for the Rayleigh limit, the reflectivity factor is approximated to be the sixth moment of the PSD.

If the reflectivity factor at a range r from the radar is $Z_e(r)$, then the measured reflectivity ($Z_m(r)$) and $Z_e(r)$ are related through,

$$Z_m(r) = Z_e(r) \exp \left[-0.2 \ln 10 \int_0^r k(s) ds \right] = Z_e(r) A(r) \quad (2.8)$$

where k is the specific attenuation and $A(r)$ is the two-way path integrated attenuation factor from radar up to range r .

Dual-frequency precipitation radar (DPR), planned on board the GPM satellite, operates at Ku- and Ka-band, which are the frequency bands where precipitation attenuation is significant. The observations from the DPR will be the attenuated version (measured reflectivity) of the intrinsic reflectivity. If there is a way that ones could generate the vertical profiles of the “measured” reflectivity using (2.8) as if they were observed by the DPR, it would be important and useful to study characteristics of precipitation observed by a dual-frequency space-based radar, and will be of use for system designs and retrieval algorithms of the DPR. This research attempts to

develop a procedure to simulate vertical profiles of the intrinsic reflectivity, specific attenuation and hence the measured reflectivity at Ku and Ka-band. Theoretical variability of the intrinsic reflectivity and the specific attenuation with frequency of precipitation, which will be discussed in the next section, are the key for developing such methodology.

2.4 Variability of Reflectivity with Frequency and Specific Attenuation and Reflectivity Relation

Theoretical computations of the specific attenuation and reflectivity described in previous sections were performed for various precipitation particles types such as rain, graupel (densely-rimed snow (Zawadzki et al., 2005)) and snow. The ranges of particle size distribution parameters used in the computation as shown in Table 2.1 were chosen from a wide variety of published observations of particle size distributions (Sekhon and Srivastava, 1970; Beheng, 1978; Passarelli, 1978; Pruppacher and Klett, 1997; Bringi et al., 1997; Gorgucci et al., 2002; Bringi et al., 2003; Liao et al., 2005). The shape parameter of the Gamma model changes from -0.99 to 4 for rain, whereas it is kept at 0 for all ice and melted-ice particles, implying exponential distribution (see section 2.2). Table 2.2 shows the variation of densities and fractional volume content of water (simply water fraction (wf)) used in the computations. The density of snow and graupel ranges from 0.05 to 0.5 g/cm^3 (Matrosov, 1992; Bringi and Chandrasekar, 2001; Liao et al., 2005; Zawadzki et al., 2005). The water fraction of melted snow and graupel are varied from 0.01 to 0.85 (Awaka et al., 1985; Thurai et al., 2001), and the density of melted particles varies with the water fraction.

The dry snowflake and graupel were model as two-phase mixture of air and ice. The effective dielectric permittivity (ϵ_{eff}) was computed using Maxwell-Garnet mixing formula (Meneghini and Liao, 1996; Bringi and Chandrasekar, 2001). The ice was the inclusion, and air is the matrix. The melted particles are modeled as a three-phase mixture of air, ice and water. The computation of the ϵ_{eff} of melted particles

was computed (also using Maxwell-Garnet mixing formula) was done in two steps. In step one, the water is the inclusion, and the the ice is the matrix. In step 2, the effective dielectric permittivity from the first step was the inclusion, and air is the matrix. The spherical model was used for all particles.

About 1000 samples of each type of hydrometeor mentioned above were generated. After generating distribution parameters samples for each hydrometeor type, the reflectivity factor and the specific attenuation k were computed using (2.6) and (2.4), respectively, at three frequency bands, namely, S-band (2.7 GHz), Ku-band (13.8 GHz), and Ka-band (35.6 GHz).

Table 2.1: Size distribution parameters of various hydrometeor type

Hydrometeor Type	$D_o(mm)$	$N_w(mm^{-1}m^{-3})$	μ
Rain	$0.5 \leq D_o \leq 2.5$	$3.0 \leq \log N_w \leq 5.0$	$-0.99 \leq \mu \leq 4.0$
Melted particles	$1.0 \leq D_o \leq 2.5$	$2.0 \leq \log N_w \leq 4.0$	0
Snow/graupel	$0.5 \leq D_o \leq 3$	$2.0 \leq \log N_w \leq 4.0$	0

Table 2.2: Densities and water fraction

Hydrometeor Type	Density (ρ)	Water fraction (wf)
Rain	1.0	-
Melted particles	vary with WF	0.01 - 0.85
Snow/graupel	0.05 - 0.5	-

A number of following figures show simulation results of reflectivity comparison and k - Z_e relation at the three frequency bands for different type of hydrometeors. Here, four categories for hydrometeor were used, namely snow, graupel with densities from 0.05 to 0.4, melted snow/graupel with various water fractions, and rain. The figures show the scatter plots of reflectivity between the two frequencies and specific attenuation vs.. reflectivity factor (k - Z_e) and theirs best fitting. Linear model ($Z_e(f_2) = a + b \times Z_e(f_1)$) fit was used to approximate reflectivity variation across frequency bands while a power law model was best fit for k - Z_e relation ($k = \alpha Z_e^\beta$).

Figure 2.1 shows scatter plot of variability of Z_e with frequency and scatter plot of Z_e vs. k for dry snow with density of 0.2 g cm^{-3} . The panels (a) to (e) shows $Z_e(\text{S})$ vs. $Z_e(\text{Ku})$, $Z_e(\text{S})$ vs. $Z_e(\text{Ku})$, $Z_e(\text{Ku})$ vs. $Z_e(\text{Ka})$, $Z_e(\text{Ku})$ vs. $k(\text{Ku})$, $Z_e(\text{Ka})$ vs. $k(\text{Ka})$, respectively. The solid line in each plot is the best fit. It is clear from Fig. 2.1 that the reflectivity plots between two frequency bands can be fitted by a simple linear model and that scatter plot of Z_e vs. k can be fitted by a power law model. As seen from Fig. 2.1 (d) and (e), the specific attenuation of snow in Ku-band ($k(\text{Ku})$) is very small and often negligible. Although, $k(\text{Ka})$ is much higher than $k(\text{Ku})$ for a given Z_e , it still relatively small for dry snow particles.

Figures 2.2 shows scatter plot of variability of Z_e with frequency and scatter plot of Z_e vs. k for dry graupel with density of 0.4 g cm^{-3} . The linear relations of reflectivity variability with frequency are apparent. The $k(\text{Ku})$ remains small although there is a sharp increase above 40 dBZ of Z_e . In this particular example, the maximum $k(\text{Ku})$ is about 0.4 dB km^{-1} at Z_e of about 50 dBZ. The $k(\text{Ka})$ becomes more significant.

Figures 2.3 and 2.4 show scatter plot of Z_e between frequencies and scatter plot of Z_e vs. k for melted graupel with water fraction of 0.2 and 0.6, respectively. It is obvious from the figures that the attenuation effect becomes significant with the increase of the water fraction. The attenuation becomes most severe when the frozen particles completely melt to raindrops, as shown in Fig. 2.5. The specific attenuation of rain in Ka-band can be as high as 40 dB km^{-1} at $Z_e(\text{Ka})$ of about 50 dBZ.

The estimated coefficients a and b of $Z_e(f_2) = a \times Z_e(f_1) + b$ relation, and α and β of $k = \alpha Z^\beta$ for the three frequencies for different hydrometeor types are shown in Table 2.3 to 2.5. Dry snow and graupel have different densities (ρ). Melted graupel and snow have different water fraction. Rain has different shape factor of the raindrops size distribution, μ .

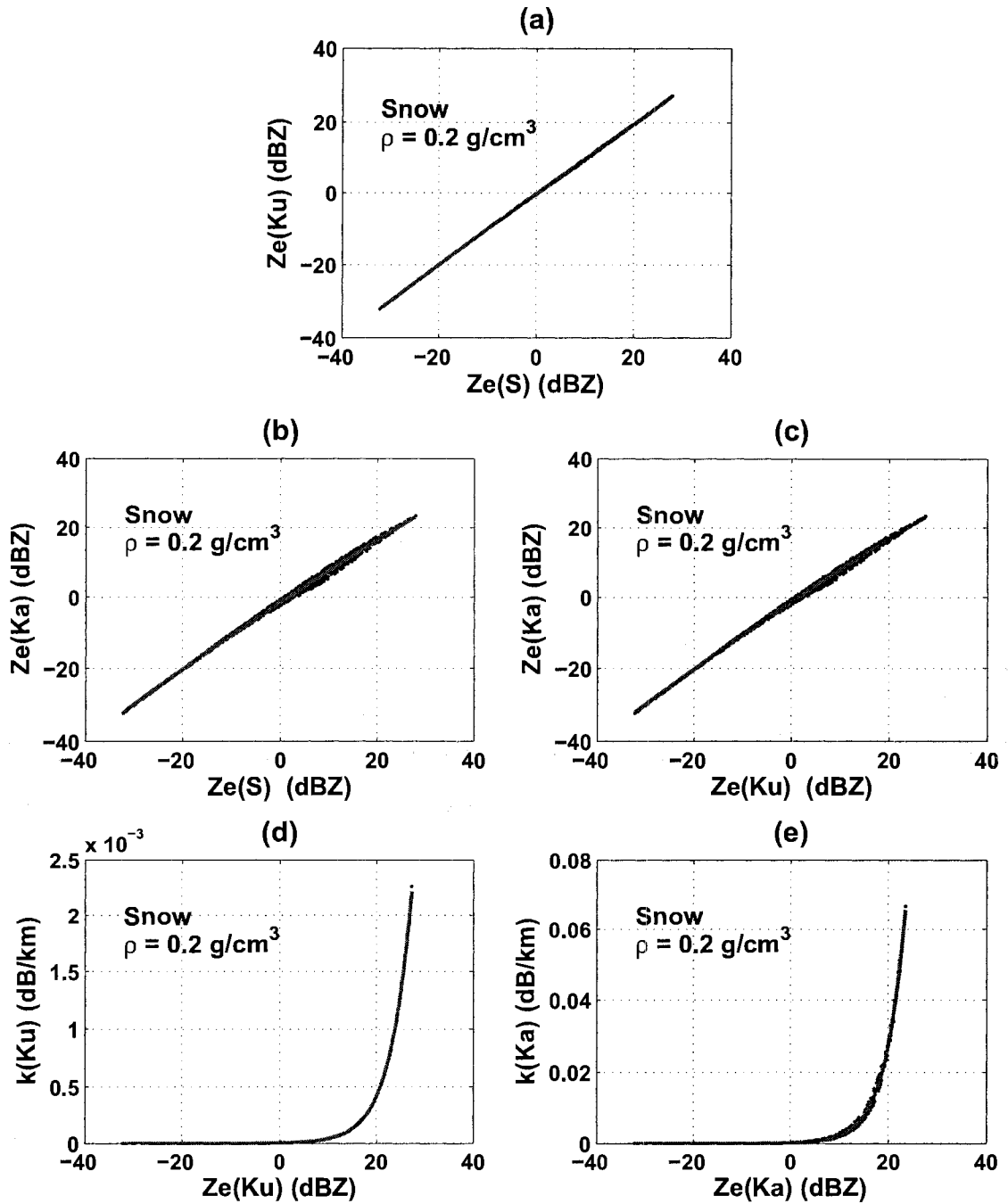


Figure 2.1: Scatter plots and the best fits of variability of reflectivity with frequency and k - Z_e relations for dry snow with density of 0.2 g cm^{-3} : (a) $Z_e(\text{S})$ vs. $Z_e(\text{Ku})$, (b) $Z_e(\text{S})$ vs. $Z_e(\text{Ka})$, (c) $Z_e(\text{Ku})$ vs. $Z_e(\text{Ka})$, (d) $Z_e(\text{Ku})$ vs. $k(\text{Ku})$ and (d) $Z_e(\text{Ka})$ vs. $k(\text{Ka})$.

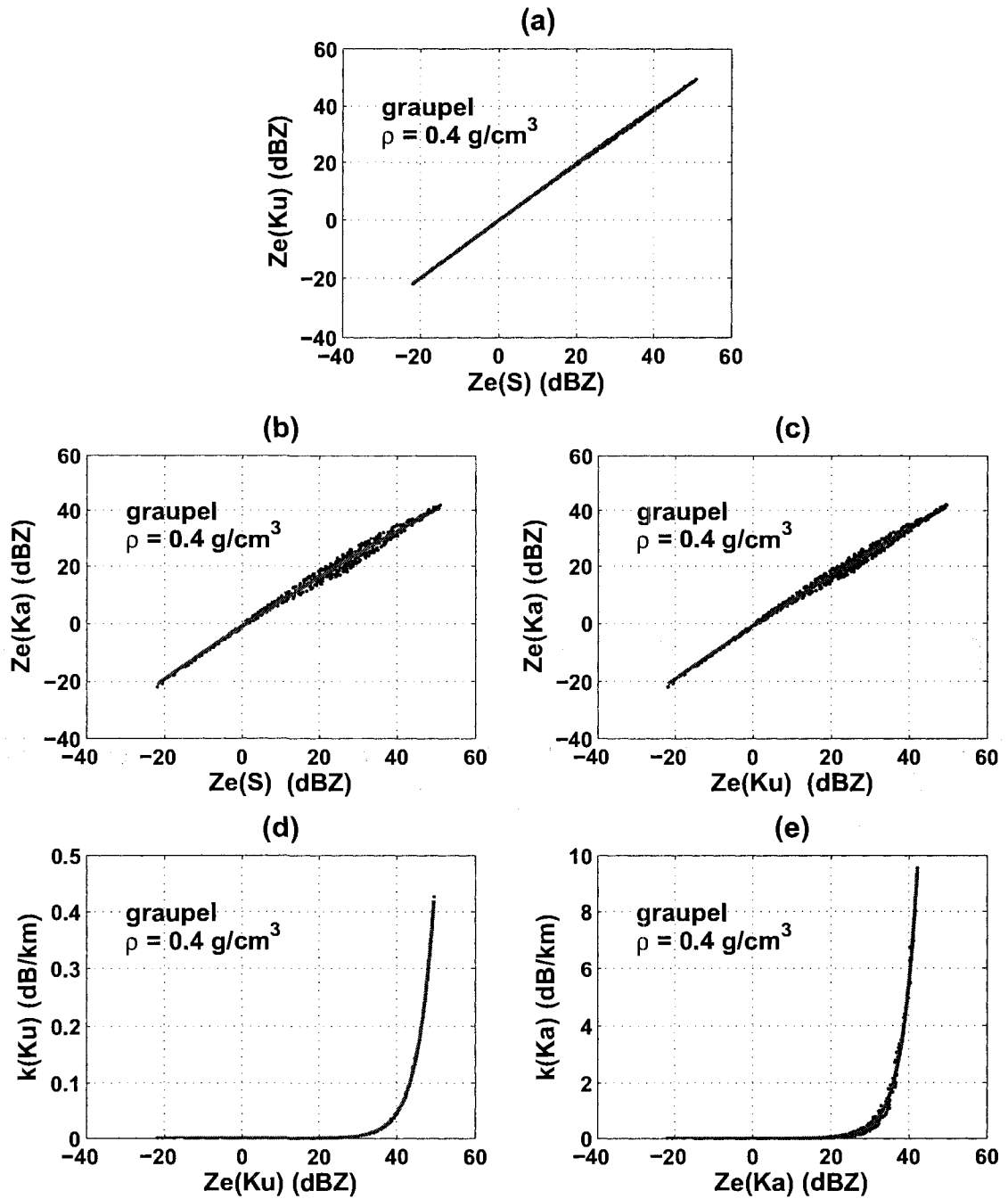


Figure 2.2: Scatter plots and the best fits of variability of reflectivity with frequency and k - Z_e relations for dry graupel with density of 0.4 g cm^{-3} : (a) $Z_e(\text{S})$ vs. $Z_e(\text{Ku})$, (b) $Z_e(\text{S})$ vs. $Z_e(\text{Ka})$, (c) $Z_e(\text{Ku})$ vs. $Z_e(\text{Ka})$, (d) $Z_e(\text{Ku})$ vs. $k(\text{Ku})$ and (e) $Z_e(\text{Ka})$ vs. $k(\text{Ka})$.

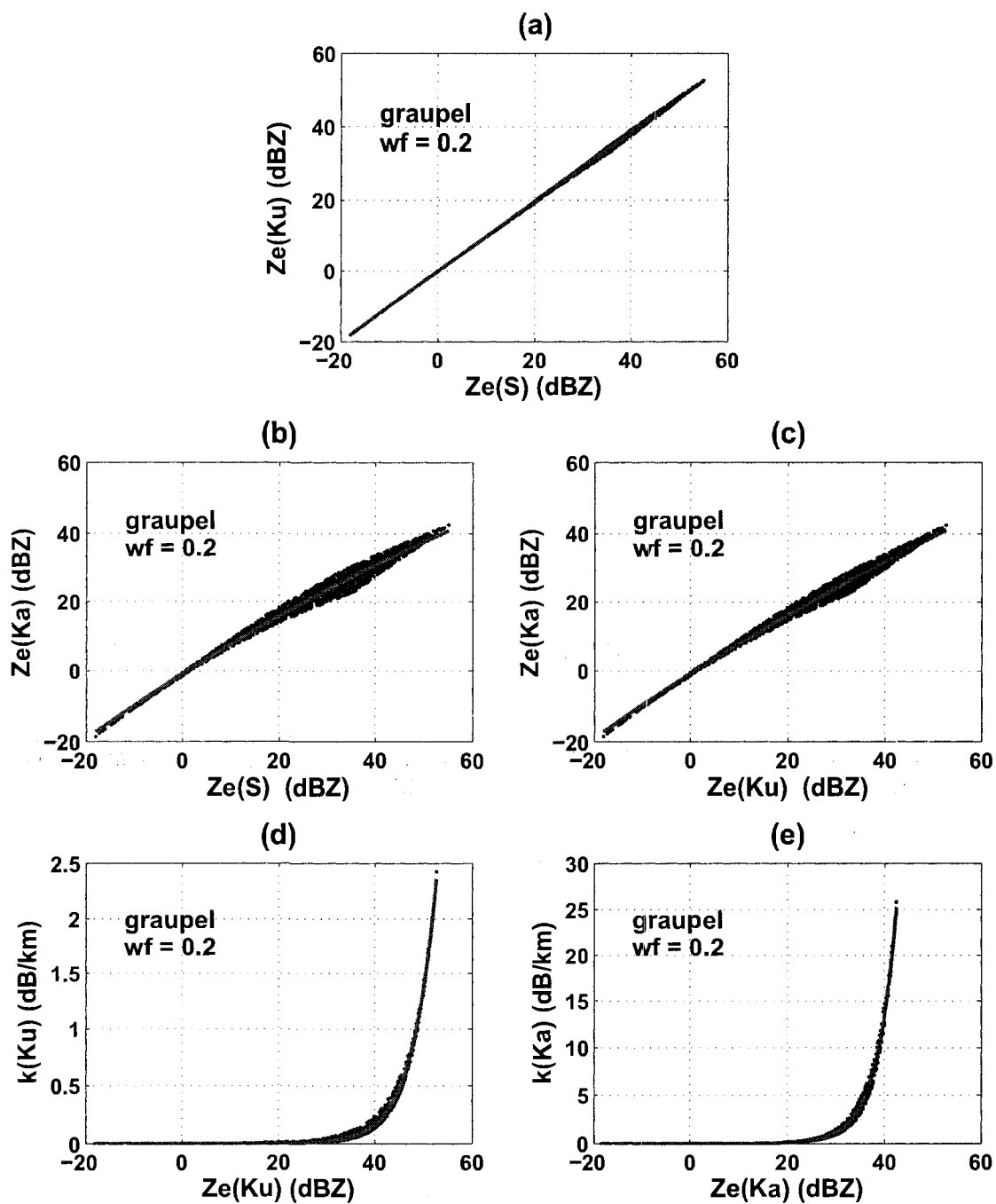


Figure 2.3: Scatter plots and the best fits of variability of reflectivity with frequency and k - Z_e relations for melted graupel with water fraction of 0.2: (a) $Z_e(\text{S})$ vs. $Z_e(\text{Ku})$, (b) $Z_e(\text{S})$ vs. $Z_e(\text{Ka})$, (c) $Z_e(\text{Ku})$ vs. $Z_e(\text{Ka})$, (d) $Z_e(\text{Ku})$ vs. $k(\text{Ku})$ and (d) $Z_e(\text{Ka})$ vs. $k(\text{Ka})$.

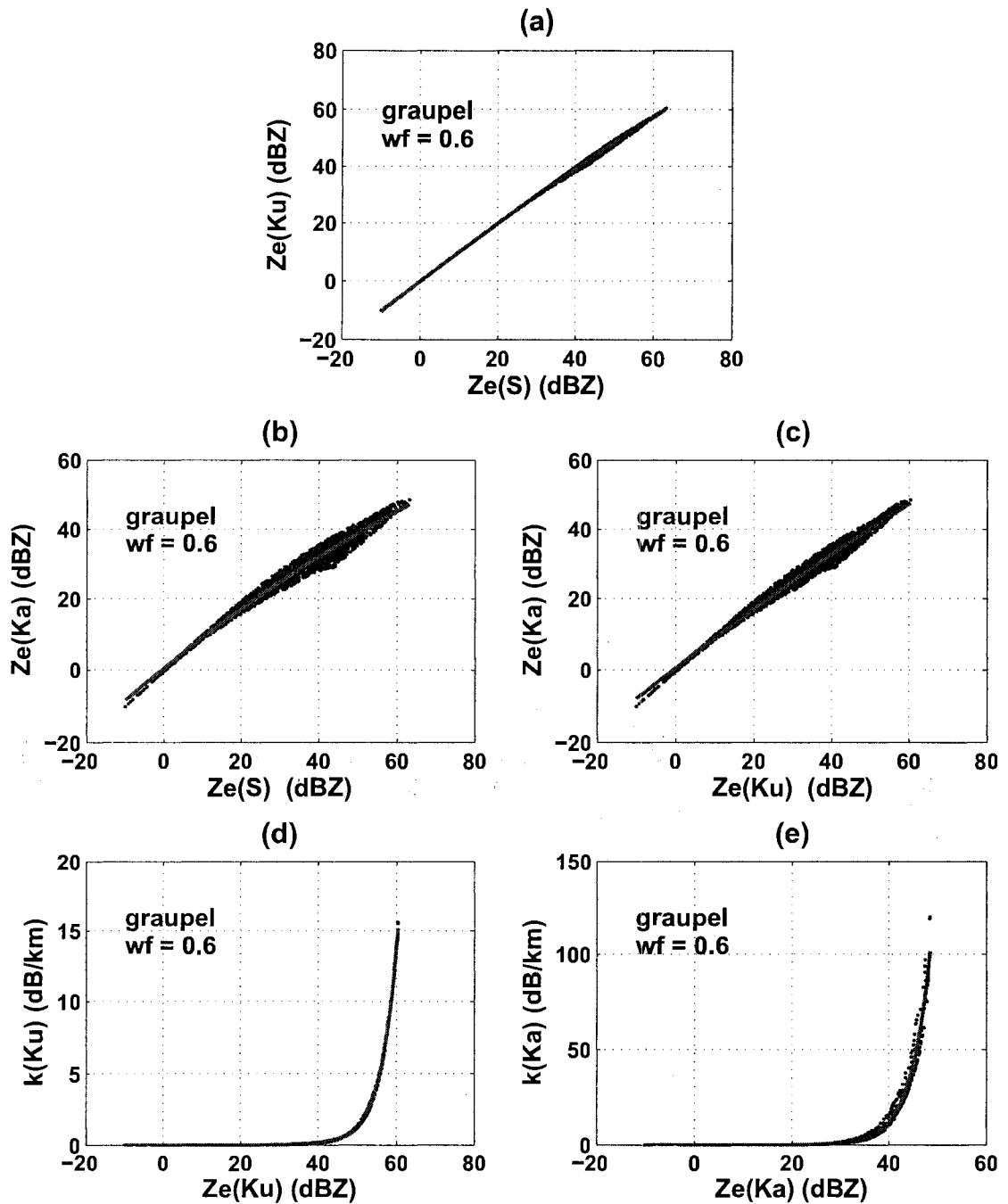


Figure 2.4: Scatter plots and the best fits of variability of reflectivity with frequency and k - Z_e relations for melted graupel with water fraction of 0.6: (a) $Z_e(\text{S})$ vs. $Z_e(\text{Ku})$, (b) $Z_e(\text{S})$ vs. $Z_e(\text{Ka})$, (c) $Z_e(\text{Ku})$ vs. $Z_e(\text{Ka})$, (d) $Z_e(\text{Ku})$ vs. $k(\text{Ku})$ and (d) $Z_e(\text{Ka})$ vs. $k(\text{Ka})$.

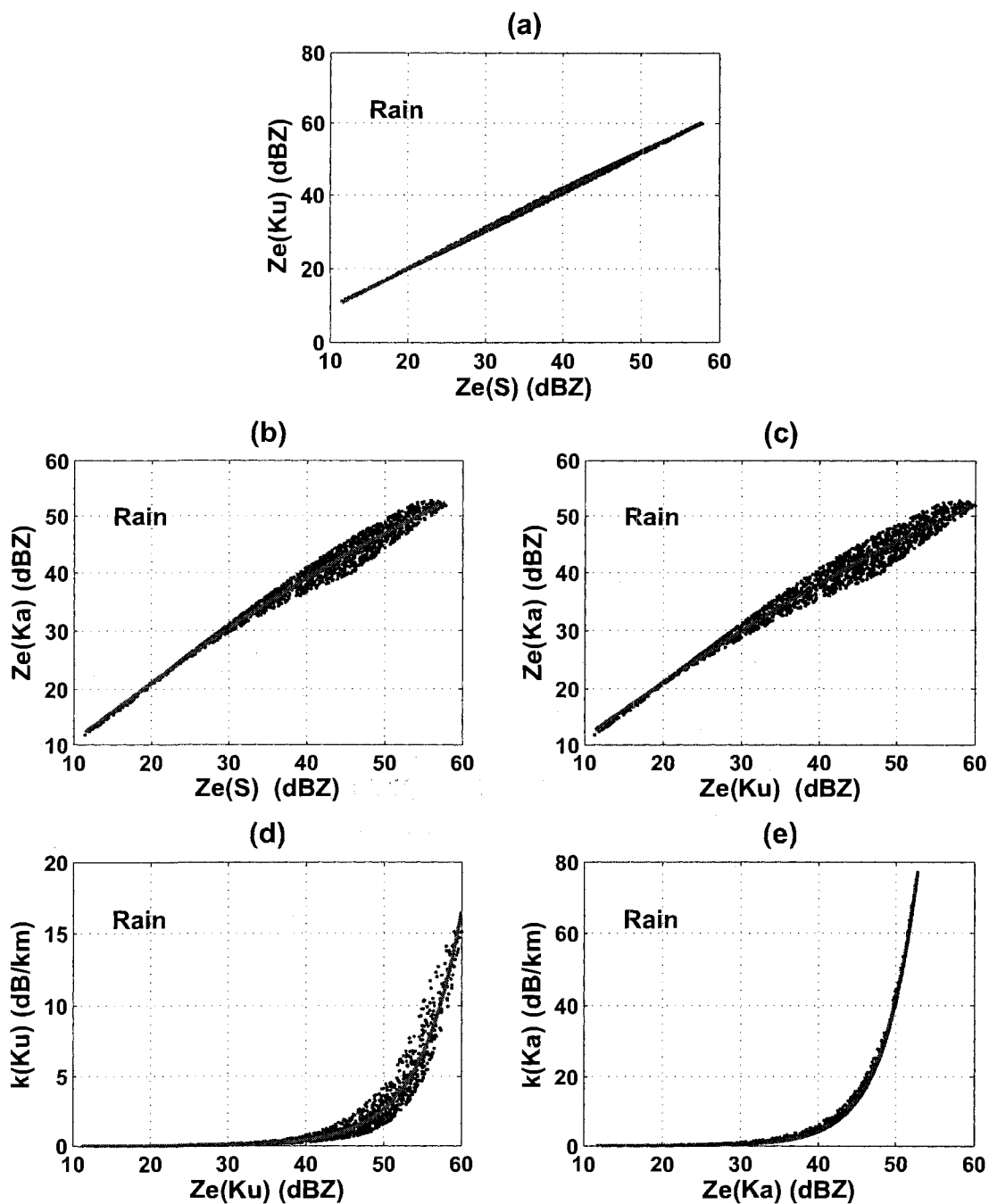


Figure 2.5: Scatter plots and the best fits of variability of reflectivity with frequency and k - Z_e relations for rain: (a) $Z_e(S)$ vs. $Z_e(Ku)$, (b) $Z_e(S)$ vs. $Z_e(Ka)$, (c) $Z_e(Ku)$ vs. $Z_e(Ka)$, (d) $Z_e(Ku)$ vs. $k(Ku)$ and (e) $Z_e(Ka)$ vs. $k(Ka)$.

Table 2.3: The coefficients of $Z_e(Ku) = a + bZ_e(S)$ and $k(Ku) = \alpha Z_e(Ku)^\beta$ relations.

Particle types	$Z_e(Ku) = a + bZ_e(S)$		$k(Ku) = \alpha Z_e(Ku)^\beta$	
	a	b	α	β
Snow/graupel density (g cm^{-3})				
$\rho = 0.05$	-0.50831	0.97897	5e-06	0.98144
$\rho = 0.10$	-0.37263	0.98202	4.5e-06	0.99343
$\rho = 0.15$	-0.29767	0.98399	4.3e-06	0.99981
$\rho = 0.20$	-0.24631	0.98551	4.2e-06	1.0025
$\rho = 0.25$	-0.20752	0.98676	4.1e-06	1.0044
$\rho = 0.30$	-0.17651	0.98785	4e-06	1.0061
$\rho = 0.35$	-0.15086	0.98882	4e-06	1.0073
$\rho = 0.40$	-0.12904	0.98969	4e-06	1.0083
Melted particles				
wf = 0.1	-0.070347	0.99508	2.23e-05	0.9402
wf = 0.2	-0.048824	1.0021	1.98e-05	0.953
wf = 0.3	-0.046588	1.0095	1.5e-05	0.97756
wf = 0.4	-0.059505	1.0168	1.13e-05	1.0055
wf = 0.5	-0.069584	1.0221	9.9e-06	1.0247
wf = 0.6	-0.01878	1.0155	1.23e-05	1.0162
wf = 0.7	0.08087	0.99349	1.53e-05	1
wf = 0.8	0.01645	0.97903	3.05e-05	0.93829
Rain				
$\mu = 0$	-1.8792	1.1099	0.0002159	0.80897
$\mu = 1$	-1.3599	1.0669	0.0002757	0.79688
$\mu = 2$	-0.92941	1.0329	0.0003321	0.78806
$\mu = 3$	-0.58841	1.007	0.0003755	0.78335

Table 2.4: The coefficients of $Z_e(Ka) = a + bZ_e(S)$ and $k(Ku) = \alpha Z_e(Ku)^\beta$ relations.

Particle types	$Z_e(Ka) = a + bZ_e(S)$		$k(Ka) = \alpha Z_e(Ka)^\beta$	
	a	b	α	β
Snow/graupel density (g cm^{-3})				
$\rho = 0.05$	-3.2575	0.87242	0.0002538	1.0764
$\rho = 0.10$	-2.4729	0.88633	0.0002273	1.0792
$\rho = 0.15$	-2.0339	0.89496	0.0002135	1.0805
$\rho = 0.20$	-1.7291	0.90146	0.000204	1.0819
$\rho = 0.25$	-1.4955	0.90678	0.000197	1.0835
$\rho = 0.30$	-1.3061	0.91135	0.0001912	1.0852
$\rho = 0.35$	-1.147	0.9154	0.0001868	1.0865
$\rho = 0.40$	-1.0098	0.91906	0.0001828	1.0883
Melted particles				
wf = 0.1	-0.73694	0.88112	0.0004432	1.1028
wf = 0.2	-0.37998	0.88791	0.0004204	1.1206
wf = 0.3	-0.048003	0.88364	0.0005359	1.1021
wf = 0.4	0.23254	0.86874	0.0009077	1.0423
wf = 0.5	0.34781	0.87103	0.0007553	1.0536
wf = 0.6	0.29574	0.89583	0.0003683	1.1151
wf = 0.7	0.35682	0.91158	0.0008656	1.0064
wf = 0.8	0.49717	0.94157	0.0006854	1.0056
Rain				
$\mu = 0$	0.75765	1.0881	0.0005468	0.97905
$\mu = 1$	-0.18462	1.1379	0.0005801	0.97163
$\mu = 2$	-0.83483	1.1721	0.0006141	0.96492
$\mu = 3$	-1.2763	1.1945	0.0006446	0.95933

Table 2.5: The coefficients of $Z_e(Ka) = a + bZ_e(Ku)$ relations.

	$Z_e(Ka) = a + bZ_e(Ku)$	
Particle types	a	b
Snow/graupel density (g cm^{-3})		
$\rho = 0.05$	-2.8102	0.91275
$\rho = 0.10$	-2.2474	0.91314
$\rho = 0.15$	-1.9064	0.91348
$\rho = 0.20$	-1.6569	0.91375
$\rho = 0.25$	-1.4578	0.91396
$\rho = 0.30$	-1.2383	0.91898
$\rho = 0.35$	-1.0945	0.91903
$\rho = 0.40$	-0.96614	0.91893
Melted particles		
$wf = 0.1$	-0.78052	0.90717
$wf = 0.2$	-0.51698	0.90564
$wf = 0.3$	-0.27278	0.9006
$wf = 0.4$	-0.078396	0.89207
$wf = 0.5$	0.062791	0.88521
$wf = 0.6$	0.15406	0.88269
$wf = 0.7$	0.14174	0.90459
$wf = 0.8$	0.12439	0.96332
Rain		
$\mu = 0$	2.2861	0.99926
$\mu = 1$	0.95818	1.0808
$\mu = 2$	-0.023823	1.1414
$\mu = 3$	-0.75494	1.186

2.5 The Concept of Vertical Profile of Reflectivity (VPR) Simulation

Based on the model relation of the radar reflectivity (Z_e) and specific attenuation (k) and variability of Z_e with frequency described in the preceding section, if a vertical profile of Z_e in one channel is available and the precipitation types along the vertical profile is known or assumed, the vertical profile of Z_e and k in the other channels can be simulated. Consequently, the vertical profile of the “measured” reflectivity (Z_m) can be generated using 2.8.

By assuming an availability of $Z_e(S)$ VPR measurement, the VPR at Ku-band ($Z_e(Ku)$) and in Ka-band ($Z_e(Ka)$) using the $Z_e(S)$ measurement can be obtained.

2.6 Summary and Conclusion

The theoretical background, which is fundamental for computing radar parameters, including electromagnetic scattering from dielectric sphere and precipitation microphysics is described. Computations of radar reflectivity (Z_e) and specific attenuation (k) for three frequencies, 2.7 GHz (S-band), 13.6 GHz (Ku-band) and 35.6 GHz (Ka-band), are performed. In each frequency, Z_e and k are computed for various particle types. Cross-frequency relations of Z_e between two frequencies are found to be reasonably linear. k - Z_e is related by the power law. Coefficients of the relations are calculated. The coefficients were used to demonstrate the concept of the simulation of vertical profile of reflectivity (VPR) from one frequency to another based on a simple assumption of particle types along the vertical profile. When the attenuation along the propagation path is taken into account, the “measured” reflectivity profile is generated based on the simulated two-way path integrated attenuation (PIA). With appropriate storm structure models and necessary parameters, the theoretically-derived relations of k - Z_e and variability of Z_e with frequency in this chapter will be used to simulate global precipitation observation for dual-frequency precipitation radar (DPR).

CHAPTER 3

TRMM-PR GLOBAL OBSERVATION ANALYSIS AND GROUND MEASUREMENTS

3.1 Introduction

Precipitation radar (PR) onboard the Tropical Rainfall Measurement Mission (TRMM) has been providing measurements of vertical profiles of precipitation in the tropics since the TRMM satellite was launched in 1997. Global observation of reflectivity profiles both over ocean and over land can be used to study characteristics of precipitation. Seasonal and regional variations on a global scale can also be analyzed, and comparisons can be made. In addition, the microphysical structure of storms can be examined. Statistics of profile characteristics and microphysics for different rain type (stratiform/convective) over land and over ocean can be established based on global analysis of PR observations. Knowledge gained from TRMM-PR global observation analysis will be useful for developing a simulation-based technique of dual-wavelength precipitation radar (DPR) observation in the Global Precipitation Measurement (GPM) era. This chapter describes the TRMM-PR system, studies of vertical profile classification of different rain type (stratiform/convective), and drop size distribution parameters estimation based on these measurements.

3.2 TRMM-PR Overview

The PR on the TRMM satellite is the first space-based radar for measuring precipitation in the tropics and subtropics (Kozu et al., 2001; Meneghini et al., 2001; Iguchi,

2003). A highlight of the PR is that it can provide unprecedented measurements of 3-dimensional precipitation structure in term of radar reflectivity at an instantaneous time with a high vertical resolution, as shown in Fig. 3.1. Such vertical structure of precipitation measured by PR benefits many research communities. The information on the vertical structure of precipitation is important for estimating latent heat profiles and for various precipitation science studies. The structure of storm and rainfall characteristics inferred from PR observations can be used to improve passive microwave rainfall retrieval accuracy (Kozu et al., 2001).

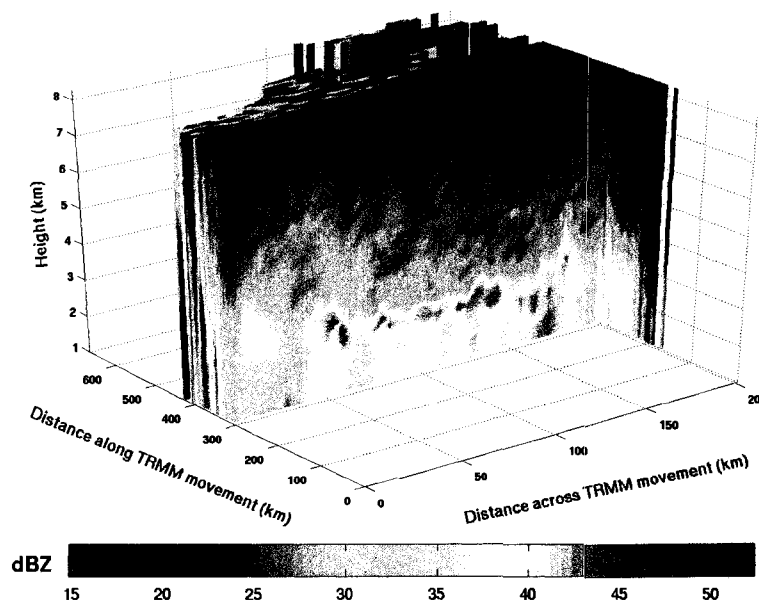


Figure 3.1: An example of 3-dimensional reflectivity of precipitation structure observed by TRMM-PR.

3.2.1 TRMM-PR system descriptions

The TRMM satellite is in a non-sunsynchronous low earth orbit with a low inclination angle of 35° . The TRMM satellite has been orbiting at an altitude of about 350 km since it was launched. In August of 2001, the satellite was boosted to an altitude of 402 km. The satellite takes about 90 minutes to finish one orbit, and orbits

the earth about 15-16 times a day. Figure 3.2 shows one-day orbit of the TRMM satellite (TRMM, 2001).

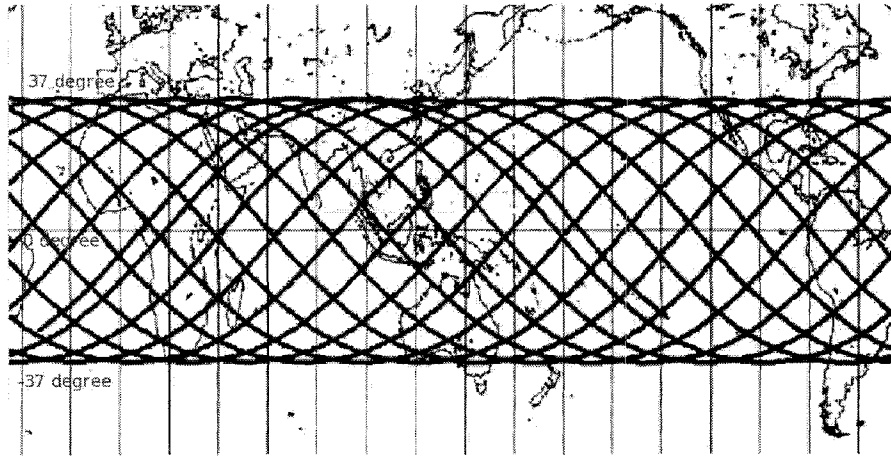


Figure 3.2: The ground track of TRMM orbit over one day (adopted from (TRMM, 2001)).

PR operates at Ku-band frequency (13.8 GHz) and uses a 2 m x 2 m phased array antenna consisting of 128 slotted waveguides. The 3 dB beamwidth is approximately 0.71° . The PR characteristics are shown in Table 3.1. The radar beam electronically scans cross-track from the right at 17° through nadir to the left at 17° , totalling an angular sector scan from right to left of 34° . Each PR scan contains 49 beams. At a certain beam, the radar collects samples from the surface up to a height of about 20 km with a vertical resolution of 250 m. PR has a swath width of about 215 km and a horizontal resolution at nadir of about 4.3 km before the boost. After the boost, the swath width increases to approximately 250 km and the horizontal resolution at nadir increases to about 5 km. The observation geometry of the PR before the altitude boost is shown in Fig. 3.3.

To achieve the required horizontal resolution near the surface at an operational altitude with an antenna size of 2 m, PR is required to use a much higher frequency (13.8 GHz Ku-band) than those typically used for ground-based weather radar (S-band and C-band) (Meneghini and Kozu, 1990; Skolnik, 2001; Meneghini et al., 2001). It is well known that radars operating at a frequency higher than S-band (3 GHz)

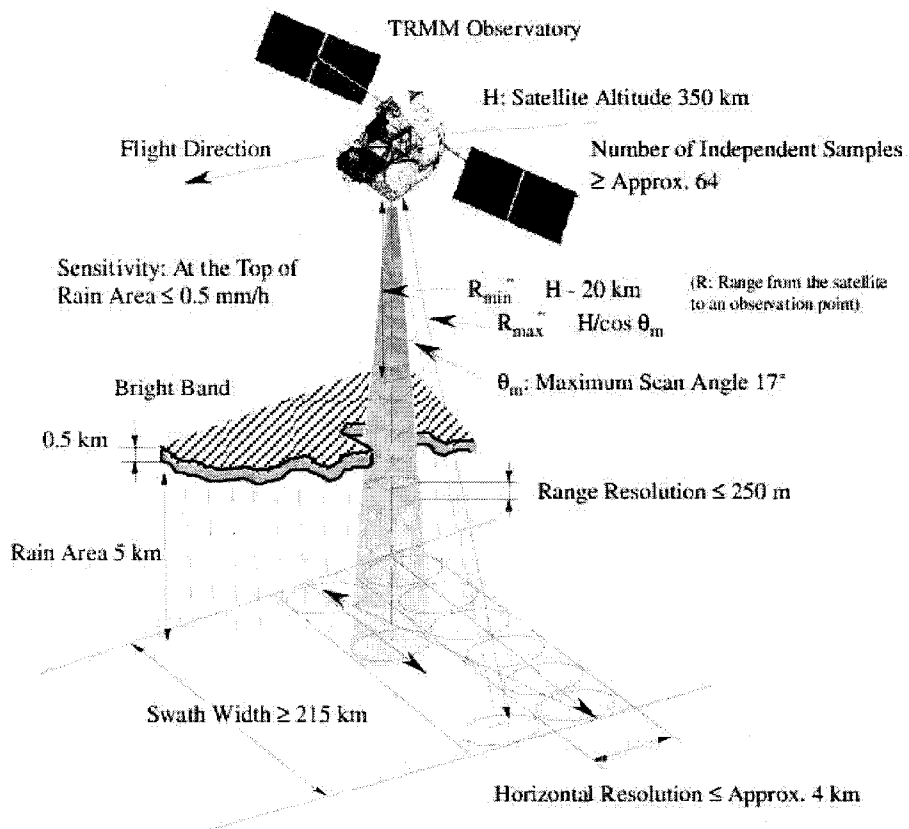


Figure 3.3: The observation geometry of the PR before the altitude boost (adopted from TRMM (2001)).

Table 3.1: Precipitation radar (PR) specifications.

Precipitation radar (PR) specifications.	
Frequency	13.796 - 13.802 GHz
Pulse width	1.6 μ sec x 2 ch
PRF	2776 Hz
Peak power	over 700 W
Observation range	about 20 km. above surface
Range resolution	250 m.
Swath width	about 220 km.
Scan angle	$\pm 17^\circ$
minimum detectable	SNR per pulse ≥ 0 dB for 0.5 mm/h rain at rain top
Horizontal resolution	4.3 km. (nadir)
Dynamic range	about 81.5 dB
Independent samples	64
Antenna type	128-element "active" phase array
Gain	about 47.4 dB
Aperture	2x2 m.
Beamwidth	0.71 \circ

suffer from attenuation caused by scattering and absorption of the electromagnetic wave propagating through the precipitation medium (Beaver and Bringi, 2003; Ippolito, 1981; Bringi and Chandrasekar, 2001). Therefore, the measured reflectivity of precipitation by PR must be corrected for attenuation before it can be used in the estimation of meteorological quantities such as rainfall rate. The PR attenuation correction algorithm is described in the following section.

3.2.2 TRMM-PR attenuation correction algorithm

PR operates at a frequency of 13.8 GHz. At this frequency, PR reflectivity measurement suffers from attenuation caused by precipitation. Attenuation needs to be corrected before rain rate is estimated with a quantitative use of reflectivity. The PR attenuation-correction technique is based on a method that is a hybrid between the Hitschfeld-Bordan (HB) (Hitschfeld and Bordan, 1954) and surface reference techniques (SRT) (Meneghini et al., 2000). The HB method assumes a k - Z relation to

solve first-order differential equations (Iguchi and Meneghini, 1994) associated with radar equations. The HB solution works well in light to moderate rain where attenuation is not significant. When attenuation is large, the solution becomes unstable. The SRT gives an independent measurement of two-way path integrated attenuation (PIA). PIA measurement by SRT is based on the assumption that a surface cross-section σ^o remains the same in both the presence and absence of precipitation along the radar beam. The difference of $\sigma^o(\Delta\sigma^o)$ between the presence and absence of precipitation is entirely caused by attenuation from precipitation. Once the PIA by SRT is applied, the α coefficient of $k = \alpha Z^\beta$ relation is adjusted in such a way that the PIA of the HB solution is consistent with the PIA from SRT, henceforth called “ α adjustment” method. The α adjustment method provides an independent estimate of drop size distribution parameters. To adjust an initial α coefficient, a correction factor(ϵ) is introduced. Governing equations of TRMM-PR attenuation-correction are as follows:

The observed or measured radar reflectivity $Z_m(r)$ at range r is related to reflectivity factor $Z_e(r)$ by the two-way attenuation factor $A(r)$ by

$$Z_m(r) = Z_e(r)A(r) \quad (3.1)$$

and $A(r)$ is given by

$$A(r) = \exp \left[-0.2 \ln 10 \int_0^r k(s) ds \right] \quad (3.2)$$

Using an assumed relationship between specific attenuation (k) and reflectivity factor (Z_e), $k = \alpha Z^\beta$, (3.1) can be solved for the attenuation factor by the Hitschfeld-Bordan method written as

$$A_{HB} = \frac{Z_m(r)}{Z_e(r)} \quad (3.3)$$

where A_{HB} is the Hitschfeld-Bordan (HB) derived attenuation factor,

$$A_{HB} = \left[1 - q\beta \int_0^r \alpha(s) Z_m^\beta(s) ds \right]^{\frac{1}{\beta}} \quad (3.4)$$

with $q = 0.2\ln 10$. The HB solution of path integral attenuation (PIA_{HB}) in (3.4) can be express in dB scale as,

$$A_{HB} = -\frac{10}{\beta} \log(1 - \zeta) \quad (3.5)$$

where

$$\zeta = q\beta \int_0^{r_s} \alpha(s) Z_m^\beta(s) ds \quad (3.6)$$

and r_s is the range to the surface.

In heavy rain where attenuation becomes large, ζ tends to exceed unity and (3.5) is no longer valid (Iguchi et al., 2000). Therefore, the HB solution becomes unstable. To overcome the instability problem of the HB solution, surface reference technique (SRT) of Meneghini et al. (2000) is used as a constraint so that $(1 - \zeta)$ in (3.5) is always larger than zero.

The SRT method provides an independent estimate of the total path-integrated attenuation (Meneghini et al., 2000) and is defined as,

$$PIA_{SR} = \Delta\sigma^o = \langle \sigma_{no-rain}^o \rangle - \langle \sigma_{rain}^o \rangle \quad (3.7)$$

where $\langle \sigma_{no-rain}^o \rangle$ indicates the average of the surface of the surface radar cross-section with no rain, and $\langle \sigma_{rain}^o \rangle$ is the average when rain is present. The objective is to find the most probable or effective path attenuation, PIA_e given both PIA_{SR} and PIA_{HB} . In the case of large attenuation (heavy rain), PIA_{SR} is believed to give a more accurate measurement of the PIA. Thus, PIA_e can be expressed as,

$$PIA_e = \Delta\sigma^o = -\frac{10}{\beta} \log(1 - \epsilon\zeta) \quad (3.8)$$

where ϵ is a correction factor.

ϵ is used to modify the α parameter of k - Z relation such that PIA_{HB} is consistent with PIA_{SR} , hence it is also called “ α adjustment” method. If PIA_{SR} is used as PIA_e , then ϵ can be expressed as,

$$\epsilon = \epsilon_s = \frac{1 - 10^{-0.1\beta\Delta\sigma^o}}{\zeta} \quad (3.9)$$

In cases of small attenuation (light to moderate rain), $\Delta\sigma^o$ is not reliable (Meneghini et al., 2000) and PIA_{SR} is completely discarded. As a result, ϵ becomes unity. That means the path attenuation estimate relies on PIA_{HB} alone. However, in intermediate rainfall rate cases where PIA_{SR} and PIA_{HB} are valid, ϵ should become unity if the k - Z relation represents the true model of precipitation and if there is no error in radar calibration or the PIA_{SR} measurement (Iguchi and Meneghini, 1994). In contrast to previous versions of the TRMM-PR attenuation correction algorithm using linear weight function for determining ϵ , the current version of the TRMM-RP algorithm is based on a probability approach to determine weight function for calculation of ϵ (Iguchi and Meneghini, 1994; Iguchi et al., 2000).

Once the correction factor (ϵ) is determined, the attenuation-corrected reflectivity (Z_e) can be calculated at all range bins by

$$Z_e(r) = \frac{Z_m(r)}{1 - \left[1 - \epsilon q \beta \int_0^r \alpha(s) Z_m^\beta(s) ds \right]^{\frac{1}{\beta}}} \quad (3.10)$$

The attenuation-corrected reflectivity (Z_e) is designated as 2A25 of the TRMM-PR data product. The TRMM-PR rainfall rate estimate uses the $R = aZ_e^b$ relation. The coefficients a and b are also adjusted as a function of the ϵ . Details about TRMM-PR data product and parameters can be found in TRMM reference document (TRMM, 2005).

To show the measured reflectivity of precipitation by PR and the reflectivity after attenuation correction, an example of PR observation of a hurricane is illustrated in Fig. 3.4 which shows (a) a horizontal cross-section of the measured reflectivity (Z_m) of a hurricane observed by PR at 2.5 km from sea level; (b) corresponding attenuation-corrected reflectivity (Z_e) of (a); (c) a vertical cross-section of (a), as indicated by the dashed line; (d) a vertical cross-section of (b), as indicated by the dashed line; (e) a vertical profile for convective rain, as indicated by A in (c) and (d); and (f) a vertical profile for stratiform rain, as indicated by B in (c) and (d).

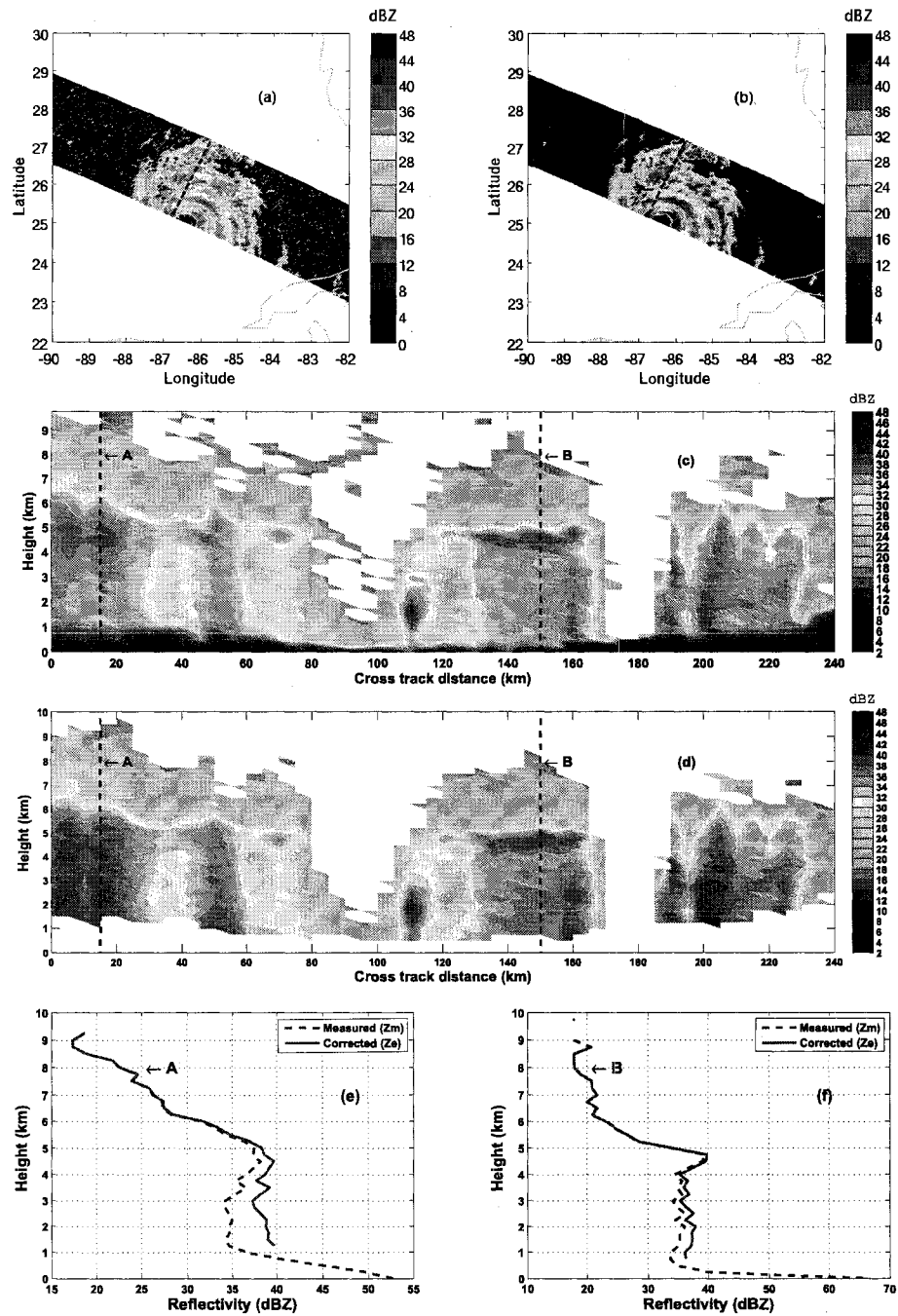


Figure 3.4: (a) a horizontal cross-section of the measured reflectivity (Z_m) of a hurricane observed by PR; (b) corresponding attenuation-corrected reflectivity (Z_e) of (a); (c) a vertical cross-section of (a), as indicated by the dashed line; (d) a vertical cross-section of (b), as indicated by the dashed line; (e) a vertical profile for convective rain, as indicated by A in (c) and (d); and (f) a vertical profile for stratiform rain, as indicated by B in (c) and (d).

In Fig. 3.4 (a) and (b), the blue stripe is the TRMM-PR swath. The reflectivity difference between the two is due to the PIA. In Fig. 3.4 (c), the strong reflectivity observed near surface is the ground clutter. The height above ground where the return from precipitation is not “contaminated” by the surface clutter increases as the scan angle moves away from nadir. This height is at a minimum at about 0.5 km. at nadir and reaches a maximum of about 1.5 km at the edge of the swath. The return signals from precipitation that are “contaminated” by ground clutter are removed, as seen in Fig. 3.4 (d). Figures 3.4 (c) and (d) show a fine vertical resolution of the TRMM-PR observations, which is very important not only for studying a variation of the vertical structure of precipitation around the globe, but also for inferring the underlying microphysics behind such a variation. The attenuation-corrected reflectivity Z_e data, as seen in Fig. 3.4 (e) and (f), are used quantitatively in the next section when we investigate the vertical reflectivity structure of precipitation in the tropics and subtropics around the globe.

3.3 Vertical Profile of Reflectivity (VPR) Analysis

It is well-known that the vertical profile of reflectivity (VPR) on a global scale has a large spatial variation. To study the characteristics of precipitation based on its vertical structure, a classification method is used to categorize the global VPR into a number of characteristic profiles. The self-organizing map (SOM) method is the tool used to perform the classification. SOM is an unsupervised learning network that forms a nonlinear mapping of data to a low dimensional map grid (Kohonen, 1990; Haykin, 1998). The attenuation-corrected reflectivity data described in the preceding section were collected in the year 2000. The results of the data analysis are used to build the statistics of vertical reflectivity structure of precipitation on a global scale. PR can provide the rain type information, either convective or stratiform (Awaka et al., 97, 1998; TRMM, 2005). Since the two rain types have different characteristics,

the characterization of VPR observed by PR will be carried out separately on profiles of stratiform and convective rain type.

3.3.1 Characterization of VPR for convective rain

Convective rain cells are small (1-10 km horizontal dimension), intense, have horizontally-inhomogeneous radar reflectivity, and typically produces a rainfall rate higher than 5 mm hr^{-1} (House, 1997; Schumacher and House, 2003). A fine vertical resolution of the PR observations enables a study of vertical reflectivity structure of convective rain. Convective storms with single or multiple cells that do not produced hail is called ordinary convective storms (Bringi and Chandrasekar, 2001). The predominant ice hydrometeor type in ordinary convective storms is observed to be graupel particles (Bringi and Chandrasekar, 2001; Fabry and Zawadzki, 1995; Fabry and Szyrmer, 1999).

By examining the values of the correction factor (ϵ), a key parameter in the PR attenuation correction algorithm described in Section 3.2.2, the information about the vertical structure of hydrometeors and the severity of the path integrated attenuation can be approximately inferred (Iguchi et al., 2000)—for example, when $\epsilon = 1$, it means that the path attenuation is approximately less than 3.5 dB (Iguchi, 2003), and when ϵ is much less than 1, it is possible that frozen particles completely melt at an altitude very close to surface (Iguchi et al., 2000). Therefore, characterization of VPR of the precipitation will be carried out separately on two sets of the ϵ values ($\epsilon = 1$ and $\epsilon \neq 1$) for two different surface backgrounds, namely, ocean and land.

The SOM method is used to categorize convective rain type into six characteristic VPRs. The objective of this classification is to advance our knowledge of vertical profile characteristics of convective rain and their variability over land and over ocean based on the corresponding ϵ values. The attenuation-corrected reflectivity data collected from TRMM-PR observations around the globe for 12 months in 2000 are used for the classification.

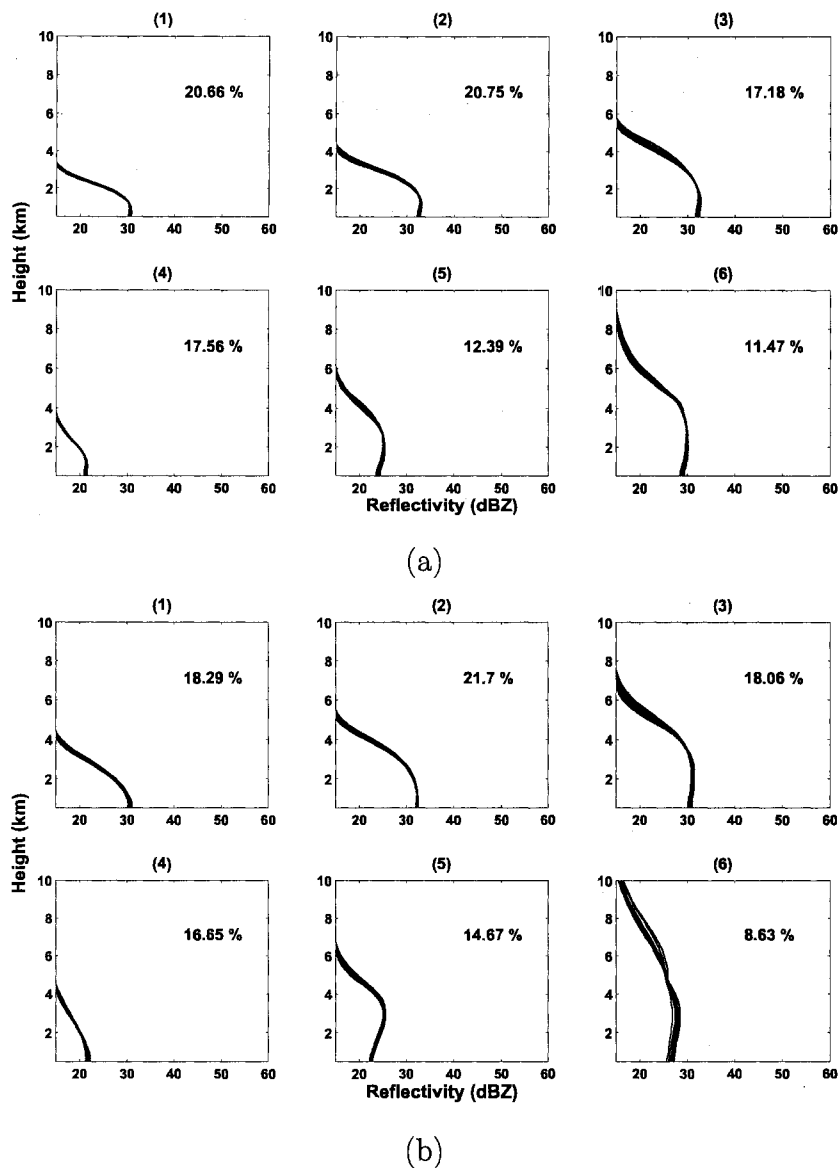


Figure 3.5: The characteristic VPRs of convective rain for $\epsilon = 1$ (a) over ocean, (b) over land for year 2000. The 12 plots in each subfigure represent 12 different months.

Figure 3.5 (a) and (b) show classification results of six different characteristic profiles of convective rain for $\epsilon = 1$ over ocean and over land, respectively, for the year 2000. Note that there are 12 plots representing 12 months in each subfigure. A comparison of the six characteristic profiles of convective rain over land and over ocean is shown in Fig. 3.6 for the month of September. Based on the six characteristic profiles, a few observations that can be made from this figure are that (1) the convective

rain with $\epsilon = 1$ over land and over ocean shows no seasonal variation. (2) The mean reflectivity near surface is less than 32 dBZ, and hence there is small attenuation. (3) About 90 % of storm top height is less than 6 km, and (4) the intensity of convective rain over land and ocean is similar despite some differences in the height of the storm top.

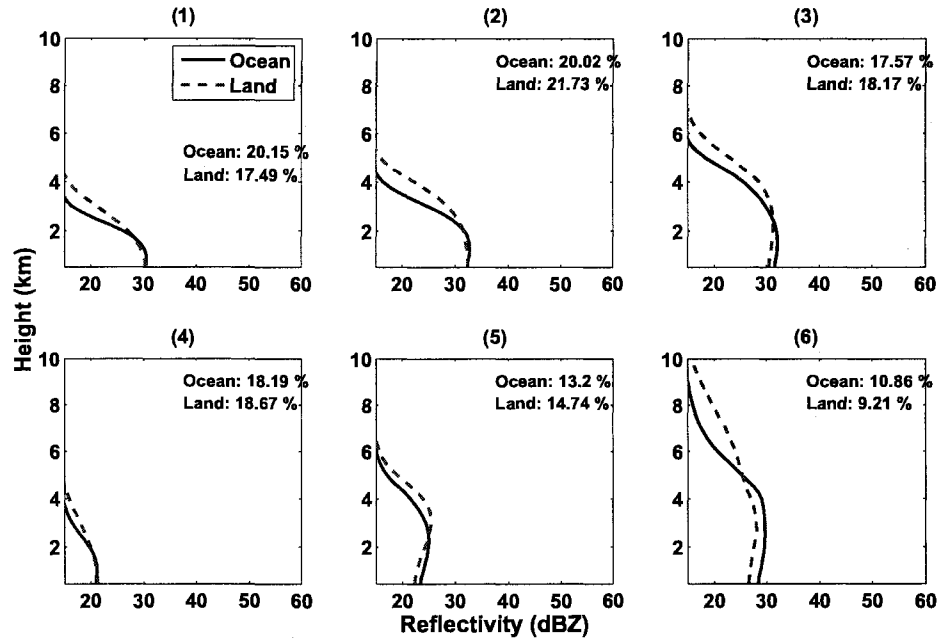


Figure 3.6: Comparison of the characteristic VPRs of convective rain for $\epsilon = 1$ over ocean and over land.

Figure 3.7 (a) and (b) show classification results of six different characteristic profiles of convective storms for $\epsilon \neq 1$ over ocean and over land, respectively, for the year 2000. Note that there are 12 plots representing 12 months in each subfigure. As seen in 3.7 (a), there are only slight variations over the year for all six characteristic VPRs over ocean, while there are noticeable but not significant variations at the height above 5 km in profiles 3 and 6 over land. Unlike the situation when $\epsilon = 1$, the intensity of the VPRs profile is much stronger and the height of the storm top take from 5 km to more than 10 km. Comparison of the six characteristic profiles of convective rain over ocean and land, as shown in Fig. 3.8, shows a remarkable difference between

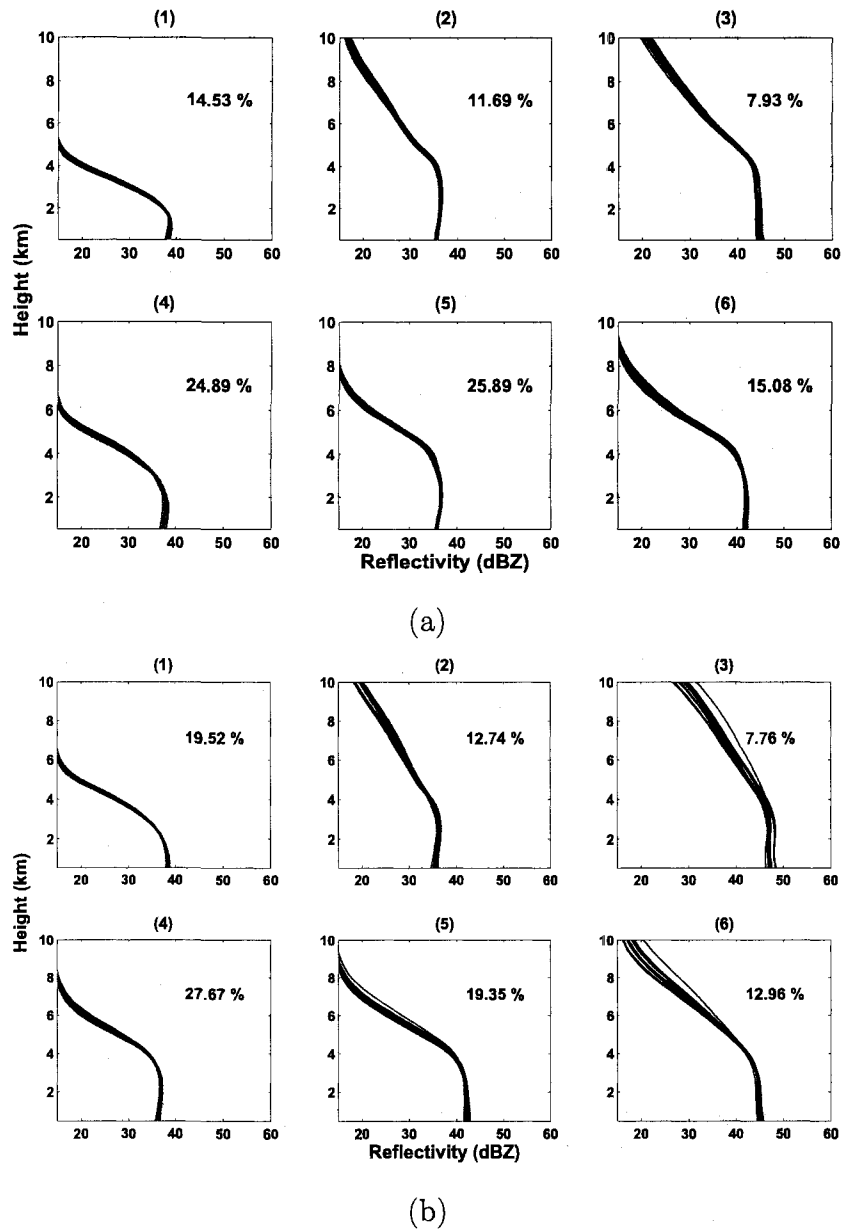


Figure 3.7: The characteristic VPRs of convective rain for $\epsilon \neq 1$ (a) over ocean, (b) over land for year 2000. The 12 plots in each subfigure represent 12 different months.

all six characteristic profiles. Such differences in the vertical profile structure of the characteristic VPRs imply a variability of the underlying microphysics, including differences in distribution of particle size and/or differences in phase-height transition of hydrometeor along the VPRs over ocean and land.

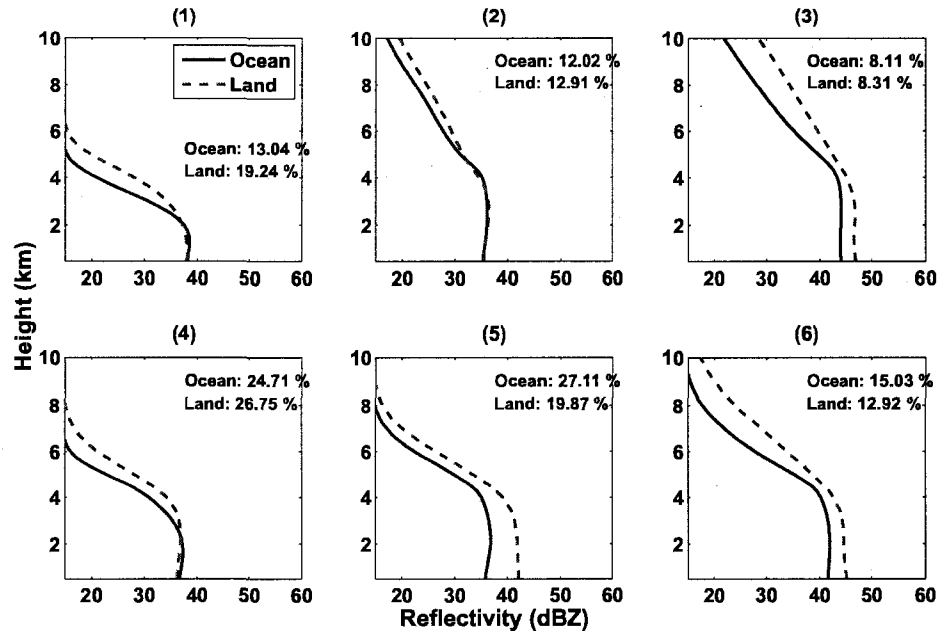


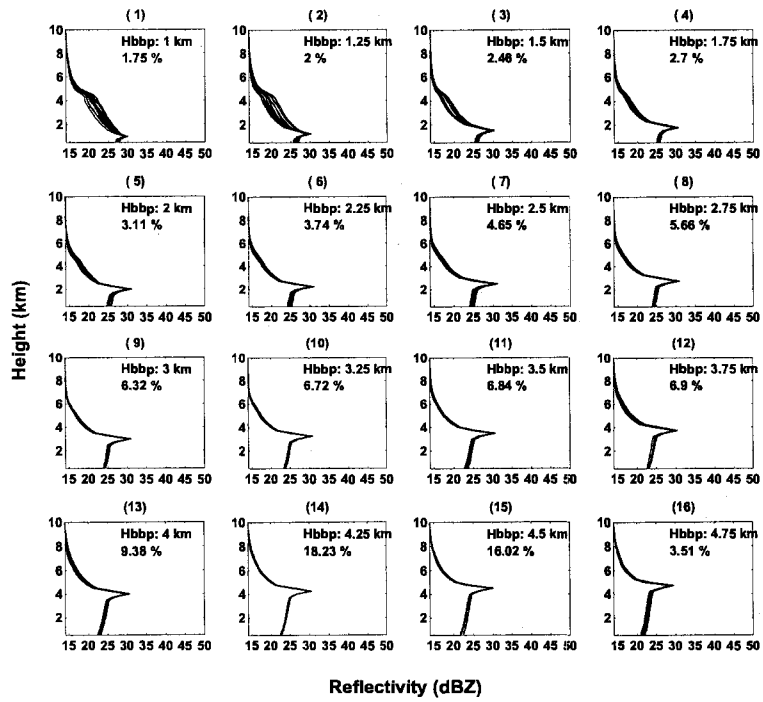
Figure 3.8: Comparison of the characteristic VPRs of convective rain for $\epsilon \neq 1$ over ocean and over land for the year 2000.

3.3.2 Characterization of VPR for stratiform rain

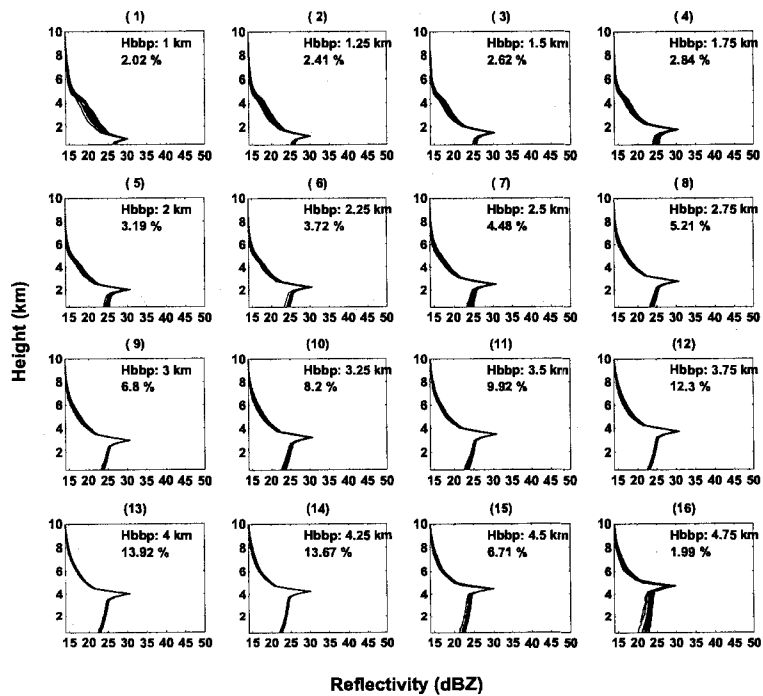
A fine vertical resolution of the PR observations enables a study of the vertical reflectivity structure of stratiform rain. It has been demonstrated that the height of the BB peak from surface varies widely around the globe. Based on attenuation-collected VPR data from the year 2000, 16 different heights of BB peak from sea level (varying from 1.00- 4.75 km with 0.25 km step) are used to generate 16 mean VPRs. Each mean VPR was generated by averaging profiles that have approximately the same height of BB peak. It should be noted that the 16 profiles are determined by a simple linear averaging, and not by SOM.

Similar to convective rain analysis, the characterization of stratiform rain is carried out on two different sets of ϵ values over land and over ocean. Figures 3.9 and 3.10 show the 16 mean profiles for $\epsilon = 1$ and $\epsilon \neq 1$. Panel (a) of each figure is data over ocean, and (b) over land. The vertical profile structure and intensity of stratiform rain for $\epsilon = 1$ both over land and over ocean are similar, as shown in Fig. 3.11 (a).

The vertical profile structure and intensity of stratiform rain for $\epsilon \neq 1$ both over land and over ocean are similar, as shown in Fig. 3.11 (b). However, when comparing the vertical profile structure and intensity corresponding to the two sets of the ϵ values over ocean and over land, the differences are evident, as shown in Fig. 3.12 (a) and (b), respectively.

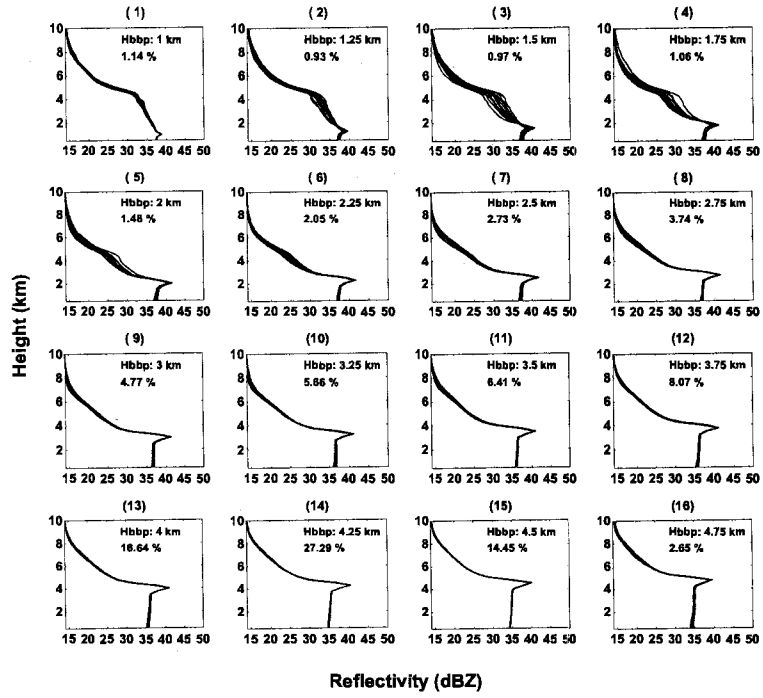


(a)

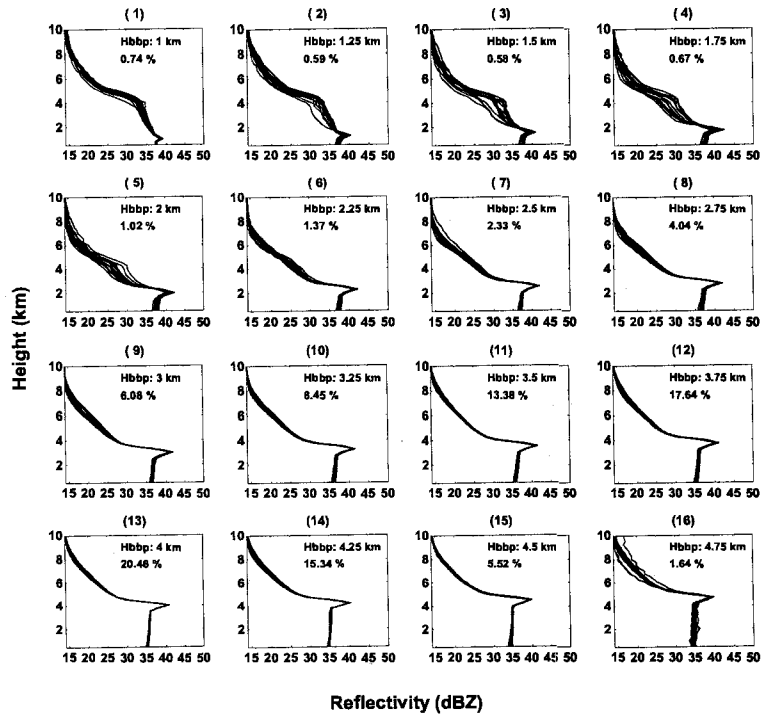


(b)

Figure 3.9: The mean vertical reflectivity profiles of stratiform rain for $\epsilon = 1$ (a) over ocean, and (b) over land for sixteen different heights of bright band peak from sea level for year 2000.

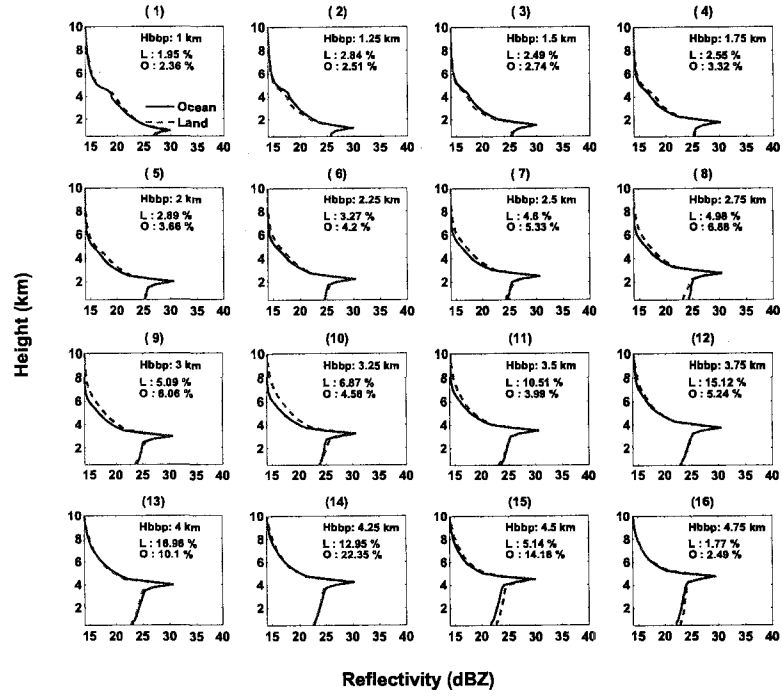


(a)

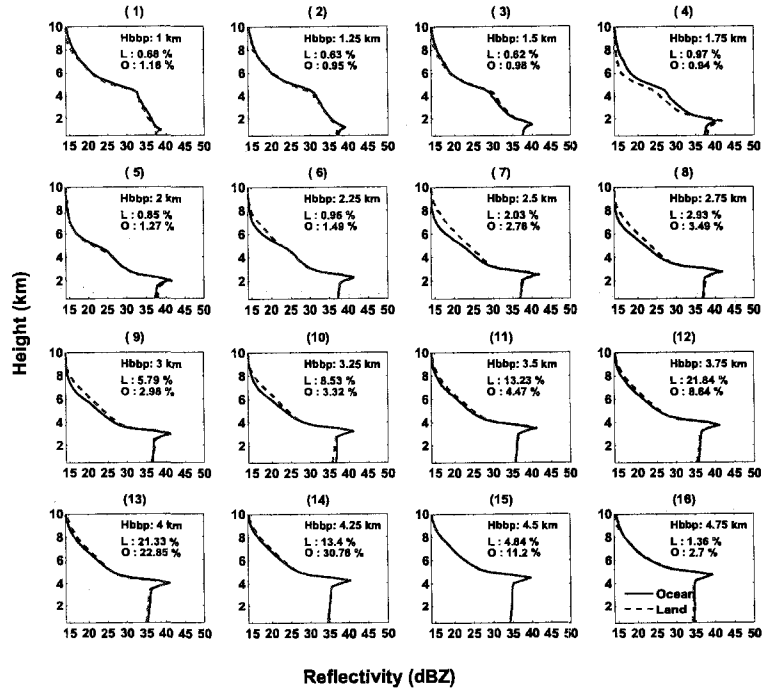


(b)

Figure 3.10: The mean vertical reflectivity profiles of stratiform rain for $\epsilon \neq 1$ (a) over ocean, and (b) over land for sixteen different heights of bright band peak from sea level for year 2000.

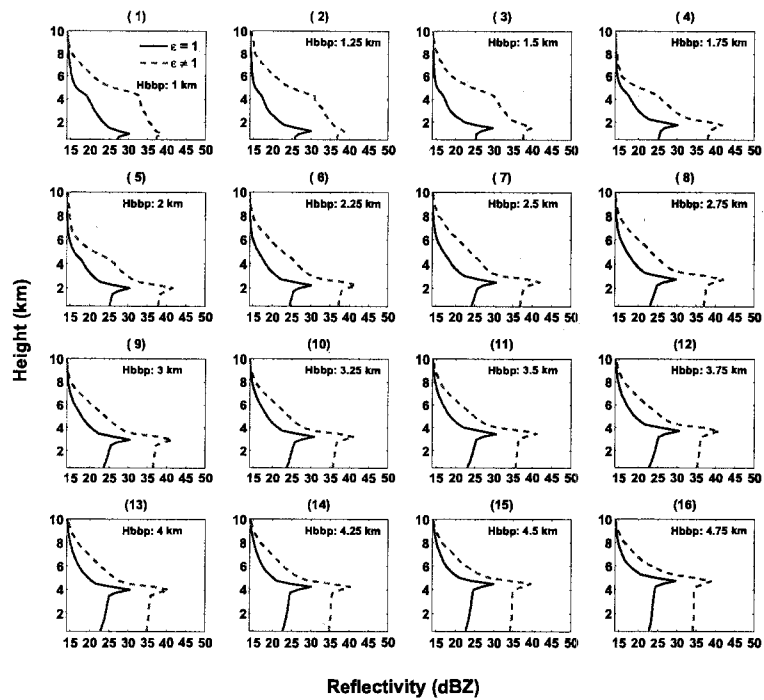


(a)

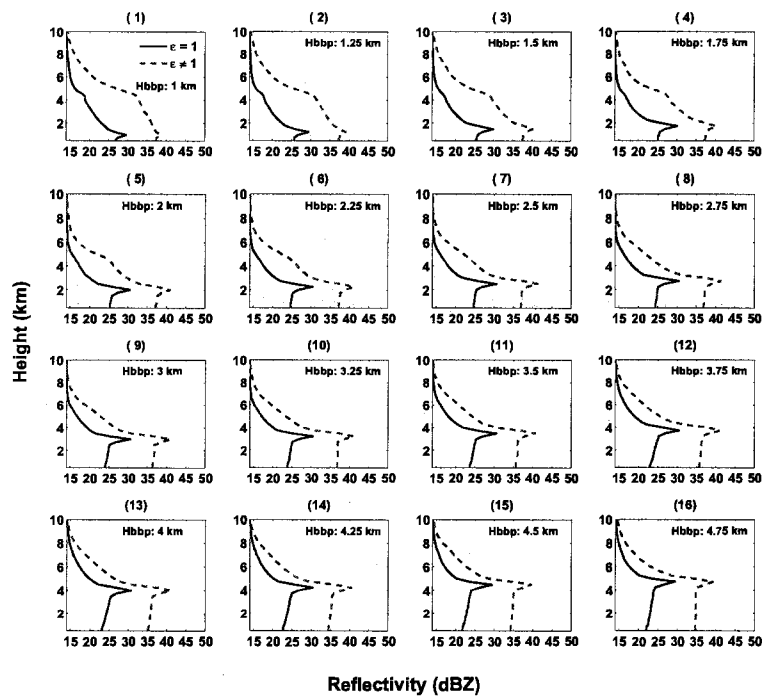


(b)

Figure 3.11: Comparison of the mean profiles of stratiform rain over ocean and over land for (a) $\epsilon = 1$, and (b) $\epsilon \neq 1$.



(a)



(b)

Figure 3.12: Comparison of the mean profiles of stratiform rain between $\epsilon = 1$ and $\epsilon \neq 1$ for (a) over ocean, and (b) over land.

3.4 Drop Size Distribution (DSD) Parameters Estimation

As mentioned in the PR attenuation correction algorithm section, the α adjustment method can provide independent estimates of DSD parameters. The methodology adapted from Chandrasekar et al. (2005) is used here and briefly described as follows: Again, the assumed relationship used in the PR-attenuation correction algorithm between specific attenuation and the reflectivity factor is expressed in the form of a power law as,

$$k = \alpha Z_e^\beta \quad (3.11)$$

If k - Z_e relationship is normalized by N_w , then the normalized k - Z_e can be written as:

$$\left(\frac{k}{N_w} \right) = \tilde{\alpha} \left(\frac{Z_e}{N_w} \right)^\beta \quad (3.12)$$

$$k = \tilde{\alpha} (N_w)^{1-\beta} Z_e^\beta \quad (3.13)$$

$$k = \alpha_{adj} Z_e^\beta \quad (3.14)$$

Where α_{adj} is the new value for α , called α adjustment as mentioned in the TRMM-PR attenuation correction process, and can be written as,

$$\alpha_{adj} = \tilde{\alpha} (N_w)^{1-\beta} \quad (3.15)$$

From Equation 3.15, N_w can be written as:

$$N_w = \left(\frac{\alpha_{adj}}{\tilde{\alpha}} \right)^{\frac{1}{1-\beta}} \quad (3.16)$$

Figure 3.13 shows the log-log plot of k/N_w versus Z_e/N_w for rain at Ku-band (13.8 GHz). By using the initial values of α for stratiform and convective rain and using the power law fitting, $\tilde{\alpha}$ can be found. $\tilde{\alpha}$ is found to be 4.5E-05 for stratiform and 4.31E-05 for convective case rain. α_{adj} can be written as:

$$\alpha_{adj} = \alpha_{ini} \epsilon \quad (3.17)$$

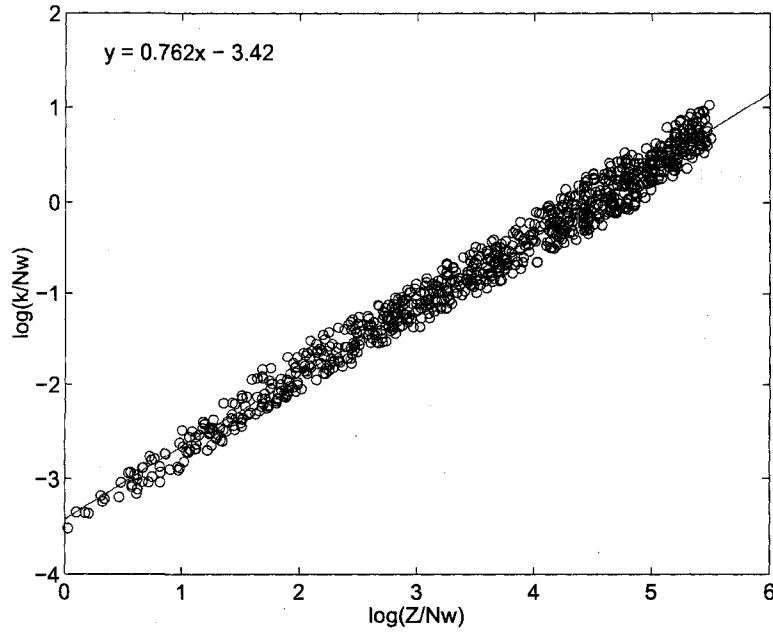


Figure 3.13: Scatter plot Z/N_w vs. k/N_w .

where ϵ is the correction factor used in the α adjustment method in the TRMM-PR attenuation correction algorithm.

Once α_{adj} is calculated, N_w can be retrieved from (3.16), The median volume diameter, D_o can be subsequently calculated as

$$D_o = \left[\frac{Z_e}{N_w C} \right]^{\frac{1}{7}} \quad (3.18)$$

Where C can be written as,

$$C = \frac{f(\mu)\Gamma(7 + \mu)}{(3.67 + \mu)^{7+\mu}} \quad (3.19)$$

As mentioned in the TRMM-PR algorithm section, when attenuation is small (low rainfall rate, less than about 5 mm/hr), SRT does not provide a reliable PIA measurement. As a result, the correction factor ϵ becomes unity, the attenuation estimate is based on HB solution alone, and the TRMM-PR does not provide independent estimates of DSD parameters. In heavy rain cases indicated by, in part, deviation of ϵ from unity, the α coefficient is adjusted, providing an independent estimate of DSD

parameters. Estimate DSD parameters using data from the year 2000 over land and over the ocean are presented.

Estimated DSD parameters presented here are divided into two categories, determined by correction factor ϵ : 1) α coefficient is not adjusted ($\epsilon = 1$); 2) α coefficient is adjusted (ϵ deviates from 1). Figure 3.14 (a) and (b) show distribution of D_o and N_w over land and over ocean, respectively, with ϵ equal to unity. Figure 3.15(a) and (b) show distribution of D_o and N_w over land and over ocean, respectively, with ϵ greater than unity. Figure 3.16(a) and (b) show distribution of D_o and N_w over land and over ocean, respectively, with ϵ less than unity.

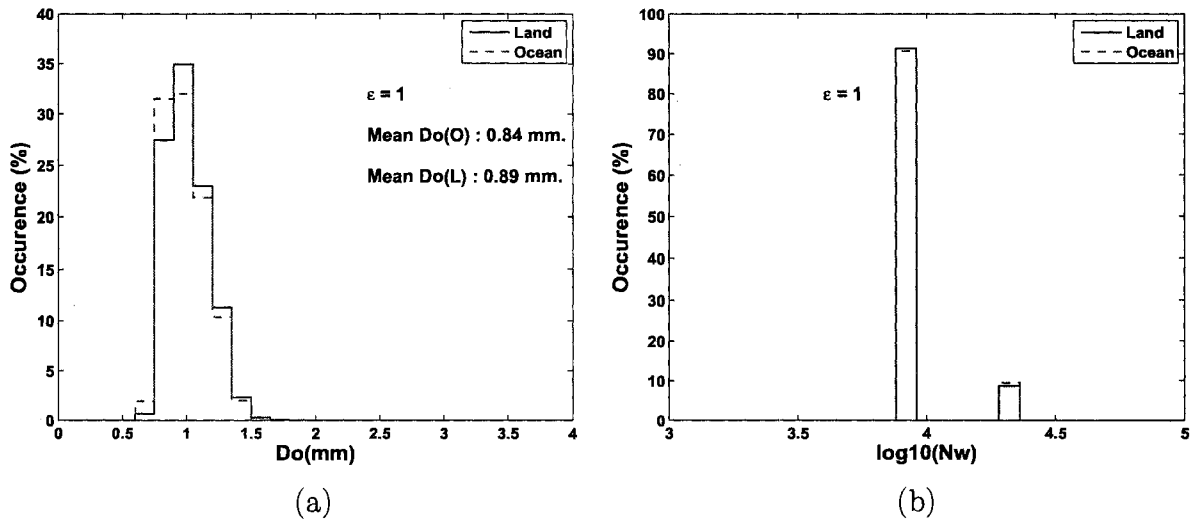


Figure 3.14: (a) Distribution of D_o , (b) N_w for $\epsilon = 1$ over land and over ocean.

It can be seen in Fig. 3.14 (a) and (b) that when ϵ is equal to unity, average D_o over ocean and over land are similar at about 0.89 mm. The two constant N_w are the default values in the TRMM-PR rain profiling algorithm (Iguchi et al., 2000; Wilheit et al., 2007). The smaller value (3.88) of N_w is the default for stratiform rain, and the larger value (4.28) for convective rain. The stratiform value is slightly lower than N_w of Marshall and Palmer (1948), which is 3.90, because it represents the N_w value aloft where the drops fall faster than at the surface. The value of D_o is relatively small compared to those which correspond to ϵ differing from unity.

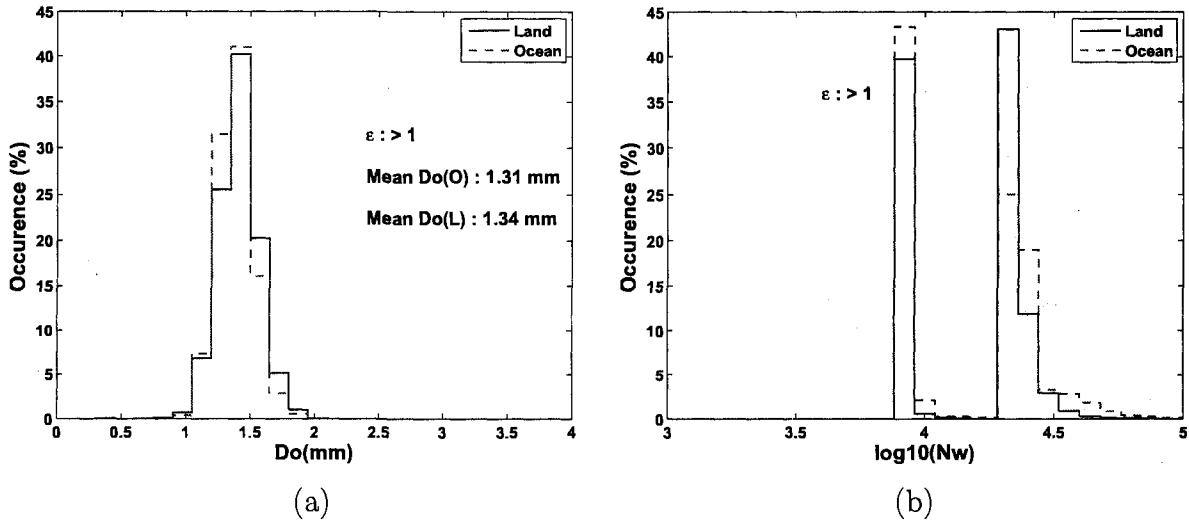


Figure 3.15: (a) Distribution of D_o , (b) N_w for $\epsilon > 1$ over land and over ocean.

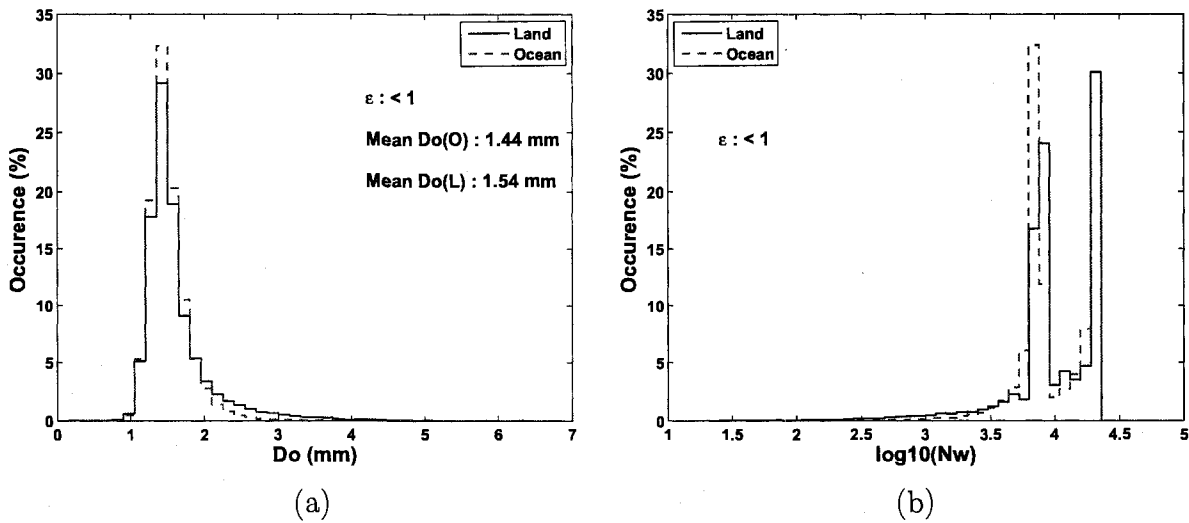


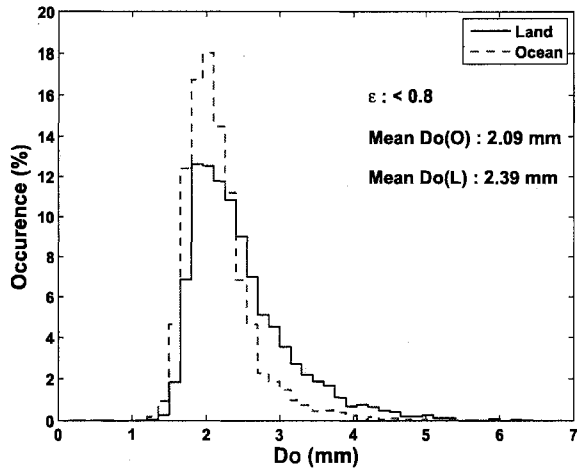
Figure 3.16: (a) Distribution of D_o , (b) N_w for $\epsilon < 1$ over land and over ocean.

Average D_o for ϵ greater than unity is about 1.31 mm. over ocean and 1.34 mm. over land. The default values of N_w this case remain prominent even though there are some N_w value start to deviate from the default values. For the case of ϵ less than 1, shown in Fig. 3.16 (a) and (b), average D_o increases both over ocean and over land at about 1.44 mm. and 1.54 mm., respectively. The default values of N_w in this case are still dominant. The tail of the N_w distribution moves toward the direction of small N_w . This can be explained by an increase of D_o .

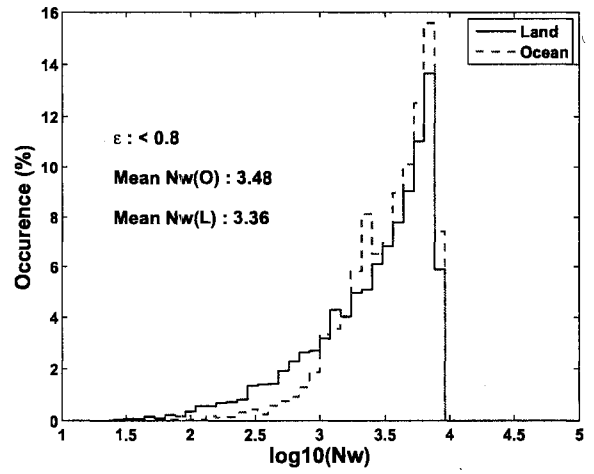
Further study in the sub-interval of ϵ was also done. Figures 3.17 (a) and (b) show the distribution of D_o and N_w over land and over ocean, respectively, with ϵ less than 0.8. Figures 3.18 (a) and (b) show distribution of D_o and N_w over land and over ocean, respectively, with ϵ less than 0.6.

As seen from Fig. 3.17 (a) and (b) when ϵ is less than 0.8, average D_o increases to 2.39 mm. over land and 2.09 mm. over ocean. N_w for this case is smaller than previous cases, as expected, and is similar between over land and over ocean. When ϵ is less than 0.6, D_o increases to as large as 3.0 mm. over land and 2.7 mm. over ocean, as shown in Fig. 3.18 (a). There are no longer the sign of default values of N_w . Average $\log_{10}N_w$ when ϵ less than 0.6, is much smaller than previous cases— about 2.7 over land and 3.0 over ocean.

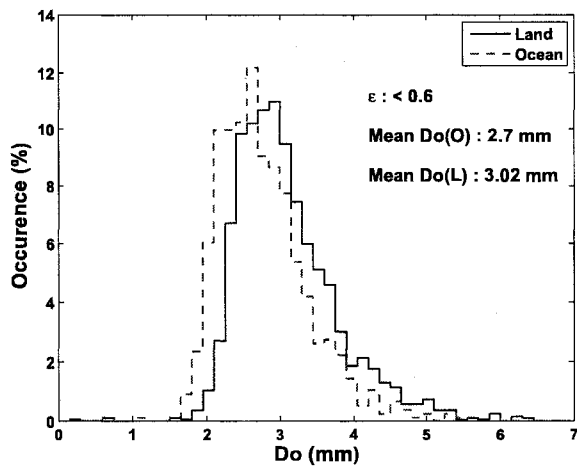
For all cases shown above, several conclusions can be drawn from this analysis. When the value of ϵ is relatively much lower than unity, D_o increases significantly and N_w decreases accordingly. The D_o value over land appears to be larger than that over ocean when ϵ deviates much lower from unity. This can be due to the predominance of ice hydrometeor type over land (Bringi and Chandrasekar, 2001). However, we want to pursue further: (a) whether or not these phenomena depend on different rain type (stratiform/convective), and (b) the proportion of occurrence over land compared with over ocean. Figures 3.19, 3.20 and 3.21 show percentage occurrence of ϵ equal 1, greater than 1, less than 1, less than 0.8, and less than 0.6 over land and over ocean for different rain types.



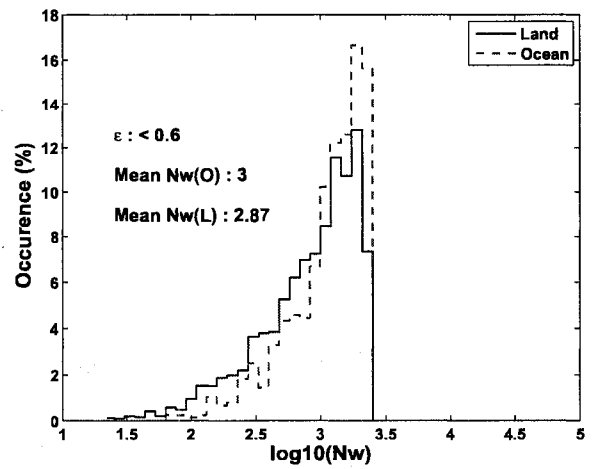
(a)



(b)

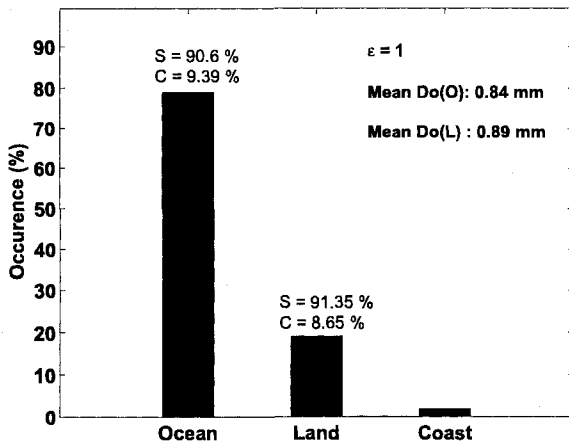
Figure 3.17: (a) Distribution of D_o , (b) N_w for $\epsilon < 0.8$ over land and over ocean.

(a)

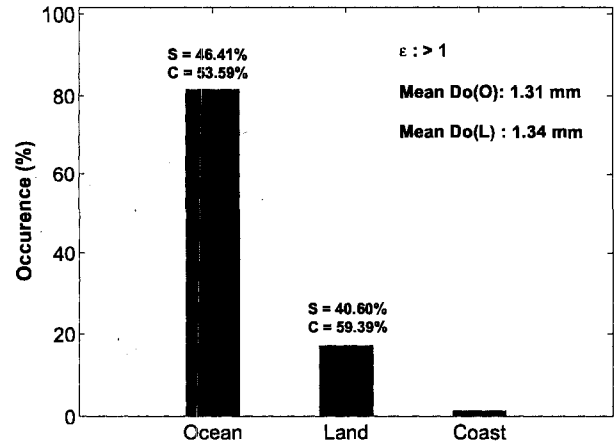


(b)

Figure 3.18: (a) Distribution of D_o , (b) N_w for $\epsilon < 0.6$ over land and over ocean.

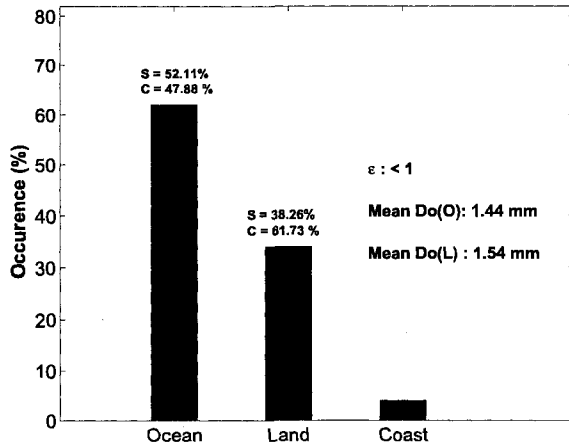


(a)

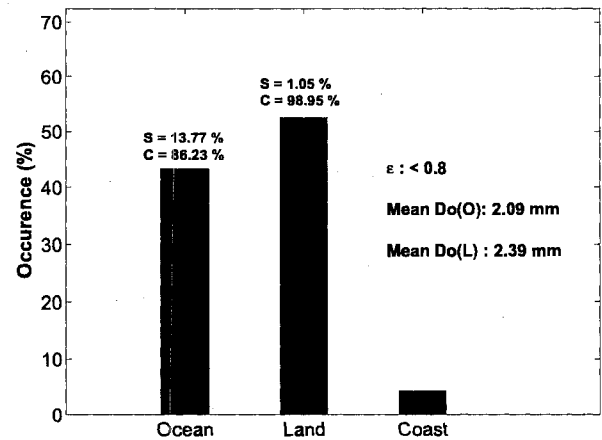


(b)

Figure 3.19: Percentage occurrence of (a) $\epsilon = 1$ and mean D_o , (b) $\epsilon > 1$ and mean D_o over land (L) and over ocean (O). Percentage occurrence of convective (C) and stratiform (S) rain type over land and ocean is shown over the bars.



(a)



(b)

Figure 3.20: Percentage occurrence of (a) $\epsilon \leq 1$ and mean D_o , (b) $\epsilon \leq 0.8$ and mean D_o over land (L) and over ocean (O). Percentage occurrence of convective (C) and stratiform (S) rain type over land and ocean is shown over the bars.

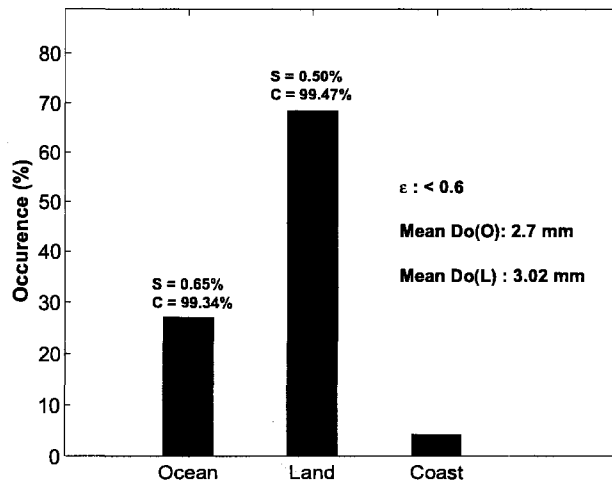


Figure 3.21: Percentage occurrence of $\epsilon < 0.6$ and mean D_o over land (L) and over ocean (O). Percentage occurrence of convective (C) and stratiform (S) rain type over land and ocean is shown over the bars.

As seen in Fig. 3.19 (a), almost 80% of ϵ equal to unity occurs over ocean, of which about 90% is stratiform rain type over both land and ocean. When ϵ is greater than unity, as shown in Fig. 3.19 (b), the frequency of occurrence over ocean increases slightly and the frequency of occurrence over land has slight decrease. When ϵ is less than unity, as shown in Fig. 3.20(a), the frequency of occurrence over land and over ocean becomes less different but it remains apparent. The portion of convective versus stratiform rain is also less different over both land and ocean. In a rather extreme case when ϵ is less than 0.6, the frequency of occurrence over land is almost 70%, of which more than 90 % is convective rain.

Some conclusions can be drawn based on these findings. For those reflectivity profiles that have ϵ much lower than unity, which occurs very frequently over land in convective rain, the particle type in radar resolution volume reflects predominance of frozen particles, and large rain drops were retrieved. On the other hand, for those reflectivity profiles that have ϵ greater than unity, which occurs very frequently over ocean with the comparable portions between convective and stratiform rain, smaller rain drops were retrieved.

3.5 Comparison of Estimated DSD parameters between TRMM-PR and Dual-polarization Ground-based Radar

Ground validation (GV) program operated by the TRMM-satellite validation office is a major part of the TRMM mission. The GV program consists of 10 validation sites worldwide as shown in Fig. 3.22. The primary goal of the GV program is to provide ground-based measurements from multiples sensors, namely, radars, disdrometers and rain gauges, that can be used to validate the TRMM observations so that the performance of the TRMM system design can be evaluated and improved (Kummerow et al., 2000; Wolff et al., 2005).

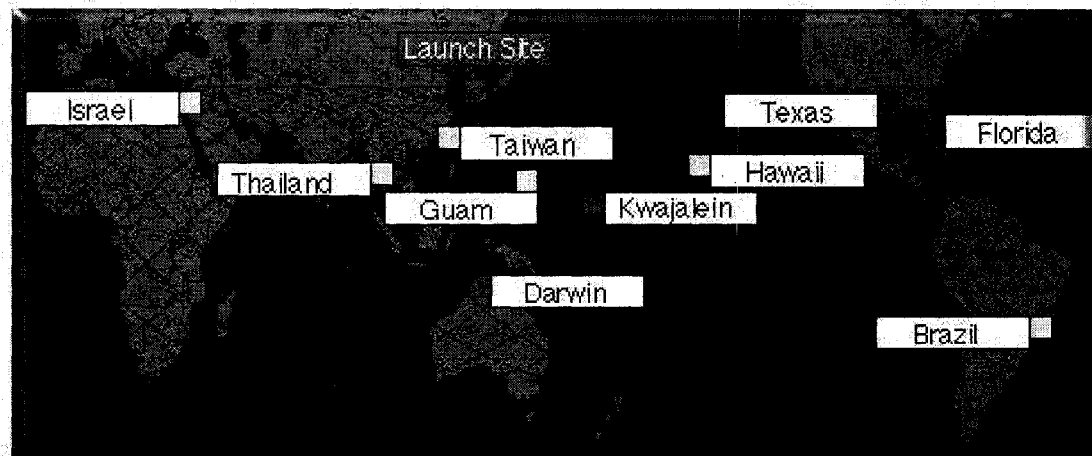


Figure 3.22: Worldwide locations of the TRMM ground validation sites (adopted from TRMM ground validation website).

The field campaign is one of the key components of the TRMM ground validation (GV) program. Several field experiments were conducted before and after launching the TRMM satellite in late 1997. The large-scale biosphere-atmosphere experiment (LBA), or TRMM-LBA is one of the major field experiments of the TRMM ground validation program. TRMM-LBA was carried out in Amazonia from 1 November 1998 to 28 February 1999 (Cifelli et al., 2002). The experiment was focused on the dynamic, microphysical, electrical and diabatic heating characteristics of tropical convection in the Amazon region. Data collected from TRMM-LBA is being used

in part to validate findings from the TRMM satellite and numerical cloud models. Observational platforms involved in the experiment included the NCAR S-Pol radar, the NASA TOGA radar, atmospheric sounding and tethered sonde systems, the NASA ER2 and UND Citation aircraft, a lightning location and detection network, rain gauges, disdrometers, and NOAA Aeronomy Laboratory UHF and S-band profilers.

In this section, statistical comparison of DSD retrieval between the TRMM-PR and the NCAR S-pol radar was made. The S-Pol radar is a dual-polarization radar operating at S-band. Characteristics of the S-pol radar are shown in Table 3.2. Fig. 3.23 shows the area of LBA experiments (latitude and longitude) and location of the S-pol radar. In the figure, 200 km. radius ring from S-Pol is indicated by the green circle. Data from a TRMM-PR overpass falling within the circled area were analyzed for DSD comparison. The TRMM-PR overpass swath is indicated by a blue stripe.

Table 3.2: NCAR S-Band Polarization Radar (S-Pol) Characteristics

S-Band Polarization Radar (S-Pol) Characteristics	
Frequency	2.7 - 2.9 GHz
Pulse width	0.3 - 1.4 μ se-tapered
PRF	0-1300 Hz
Peak power	1 Mw
Polarization	H and V alternating or H only
minimum detectable at 50 km/1km	-15 dBZ/-52 dBZ at -6 dBZ SNR
Noise power	-115.5 dBm
Dynamic range	90 dB
Bandwidth	0.738
Antenna	Parabolic, center feed
Gain	44.5 dB including wave guide loss
Diameter	8.5 m(28 ft.)
Beamwidth	0.91 degrees
Recorded variables	$P_{hh}, P_{vv}, V, W, R(1)_{hv}, Phi_{DP},$ $Phi_{hv}, Z_h, Z_{dr}, LDR, K_{dp}$

The meteorological regime for this experiment were characterized into two regimes, namely, easterly and westerly, which was described in Cifelli et al. (2002). The DSD

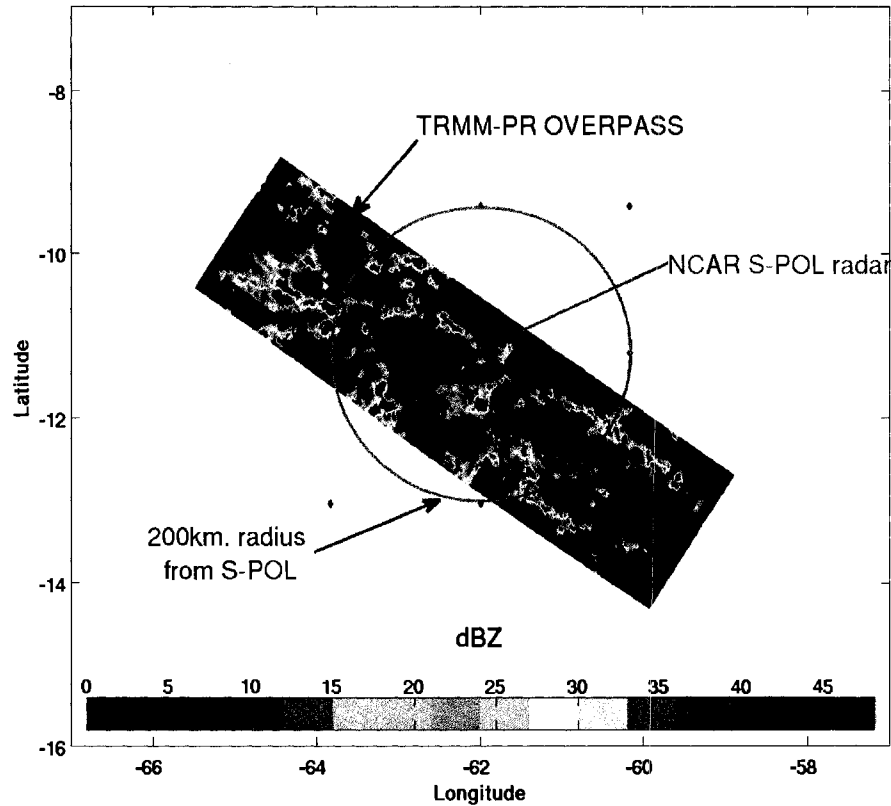


Figure 3.23: Illustration of location of NCAR S-Pol radar of Large scale Biosphere-Atmosphere (LBA) experiment and TRMM-PR overpass at area of LBA experiment Green circle indicates 200 km. radius from S-Pol within the area where TRMM-PR data was analyzed for DSD comparison.

retrieval algorithm for TRMM-PR developed by Chandrasekar et al. (2003a) was used here (The DSD retrieval for the S-Pol radar was provided by Robert Cifelli). The statistical comparisons are made, including comparison of distribution of DSD and comparison of the vertical structure of reflectivity profiles from TRMM-PR observations in easterly and westerly.

Figures 3.24 (a) and (b) show the distributions of retrieved D_o from the TRMM-PR and the S-pol data in easterly regimes for all data and convective rain, respectively. The D_o distributions from TRMM-PR and S-pol have a similar shape. Despite the minor differences in the frequency of occurrences and the width of the distributions,

the modes of the distributions agree well within 0.1 mm. The modes of D_o distributions from TRMM-PR and S-pol for all data are 0.9 and 1 mm., respectively (see Fig. 3.24 (a)). The modes of D_o distributions from TRMM-PR and S-pol for convective rain are 1.2 and 1.3 mm., respectively (see Fig. 3.24 (b)).

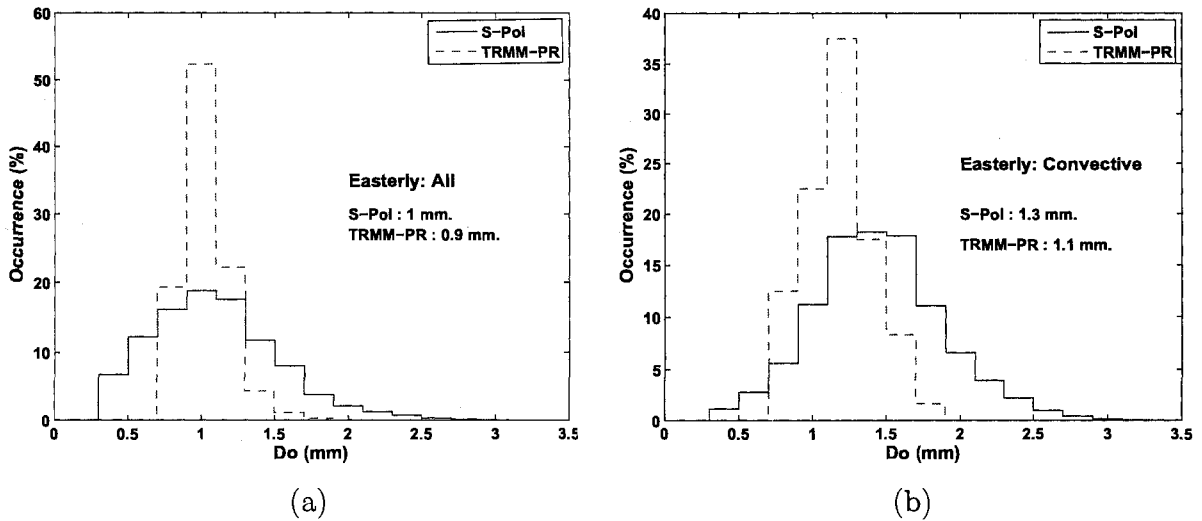


Figure 3.24: Comparison of distributions of retrieved D_o from TRMM-PR and S-pol data in easterly regime for (a) all rain type, and (b) convective rain type

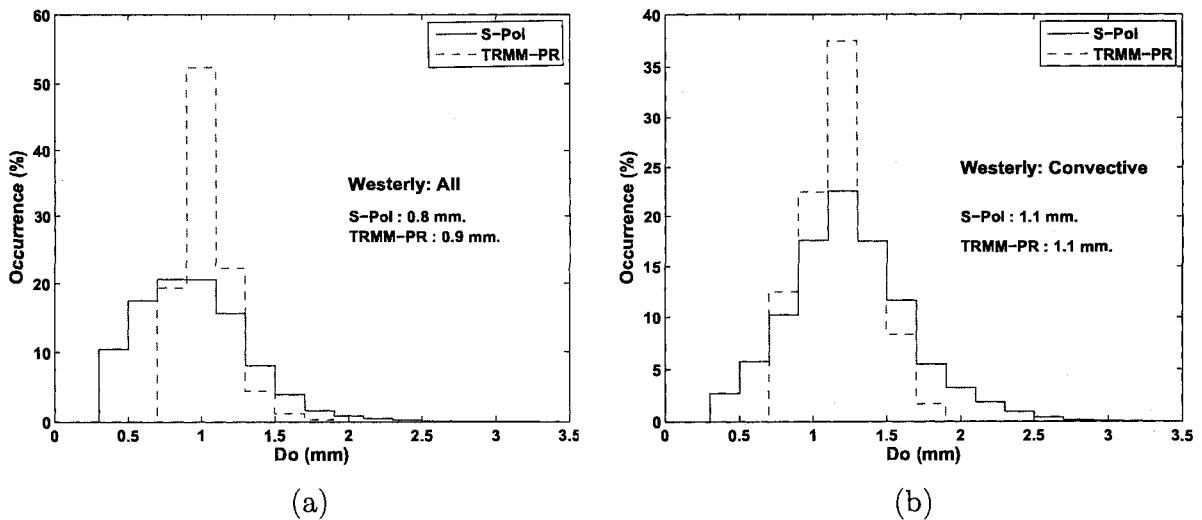


Figure 3.25: Comparison of distributions of retrieved D_o from TRMM-PR and S-pol data in westerly regime for (a) all rain type, and (b) convective rain type

Similar to what appears in the easterly regime, D_o distributions from TRMM-PR

and S-pol for all data and convective rain in the westerly regime have similar shapes. The percentages of occurrences at the mode of TRMM-PR are much higher than that of S-pol. This results in the narrower distributions in TRMM-PR. The modes of the D_o distributions between the two radar systems for both data sets agree very well, especially in convective rain, the modes are exactly the same at 1.1 mm, as seen in Fig. 3.25 (b). Differences between the easterly and westerly can be seen as well. The modes of D_o distributions in the easterly are larger than that in the westerly for both all data set and convective rain.

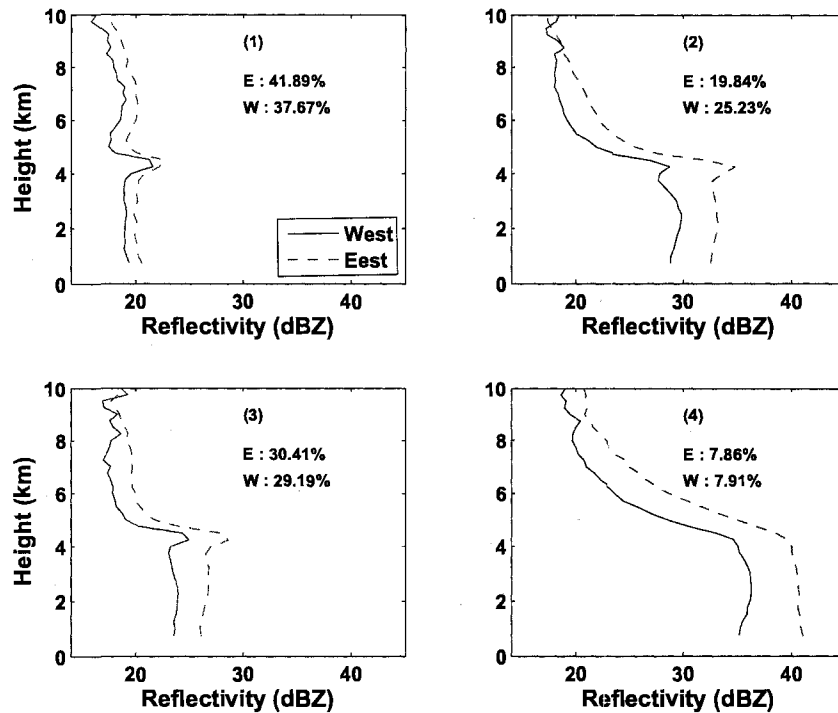


Figure 3.26: Comparison of four characteristic reflectivity profiles between the westerly and easterly regimes based on the classification of TRMM-PR data.

It is worth comparing the reflectivity profile structure between the two regimes. The 2x2 SOM classification of reflectivity profiles from both easterly and westerly are shown in Fig. 3.26. The class number is indicated by number 1 to 4 in the figure. It can be seen from the Fig.3.26 that the characteristic profiles in the easterly are

stronger than that in the westerly regime. This results are similar to the results of D_o . The difference in reflectivity is largest in the convective rain (class 4)—about 6 dBZ near the surface. More than 90% (from class 1, 2 and 3) are stratiform rain. Despite minor differences in the structure of the four profiles between the easterly and the westerly, in general, they have similar reflectivity profile structures.

3.6 Summary and Conclusion

TRMM-PR retrieval algorithm and analysis of the PR observation for 12 months are presented. The SOM technique is used to characterize vertical profile of reflectivity (VPR) into a number of characteristic profiles, according to rain type and the correction factor (ϵ) over land and over ocean. The profiles associated with $\epsilon = 1$ have relatively weak reflectivity, and hence small attenuation. The characteristic profiles with $\epsilon = 1$ over land and ocean are similar. For $\epsilon \neq 1$, the characteristic profiles for convective rain over land is more intense than that over ocean. Also, the characteristics profile with $\epsilon \neq 1$ are stronger than those with $\epsilon = 1$. In stratiform rain with bright band, VPR are characterized into a number of mean profiles using the height of the bright band peak. Similar to convective rain, the mean profiles with $\epsilon = 1$ have weaker reflectivity than those with $\epsilon \neq 1$. The mean profiles over land and over ocean are similar for $\epsilon = 1$ and $\epsilon \neq 1$.

Drop Size Distribution (DSD) parameters from TRMM-PR observations were estimated and interpreted in accordance with the correction factor ϵ , used in the attenuation-correction algorithm, and rain type. Such interpretation of the results allows us to discover similarities and systematic differences of estimated DSD over land and over ocean as well as in different rain types. There are relatively more large rain drops and fewer small rain drops over land than over ocean. Such results are associated with a low value of ϵ . In addition, a very low ϵ could indicate predominant ice particles near the ground, especially in convective rain over land. Retrieved D_o based on TRMM-PR observations and a dual-polarization ground-based radar

measurements from the TRMM-LBA field experiment was compared. Based on the analyzed data, the retrieved D_o between the two radar systems, in general, agree well.

Knowledge gained from TRMM-PR observations analysis, including examining natural variation of vertical profile of radar reflectivity and precipitation microphysics, is very important and useful for developing simulation techniques and retrieval methods in the Global Precipitation Measurement (GPM) era.

CHAPTER 4

GPM-DPR : SYSTEM AND RETRIEVAL METHODS

4.1 Introduction

Following the success of the TRMM, which has been providing global observations of precipitation over the tropics for more than ten years, the next mission on precipitation measurement from space has been planned. The mission is Global Precipitation Measurement (GPM) and also a joint mission between the Japan Aerospace Exploration Agency (JAXA) and the US National Aeronautics and Space Administration (NASA). The scientific objectives of GPM are as follows (Adam, 2002),

- Improving the scientific understanding of the global water cycle and fresh water availability,
- Improving the accuracy of precipitation forecasting and its impact on weather,
- Providing frequent and complete sampling of the Earth's precipitation.

4.2 GPM-DPR Overview

The GPM “core satellite” will carry two main instruments, namely dual-frequency precipitation radar (DPR) and a GPM microwave imager (GMI). The satellite will orbit at an altitude about 400 km with a 65° inclination angle. The DPR consists of Ku-band (13.4 GHz) radar (henceforth KuPR), and Ka-band (35.5 GHz) radar (henceforth KaPR). The Ku-band radar is approximately the same as TRMM precipitation radar (PR) with some improvements (Iguchi, 2003). The three main objectives

of DPR are: 1) to provide a three-dimensional precipitation structure, 2) to improve the sensitivity and accuracy of precipitation measurement, and (3) to calibrate the precipitation amount estimated by microwave radiometers on the constellation satellites. A graphical illustration of GPM system, which consists of the “core satellite” and several constellation satellites, is shown in Fig. 4.1. The DPR scan geometry and its main characteristics are shown in Fig. 4.2 and Table 4.1, respectively.

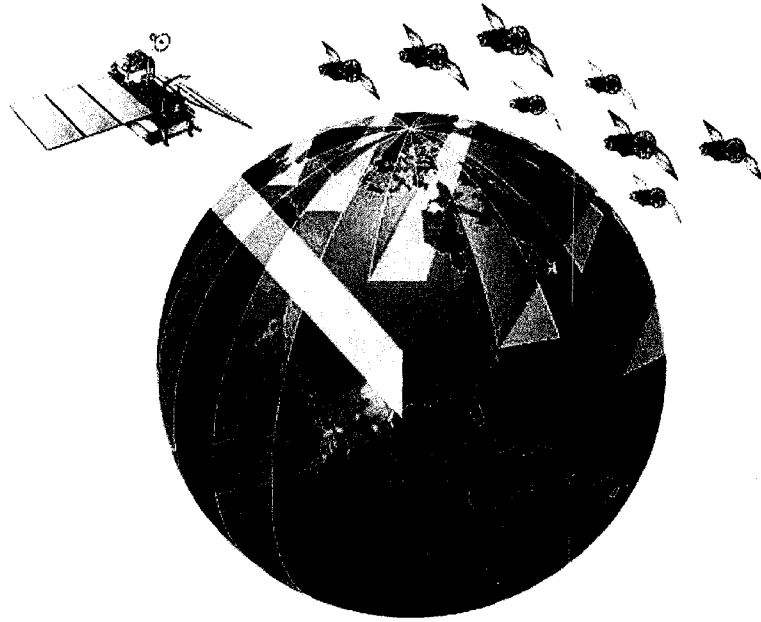
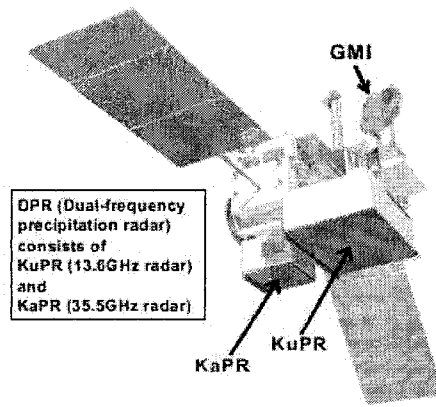
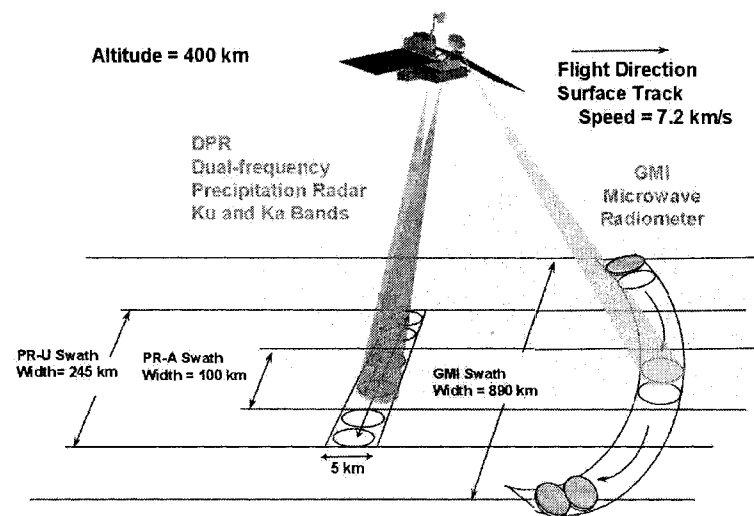


Figure 4.1: Graphical illustration of GPM system.

KuPR has a swath width of about 245 km, which is formed by a $\pm 17^\circ$ scan. KaPR has a narrower swath width of about 120 km, which is formed by a $\pm 8^\circ$ scan. At the altitude of 400 km, the horizontal resolution at nadir is 5 km (the same for both radars). The minimum detectable reflectivity in KuPR is 18 dBZ and 12 dBZ in KaPR. Because KaPR has a higher sensitivity, it will detect snow and light rain, while KuPR will detect moderate to heavy rain. In the matched beam mode, DPR will provide improved accuracy of drop size distribution and rainfall rate estimates using a combination of KuPR and KaPR radar measurements (Iguchi, 2003). Figure 4.3 shows the concept of dual-frequency measurement of precipitation by DPR.



(a)



(b)

Figure 4.2: (a) Dual-frequency precipitation radar (DPR), (b) Scan geometry of DPR (adopted from Senbokuya et al. (2004)).

4.3 Dual-frequency Retrieval Methods

In contrast to the single-frequency method used by the TRMM-PR, dual-frequency retrieval methods will be used to estimate DSD parameters and rainfall rate. The underlying microphysics of precipitation structures and DSDs dictate the types of models and retrieval algorithms that can be used to estimate precipitation. There are a number of dual-frequency methods proposed for the DPR (Meneghini et al., 1992,

Table 4.1: Main characteristics of DPR.

	KuPR	KaPR
Frequency	13.597 & 13.603 GHz	35.547 & 35.553 GHz
Antenna type	Active phase array	Active phase array
Swath width	245 km	120 km
Horizontal resolution	5 km (at nadir)	5 km. (at nadir)
Beam width	0.7°	0.7°
Tx pulse width	1.6 μ s (x2)	1.6/ 3.2 μ s (x2)
Range resolution	250 m	250/500 m
Observation range	18 km to -5 km ASL	18 km to -3 km ASL
Tx Peak power	1000 W	144 W
Minimum detectable: rain rate (reflectivity)	0.5 mm hr ⁻¹ (18 dBZ)	0.2 mm hr ⁻¹ (12 dBZ)
Measurement accuracy	within $\pm 1dB$	$\pm 1dB$
Data rate	95 kbps	95 kbps
Weight	370 kg	290 kg
Power consumption	max 352 W	max 331 W
Size	2.4x2.4x0.6 m	1.44x1.07x0.7 m

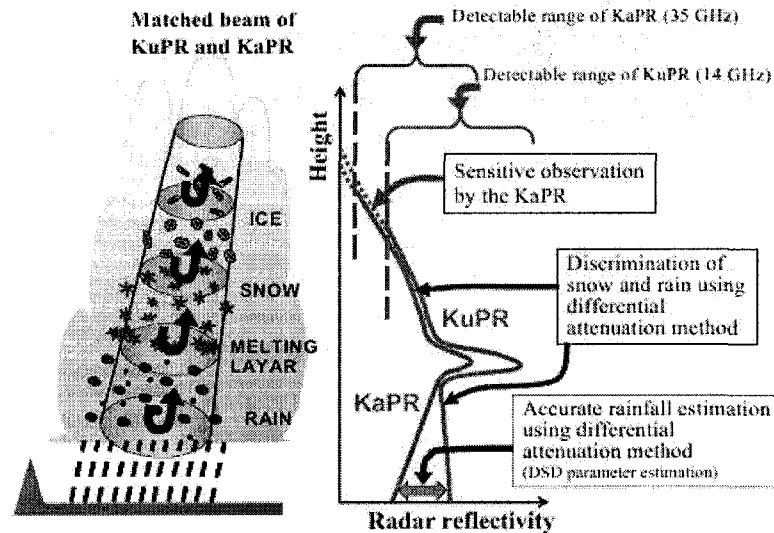


Figure 4.3: Concept of the dual-frequency measurement of precipitation (adopted from Senbokuya et al. (2004)).

1997; Iguchi and Meneghini, 1995; Mardiana et al., 2004; Rose and Chandrasekar, 2006a). They can be categorized into two types. One is the standard dual-frequency

method based on the conversion of differential attenuation to rain rate. The other is based on reflectivity, which is corrected for attenuation, and DSD parameters are inferred by non-Rayleigh scattering. The latter can be formulated either in integral equations (Meneghini et al., 1997) or a first-order differential equation (Iguchi and Meneghini, 1995).

The integral equation can be solved either in a forward (forward method) or backward direction (backward method). In the forward method, DSDs are calculated at each bin starting from the top bin and moving to the bottom (see Fig. 4.4). In contrast to the forward method, the backward method begins at the bottom bin and moves upward to the top, calculating the DSD parameters and attenuation along the path. The assumption with the forward method is that there is no attenuation above the top bin and that the integral equations can be solved in a single pass through the hydrometeor regions. The forward method has limited application because of a tendency to diverge in regions of moderate to heavy attenuation (moderate to heavy rainfall). The backward method tends to be more stable than the forward method but generally requires an a priori knowledge of the total path-integrated-attenuation (PIA). The backward method can also be solved iteratively without SRT (Mardiana et al., 2004; Rose and Chandrasekar, 2006a). This technique randomly initializes the PIA at the bottom and solves recursively for DSDs along the path upward to the top. The iterations stop when retrieved DSDs can reconstruct the measured reflectivity at the bottom bin. The limitation of this technique is that it seems to fail when a strong PIA is present (a combination of large D_o and N_w). Rose and Chandrasekar (2006a) used linear model for N_w along rain profile as a constraint to remedy this problem to some extent.

Although the standard dual-frequency technique, in principle, relies on Rayleigh scattering and uniform rain assumptions, it is simple and can provide a robust rain rate estimate as suggested by Iguchi (2005). In addition, when the PIA from SRT is not available, this technique can be used to estimate the PIA when applied to full

path. Meneghini et al. (2002) used PIA estimated by standard dual-frequency in the backward method to estimate DSDs. Moreover, uncertainties of the technique are also easy to evaluate. This chapter describes integral equations for dual-frequency retrieval methods and focuses on an extensive study of standard dual-frequency. The bias of path-averaged rainfall rate estimate deduced from violations of the assumptions on which this method lies is also extensively examined.

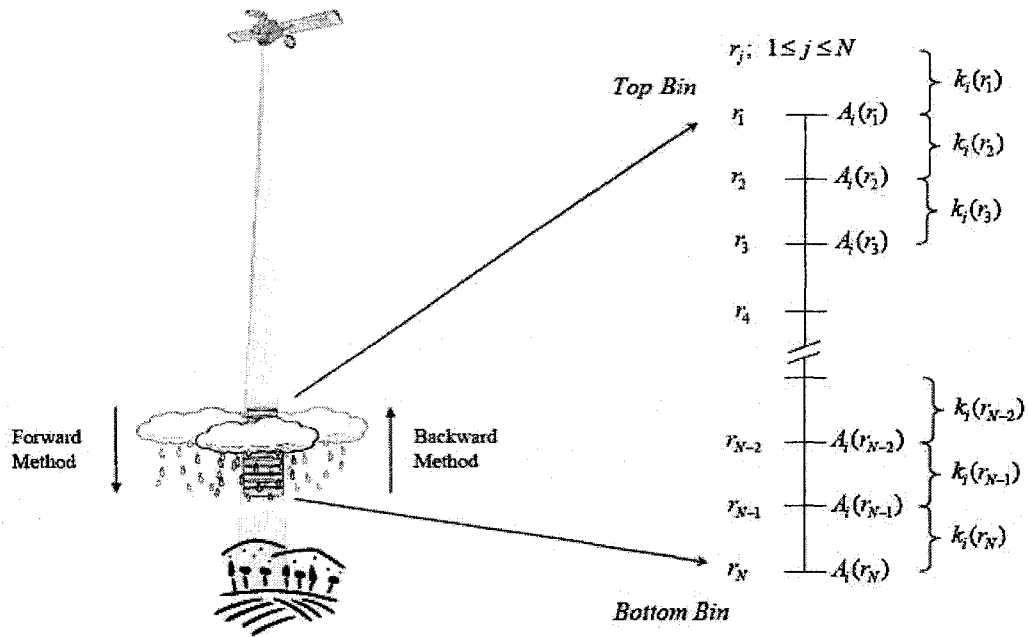


Figure 4.4: Schematic illustration of dual-frequency radar observation along vertical profile of precipitation (adapted from Rose 2004).

4.3.1 Integral Equations for the Dual-frequency Method

The dual-frequency integral equations described by Meneghini et al. (1992) solve for the two important DSD parameters, D_o and N_w , at each range bin based on the assumed microphysical model of hydrometeors and two-way path attenuation. The governing equations in integral form are as follows:

Measured reflectivity at a certain range bin can be expressed in terms of effective radar reflectivity, Z_{ei} , and two-way path-integral attenuation factor, A_i , up to that

range bin as,

$$Z_{mi}(r_j) = Z_{ei}(r_j)A_i(r_j) \quad (4.1)$$

The subscript i ($i=1, 2$) represents the 13.6 and 35.6 GHz, respectively, and j represents j^{th} range bin where $1 < j < N$. N represents the range bin at the bottom (surface). The specific attenuation, k_i , for each frequency is defined for the region between bins, as seen in Fig. 4.4.

The normalized gamma model of drop-size distribution (DSD), as described in section 2.2 is expressed as

$$N(D) = N_w f(\mu) \left(\frac{D}{D_o} \right)^\mu e^{-\Lambda D} \quad (4.2)$$

where

$$\Lambda = \frac{3.67 + \mu}{D_o} \quad (4.3a)$$

$$f(\mu) = \frac{6}{3.67^4} \frac{(3.67 + \mu)^{\mu+4}}{\Gamma(\mu + 4)} \quad (4.3b)$$

The effective radar reflectivity based on the normalized gamma DSD can be expressed as

$$\begin{aligned} Z_{ei}(r_j) &= c_{zi} \int_D \sigma_{bi}(D) N(D) dD \quad \text{mm}^6 \text{m}^{-3} \\ &= c_{zi} \int_D \sigma_{bi}(D) N_w f(\mu) \left(\frac{D}{D_o} \right)^\mu e^{-\Lambda D} dD \\ &= N_w f(\mu) D_o^{-\mu} c_{zi} \int_D \sigma_{bi}(D) D^{-\mu} e^{-\Lambda D} dD \\ &= N_o I_{bi}(D_o) \end{aligned} \quad (4.4)$$

where

$$I_{bi}(D_o) = c_{zi} \int_D \sigma_{bi}(D) D^{-\mu} e^{-\Lambda D} dD \quad (4.5a)$$

$$c_{zi} = \frac{\lambda_i^4}{\pi^5 |K|^2} \quad (4.5b)$$

where σ_{bi} is the radar backscatter cross-section as described in section 2.3.2. λ_i is the operating radar wavelength, and K is dielectric factor defined as

$$K = \frac{\epsilon_r^2 - 1}{\epsilon_r^2 + 2} \quad (4.6)$$

where ϵ_r is the dielectric constant of particle.

Taking the ratio of Z_{ei} for both frequencies yields

$$\begin{aligned} \frac{Z_{e1}}{Z_{e2}} &= \frac{C_{Z1} \int_D \sigma_{b1}(D) D^{-\mu} e^{-\Lambda D} dD}{C_{Z2} \int_D \sigma_{b2}(D) D^{-\mu} e^{-\Lambda D} dD} \\ &= \frac{I_{b1}(D_o)}{I_{b2}(D_o)} \\ &= f_2(D_o) \end{aligned} \quad (4.7)$$

and taking 10log of both sides (note that $\log = \log_{10}$, and $\ln = \log_e$), (4.7) can be rewritten as

$$\begin{aligned} 10 \log(Z_{e1}) - 10 \log(Z_{e2}) &= 10 \log[f_2(D_o)] \\ DFR &= dBZ_{e1} - dBZ_{e2} \\ &= f_3(D_o) \end{aligned} \quad (4.8)$$

where DFR is the dual-frequency ratio in decibels (Liao et al., 2005), f_3 is a function of D_o and (4.8) can be expressed as

$$DFR = f_3(D_o) \quad (4.9)$$

and D_o can be expressed in inverse formulation of f_3 denoted by f_4 as,

$$D_o = f_4(DFR) \quad (4.10)$$

Several curves of D_o versus DFR have been shown (Meneghini et al., 1997; Liao et al., 2005; Mardiana et al., 2004) for both snow and rain. Using (4.9), and appropriate microphysical models, the ratio of effective reflectivity between both frequencies can be used to directly estimate the median volume diameter, D_o .

The specific attenuation, k_i , at a particular range r can also be derived as

$$\begin{aligned}
k_i &= c_{ki} \int_D \sigma_{ti}(D) N(D) dD \\
&= c_{ki} N_w f(\mu) D_o^{-\mu} \int_D \sigma_{ti}(D) D^{-\mu} e^{-\Lambda D} dD \\
&= N_w f(\mu) D_o^{-\mu} I_{ti}(D_o) \\
&= N_o I_{ti}(D_o)
\end{aligned} \tag{4.11}$$

and

$$\begin{aligned}
C_{ki} &= 4.343 \times 10^{-3} \\
I_{ti}(D_o) &= c_{ki} \int_D \sigma_{ti}(D) D^{-\mu} e^{-\Lambda D} dD
\end{aligned} \tag{4.12}$$

where σ_{ti} is the radar extinction cross-section, as described in Section 2.3.1.

The value of N_w at a particular range r can be found from (4.1) and (4.4) as

$$N_w = \frac{Z_{mi}}{f(\mu) D_o^{-\mu} I_{bi}(D_o) A_i} \tag{4.13}$$

Given the attenuation at the bottom bin, and that D_o and N_w are known at that bin, specific attenuation can be estimated between the bottom and next higher bin, and consequently A_i at the next higher bin.

Referring to Fig. 4.4, the attenuation at the next higher bin, r_{j-1} , can be found from the information at the r_j bin using

$$\begin{aligned}
A_i(r_{j-1}) &= A_i(r_j) \exp \left[0.2 \ln(10) \int_{r_{j-1}}^{r_j} k_i(s) ds \right] \\
&= A_i(r_j) \exp \left[0.2 \ln(10) h N_w f(\mu) D_o^{-\mu} I_{ti}(D_o) \right]
\end{aligned} \tag{4.14}$$

4.3.2 Standard Dual-frequency Method

Standard dual-frequency is the well-known and fundamental method among the existing dual-frequency methods. The principle of this method is that path-averaged rain rate (PAR) can be estimated from differential attenuation using the empirical relation between specific attenuation and rain rate, k - R . The differential attenuation

is obtained by performing the frequency difference of the apparent reflectivity at specified r_1 and r_2 in each frequency, and then taking a difference of these differences. This leads to another name for this method, difference of attenuation difference (DAD) (Iguchi, 2005). Typically, r_1 is specified at the altitude above ground higher than r_2 within the rain region.

The standard dual-frequency method is based on two assumptions, Rayleigh scattering, and uniform rain. In other words, drop diameter should be relatively small compared to the wavelength of both channels, and the drop size distribution should not significantly change between r_1 and r_2 . A limitation is placed on applying this method when the two requirements are not satisfied. Although these two requirements are not always valid for the entire dynamic range of rainfall rate, it will be shown that this method provides a robust PAR estimate in the usual rain rate. Because of insensitivity to variation of DSD parameters of k - R relation (Atlas and Ulbrich, 1977) and independence from radar calibration, the DAD method demonstrate the attractive features for operational retrieval-algorithm design for the GPM-DPR. The governing equations of the DAD method are as follows:

The two-way path-integrated attenuation from the storm top to a range bin can be expressed as

$$\begin{aligned} A_i(r_j) &= 2 \int_0^{r_j} k_i(s) ds \\ &= 2 \int_0^{r_j} N_o(s) I_{ti}(D_o(s)) ds \end{aligned} \quad (4.15)$$

From (4.1) and (4.4), it follows that

$$10 \log_{10} Z_{mi}(r_j) = 10 \log_{10} N_o(r_j) + 10 \log_{10} I_{bi}(r_j) - A_i(r_j) \quad (4.16)$$

For dual-frequency, from (4.16), this yields

$$\begin{aligned} &[dBZ_{m1}(r_1) - dBZ_{m1}(r_2)] - [dBZ_{m2}(r_1) - dBZ_{m2}(r_2)] \\ &= 10 \log_{10} \left(\frac{I_{b1}(D_o(r_1)) I_{b2}(D_o(r_2))}{I_{b1}(D_o(r_2)) I_{b2}(D_o(r_1))} \right) - [A_1(r_1) - A_1(r_2)] + [A_2(r_1) - A_2(r_2)] \end{aligned} \quad (4.17)$$

From (4.17), an M parameter is defined as

$$M = \frac{I_{b1}(D_o(r_1))I_{b2}(D_o(r_2))}{I_{b1}(D_o(r_2))I_{b2}(D_o(r_1))} \quad (4.18)$$

If M is assumed to be unity, then the left-hand side of (4.17) represents the difference of the attenuation difference between r_1 and r_2 . By using k - R relation and the assumption in (4.18), (4.17) becomes

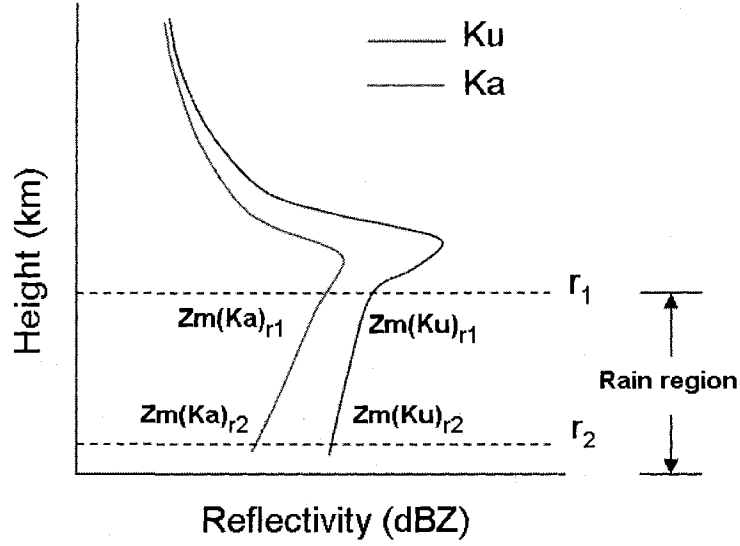


Figure 4.5: Schematic illustration of storm profile for difference of attenuation difference (DAD).

$$\begin{aligned} & [dBZ_{m1}(r_1) - dBZ_{m1}(r_2)] - [dBZ_{m2}(r_1) - dBZ_{m2}(r_2)] \\ &= -\left[\int_0^{r_1} k_1(s)ds - \int_0^{r_2} k_1(s)ds\right] + \left[\int_0^{r_1} k_2(s)ds - \int_0^{r_2} k_2(s)ds\right] \\ &= \left[\int_0^{r_2} a_1 R^{b_1}(s)ds - \int_0^{r_1} a_1 R^{b_1}(s)ds\right] + \left[\int_0^{r_2} a_2 R^{b_2}(s)ds - \int_0^{r_1} a_2 R^{b_2}(s)ds\right] \\ &= 2 \int_{r_1}^{r_2} (a_1 R^{b_1}(s) - a_2 R^{b_2}(s))ds \\ &\approx 2(r_2 - r_1)(a_1 \bar{R}^{b_1} - a_2 \bar{R}^{b_2}) \end{aligned} \quad (4.19)$$

If channel 1 is the Ka-band (35.5 GHz) and channel 2 is the Ku-band (13.6 GHz) as shown in Fig. 4.5, b_1 is not very different from b_2 , and hence $k_1 \gg k_2$. If the

left-hand side of (4.19) denotes as DAD, then (4.19) can be approximately rewritten as

$$\bar{R} = \left(\frac{DAD}{2(a_1 - a_2)(r_2 - r_1)} \right)^{1/b_1} \quad (4.20)$$

Where \bar{R} is the path-averaged rainfall rate (PAR) over the interval r_1 and r_2 . This approximation is valid as long as its relative fluctuation remains small. Since $a_2 \ll a_1$ and b_1 is comparable to b_2 , the relative error is rather small.

Non-Rayleigh scattering and non-uniform rain effect

As the principle of this method, the M value in (4.18) is assumed to be unity. For this assumption to be valid, at least one of the following two conditions must occur. The first one is when $I_{b_1}(D_o(r_1)) = I_{b_2}(D_o(r_1))$ and $I_{b_1}(D_o(r_2)) = I_{b_2}(D_o(r_2))$. This implies the existence of Rayleigh scattering. The second condition exists when $I_{b_1}(D_o(r_1)) = I_{b_1}(D_o(r_2))$ and $I_{b_2}(D_o(r_1)) = I_{b_2}(D_o(r_2))$. The latter happens when $D_o(r_1) = D_o(r_2)$ and, in a sense, implies that vertical rain is uniform. It is obvious that the value of M depends on D_o at r_1 and r_2 . To show the dependency, Fig. 4.6 illustrates the plot of $I_{b_1}(D_o)/I_{b_2}(D_o)$ as function of D_o . I_{b_1} and I_{b_2} represents the I_b value at 35.5 GHz and 13.6 GHz, respectively.

As seen from Fig. 4.6, the relation of $I_{b_1}(D_o)/I_{b_2}(D_o)$ and D_o is nonlinear and the value of $I_{b_1}(D_o)/I_{b_2}(D_o)$ approaches unity as D_o moves toward zero. This explains that Rayleigh scattering occurs in both channels at D_o less than about 0.3 mm. As mentioned earlier, if $D_o(r_1) = D_o(r_2)$, the value on the y-axis in Fig. 4.6 is always unity. Now if we assume that $D_o(r_1)$ is smaller than $D_o(r_2)$ - for example, if $D_o(r_1) = 1.1$ mm and $D_o(r_2) = 1.3$ mm, and hence $\delta D_o = D_o(r_2) - D_o(r_1) = 0.2$ mm, this yields $I_{b_1}(D_o(r_1))/I_{b_2}(D_o(r_1))$ and $I_{b_1}(D_o(r_2))/I_{b_2}(D_o(r_2)) = 1.141$ and 0.887 , respectively. Thus, the value of M is 1.0936. Conversely, if $D_o(r_1) = 1.3$ mm and $D_o(r_2) = 1.1$ mm, resulting in $M = -1.039$. The effect of the deviation of the M value from 0 dB on the rainfall rate estimate in this method will be discussed in more detail in a later section.

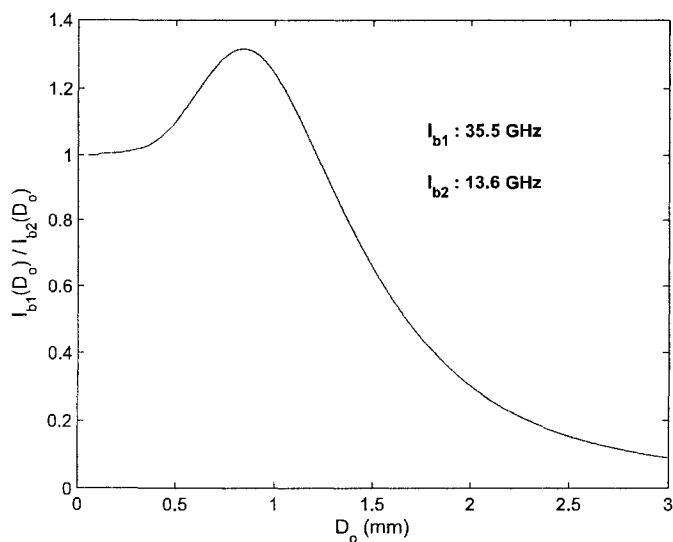


Figure 4.6: Plot of $I_{b1}(D_o)/I_{b2}(D_o)$ versus D_o . Note that subscripts 1 and 2 refer to Ka-band and Ku-band channel, respectively.

Another point worth noting is that, for the same δD_o , the deviation of M from 0 dB at larger D_o is more than that at smaller D_o . For example, if $D_o(r_1) = 2$ mm and $D_o(r_2) = 2.2$ mm, $I_{b1}(D_o(r_1))/I_{b2}(D_o(r_1))$ and $I_{b1}(D_o(r_2))/I_{b2}(D_o(r_2)) = 0.3021$ and 0.2276, yielding $M = 1.2298$, which is greater than the case $D_o = 1.1$ mm and 1.3 mm, in which $M = 1.0936$.

The k - R relation

This method utilizes the k - R power law relation ($k = aR^b$) to convert differential attenuation between two range gates to the rainfall rate. Some approximations are made based on using 35.3 GHz and 13.6 GHz. The least error from such approximation is expected. To illustrate these approximations, Fig. 4.7 shows the scatter and fit lines of k - R relation with associated coefficients for both frequencies. Specific attenuation (k) and rainfall rate (R) are simulated from a wide variety of D_o and N_w for fixed $\mu = 1$.

From Fig. 4.7, coefficients a and b of $k = aR^b$ for μ fixed at 1 are:

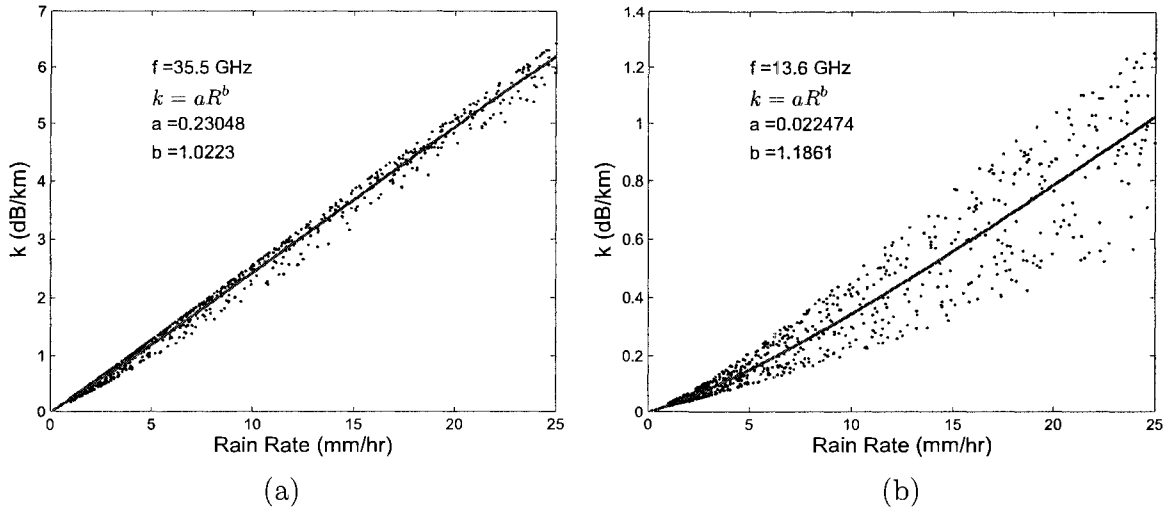


Figure 4.7: Scattering plot and power law fit (red) of k - R relation: (a) 35.5 GHz, (b) 13.6 GHz. The associated coefficients for each frequency are also shown.

For 35.5 GHz

$$a_1 = 0.2305 \quad b_1 = 1.0223$$

For 13.6 GHz

$$a_2 = 0.0225 \quad b_2 = 1.1861$$

Subscript 1 and 2 refer to the 35.5 and 13.6 GHz channel, respectively.

As mentioned earlier, an expression of path-averaged rainfall rate in (4.20) is obtained based on two approximations (if the two applied frequencies are sufficiently different), which are: 1) $a_2 \ll a_1$ and 2) $b_1 \approx b_2$. According to simulation results of the coefficients presented, the two approximations yield a tolerable error.

One of several advantages of using this method to estimate PAR is the insensitivity of the k - R relation to variation of drop size distribution (DSD)'s parameters, especially at the higher frequency. To demonstrate such insensitivity, another three sets of a and b coefficients—two from simulation data with μ fixed at 3 and 6 and the another from disdrometer measurement (Atlas and Ulbrich, 1977), denoted as A-U—are shown in Table 4.2 and compared with those at $\mu = 1$.

Table 4.2: Coefficients a and b of the $k = aR^b$ relation based on simulation data for three different values of μ . A-U refers to resultant coefficients based on disdrometer measurement from Atlas and Ulbrich (1977).

	35.5 GHz		13.6 GHz	
	a	b	a	b
1	0.2305	1.0223	0.0225	1.1861
3	0.2270	1.0341	0.0238	1.1395
6	0.2237	1.0391	0.0231	1.1393
A-U	0.2190	1.0400	NaN	NaN

As seen from Table 4.2, coefficients a and b of the $k = aR^b$ power law relation from simulation data for various μ values and from disdrometer measurements are very similar. Note that for 13.6 GHz, the coefficients from disdrometer measurement have not been presented in the literature and are denoted in Table 4.2 as NaNs. To further demonstrate insensitivity of the k - R relation to the DSD parameter in estimated rainfall rate, three sets of coefficient a and b corresponding to three different values of μ are used to compute path-averaged rainfall rate using (4.20). The simulated-unbiased “measured” reflectivity for both frequencies are used. The comparison of computed rainfall rate is shown in Fig. 4.8. The M value is assumed to be unity at the moment.

It is rather evident from Fig. 4.8 that path-averaged rainfall rate estimated by the method of difference attenuation difference is insensitive to change of drop size distribution (DSD) parameters because at each data number on the x-axis the rainfall rate on the y-axis is barely different.

In preceding discussion, the M value in (4.18) is assumed to be 1, reflecting the existence of Rayleigh scattering in both frequencies and/or $D_o(r_1) = D_o(r_2)$ conditions. As shown in Fig. 4.6, however, Rayleigh scattering occurs only when the size of D_o approximately ≤ 0.3 mm. Because the typical range of D_o of raindrops is 0.5 - 2.5 mm, $D_o \leq 0.3$ mm seem unlikely or to occur very rarely. For that reason, the $D_o(r_1) = D_o(r_2)$ scenario will be focused on here.

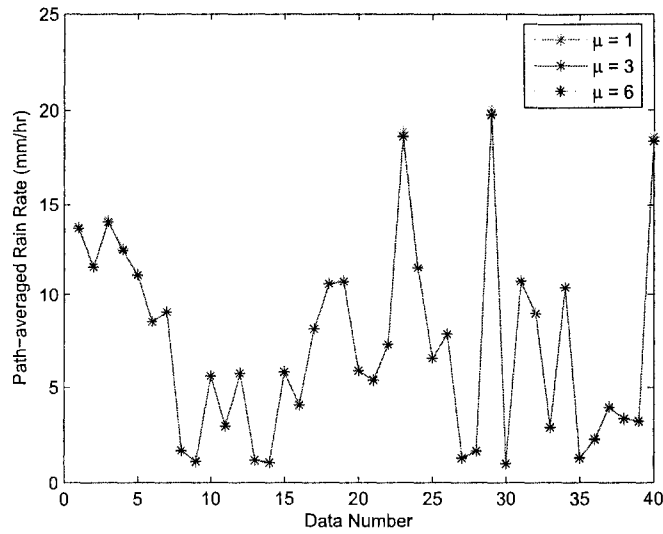


Figure 4.8: Comparison of path-averaged rainfall rate over range r_1 and r_2 computed using (4.20) for different values of μ .

It is expected that for a usual rainfall rate where rainfall rate does not significantly change between range r_1 and r_2 , $D_o(r_2)$ is unlikely to change much compared to $D_o(r_1)$. A study of estimating D_o profiles in the rain region (ranging within altitude 0.5 - 4.00 km above ground) using ground-based, airborne, and spaceborne radar has been presented in the literature. Chandrasekar et al. (2003a) presented a comparison of D_o profile within 0.5 to 4.0 km. in the rain region between data from a ground base radar and from spaceborne radar. D_o profiling in their study is rather uniform.

The estimated rainfall rate by the DAD method is based on the assumption that $M = 1$. The “true” rainfall rate is estimated using the actual value of M . In practice, in the DAD method, $D_o(r_1)$ and $D_o(r_2)$ are not known. Thus, the value of M deviating from unity is not known either. Base on the simulation, the “measured” reflectivity from both frequencies at r_1 and r_2 are generated from known D_o and N_w . Rainfall rate based on the $M = 1$ assumption and the actual value of M are calculated. The difference between the two rainfall rates is considered as an error of the DAD method. The error could be expected to be dependent on the difference of $D_o(r_1)$ and $D_o(r_2)$ denoted as δD_o . What needs to be investigated is how much the estimated rainfall

rate deviates from “true” rainfall rate as function of δD_o . Moreover, for the same δD_o , the error could be a function of the $D_o(r_1)$ value itself. The purpose of the following section is to investigate inherent errors in rainfall rate estimation the using DAD method because of the difference between $D_o(r_1)$ and $D_o(r_2)$.

Path-averaged rainfall rate (PAR) calculation

As previously mentioned, if Rayleigh scattering and/or uniform D_o is not valid, PAR calculated using the DAD method is in error. To investigate the impact of the non-Rayleigh effect and/or non-uniform rain on estimated PAR, two PAR calculations are performed based on simulation data. Known D_o and N_w combination sets and fixed $\mu = 1$ are used to generate the “measured” reflectivity profile of rain region within 3 km interval starting at 0.5 above ground with 0.25 km resolution for both frequencies. An example of “measured” reflectivity is shown in Fig. 4.9.

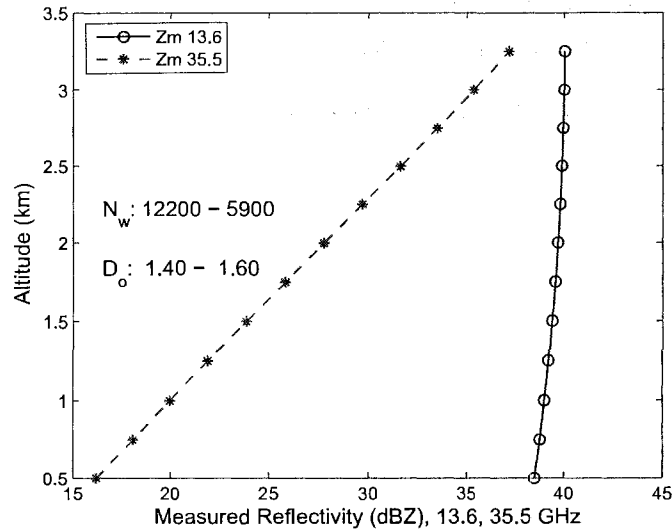


Figure 4.9: “Measured” reflectivity of 35.5 and 13.6 GHz as a function of altitude. D_o at 3.25 km. is 1.4 and 0.5 km. is 1.6 and N_w at 3.25 km. and 0.5 km. are 8000 and 4400, respectively.

Figure 4.9 shows “measured” reflectivity for 35.5 and 13.6 GHz. The reflectivity profiles are simulated based on specified D_o and N_w at the bottom (r_2) and top (r_1)

of the rain region. It is assumed that D_o increases linearly from the top bin downward to the bottom bin while N_w decreases linearly in the same manner to maintain nearly uniform rainfall rate within the interval r_1 and r_2 . In this figure, $D_o(r_1)$ and $D_o(r_2)$ are set to 1.4 mm and 1.6 mm ($\delta D_o = 0.2$) and $N_w(r_1)$ and $N_w(r_2)$ are set to 8000 and 4400, respectively. Each set of D_o and N_w is specified to produce approximately uniform rainfall rate throughout the profile.

Once the measured reflectivity profiles are generated, rainfall rate can be calculated. Two rainfall rate calculations are performed using (4.20). The first one is calculated using the actual value of M which produces “true” rainfall rate. The second one is calculated under the assumption that $M = 1$. The latter one yields a different rain rate from the former one if the actual value of M deviates from unity. The discrepancy between the two calculated PARs is the error on PAR by the DAD method. The main purpose of the simulation is to determine the error of the PAR estimate using the DAD method. For the purpose of comparison, PAR calculated from DSD parameters by (4.21) is used.

Rainfall rate for given D_o , N_w and μ can be expressed (Bringi and Chandrasekar, 2001) as

$$R = 0.6 \times 10^{-3} \pi N_w f(\mu) D_o^{-\mu} \int_D v(D) D^{\mu+3} e^{\Lambda D} dD \quad (4.21)$$

where

$$\begin{aligned} f(\mu) &= \frac{6}{3.67^4} \frac{(3.67 + \mu)^{\mu+4}}{\Gamma(\mu + 4)} \\ v(D) &= 4.854 D e^{-0.195 D} \end{aligned} \quad (4.22)$$

$v(D)$ is the Gunn-kinzer terminal velocity. μ in this case is 1.

The same set of D_o and N_w profiles used to generate measured reflectivity profiles are used to compute rainfall rate profiles using the DSD method. The PAR estimate using the DSD method is made by averaging over specified r_1 and r_2 . Four PAR values that cover the large contribution of rain rate, namely, 5, 10, 15, and 20 mm

hr^{-1} (Iguchi et al., 2001; Rose and Chandrasekar, 2004) are studied. For each PAR value, three values of $D_o(r_1)$ are studied with the same maximum $\delta D_o = 0.2$ mm. For example, for the case of 5 mm hr^{-1} , three different values of $D_o(r_1)$, 1.0, 1.2 and 1.4 mm, are used. When the maximum δD_o is set to 0.2 mm, then the corresponding maximum $D_o(r_2)$ are 1.2, 1.4 and 1.6 mm, respectively. Associated N_w sets are chosen in such a way that D_o and N_w combinations produce approximately the same rain rate profile of 5 mm hr^{-1} . Basically, this study attempts to answer two questions: 1) Does the bias of the PAR estimate depend on the $D_o(r)$?, 2) What is the relation between the δD_o and the bias in PAR estimated by the DAD method?

The results presented in the following figures reveal answers for those questions. Figures 4.10 to 4.13 show the results for four different PARs, 5, 10, 15, and 20 mm hr^{-1} , respectively. In each figure, (a), (c), and (e) present a comparison of the three PAR estimates. Two estimates are calculated by the DAD method—one is calculated under the assumption that $M = 1$, denoted as PAR_{DAD} , and the other uses the actual M value in the calculation, denoted as PAR_{DADM} . The third estimate is calculated based on the known DSDs using (4.21) and denoted as PAR_{DSD} .

In Fig. 4.10 (a) and (b), the $D_o(r_1)$ is 1.00 mm and the maximum $D_o(r_2)$ is 1.2 mm. PAR_{DADM} and PAR_{DSD} track each other very well. The largest difference between the two is only 0.4 mm hr^{-1} at $D_o = 1.0$ mm, and the smallest difference is about 0.2 mm hr^{-1} at $D_o = 1.2$ mm. PAR_{DAD} is equal to PAR_{DADM} at 1.0 mm because $D_o(r_1) = D_o(r_2)$. PAR_{DAD} becomes more different from PAR_{DADM} when $D_o(r_2)$ gets larger, and the largest difference of 0.71 mm hr^{-1} occurs at $D_o(r_2) = 1.2$ mm, as shown in (b). The difference between PAR_{DAD} and PAR_{DADM} (ΔPAR) is plotted as a function of δD_o in (b) along with a linear fit ($y = a + bx$). The coefficients a and b of the fit are -0.0324 and 3.6494, respectively.

Figures 4.10 (c) and (d) show a similar situation for $D_o(r_1) = 1.2$ mm and the maximum $D_o(r_2) = 1.4$ mm. In (c), PAR_{DADM} and PAR_{DSD} agree very well. Similarly to the preceding case, PAR_{DAD} starts to deviate from PAR_{DADM} when $D_o(r_2)$

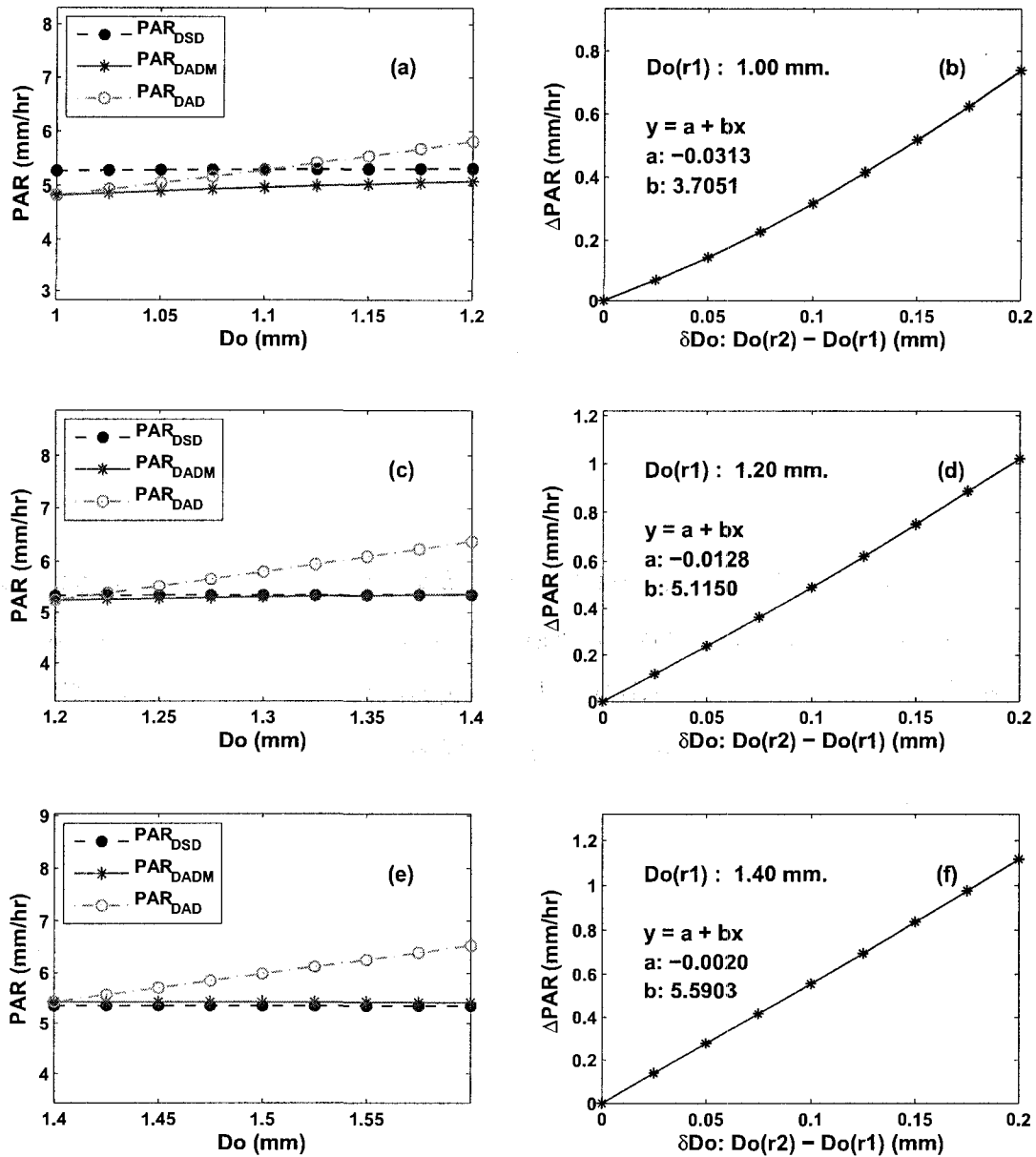


Figure 4.10: (a), (c), and (e) show the comparison of three path-averaged rainfall rate (PAR) estimates as a function of D_o . The “true” PAR is approximately 5 mm hr⁻¹. In (a), $D_o(r_1) = 1.0$ mm, and $D_o(r_2)$ varies from 1.0 to 1.2 mm, giving the maximum $\delta D_o = 0.2$ mm; (b) shows ΔPAR as a function of δD_o . (c), (d), (e), and (f) are similar to (a), (b), except $D_o(r_1) = 1.2$ mm in (c) and 1.4 mm in (e), respectively.

gets larger. The largest difference between PAR_{DAD} and PAR_{DADM} (ΔPAR) is 1 mm hr^{-1} at $D_o(r_2) = 1.4 \text{ mm hr}^{-1}$. The coefficients a and b of the linear fit between δD_o and ΔPAR are -0.0143 and 5.1092 . Figures 4.10 (e) and (f) show a similar result for $D_o(r_1) = 1.4 \text{ mm}$ and the maximum $D_o(r_2) = 1.6 \text{ mm}$. In (e), PAR_{DADM} and PAR_{DSD} are almost the same. As in the two preceding cases, ΔPAR increases as the $D_o(r_2)$ increases. The relation between δD_o and ΔPAR is still strongly linear, with coefficients $a = -0.0035$ and $b = 5.6169$. The largest value of ΔPAR at $D_o(r_2) = 1.6 \text{ mm}$ is 1.1 mm hr^{-1} , which is 0.1 mm hr^{-1} higher than that in (d).

The important observations from the results presented in Fig. 4.10 for path-averaged rainfall rate (PAR) about 5 mm hr^{-1} with maximum $\delta D_o = 0.2 \text{ mm}$ are: 1) PAR_{DADM} and PAR_{DSD} for D_o ranging from 1.0 to 1.6 mm agree well. 2) As expected, when $D_o(r_2)$ becomes more different from $D_o(r_1)$ —in all cases, it is greater than $D_o(r_1)$ — PAR_{DAD} becomes greater than PAR_{DADM} . δD_o and ΔPAR appear to be linearly related. The linear relations change for $D_o(r_1) = 1.00, 1.2, \text{ and } 1.4 \text{ mm}$. As shown in Figure 4.10 (b), (d) and (f), ΔPAR approximately is 3.7 times, 5.1 times and 5.6 times of δD_o for $D_o(r_1) = 1.00, 1.2, \text{ and } 1.4 \text{ mm}$, respectively.

Similar plots for 10 mm hr^{-1} is presented in Fig. 4.11. In Fig. 4.11, three different values of $D_o(r_1)$, 1.2 mm , 1.4 mm and 1.6 mm , are studied. PAR_{DSD} and PAR_{DADM} for all cases agree very well. ΔPAR and δD_o show a strong linear relation.

When $D_o(r_1) = 1.2 \text{ mm}$, as seen in Fig. 4.11(b), the maximum of ΔPAR at $\delta D_o = 0.2 \text{ mm}$ is 1 mm hr^{-1} . It increases to 1.1 mm hr^{-1} for cases of $D_o(r_1) = 1.4 \text{ mm}$ and 1.6 mm in (d) and (f). According to coefficient a and b in (b), (d), and (f), ΔPAR is about 5 times δD_o .

From Figs. 4.10 and 4.11, it can be seen that a few things commonly occur in both PAR values: 1) ΔPAR is a linear function of δD_o ; 2) for the maximum value of $\delta D_o = 0.2 \text{ mm}$, ΔPAR is slightly dependent on $D_o(r_1)$; and 3) since the results from the two different PAR values do not show significant differences, it may be concluded

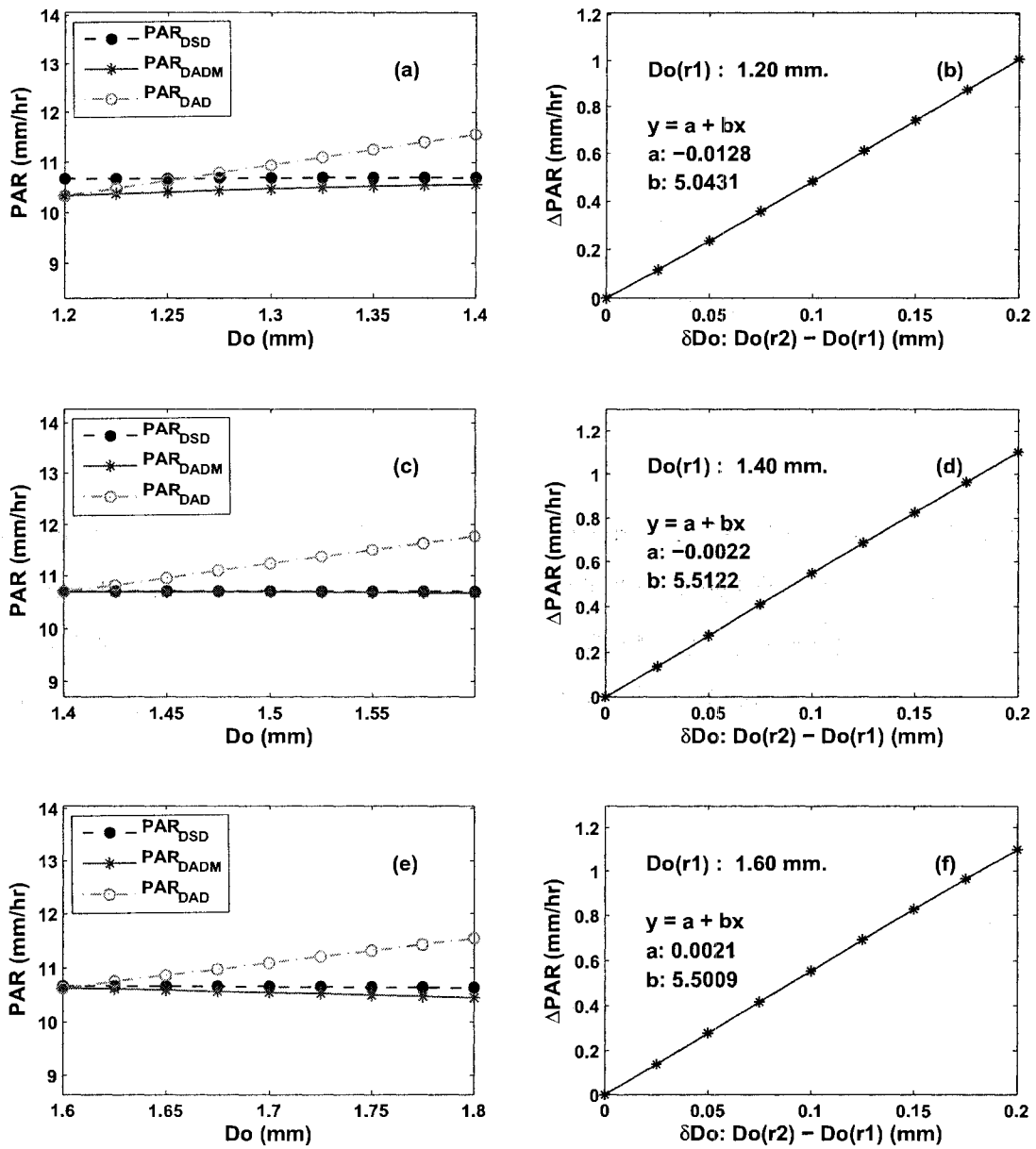


Figure 4.11: Similar to Fig. 4.10 except $D_o(r_1)$ are 1.2, 1.4 and 1.6 mm and “true” PAR is about 10 mm hr^{-1} .

that ΔPAR is independent of PAR value. To increase confidence in reaching such a conclusion, two more PAR values are discussed, as shown in Figs. 4.12 and 4.13.

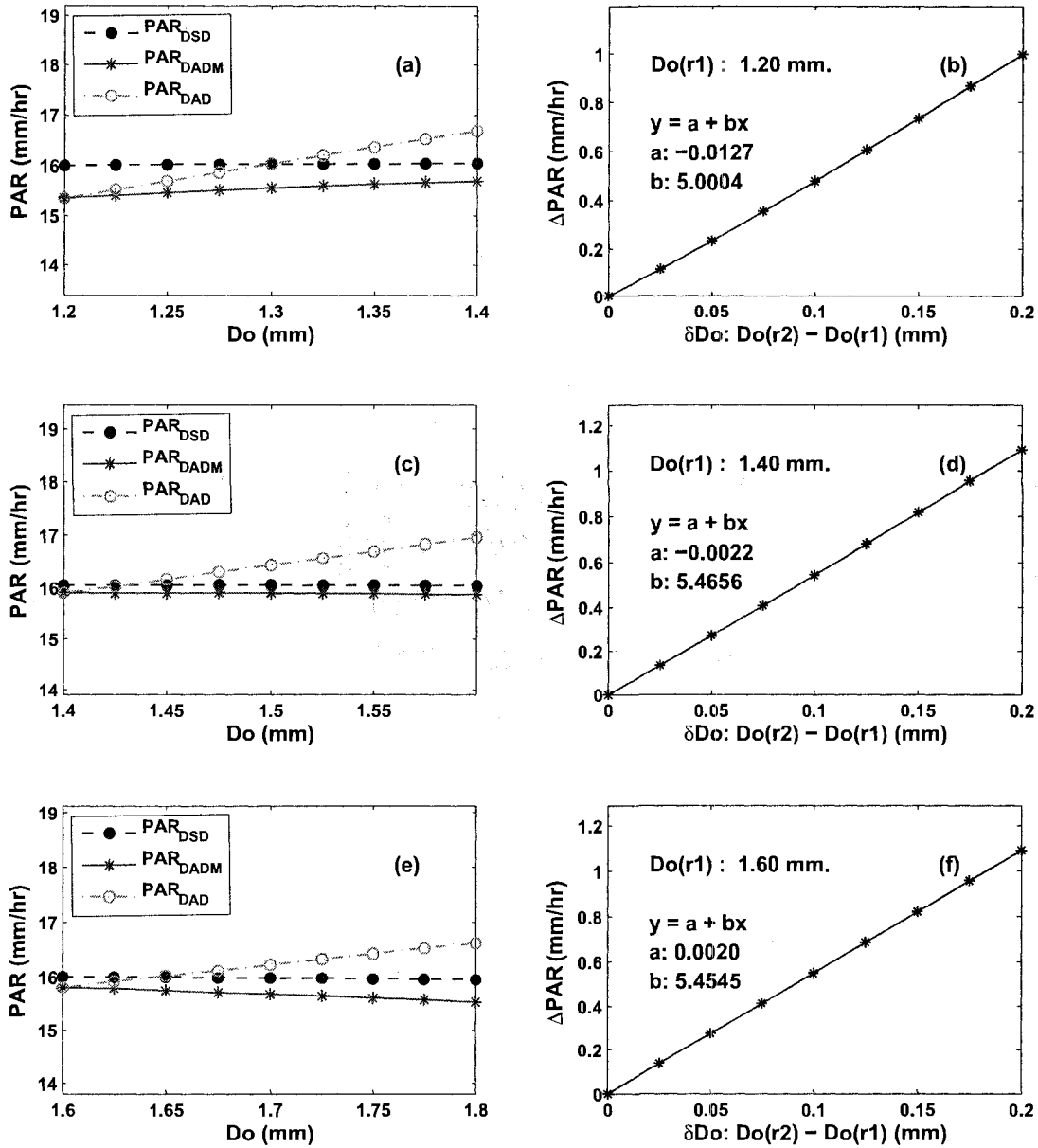


Figure 4.12: Similar to Fig. 4.10, except $D_o(r_1)$ are 1.2, 1.4, and 1.6 mm and “true” PAR is about 15 mm hr^{-1} .

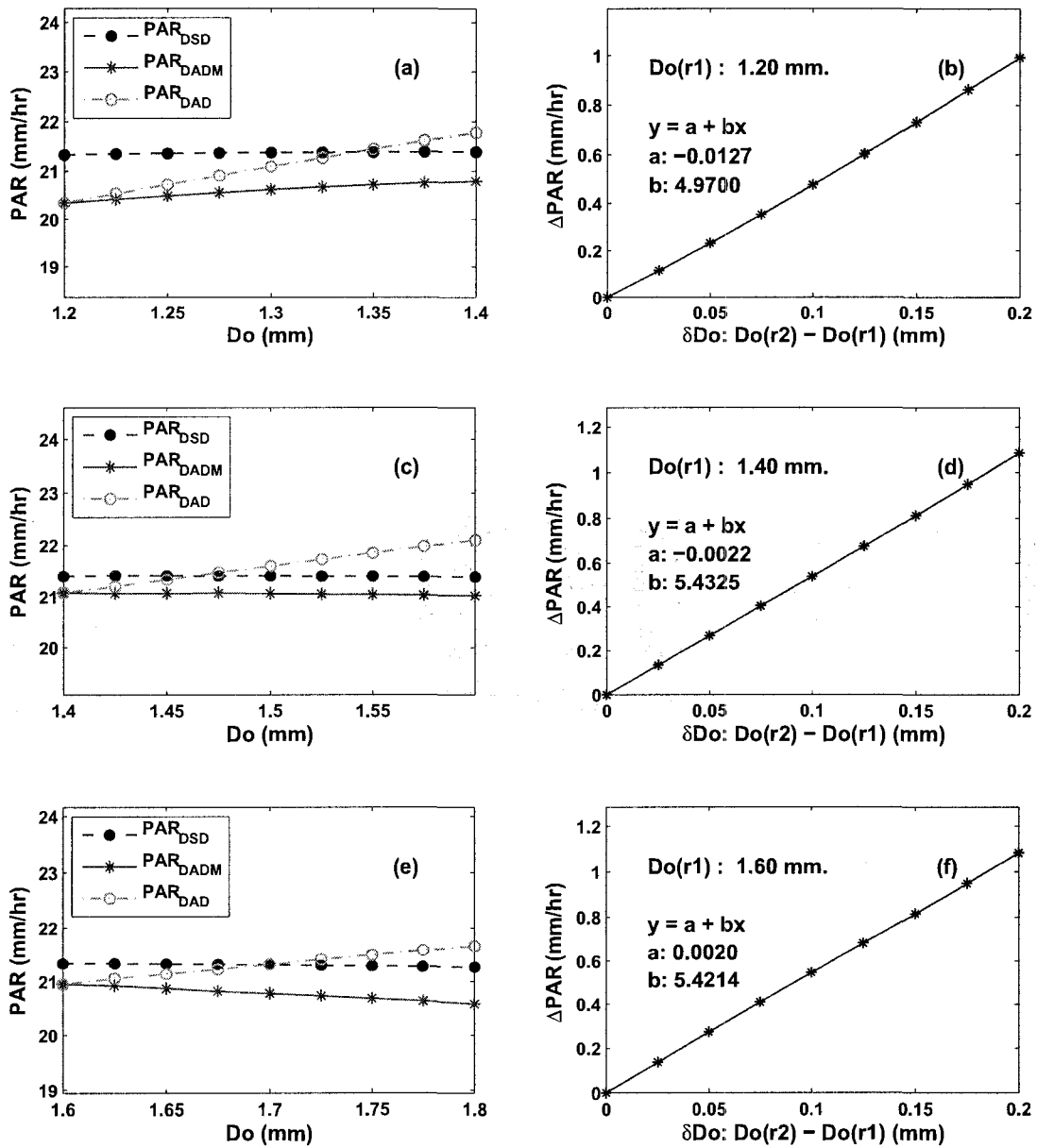


Figure 4.13: Similar to Fig. 4.10, except $D_0(r_1)$ are 1.2, 1.4, and 1.6 mm and “true” PAR is about 20 mm hr⁻¹.

Figure 4.12 shows results for 15 mm hr⁻¹ PAR. Three $D_o(r_1)$ values are used: 1.2 mm, 1.4 mm, and 1.6 mm. PAR_{DADM} and PAR_{DSD} still agree very well. Strongly linear relations between δD_o and ΔPAR are evident. On average, ΔPAR is about 5.25 times δD_o , giving the ΔPAR less than 1.1 mm hr⁻¹ at the $\delta D_o = 0.2$ mm. Figure 4.13 shows results for 20 mm hr⁻¹ PAR. Three $D_o(r_1)$ values are used: 1.4 mm, 1.6 mm, and 1.8 mm. PAR_{DADM} and PAR_{DSD} agree well. Strongly linear relations between δD_o and ΔPAR are evident. On average, ΔPAR is about 5.20 times δD_o , giving ΔPAR less than 1.1 mm hr⁻¹ at $\delta D_o = 0.2$ mm.

From the results shown in Figs. 4.10, 4.11, 4.12, and 4.13, the following conclusions are made:

- 1) ΔPAR , which can be expressed as a linear function of δD_o , is very slightly dependent on the value of PAR.
- 2) A positive ΔPAR ($PAR_{DAD} - PAR_{DADM}$) is a linear function ($y = a + bx$) of a positive δD_o ($D_o(r_2) - D_o(r_1)$).
- 3) Because the different $D_o(r_1)$ values produce almost the same linear coefficients a and b , ΔPAR is independent of $D_o(r_1)$.
- 4) ΔPAR is approximately 5.25 times δD_o .

From the findings above, the path average rain rate estimated from the DAD method is nearly insensitive to the value of D_o and the value of PAR. It is primarily a function of δD_o .

Estimation of path attenuation in rain region using DAD

The path attenuation in rain region for Ku and Ka-band can be estimated via the constructed relations between DAD and PIA(Ku) and PIA(Ka) in the rain region. About 1000 Z_m (Ku) and Z_m (Ka) rain profiles are simulated based on a wide variation of DSD parameters. Then DAD are calculated, and the scatter plot between PIA(Ku) and DAD, and PIA(Ka) and DAD are made. The scatter plots appear to be best fitted by the power law relations, as shown in Figs. 4.14 and 4.15. If the path

attenuation above the rain region is given, combining with the path attenuation estimated in the rain region by this technique provides us with the two-way path-integrated attenuation for the whole vertical profiles. This technique can be used an alternative to estimate PIA when PIA from the SRT technique, which is important for retrieval algorithm, is not available or not reliable.

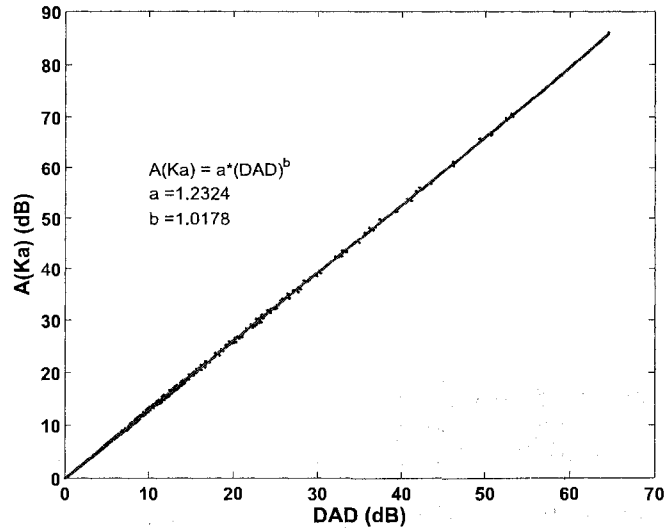


Figure 4.14: Scatter plot between PIA(Ku) and DAD, along with the best fit in the power law form.

4.4 Summary and Conclusions

The dual-wavelength retrieval methods are presented. The governing equations in the integral form, which is formulated to solve DSD parameters D_o and N_w in the normalized gamma model are discussed. The integral equations can be solved by forward and backward as well as iterative methods. The forward method assumes that there is no attenuation at storm top, and the DSD retrieval begins at the top and move the surface. The backward method, on the other hand, starts at the surface range bin and move to the storm top and requires a prior knowledge of path-integrated attenuation from the storm top to the surface. The iterative method is a

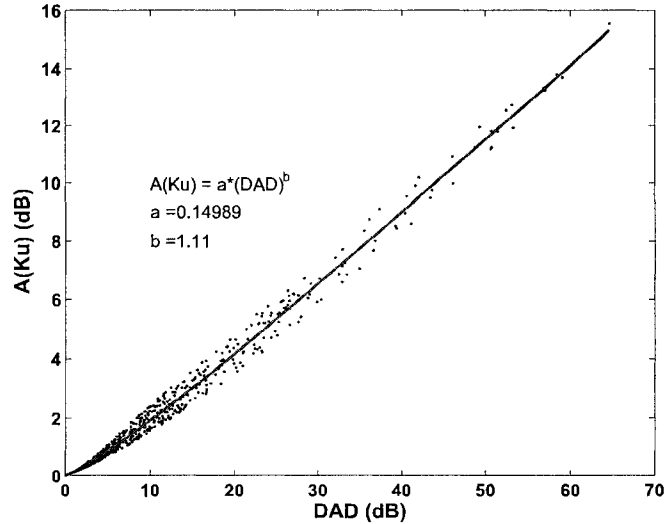


Figure 4.15: Scatter plot between PIA(Ka) and DAD, along with the best fit in the power law form.

self-consistent non-SRT. The standard dual-wavelength or difference of attenuation difference (DAD) is discussed in detail.

The DAD method provides a promising path-averaged rain rate (PAR) estimation under two assumptions, Rayleigh scattering and the constant D_o s between the two specified range gates. An extensive study of the bias of PAR estimation, which is deduced when the two assumptions are not valid, are discussed. The simulation results show that the DAD method maintains a high degree of accuracy of PAR estimate for dual-frequencies of 13.6 and 35.6 GHz despite non-Rayleigh scattering. The key factor that dictates the accuracy of the estimated PAR is the difference between D_o at r_1 and r_2 defined as $D_o(r_2) - D_o(r_1)$ (δD_o). Studying four different PAR values (ΔPAR), it was found that the largest difference between the estimated PAR under the assumptions PAR_{DAD} and the “actual” PAR (PAR_{DADM}) is less than 1 mm hr^{-1} when the maximum of δD_o is 0.2 mm, and it is slightly dependent on the PAR values. ΔPAR is approximately 5.2 times δD_o . This finding suggests that the DAD method can provide a robust estimation of path-averaged rain rate for the dual-frequency precipitation radar (DPR) for the GPM mission. In addition, path attenuation in the

rain region can be estimated via the estimation of DAD and the constructed relations between DAD and path attenuation in each channel. If the path attenuation above melting layer in both each channels are given, the PIA in both channels of the whole profile can be obtained. This technique can be used as an alternative to estimate PIA, when PIA from SRT technique is not available or not reliable.

Retrieval algorithms described in this chapter will be applied to dual-frequency radar measurements from an airborne experiment to develop a microphysical model for the simulation in the next chapter.

CHAPTER 5

DEVELOPMENT OF A MICROPHYSICAL MODEL FOR SIMULATION OF PRECIPITATION OBSERVATIONS

5.1 Introduction

In Chapter 2, we discussed the scattering characteristics of electromagnetic waves on precipitation particles. The theoretical computation of radar reflectivity factor (Z_e) and specific attenuation (k) for the volume target were described based on the scattering model and the microphysical model of precipitation (particle size distribution of precipitation). The concept of the simulation of the vertical profile of reflectivity, based on parameterization between Z_e and k , and variability of Z_e with frequency for various types of precipitation particles and a wide variety of particle size distribution parameters, was also discussed. In Chapter 3, the vertical profile of reflectivity measured by a single-frequency spaceborne precipitation radar (PR) on board the tropical rainfall measurement mission (TRMM) satellite was extensively analyzed. The drop size distribution parameters estimation of precipitation associated with vertical profiles was described and compared with that estimated from dual-polarization ground-based radar. In Chapter 4, the concept of precipitation measurement by the dual-frequency precipitation radar (DPR), which is being planned to be placed on board the global precipitation measurement (GPM) satellite, and an overview of the DPR were described. The fundamental concepts of different dual-frequency retrieval techniques were described; the difference of attenuation difference (DAD) method was intensively analyzed in terms of its robustness and uncertainty.

The DPR on the GPM will be the first dual-frequency space-based precipitation radar operating at high frequencies. Since it is the first of its kind, a simulation-based study is essential for evaluating GPM system designs, algorithm developments, and system evaluation. The underlying microphysics of precipitation structures are important in developing a simulation model. This chapter focuses on the development of a microphysical model along vertical structure of precipitation based on dual-frequency airborne radar observations. The microphysical model developed here is then used as a basis for generation of the Z_e and k relation, as well as variability of Z_e with frequency along the vertical profiles.

5.2 Development of a Microphysical Model for Simulation Based on Airborne Radar Observations

5.2.1 Airborne radar observations

A series of airborne experiments were conducted with the objective of supporting the study of the space-based dual-frequency precipitation radar (DPR) that is planned for installation on the “core” satellite of the Global Precipitation Measurement (GPM) mission. The second-generation airborne precipitation radar (APR-2) developed at the Jet Propulsion Laboratory (JPL) was deployed in several experiments, such as the Fourth Convection and Moisture Experiment (CAMEX-4) in 2001, the Wakasa Bay Experiment in 2003, and the NASA African Monsoon Multi-disciplinary Analyses (NAMMA) in 2006. APR-2 was primarily designed to emulate the DPR. The scanning geometry of APR-2 is shown in Fig. 5.1; it looks downward and scans its beams across-track, with each scan beginning at 25 degrees to the left of nadir and ending at 25 degrees to the right. Characteristics of APR-2 are shown in Table 5.1.

The NAMMA experiment focused on examining the evolution and structure of african easterly waves (AEWs) and mesoscale convective systems over continental western Africa, with their associated impacts on regional water and energy budgets.

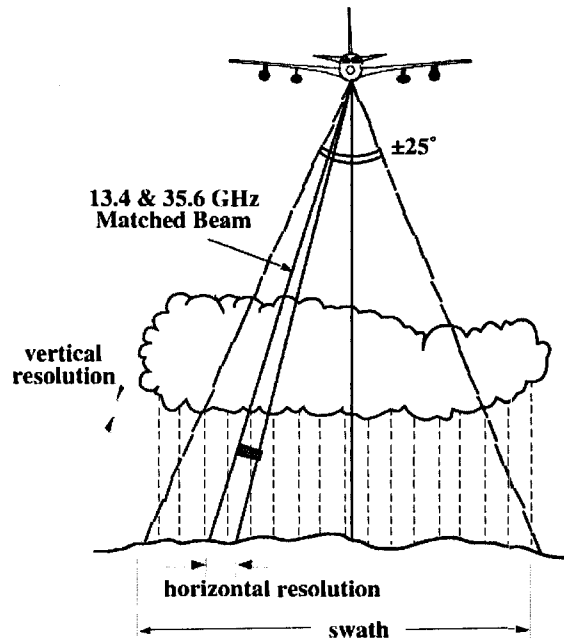


Figure 5.1: APR-2 scanning geometry on the NASA DC-8 aircraft. Antenna is scanned in cross-track plane (adopted from Im et al. (2002)).

Table 5.1: APR-2 characteristics (Tanelli et al. (2004)).

Airborne PR-2 Characteristics		
Frequency	13.4 GHz	35.6 GHz
Polarization	HH, HV	HH, HV
Antenna diameter (effective)	0.4 m	0.14 m
Antenna gain	34 dBi	33 dBi
Antenna sidelobe level	-30 dB	-30 dB
Peak power	200 W	100 W
Pulse width	10 - 40 μ s	10 - 40 μ s
PRF	5 kHz	5 kHz
Range bin spacing	30 m	30 m
Horizontal res (a/c at 6 km alt)	400 km	500 m
Ground swath (a/c at 6 km alt)	4.5 km	4.5 km
Noise equivalent Z_e (at 10 km range)	5 dB	5 dB
Doppler precision	0.4 m/s	1 m/s

NAMMA was conducted in August 2006. The NAMMA experiment area is shown in Fig. 5.2. Figure 5.3 shows a vertical cross-section of the along-track data at nadir.

Figure 5.3 (a) shows reflectivity at Ku-band, (b) reflectivity at Ka-band, (c) LDR at Ku-band, and (d) Doppler velocity.

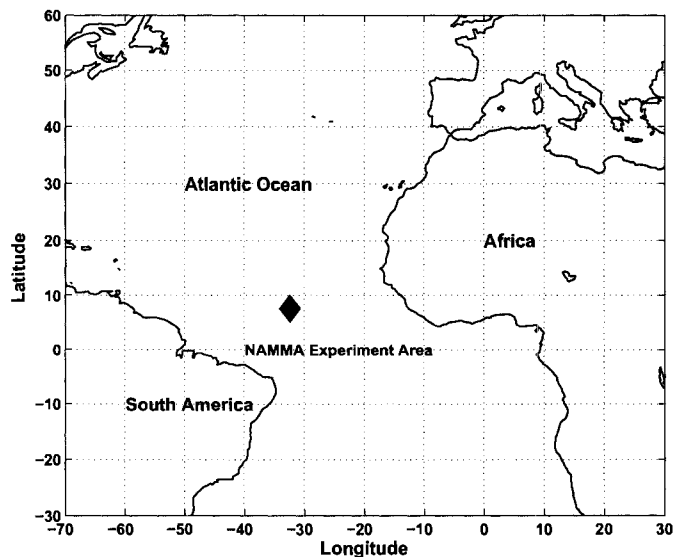


Figure 5.2: NAMMA experiment area.

Two examples of convective reflectivity profiles are shown in Figs. 5.4 and 5.5, as marked as A and B in Fig. 5.3. Two stratiform reflectivity profiles with bright band are shown in Figs. 5.6 and 5.7, as marked as C and D in Fig. 5.3. In each figure, the (a) panel shows the two channels of reflectivity profiles, the (b) panel shows the reflectivity difference profile between the two channels, the (c) panel shows the linear depolarization ratio (LDR) profile at Ku-band, and the (d) panel shows the Doppler velocity at Ku-band. The dashed lines indicate the boundary of the melting layer, which was determined by reflectivity, LDR, and fall velocity (Straka et al., 2000; Fabry and Zawadzki, 1995; Zawadzki et al., 2005). It can be seen that in convective rain at Ka-band, the radar signal went below the minimum detectable reflectivity of Ka-band radar (5 dBZ) at about 1 km in Fig. 5.4 and 5.5 because of strong attenuation.

Examining fall velocity and reflectivity profiles helps determine the hydrometeor type above the melting layer. Considering Figs. 5.4 and 5.5, showing convective rain

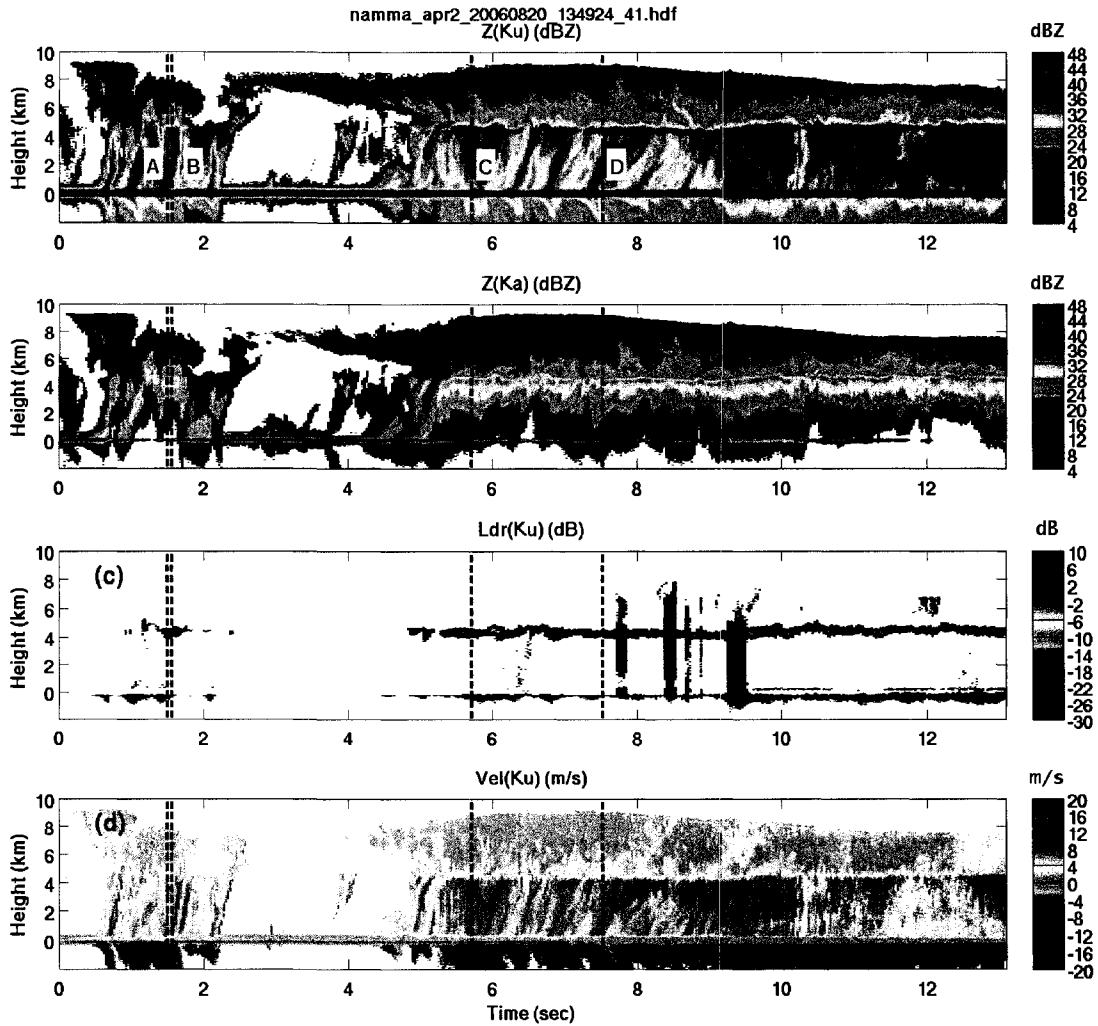


Figure 5.3: Along-track observations at nadir of the APR-2 radar in the NAMMA experiment. The (a) panel is reflectivity at Ku-band, the (b) panel is reflectivity in Ka-band, the (c) panel is LDR at Ku-band, and the (d) panel is velocity at Ku-band.

profiles, the particles above the melting layer fall at a speed between 3 to 6 ms^{-1} at 0.5 to 2 km. There is no clear sharp increase of reflectivity in the melting layer. All these conditions indicate the presence of denser rimed-snow (graupel) particles. When high-density particles begin to melt, the shape and density do not change significantly. As a result, there is no large increase of reflectivity, and the reflectivity remains at close to peak value below the melting layer (Zawadzki et al., 2005). In

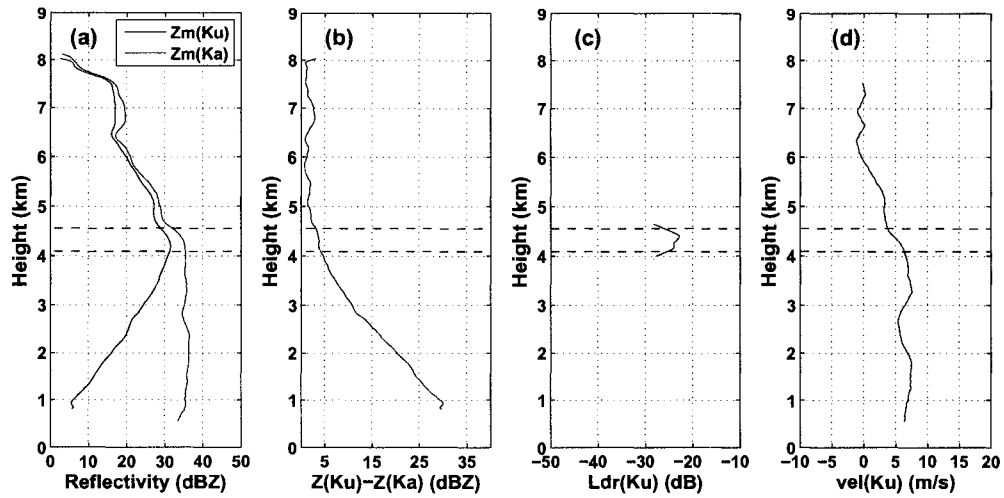


Figure 5.4: Convective rain profiles at location A in Fig. 5.3. (a) Reflectivity profile of the two channels, (b) the difference of reflectivity between the two channels, (c) linear depolarized ratio (LDR) in Ku-band, and (d) fall velocity in Ku-band. The dashed lines indicate the melting layer boundary.

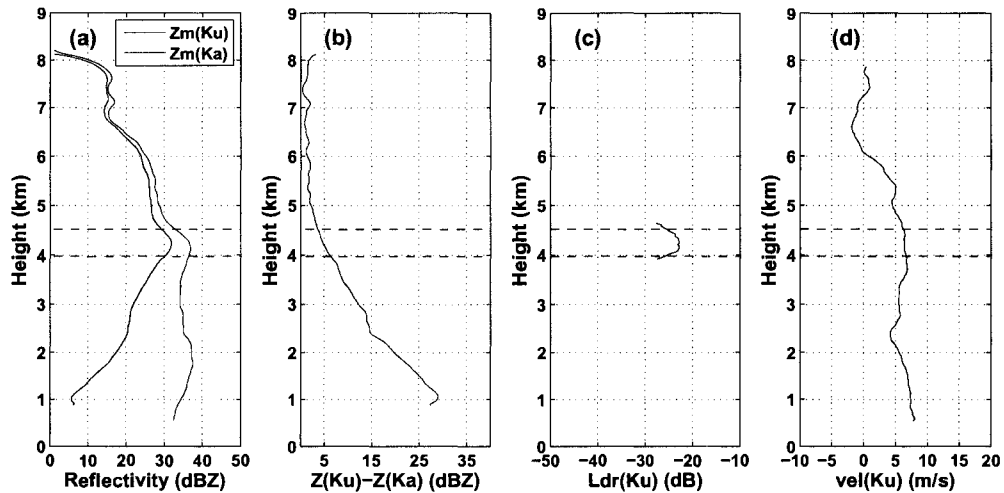


Figure 5.5: Same as in Fig. 5.4 for location B.

Figs. 5.4 and 5.5, the increase of reflectivity is about 5 dBZ. Because graupel falls at higher speed, their fall speed does not increase dramatically. In these cases, the fall speed increases only by about 3 ms^{-1} .

The same convention is used to examine the stratiform rain profiles in Figs. 5.6 and 5.7, showing stratiform rain profiles with bright band. The fall speed of the

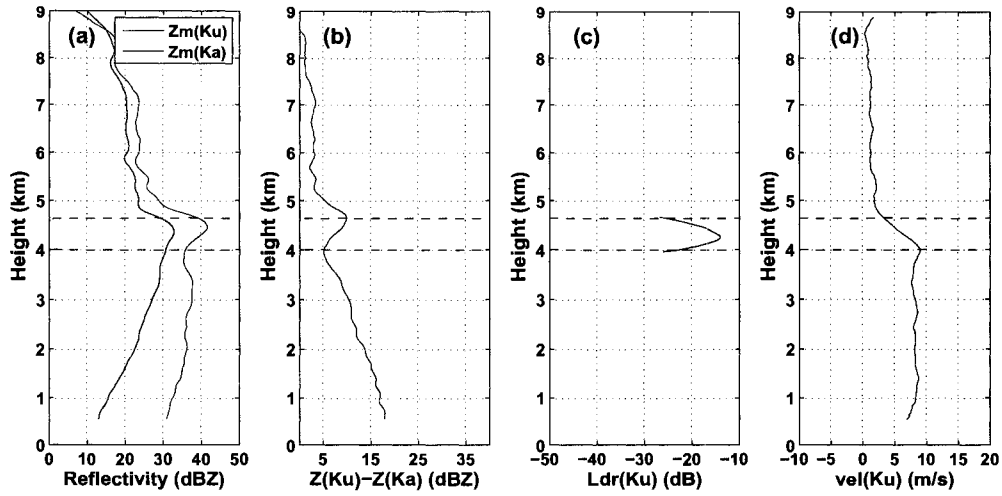


Figure 5.6: Stratiform rain profile with bright band at location C in Fig. 5.3. (a) Reflectivity profile of the two channels, (b) the difference of reflectivity between the two channels, (c) linear depolarized ratio (LDR) in Ku-band, and (d) fall velocity in Ku-band. The dashed lines indicate the melting layer boundary.

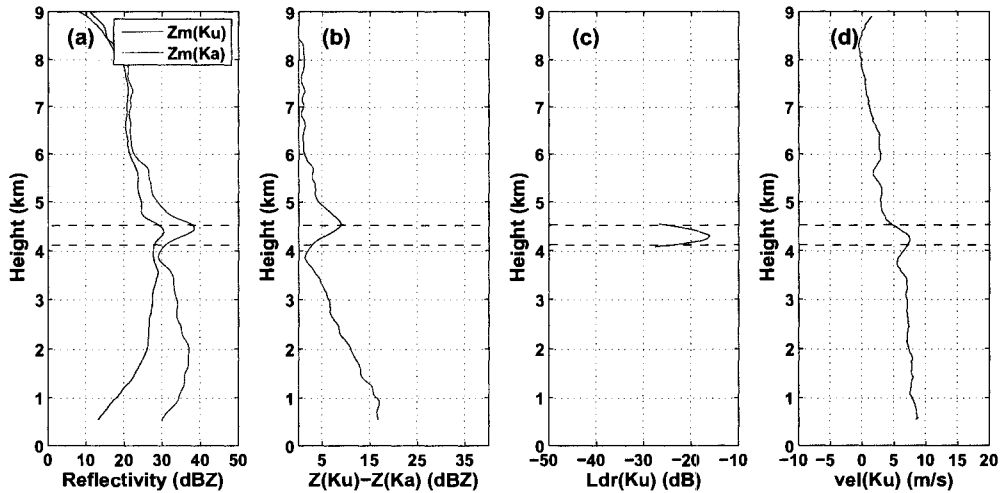


Figure 5.7: Same as in Fig. 5.6 for location D.

hydrometeor above melting layer (above 5 km) is about 1 to 4 ms^{-1} , and there is a sharp increase of reflectivity in the melting layer. This indicates the presence of dry snowflakes above melting layer, which could be rimed or non-rimed snow. The low-density, non-rimed snowflake causes a strong increase in reflectivity, which can be as high as 15 dBZ in the melting layer (bright band), and falls at a speed of about 1

to 2 ms^{-1} . On the other hand, the heavily-rimed snowflake has a fall speed more than twice (2 to 4 ms^{-1}) that of non-rimed snow, but causes less peak-to-rain reflectivity, typically less than 7 dBZ (Fabry and Zawadzki, 1995; Zawadzki et al., 2005).

5.2.2 Generation of particle size distribution parameters along the vertical profile

In chapter 2, parameterization between Z_e and k , and variability of Z_e with frequency for various types of precipitation particles, namely, snow, graupel and rain, based on a wide variety of particle size distribution parameters was described and demonstrated. However, it was shown by Passarelli (1978) that snow size distribution parameters vary with height. Therefore, to simulate realistic vertical reflectivity profiles, a knowledge of the particle size distribution along the profile is desired. The dual-frequency retrieval methods are applied to a large data set from the NAMMA experiment to obtain a variability of particle size distribution along the vertical profile.

A. Stratiform rain

The backscattering properties of dry snow at different microwave frequencies were examined by Matrosov (1992). The author concluded that dual-frequency radar measurements can be used to estimate the effective sizes of snow particles. For dual-frequency radar to yield promising results in estimating snow particle size distribution, it is essential that one or both channels operate in the non-Rayleigh region (Liao et al., 2005; Meneghini et al., 1992, 1997; Matrosov, 1992; Mardiana et al., 2004). For the APR-2 radar, the non-Rayleigh scattering typically occurs in the Ka-band channel.

Dry snow is a mixture of air and ice. The density of the snow is the primary parameter that determines the effective dielectric constant that is needed for computation of the backscattering cross-section, $\sigma_b(D, \lambda)$ and $\sigma_{ext}(D, \lambda)$ (Liao et al., 2005). Expressions of $\sigma_b(D, \lambda)$ and $\sigma_{ext}(D, \lambda)$ in Rayleigh and Mie scattering are given in

section 2.3.2. A spherical model of dry snow is used, and the dielectric constant is calculated using the Maxwell-Garnet mixing formula.

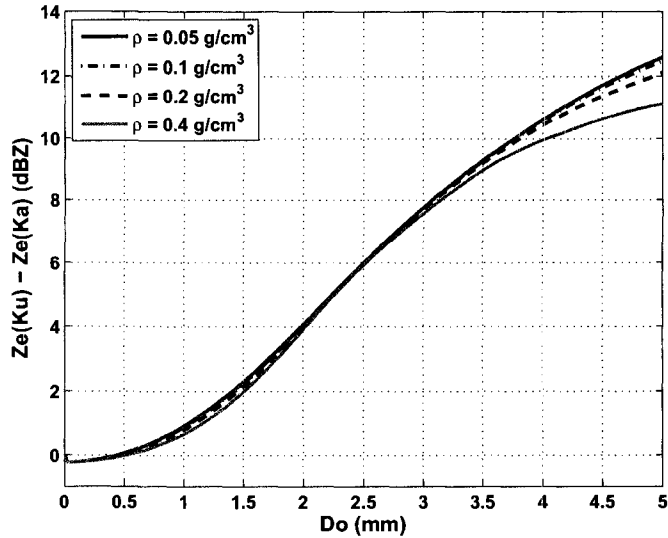


Figure 5.8: DFR vs D_o for snow densities of 0.05, 0.1, 0.2, and 0.4 g cm^{-3} when $\mu = 0$ (implying exponential size distribution).

The principle of dual-frequency methods for estimating D_o described in section 4.3 shows that the D_o parameter can be determined directly from DFR. For a constant snow density, the DFR and D_o relation is virtually independent of snow density, which was recognized by Matrosov (1992, 1998). The plot of DFR ($Z_e(\text{Ku}) - Z_e(\text{Ka})$) vs D_o for various snow densities is shown in Fig. 5.8.

The forward method of dual-frequency retrievals described in section 4.3 is used to estimate D_o along the vertical profile above the melting layer (bright band) in stratiform rain. A wide range of snow density is reported by a number of studies such as Matrosov (1992); Liao et al. (2005); Zawadzki et al. (2005). In this case, the DFR vs D_o for a fixed snow density of 0.1 g cm^{-3} is assumed. The dry snow region is determined by the LDR and fall velocity information.

Figure 5.9 (a) and (b) show the distribution of the retrieved D_o and N_w , respectively, of dry snow along the height above the bright band. As seen in Fig. 5.9 (a),

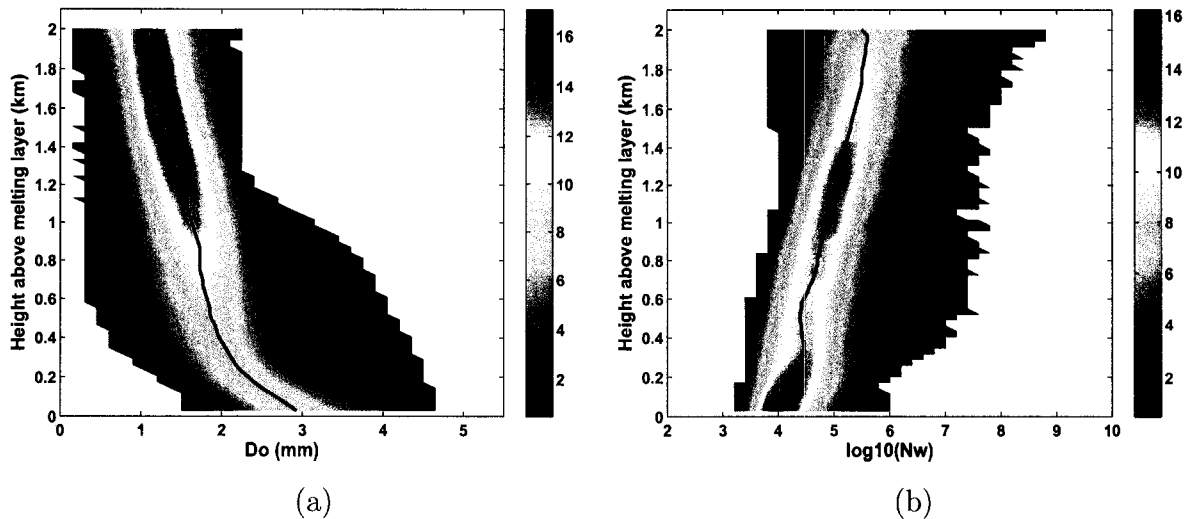


Figure 5.9: Distribution of the retrieved (a) D_o , and (b) N_w along the height of dry snow using a density of 0.1 g cm^{-3} . The solid line is the best fit. The y-axis is the height above the bright band.

the retrieved D_o increases as the height decreases, while the retrieved N_w decreases as the height decreases. Figure 5.10 (a) and (b) show distributions of the retrieved D_o and N_w , respectively, at four different height levels, namely, 0.5, 1, 1.5 and 2 km above the bright band.

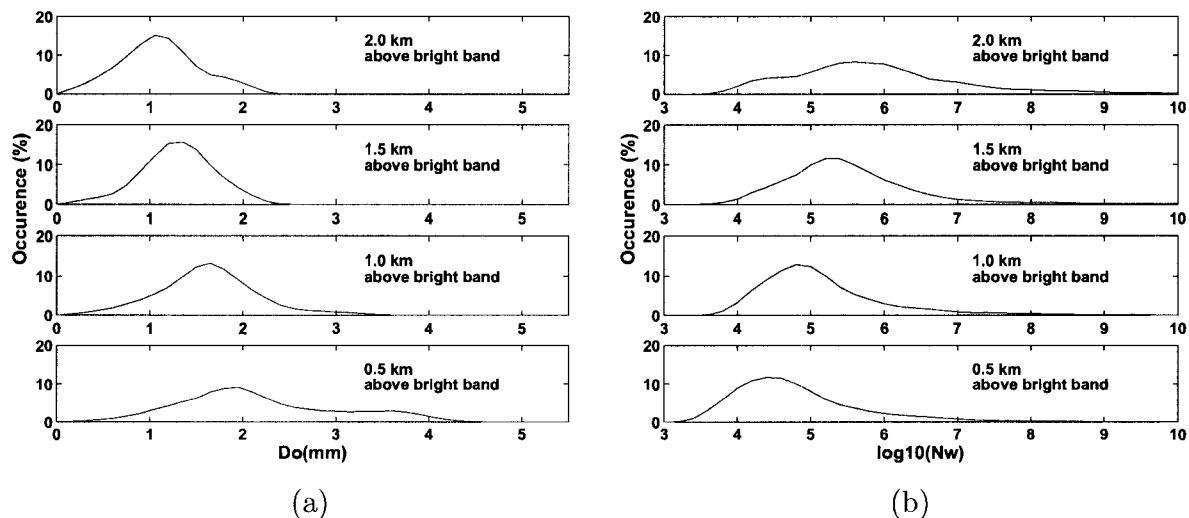


Figure 5.10: Distributions of the retrieved (a) D_o , and (b) N_w for four different height levels, namely, 0.5, 1, 1.5 and 2 km above the bright band (BB), with a snow density of 0.1 g cm^{-3} .

In the bright band, the particle is assumed to be melted snow (wet snow). The spherical model of wet snow composed of a homogeneous mixture of ice, air and water is used, and the Maxwell-Garnet mixing formula is used to calculate the dielectric constant of the wet snow model. The fractional volume content of water—water fraction (wf) for short—is assumed to change from 0.01 to 0.85. Similarly to the dry snow case, the D_o of the wet snow can be directly estimated by DFR ($Z_e(\text{Ku}) - Z_e(\text{Ka})$). The plot of DFR vs D_o of wet snow for various values of the water fraction is shown in Fig. 5.11. Wet snow size distribution parameters are estimated by the forward method using equations described in section 4.3.1.

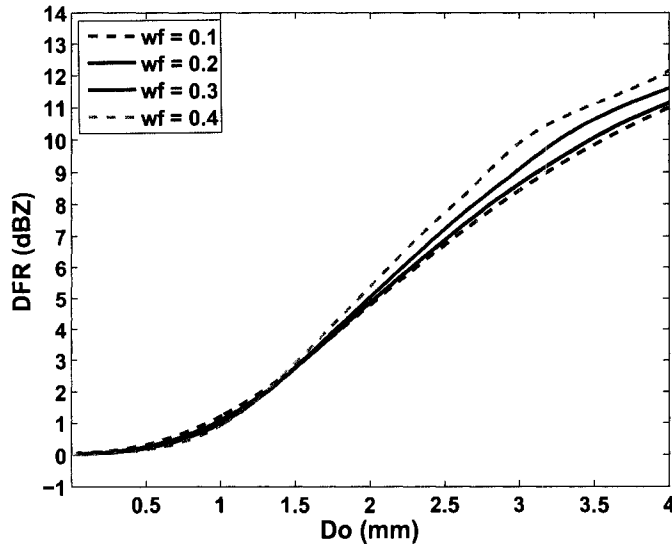


Figure 5.11: DFR vs D_o for wet snow with water fraction (wf) of 0.1, 0.2, 0.3, and 0.4.

Figure 5.12 (a) and (b) show the distribution of the retrieved D_o , and N_w of wet snow along the height, respectively. The height on the y-axis is the height above and below the bright band peak. The bright band peak is indicated by 0 km. Above and below the bright band, the height is indicated by positive and negative values, respectively. As seen in Fig. 5.12 (a), the retrieved D_o has a sharp decrease at the height just below the bright band peak, while the retrieved N_w sharply increases. Figure 5.13 (a) and (b) show distributions of the retrieved D_o , and N_w , respectively,

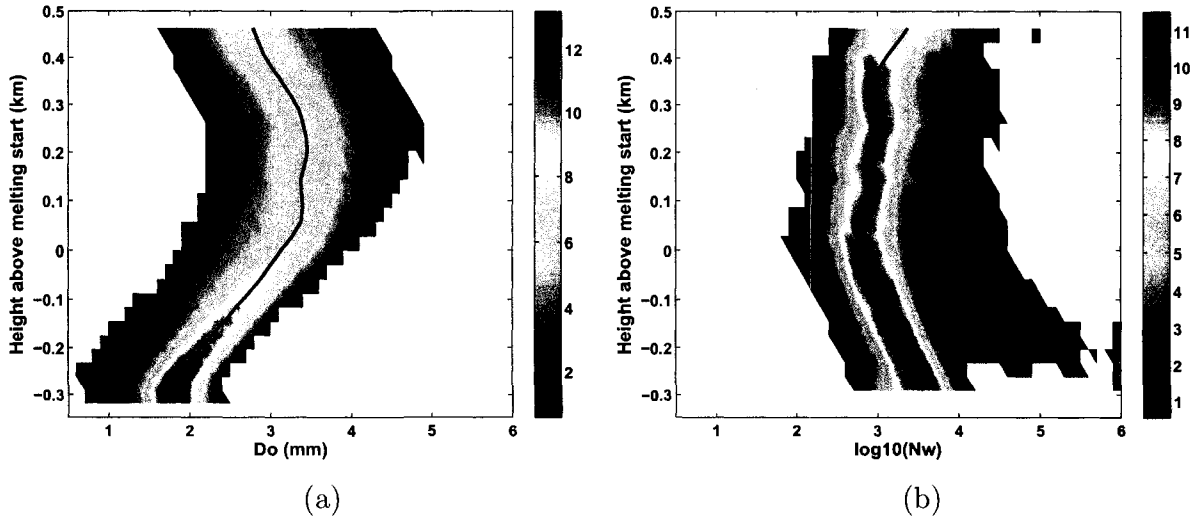


Figure 5.12: Distributions of the retrieved (a) D_o and (b) N_w of wet snow along the height. The positive and negative values represent the above and below the bright band peak, respectively. The bright band peak is indicated by 0 km. The solid line is the best fit.

at four different height levels, namely, 0.1 and 0.3 km above (+) and below (-) the BB peak.

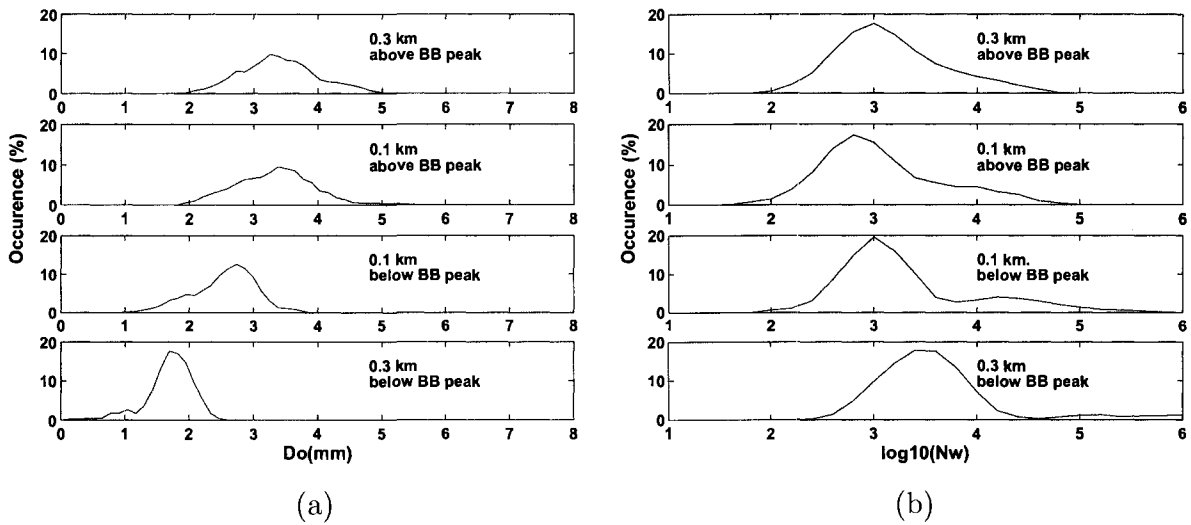


Figure 5.13: Distributions of the retrieved (a) D_o , and (b) N_w of wet snow for four different height levels, namely, 0.1 and 0.3 km above (+) and below (-) the bright band (BB) peak.

Below the bright band, raindrops are assumed. The backward method is used to estimate raindrop size distribution parameters in the rain region. The backward

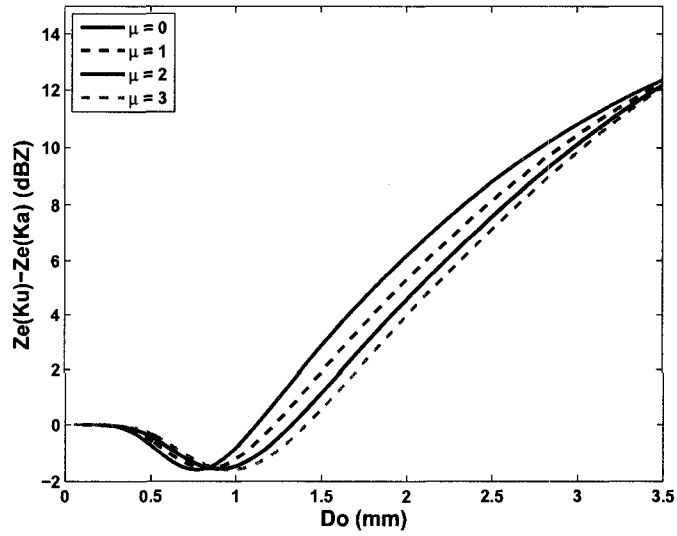


Figure 5.14: DFR vs D_o for raindrops for 4 different μ values, 0, 1, 2 and 4.

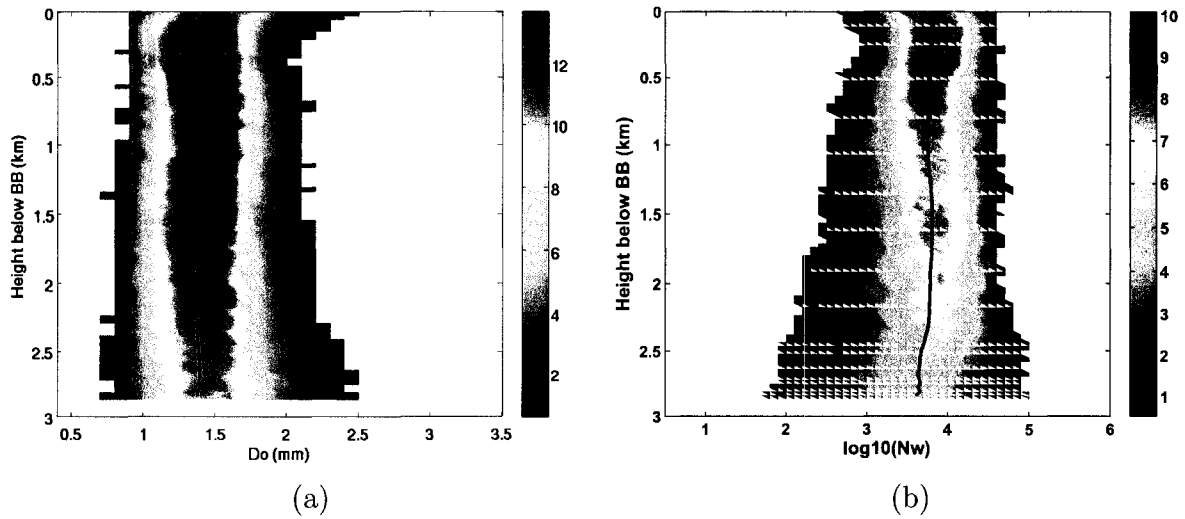


Figure 5.15: Distributions of the retrieved (a) D_o and (b) N_w of raindrops along the height. The solid line is the best fit.

method, as described in section 4.3, can be solved by either using SRT or the iterative method. Since a convergence to a wrong solution in the iterative method occurs when there is strong attenuation, as extensively analyzed by Rose and Chandrasekar (2004), the SRT method is used here. The technique for estimating the total attenuation, as described in section 4.3.2, is used to estimate the PIA. The plot of DFR vs D_o of rain

for various values of μ is shown in Fig. 5.14. In this retrieval, $\mu = 1$ is used.

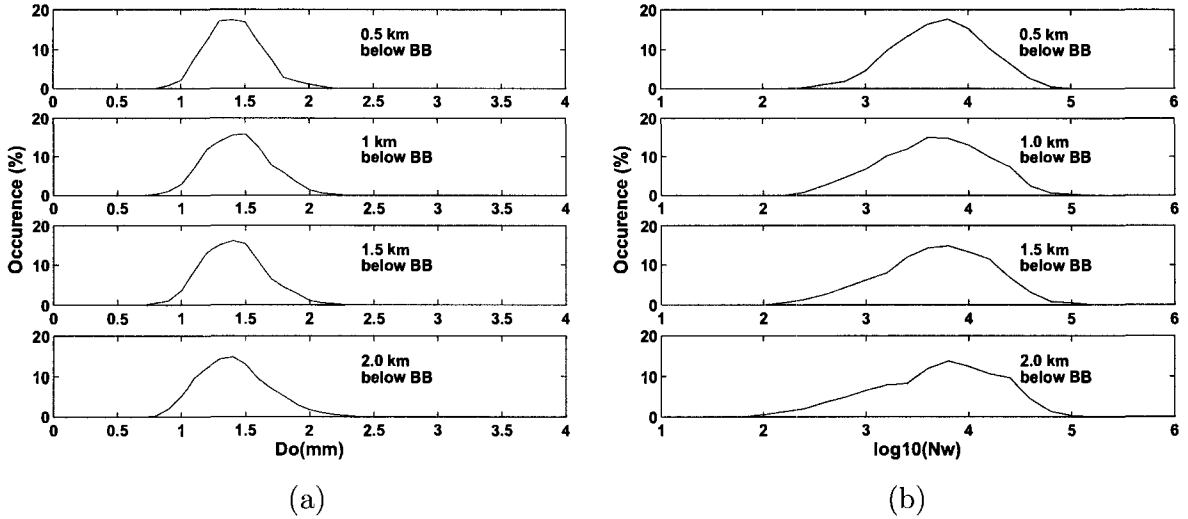


Figure 5.16: Distributions of the retrieved (a) D_o and (b) N_w of raindrops for four different height levels, namely, 0, 0.5, 1, and 2 km below the bright band.

Figure 5.15 (a) and (b) show distributions of the retrieved D_o and N_w , respectively, of raindrops along the height of stratiform rain. The height on the y-axis is the height below the bright band. As seen in Fig. 5.15 (a), the best fit of the retrieved D_o is nearly constant along the height. Similarly to the retrieved D_o , the best fit of the retrieved N_w is almost constant along the height, with a mild variation. Figure 5.16 (a) and (b) show distributions of the retrieved D_o and N_w , respectively, in the rain region at four different height levels, namely, 0, 0.5, 1, and 2 km below the bright band.

A. Convective rain case

For convective rain, the particle above melting layer is assumed to be dry graupel. A wide range of density of dry graupel is reported in the literature (Bringi and Chandrasekar, 2001; Zawadzki et al., 2005; Liao et al., 2005). In this research, the density of dry graupel is assumed to be 0.4 g cm^{-3} . The DFR vs D_o of dry graupel is shown in Fig.5.17.

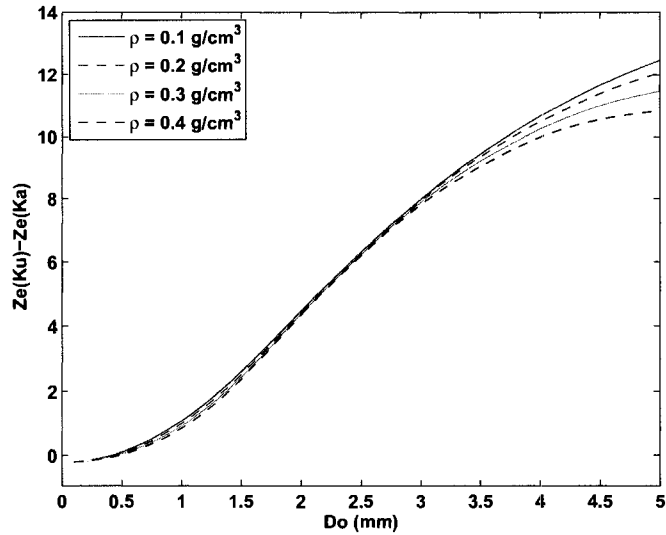


Figure 5.17: DFR vs D_o for snow densities of 0.05, 0.1, 0.2, and 0.4 g cm^{-3} . when $\mu = 0$ (implying exponential size distribution).

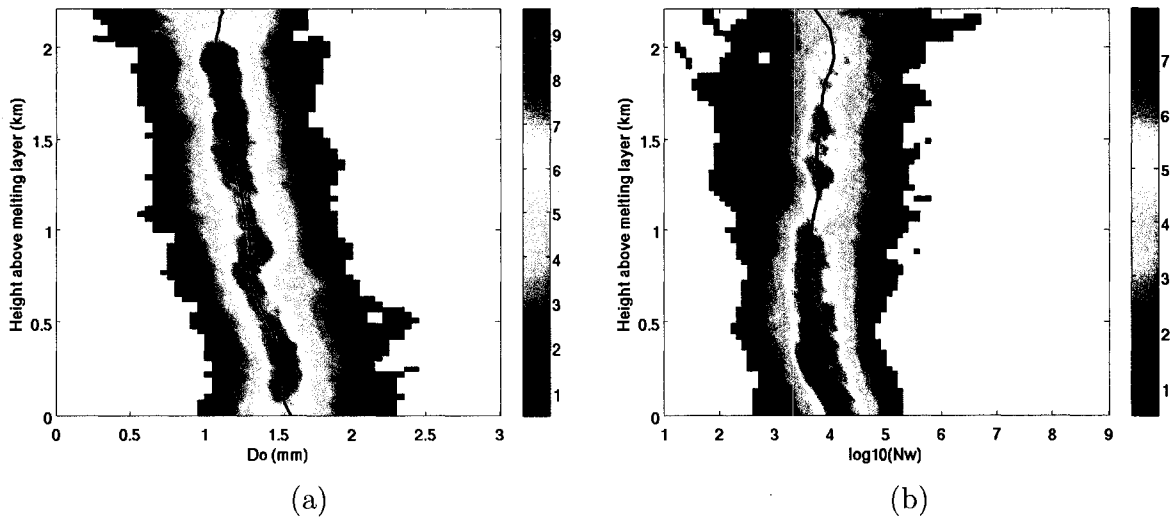


Figure 5.18: Distributions of the retrieved (a) D_o and (b) N_w of dry graupel along the height in convective rain. The solid line is the best fit.

Figure 5.18 (a) and (b) show the distribution of the retrieved D_o , and N_w , respectively, of dry graupel along the height. The height on the y-axis is the height above the melting layer. As seen in Fig. 5.18 (a), the retrieved D_o increases almost linearly as the height decreases. However, the increase of the D_o , when compared with the

dry snow case, is less pronounced. The difference of the D_o best fit for dry graupel between 0 and 2 km above the melting layer is about 0.5 mm, whereas that for wet snow is almost 2 mm. Despite of a slight increase as the height reaches the top of the melting layer, the retrieved N_w is nearly constant along the height. Figure 5.19 (a) and (b) show distributions of the retrieved D_o and N_w , respectively, for dry graupel at four different height levels, namely, 0, 0.5, 1, and 2 km above the melting layer.

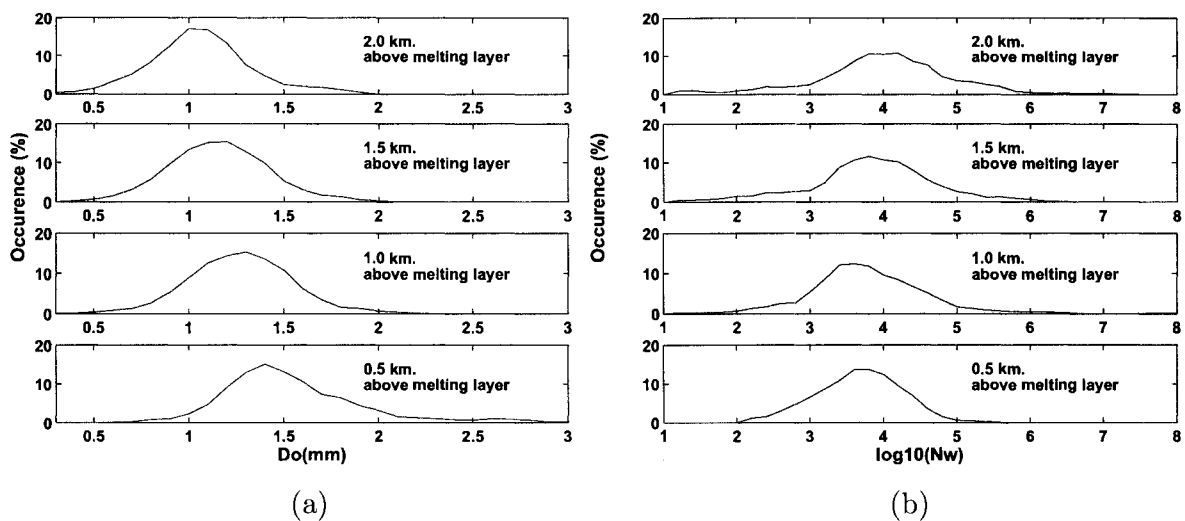


Figure 5.19: Distributions of the retrieved (a) D_o and (b) N_w of dry graupel in convective rain at 4 different height levels, namely, 0.5, 1, 1.5, and 2 km above the melting layer.

A melted (wet) graupel particle is assumed in the melting layer for convective rain. The melting layer boundaries are determined using LDR and fall velocity information. The spherical model of wet graupel composed of a homogeneous mixture of ice, air, and water is used. The dielectric constant of the wet graupel model is calculated using the Maxwell-Garnet mixing formula. The fractional volume content of water (water fraction) is assumed to change from 0.01 to 0.85. The DFR vs D_o for wet graupel is shown in Fig.5.20. The D_o and N_w for wet graupel were estimated by using the forward and iterative method. Both methods yield similar results.

Figure 5.21 (a) and (b) show the distribution of the retrieved D_o , and N_w of wet graupel along the height. The height on the y-axis is the height above and below the

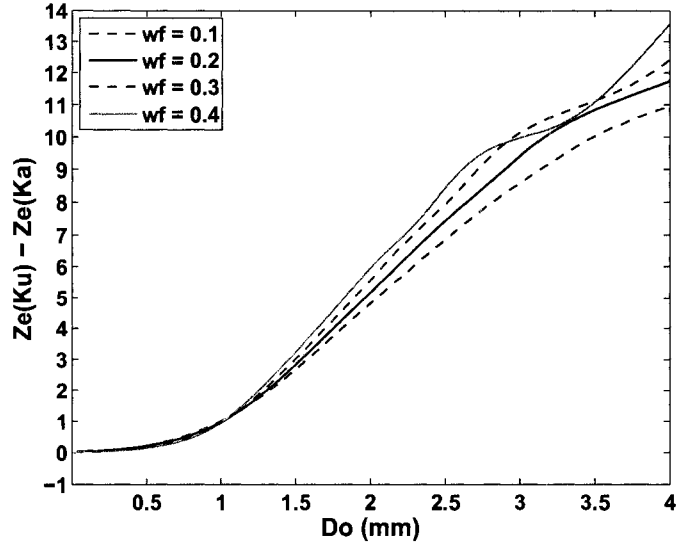


Figure 5.20: DFR vs D_o for wet graupel for water fraction (wf) of 0.05, 0.1, 0.2, and 0.4 g cm^{-3} .

center of the melting layer, which is determined by the LDR information. As seen in Fig. 5.18 (a), unlike the wet snow case, the retrieved D_o for wet graupel is nearly constant within the melting layer. Similarly to the retrieved D_o , the retrieved N_w is almost constant within the melting layer, despite a slight variation along the height. Figure 5.22 (a) and (b) show distributions of the retrieved D_o and N_w , respectively, for wet graupel at four different height levels, namely, 0.1 and 0.3 km above and below the center of the melting layer.

The backward method using PIA, which is estimated using the same technique as in stratiform rain, is used to estimate raindrop size distribution parameters. Figure 5.23 (a) and (b) show the distribution of the retrieved D_o , and N_w , respectively, of raindrops along the height of convective rain. The height on the y-axis is the height below the melting layer. As seen in Fig. 5.23 (a), the best fit of the retrieved D_o is nearly constant along the height. Similarly to the retrieved D_o , the best fit of the retrieved N_w is almost constant along the height. Figure 5.24 (a) and (b) show distributions of the retrieved D_o , and N_w in the rain region, respectively, at four different height levels, namely, 0, 0.5, 1 and 2 km below the melting layer.

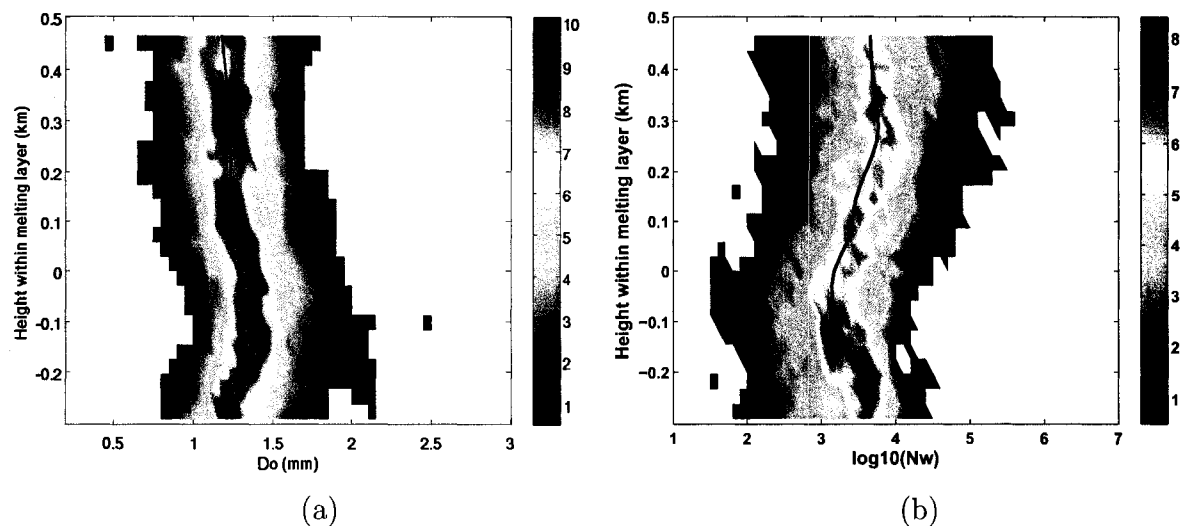


Figure 5.21: Distributions of the retrieved (a) D_o and (b) N_w of wet graupel along the height within the melting layer for convective rain. The positive and negative values represent the above and below the center of the melting layer, respectively. The center of the melting layer is indicated by 0 km. The solid line is the best fit.

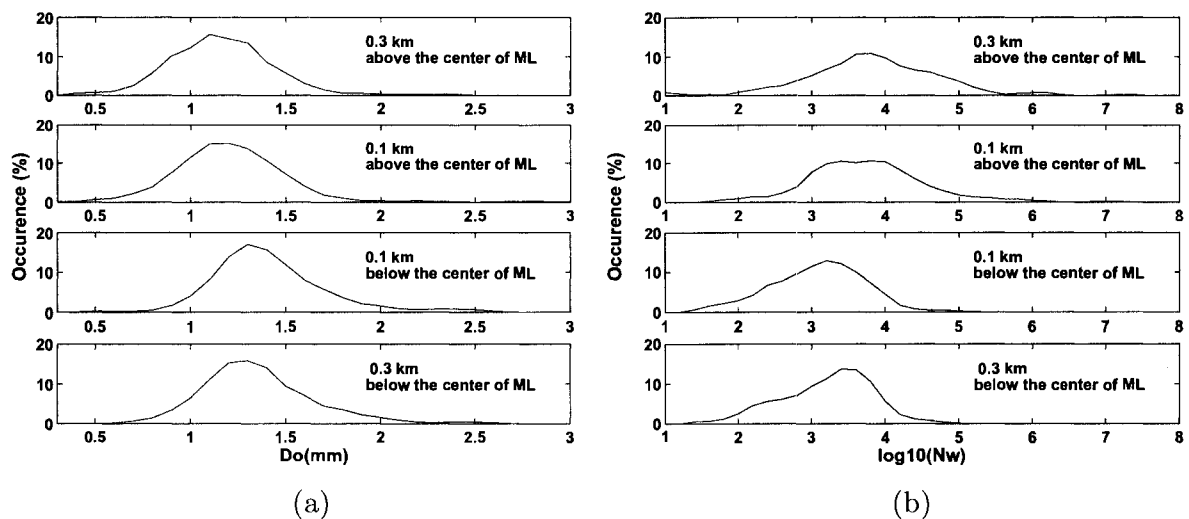


Figure 5.22: Distributions of the retrieved (a) D_o and (b) N_w of wet graupel in convective rain at four different height levels, namely, 0.1 and 0.3 km above (+) and below (-) the center of the melting layer (ML).

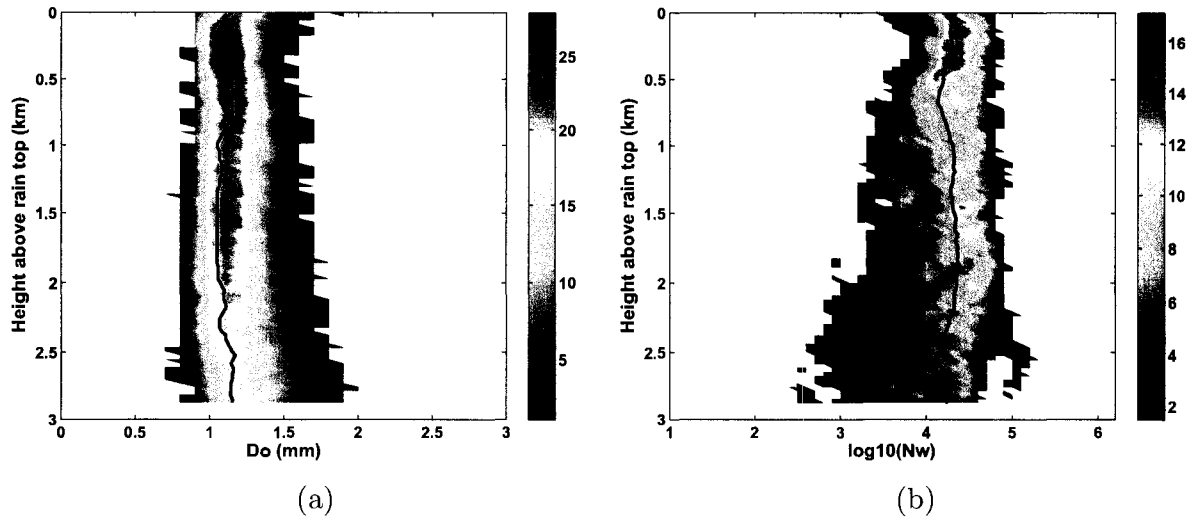


Figure 5.23: Distributions of the retrieved (a) D_o and (b) N_w of raindrops along the height below the melting layer. The solid line is the best fit.

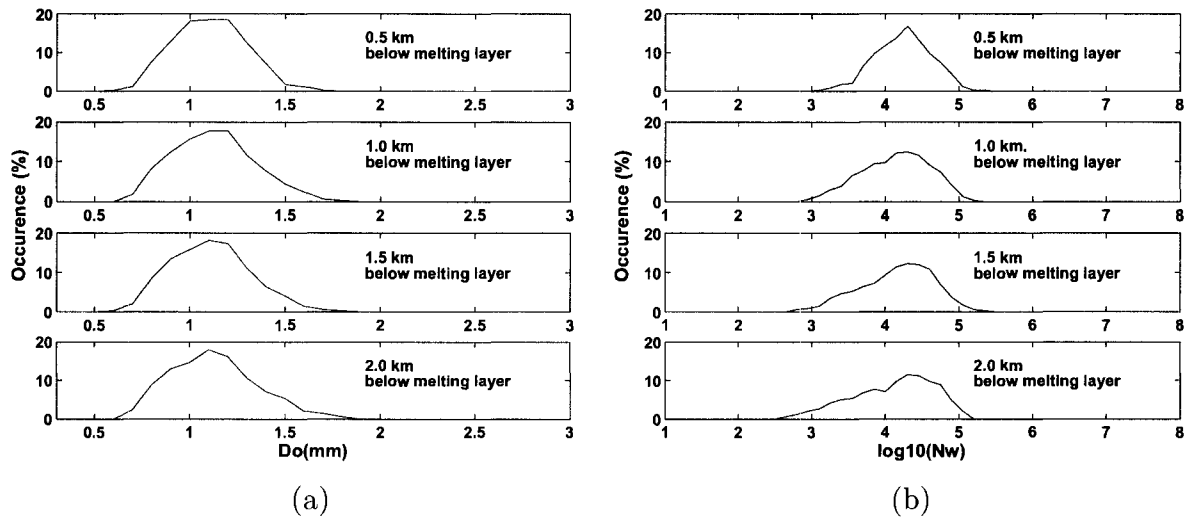


Figure 5.24: Distributions of the retrieved (a) D_o and (b) N_w of raindrops in convective rain at four different height levels, namely, 0, 0.5, 1, and 2 km below the melting layer.

- The D_o and N_w of rain are constant along the height.

The model of convective rain is as follows,

- The vertical profile of hydrometeors in convective rain consists of three types of hydrometeors—dry graupel above the melting layer, wet graupel within the melting layer, and rain below the melting layer.
- The D_o of dry graupel increases as the height decreases, whereas the N_w decreases as the height decreases.
- The D_o of wet graupel slightly decreases as the height decreases, whereas the N_w slightly increases as the height decreases.

The coefficients of parameterization between Z_e and k and variability of Z_e with frequency are generated along the vertical profile, based on the distributions of the retrieved D_o and N_w of the particle type along the vertical profile for each rain type model. An example of coefficients of Z_e and k relation, and variability of Z_e with frequency between Ku- and Ka-band for dry snow is shown in Table 5.2. The complete sets of the coefficients as a function of height for each rain model with three different frequency bands, namely, 2.7 GHz (S-band), 13.6 GHz (Ku-band), and 35.6 GHz (Ka-band) are shown in Appendix B.

The generated coefficients, in a sense, are the inference of the natural variation of microphysical characteristics along the vertical profile, and will be used quantitatively for simulating Ka-band radar observations using TRMM-PR observations, and for simulating Ku-band and Ka-band observations using ground-based radar measurements. The simulation procedure will be elaborated in the next chapter.

5.3 Summary and Conclusions

The development of a microphysical model of precipitation along the vertical profiles using airborne radar data was described. The models were developed separately

Table 5.2: The coefficients of $Z_e(Ka) = a + b*Z_e(Ku)$ and $k(Ka) = \alpha*Z_e(Ka)^\beta$ relations for dry snow as a function of height above the bright band.

Height (km)	$Z_e(Ka) = a + b*Z_e(Ku)$		$k(Ka) = \alpha*Z_e(Ka)^\beta$	
	a	b	α	β
5	0.088607	0.98357	0.0001699	1.0065
4.75	0.0675	0.98125	0.0001652	1.0117
4.5	0.072445	0.97725	0.000161	1.017
4.25	0.035347	0.9763	0.0001581	1.0214
4	0.010336	0.97194	0.0001566	1.0254
3.75	-0.014642	0.96789	0.0001525	1.0319
3.5	-0.047674	0.96355	0.0001605	1.0297
3.25	-0.069519	0.95921	0.0001414	1.0492
3	-0.070168	0.9543	0.0001328	1.0612
2.75	-0.15822	0.94898	0.0001397	1.0613
2.5	-0.18428	0.943	0.0001359	1.0715
2.25	-0.18184	0.93396	0.0001304	1.0822
2	-0.010835	0.91912	0.0001221	1.0982
1.75	0.2184	0.89782	0.0001615	1.0765
1.5	0.47705	0.87946	0.0001279	1.1141
1.25	0.48295	0.8656	0.0001188	1.1343
1	0.67568	0.84182	0.0001294	1.1399
0.75	0.82335	0.81829	0.0001362	1.1494
0.5	0.81024	0.80191	0.0001264	1.1789
0.25	0.4178	0.79296	0.0001453	1.1837

for stratiform and convective rain. The region above the bright band in stratiform rain is assumed to be dry snow. In the model, the precipitation particle above the melting layer are dry snow and dry graupel for stratiform and convective rain, respectively. Within the melting layer, the precipitation particle are melted snow and melted graupel for stratiform and convective rain, respectively. Below the melting layer, the precipitation particle are raindrops for both rain models. The particle size distribution parameters vary as a function of height for each rain model. The coefficients of the k and Z_e relation and the variation of Z_e with frequency were generated as a function of height. The microphysical model of precipitation developed in this chapter will be used to simulate the observations of the GPM-DPR in the next

chapter.

CHAPTER 6

SIMULATION OF SPACEBORNE PRECIPITATION RADAR OBSERVATIONS : APPLICATION TO GPM-DPR

6.1 Introduction

The era of the TRMM satellite, carrying a single-frequency precipitation radar (PR), will transition to the era of GPM. The global precipitation mission (GPM) satellite will carry the first space-based dual-frequency precipitation radar (DPR). Because the DPR is the first of its kind, a simulation of what would be observed by the DPR is necessary for algorithm development, and system evaluation. The simulation of the dual-frequency spaceborne radar observations of precipitation is described this chapter. The microphysical models developed in chapter 5 will be used for the simulation in this chapter. Since this research primarily aims to have an impact on the ongoing research for the GPM mission, the frequency selection for the simulation emulates the DPR operational frequencies, which are Ku-band (13.6 GHz) and Ka-band (35.6 GHz). The simulations are performed using both TRMM-PR observations and ground-based radar measurements for various precipitation types and conditions. For the TRMM-PR part, the Ka-band radar observations are simulated using Ku-band radar observations by PR. For the ground-based radar part, the Ku- and Ka-band radar observations are simulated using S-band radar measurements, both single- and dual-polarization radars. Applicability of dual-frequency retrieval techniques that can be applied to a wide variety of simulated observations are discussed.

6.2 The Simulation of Ka-band Radar Observations Based on Ku-band Radar Observations

6.2.1 Case Study: The simulation of Ka-band radar observations based on TRMM-PR observations

The precipitation radar (PR) made observations precipitation over the NAMMA experiment area. The attenuation-corrected reflectivity (Z_e) of an overpass and an aircraft path in the NAMMA experiment are shown in Fig. 6.1. The Z_e at Ku-band (PR), hereafter $Z_e(\text{Ku})$, is used to simulate Z_e at Ka-band, hereafter $Z_e(\text{Ka})$, and to simulate the measured reflectivity (Z_m) at Ka-band, hereafter $Z_m(\text{Ka})$.

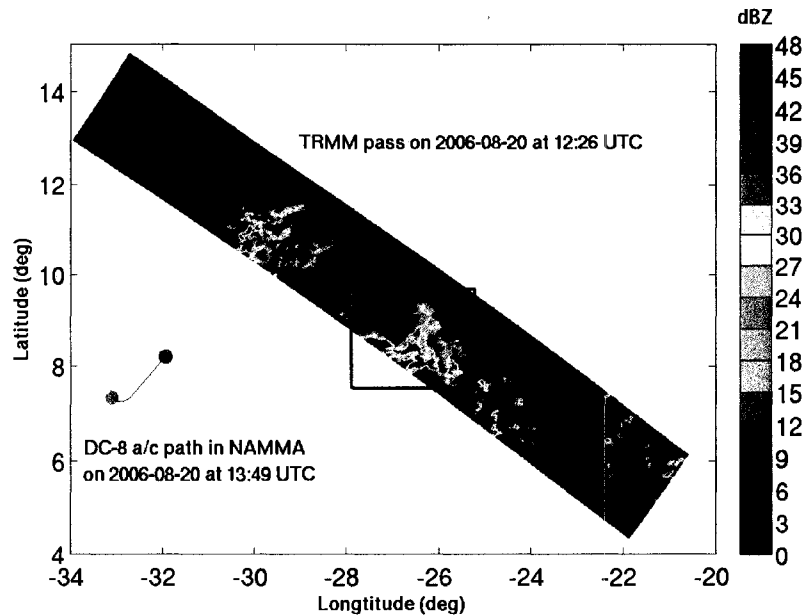


Figure 6.1: An overpassing orbit of the TRMM-PR over the area of the NAMMA experiment. The precipitation in the rectangle is used in the simulation.

The $Z_e(\text{Ku})$ used in this simulation is marked by the rectangle in Fig. 6.1 and shown in Fig. 6.2: (a) a horizontal cross-section of $Z_e(\text{Ku})$ at 2 km above sea level; (b) a vertical cross-section of $Z_e(\text{Ku})$ across the PR ground track, as indicated by the dashed line in (a); (c) and (d) two vertical profiles of $Z_e(\text{Ku})$ at the locations A and

B, as indicated by the dashed lines in (b), respectively.

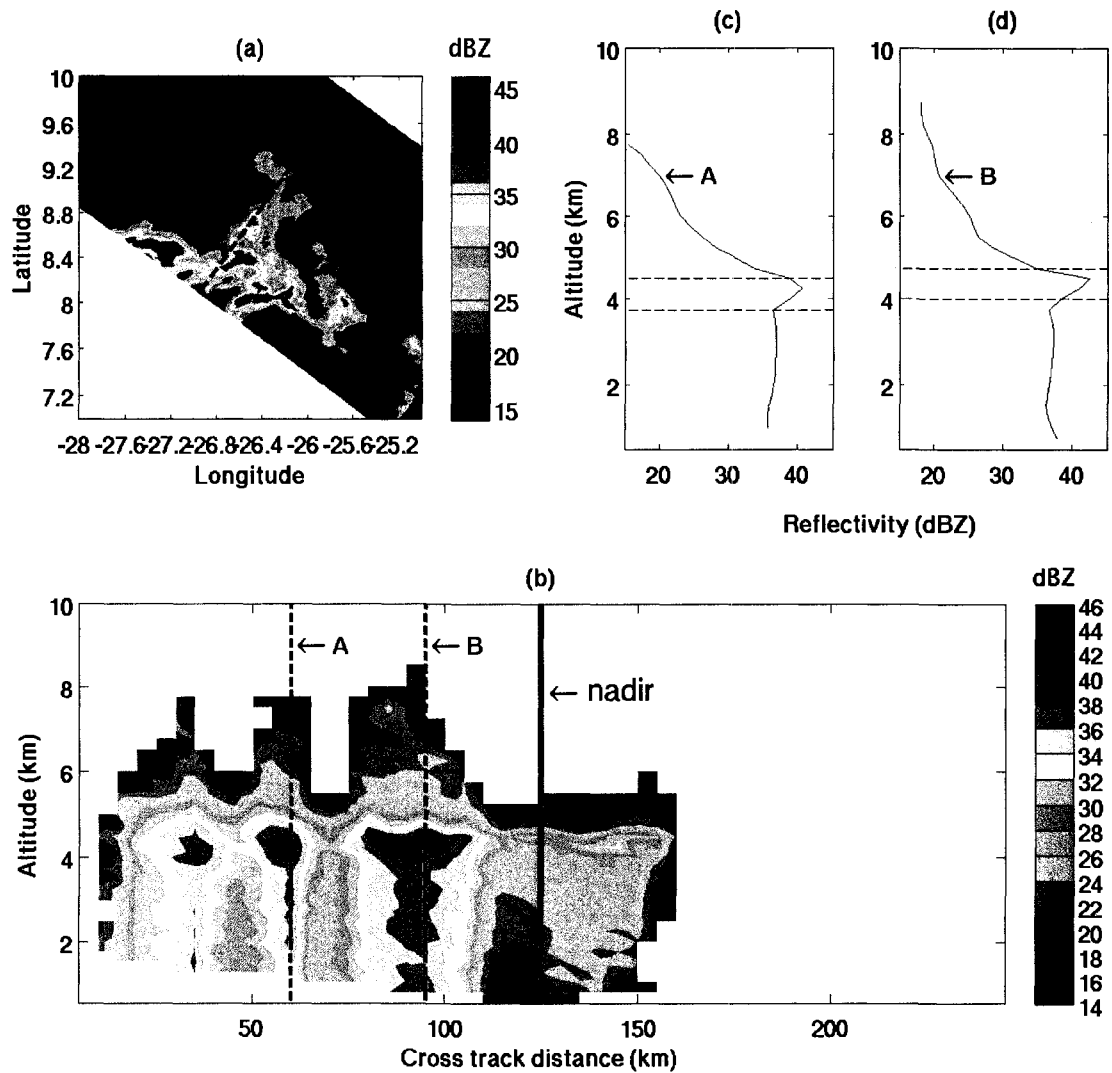


Figure 6.2: The attenuation-corrected reflectivity at Ku-band ($Z_e(\text{Ku})$): (a) a horizontal cross-section at 2 km; (b) a vertical cross-section across PR ground track, as indicated by the dashed line in (a); (c) and (d) vertical profiles at the locations A and B, as indicated in (b), respectively.

The simulation is performed along the vertical profiles of $Z_e(\text{Ku})$ corresponding to their rain types, which are provided in the TRMM-PR data. The available rain types in the TRMM-PR data are 1) stratiform rain with detection of bright band, 2) convective rain, and 3) stratiform rain without a detection of a bright band. In

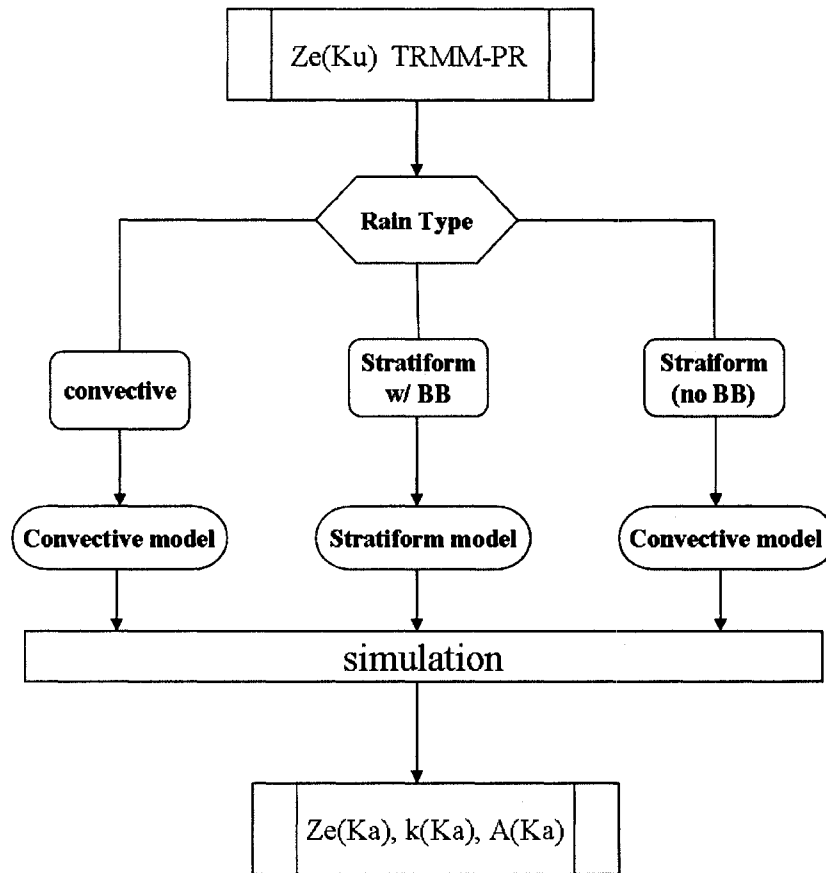


Figure 6.3: A simple diagram of the simulation procedure based on TRMM-PR observations.

stratiform rain with a bright band, the boundary of the bright band is assumed to be 1 km—500 m above and 500 m below the bright band peak. In convective rain, the boundary of the melting layer is also assumed to be 1 km—500 above and 500 below the freezing height, which is available in the TRMM-PR data. The freezing height is defined along the vertical profile where the temperature is 0°C , which is estimated using the climatological surface temperature and a lapse rate of $5^{\circ}\text{C km}^{-1}$ (Iguchi et al., 2000). In stratiform rain without a bright band, an alternative model is used. When shallow rain is present, those profiles that have the storm top height below the freezing height are treated as a rain region in the convective rain model; otherwise, they are treated as a convective rain type. A flow diagram of the simulation procedure is shown in Fig. 6.3.

Figure 6.4 shows the three main rain types on the horizontal cross-section of the precipitation cell used in this simulation: (a) all rain types, (b) stratiform rain with a bright band, (c) convective rain, and (d) stratiform rain without a bright band. It is clear from Fig. 6.4 that the majority of this particular precipitation cell observed by TRMM-PR is stratiform with bright band, and only small fractions are convective and stratiform rain without a bright band.

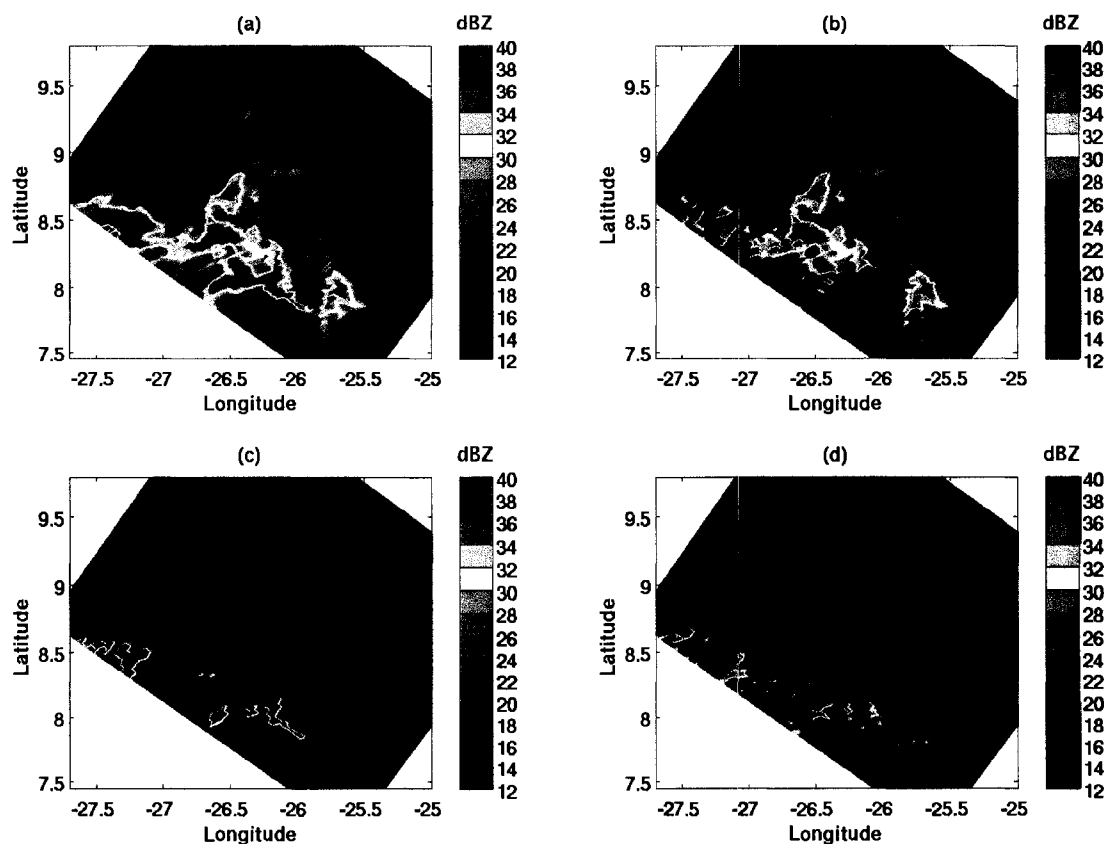


Figure 6.4: A horizontal cross-section of $Z_e(Ku)$, separated based on the rain-type information of the precipitation observed by the TRMM-PR in this case study: (a) all rain types; (b) stratiform rain with a bright band; (c) convective rain, and (d) stratiform rain without a bright band.

Figure 6.5 shows a horizontal cross-section of the $Z_e(Ku)$ and the simulated $Z_e(Ka)$ at three different altitudes corresponding to the three different types of precipitation particle, namely, 2 km (rain), 4.5 km (melted snow/graupel) and 6 km (dry

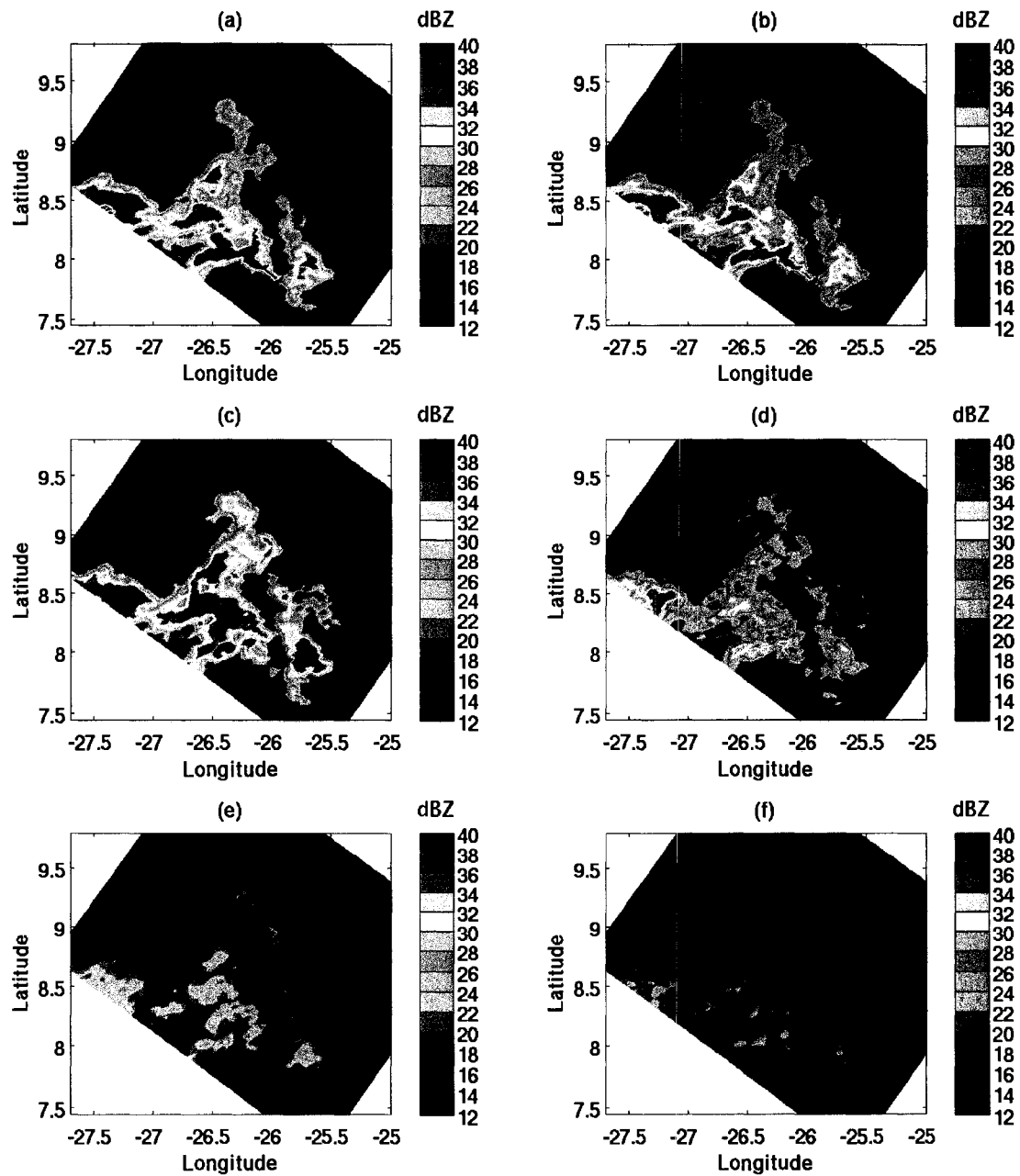


Figure 6.5: $Z_e(\text{Ku})$ and simulated $Z_e(\text{Ka})$ at three different horizontal cross-section heights above the surface: (a) and (b) for the rain region at 2 km, (c) and (d) for the melted particle (snow/graupel) region at 4.5 km, and (e) and (f) for the dry snow/graupel region at 6 km.

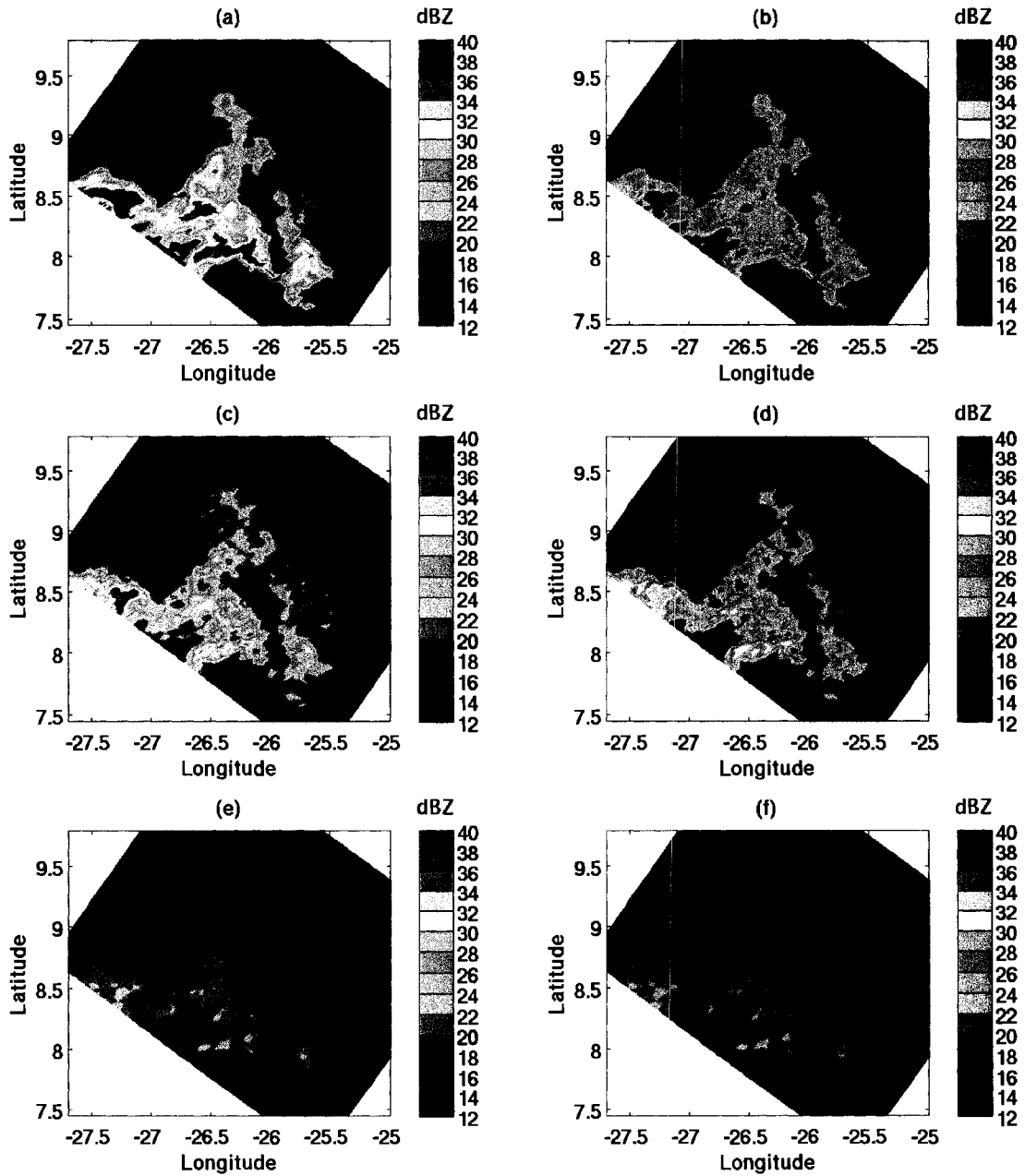


Figure 6.6: $Z_e(\text{Ka})$ and simulated $Z_m(\text{Ka})$ at 3 different horizontal cross-section heights above the surface. The (a) and (b) for the rain region at 2 km, (c) and (d) for the melted particles (snow/graupel) region at 4.5 km, and (e) and (f) for the dry snow/graupel region at 6 km.

snow/graupel), are shown in Fig. 6.5 . It is clear from Fig. 6.5 that the simulated $Z_e(\text{Ka})$ at the three altitudes are smaller than $Z_e(\text{Ku})$. In the wet snow, the difference is quite significant. This is caused by the non-Rayleigh scattering in one or both frequency bands. The simulated $Z_m(\text{Ka})$, as shown in Fig. 6.6, associated with the simulated $Z_e(\text{Ka})$ in Fig. 6.5 is what actually would be observed by the Ka-band radar. It is obvious that the simulated $Z_m(\text{Ka})$ is much lower than $Z_e(\text{Ka})$ because of the strong attenuation in this frequency band. The simulated two-way path integrated attenuation (PIA) in both channels is shown in Fig. 6.7.

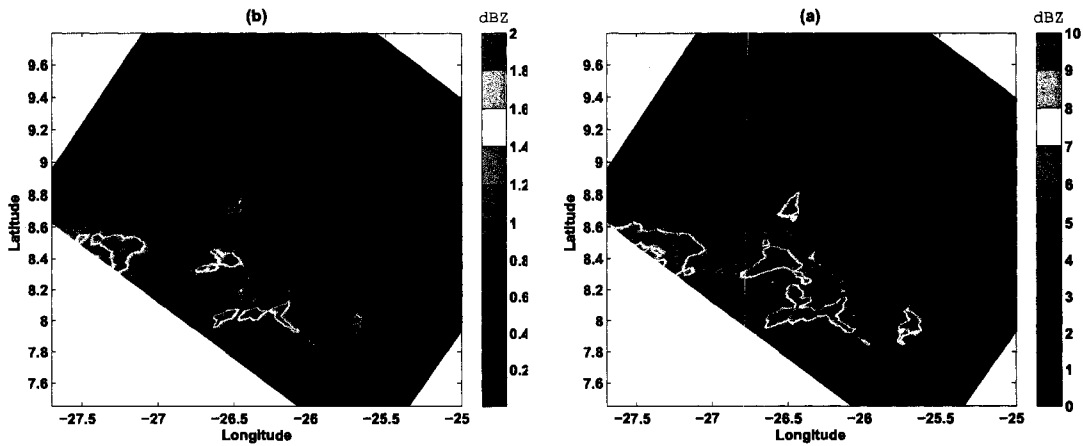


Figure 6.7: Simulated path-integrated attenuation: (a) Ku-band; (b) Ka-band.

It is clear from Fig. 6.7 that the simulated PIA(Ka) is higher than the simulated PIA(Ku). For very strong reflectivity profiles, the PIA(Ka) can be as high as 10 times PIA(Ku). An advantage of this characteristic is that the larger PIA in the Ka-band channel can extend the use of the surface reference technique (SRT) for a TRMM-like retrieval algorithm, as described in section 3.2.2, which is limited in Ku-band when the PIA is small. A shortcoming is that when the PIA is too large, it causes a loss of signal in the Ka-band channel, and hence dual-frequency algorithms cannot be used.

A vertical cross-section of $Z_e(\text{Ku})$, the simulated $Z_e(\text{Ka})$, the simulated $Z_m(\text{Ku})$, and the simulated $Z_m(\text{Ka})$ in the stratiform rain across the TRMM ground track, as indicated by the dashed line at A in Fig. 6.8, is shown in Fig. 6.9. The difference

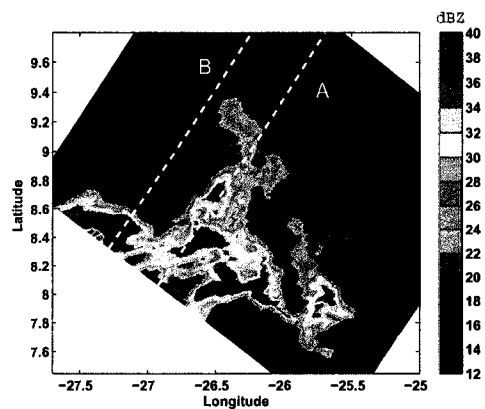


Figure 6.8: Location of vertical cross-section across TRMM ground track. Location A is stratiform rain and B is convective.

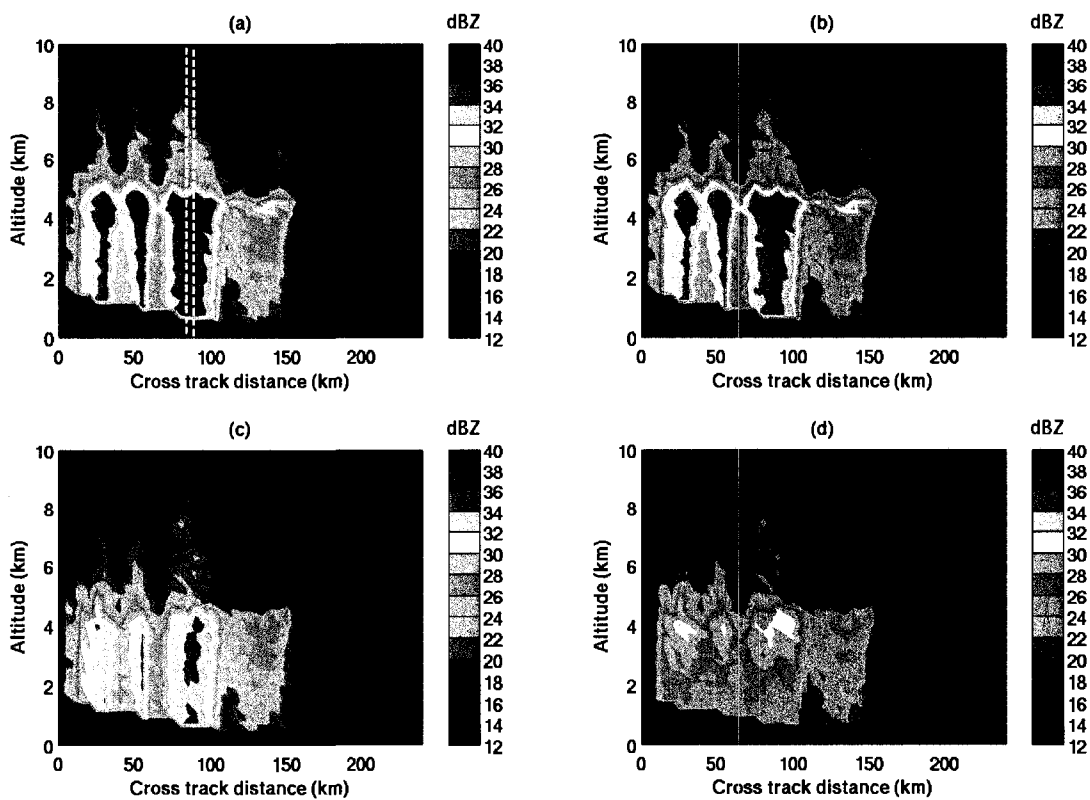


Figure 6.9: A vertical cross-section of stratiform rain, as indicated by the dashed line at A in Fig. 6.8: (a) $Z_e(\text{Ku})$; (b) the simulated $Z_m(\text{Ku})$; (c) the simulated $Z_e(\text{Ka})$; and (d) the simulated $Z_m(\text{Ka})$.

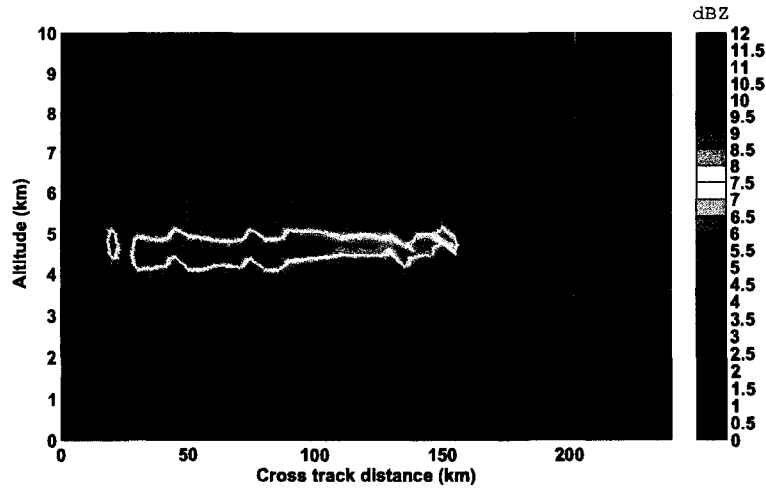


Figure 6.10: The difference between a vertical cross-section of $Z_e(\text{Ku})$ (Fig. 6.9 (a)) and the simulated $Z_e(\text{Ka})$ (Fig. 6.9 (c)) in stratiform rain.

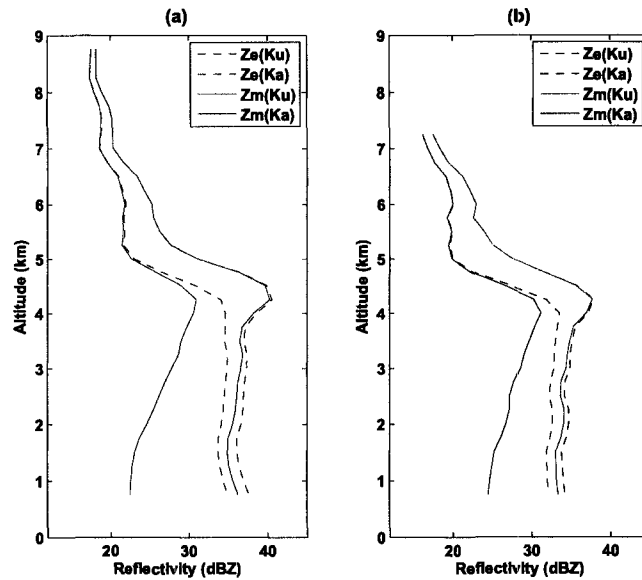


Figure 6.11: Two vertical profiles of reflectivity in stratiform rain with a bright band, as indicated by two dashed lines in Fig. 6.9 (a). The dashed lines represent $Z_e(\text{Ku})$ and the simulated $Z_e(\text{Ka})$, while the solid lines represent the simulated $Z_m(\text{Ku})$ and $Z_m(\text{Ka})$.

between $Z_e(\text{Ku})$ (Fig. 6.9 (a)) and $Z_e(\text{Ka})$ (Fig. 6.9 (c)) is shown in Fig. 6.10. It is clear that large differences occur in the bright band region. In this case, the difference can be observed to be as large as about 11 dBZ. A strong attenuation in the rain band in the Ka-band channel is quite apparent, as seen when comparing $Z_e(\text{Ka})$ and

$Z_m(\text{Ka})$ in Fig. 6.9 (c) and (d), respectively.

Two reflectivity profiles, as indicated by two dashed lines in Fig. 6.9 (a), are shown in Fig. 6.11. It can be seen from Fig. 6.11 that, in the bright band region, the simulated $Z_e(\text{Ka})$ does not have a sharp increase as appears in the Ku-band channel. In the snow region, the differences between $Z_e(\text{Ku})$ and the simulated $Z_e(\text{Ka})$ increase as the altitude increases. When comparing the Z_e and Z_m in the snow region, it is clear that there is almost no attenuation for both channels.

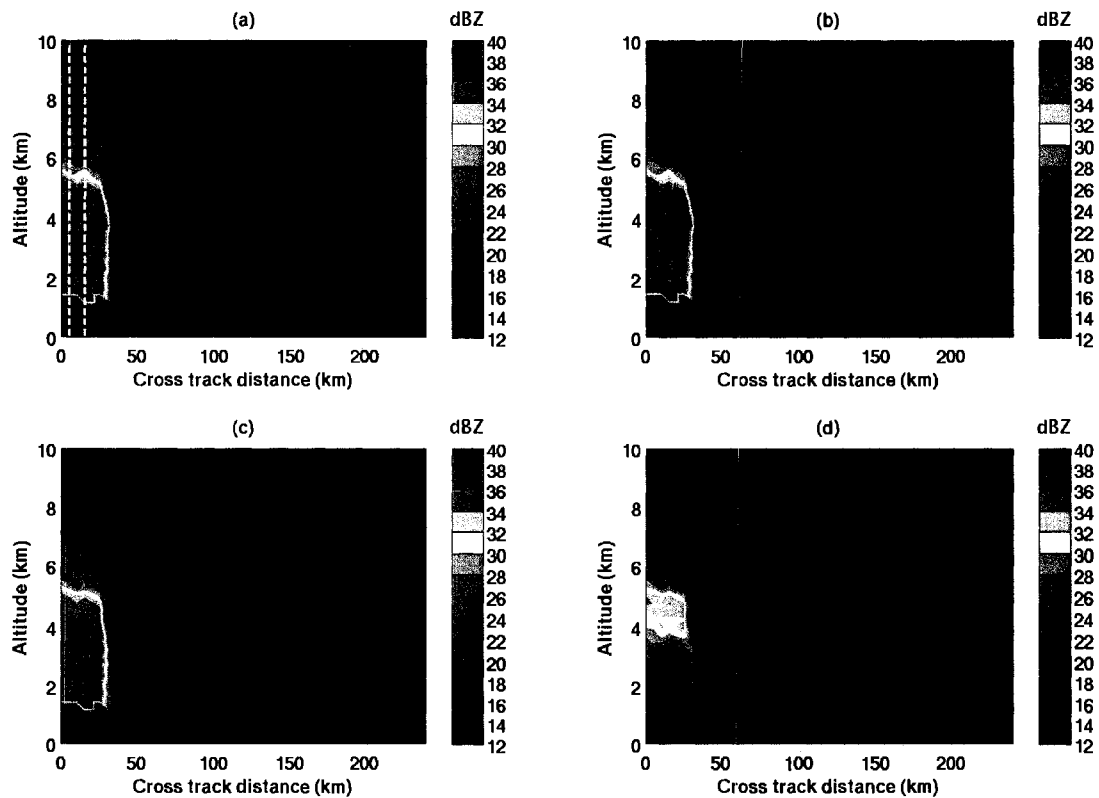


Figure 6.12: A vertical cross-section of: (a) $Z_e(\text{Ku})$; (b) simulated $Z_m(\text{Ku})$; (c) simulated $Z_e(\text{Ka})$, and (d) simulated $Z_m(\text{Ka})$, as indicated by the dashed line at B in Fig. 6.8 in the convective rain.

A vertical cross-section of the $Z_e(\text{Ku})$ and the simulated $Z_e(\text{Ka})$, the simulated $Z_m(\text{Ku})$, and the simulated $Z_m(\text{Ka})$ in convective rain, as indicated by the dashed line at B in Fig. 6.8, is shown in Fig. 6.12. Considering parts (a) and (c) of Fig.

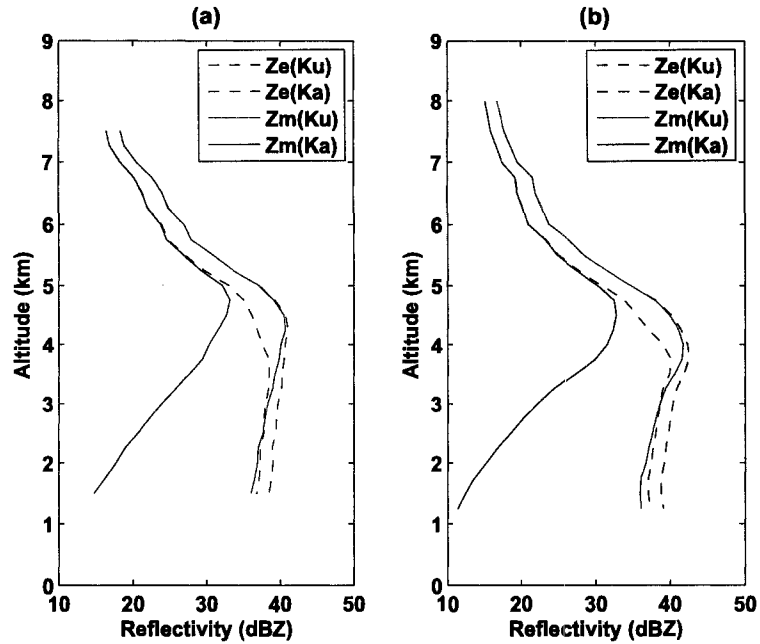


Figure 6.13: Two vertical profiles of reflectivity in convective rain, as indicated by the two dashed lines in Fig. 6.12 (a). The dashed lines represent $Z_e(\text{Ku})$ and the simulated $Z_e(\text{Ka})$, while the solid lines represent the simulated $Z_m(\text{Ku})$ and $Z_m(\text{Ka})$.

6.12, the differences between $Z_e(\text{Ku})$ and the simulated $Z_e(\text{Ka})$ along the vertical profiles can be observed but are not very significant. A strong attenuation in the rain band in Ka-band is quite apparent, and causes a loss of signal because the received signal is below the minimum detectable reflectivity at Ka-band, which is 12 dBZ (Senbokuya et al., 2004), at a low altitude. Similarly to the stratiform rain case, the large differences occur in the melting layer. However, the difference is not as large as that in the stratiform rain case.

Two reflectivity profiles in the convective rain, as indicated by the two dashed lines in Fig. 6.12 (a), are shown in Fig. 6.13. Unlike the stratiform rain case, the difference between $Z_e(\text{Ku})$ and the simulated $Z_e(\text{Ka})$ does not change much as the height increases in the dry graupel region. When comparing the Z_e and Z_m in the dry graupel region, it is clear that there is almost no attenuation in both channels.

6.3 Simulation of Ku- and Ka-band Radar Observations Based on Ground Radar Measurements

6.3.1 Case Study: A simulation using ground-based NEXRAD radar measurements

In the GPM era, the ground validation system (GVS) prototype consists of a network of Weather Surveillance Radar-1988 Doppler (WSR-88D or “NEXRAD”) (GVS, 2007). There are a number of NEXRAD sites in the US. Simulation of the Ku- and Ka-band using the NEXRAD measurements offer a great opportunity to study characteristics of precipitation that would be observed by the dual-frequency precipitation radar (DPR) planned for the GPM. Since the NEXRAD operates at about 2.7-3 GHz (S-band), which does not suffer from attenuation by precipitation media, the simulation is not affected by the attenuation. The NEXRAD is a single-polarization radar, producing two products, reflectivity and velocity. In this simulation, the reflectivity measurements from two NEXRAD sites, hereafter $Z_e(S)$, namely, KMLB and KTBW, located in Melbourne and Ruskin/Tampa Bay, FL, respectively, were used. The locations of KMLB and KTBW are shown in Fig. 6.14.

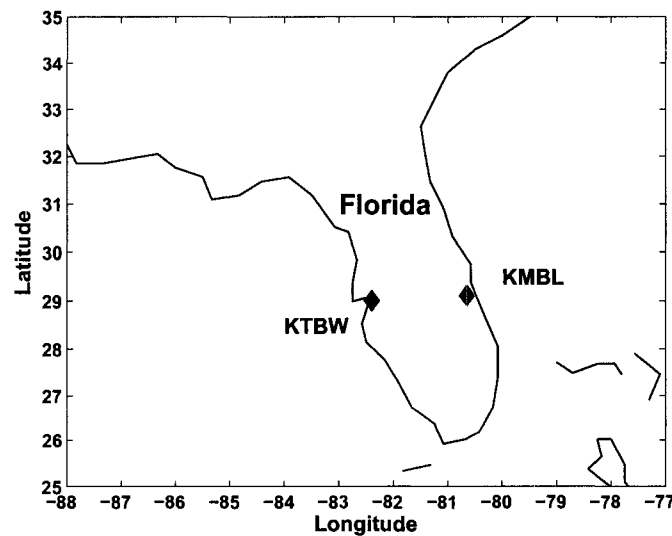


Figure 6.14: A simple schematic diagram of the simulation procedure based TRMM-PR observations.

Unlike the TRMM-PR data, rain type information is not available in the NEXRAD data. Therefore, the rain type classification methods (H- and V-methods) (Awaka et al., 97), as used in the TRMM-PR, are used here, with a modification. The H-method primarily detects convective rain. To be consistent with what is done in the simulation using TRMM-PR data, the rain types are also classified into three types—convective, stratiform with a bright band, and stratiform without a bright band. The modified H-method first detects convective rain. The rain profiles that are not classified as convective rain are classified as stratiform rain. The modified V-method is then used to detect the bright band in those profiles that are classified as stratiform rain. It should be noted that due to a coarse vertical resolution of the ground radar observations, as will be seen later, the bright band detection will be uncertain. The freezing height of profiles that are classified as convective rain is determined by the TRMM-PR freezing height data that are both temporal and spatial proximity to the ground radar measurements used in the simulation. The storm top height is determined as the height above surface where the reflectivity measurement is below a certain threshold. Convective rain profiles that have storm heights lower than their freezing heights, are treated as rain.

Case I. Simulation using KMLB observations

A case of KMLB radar measurement on June 2, 2005, is used in this simulation. Figures 6.15 and 6.16 show horizontal cross-sections of simulated $Z_e(\text{Ku})$ and $Z_e(\text{Ka})$ using KMLB measurements, hereafter $Z_e(\text{S})$, respectively. The horizontal cross-sections are at three different height levels, corresponding to three different types of hydrometeors, namely, 2 km (rain), 4.5 km (melted snow/graupel, and 6 km (dry snow/graupel). The subfigures (a), (c), and (e) in 6.15 and 6.16 show $Z_e(\text{S})$ at the three altitudes, and (b), (d), and (f) show the simulated Z_e at the three altitudes. As seen in Fig. 6.15, the $Z_e(\text{S})$ and simulated $Z_e(\text{Ku})$ for all three altitudes are barely different. This is because of Rayleigh scattering in both channels. On the other hand,

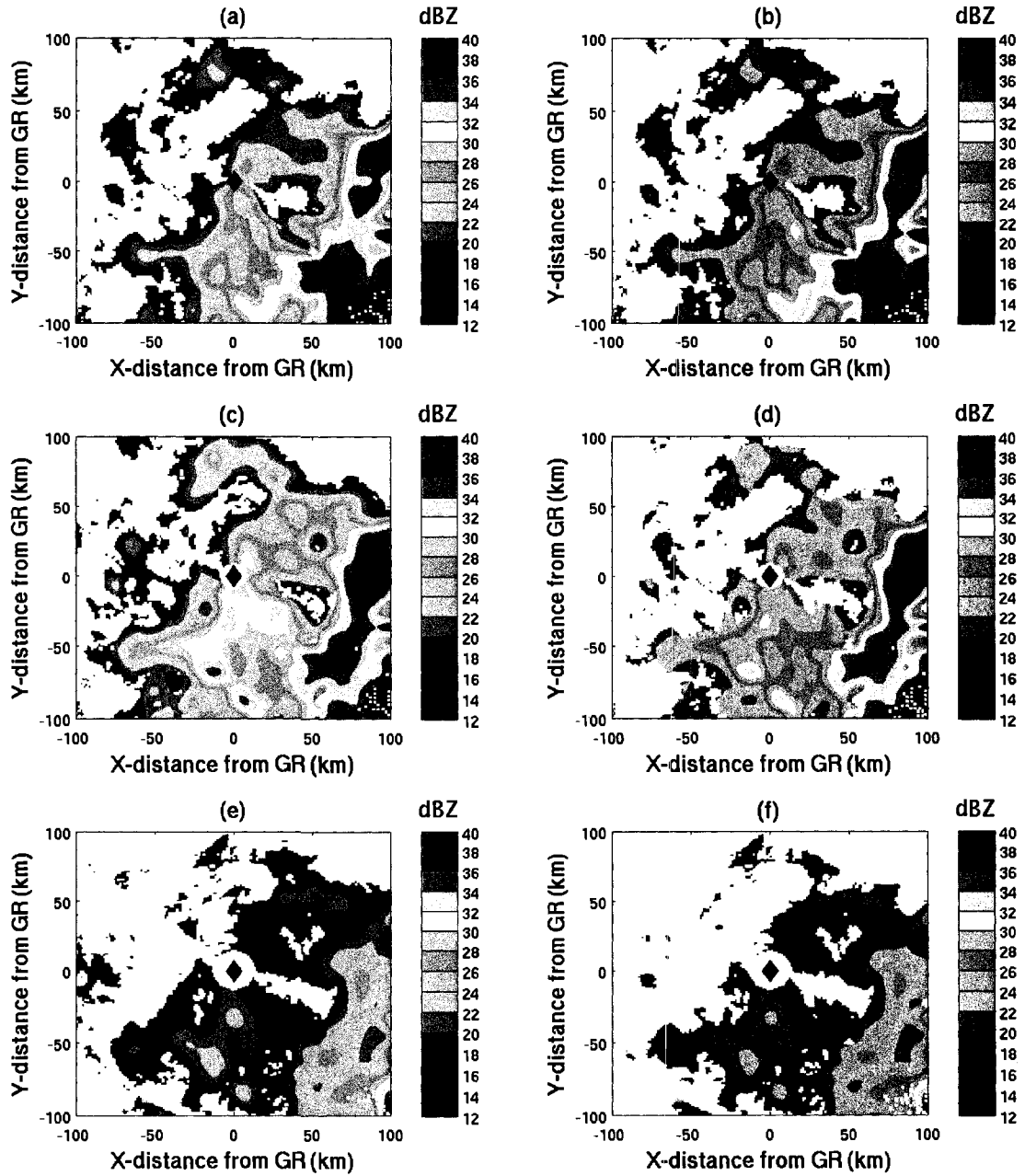


Figure 6.15: The simulation of $Z_e(\text{Ku})$ using KMLB measurements ($Z_e(\text{S})$) for three different height levels above the surface. In (a) and (b) the $Z_e(\text{S})$ and $Z_e(\text{Ku})$ at 2 km, (c) and (d) the $Z_e(\text{S})$ and $Z_e(\text{Ku})$ at 4.5 km, and (e) and (f) the $Z_e(\text{S})$ and $Z_e(\text{Ku})$ at 6 km.

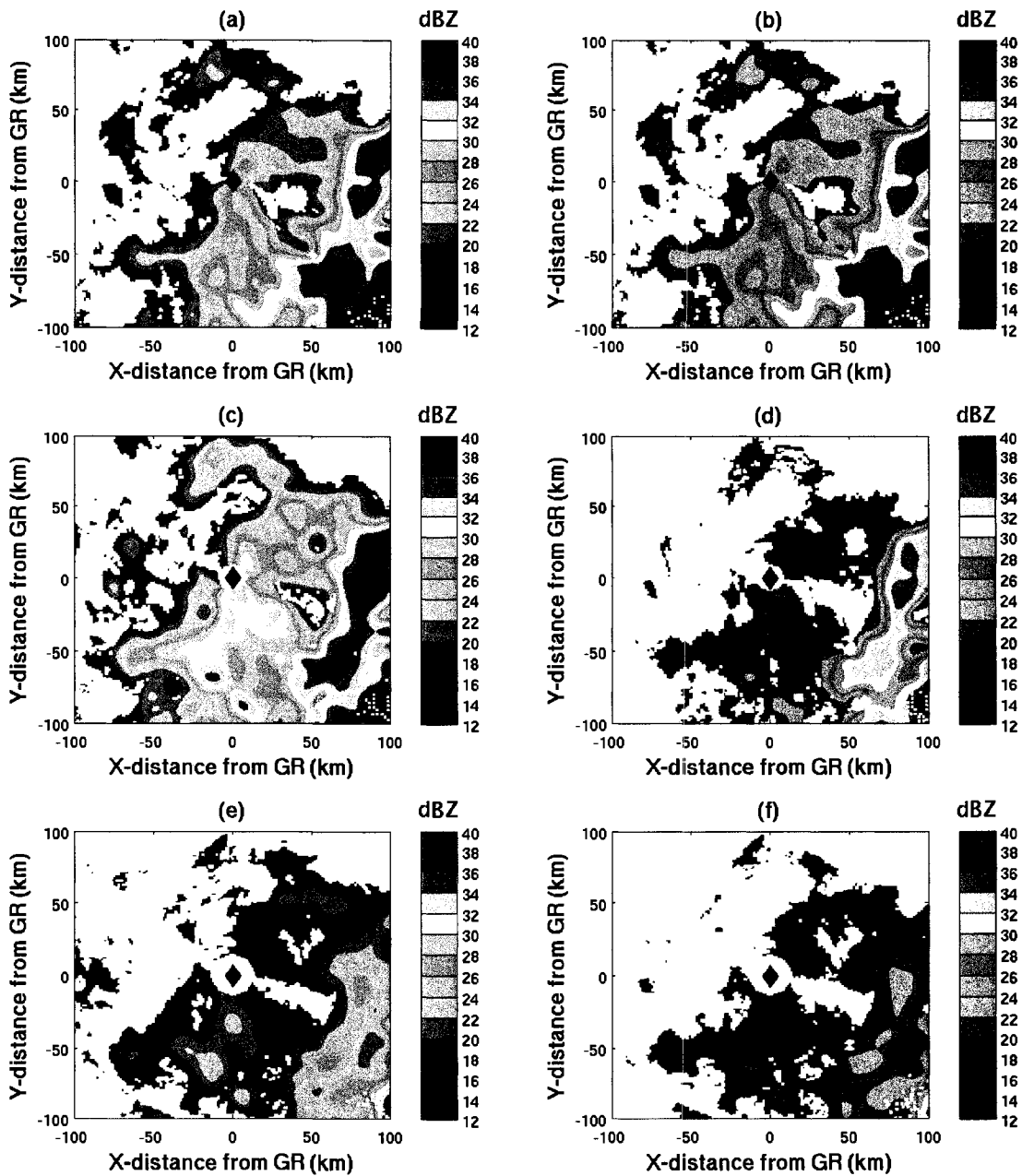


Figure 6.16: The same as Fig. 6.15 for Ka-band

the $Z_e(\text{Ka})$ are lower than $Z_e(\text{S})$ for all three altitudes. This is caused by the non-Rayleigh scattering in the Ka-band and Rayleigh scattering in the S-band. Figure

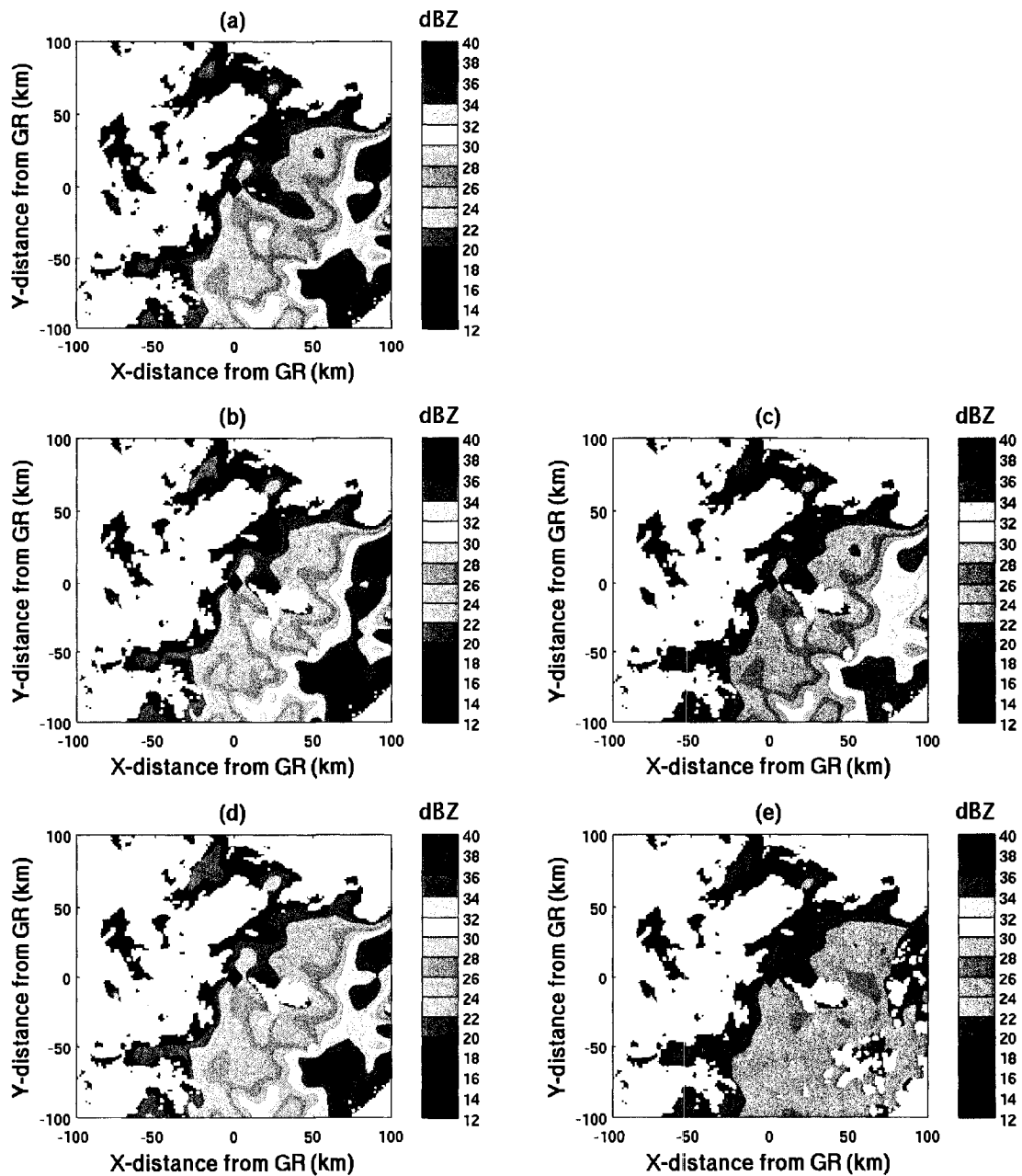


Figure 6.17: The horizontal cross-section of reflectivity at altitude of 1 km above the surface: (a) the $Z_e(S)$ measurement from KMLB radar; (b) and (c) the simulated $Z_e(Ku)$, and $Z_m(Ku)$, respectively; (d) and (e) the simulated $Z_e(Ka)$, and $Z_m(Ka)$, respectively.

6.17 shows the horizontal cross-section of reflectivity at an altitude of 1 km above the surface for: (a) $Z_e(S)$, (b) $Z_e(Ku)$, (c) $Z_e(Ka)$, (d) $Z_m(Ku)$ and (e) $Z_m(Ka)$. The attenuation in Ka-band ($PIA(Ka)$) causes the loss of signal in the center of convective rain (see Fig. 6.17 (e)), but is not significant in Ku-band channel.

Vertical cross-sections of $Z_e(S)$ and the simulated $Z_e(Ku)$, $Z_m(Ku)$, $Z_e(Ka)$ and $Z_m(Ka)$ are shown in Fig. 6.18. The dashed line in Fig. 6.18 (a) shows the location of the vertical cross-section. Fig. 6.18 (b), (c), (d), and (e) show vertical cross-sections of the simulated $Z_e(Ku)$, $Z_m(Ku)$, $Z_e(Ka)$ and $Z_m(Ka)$, respectively. It is clear from Fig. 6.18 (e) and (f) that the simulated $Z_e(Ka)$ is attenuated significantly in the convective rain cell. Two vertical profiles of reflectivity are shown in Fig. 6.19. The locations of the profiles are marked as dashed lines in Fig. 6.19 (a), and the two profiles are shown in Fig. 6.19 (b), and (c). The profile in Fig. 6.19 (b) is stratiform rain with a bright band. Because of the coarse vertical resolution of the ground radar, the bright band appears wider than what appeared in the TRMM-PR observations. It is clear from the two profiles that the $PIA(Ka)$ at 0.5 km above the ground are much stronger than $PIA(Ku)$. For this case, the $PIA(Ka)$ in the convective rain, shown in Fig. 6.19 (c), is as high as about 25 dB, which is about 7.5 times $PIA(Ku)$.

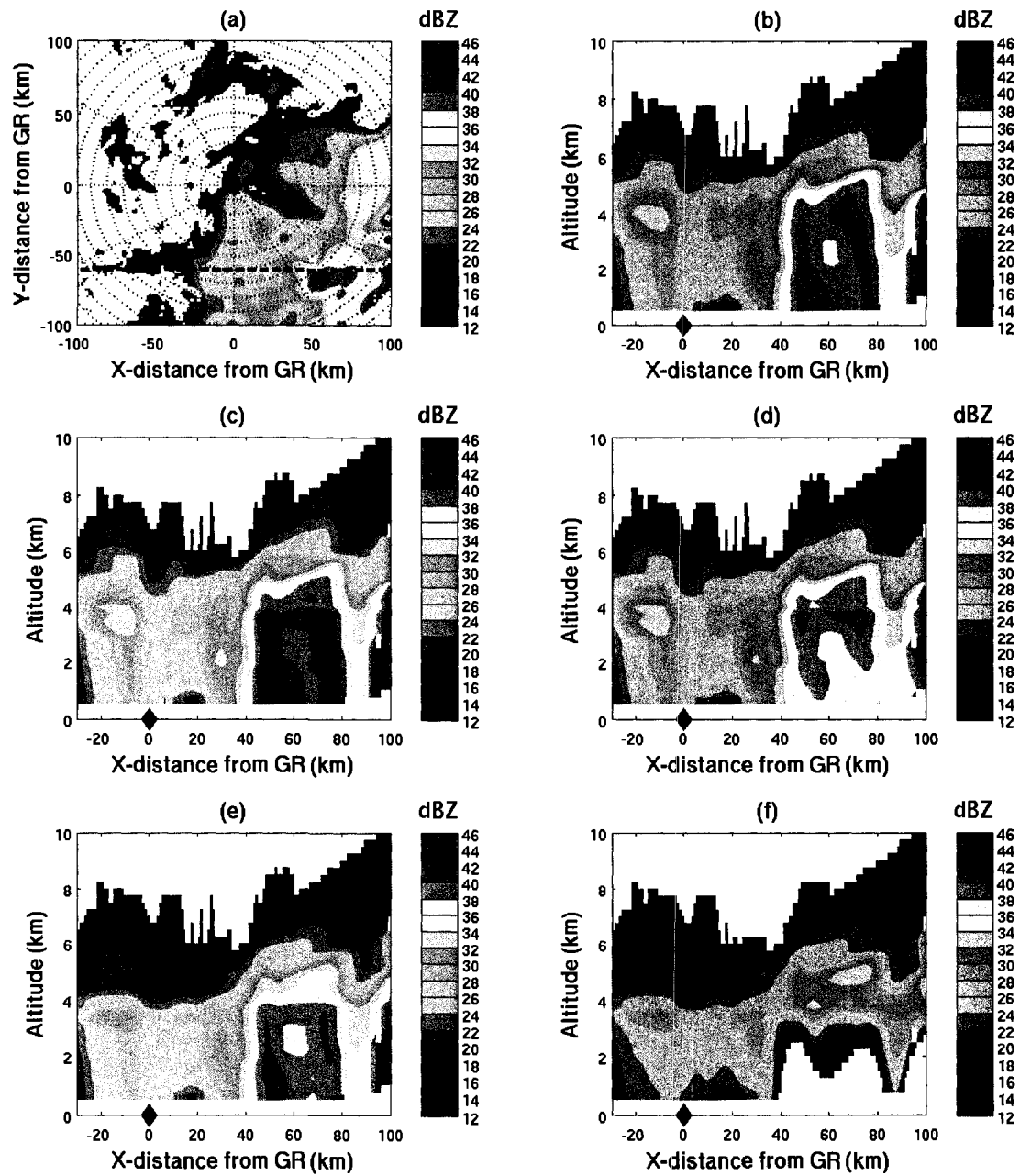


Figure 6.18: The vertical cross-section of reflectivity: (a) and (b) the horizontal and vertical cross-section of the $Z_e(S)$ measurement from KMLB radar, respectively; (c) and (d) the vertical cross-section of the simulated $Z_e(Ku)$ and $Z_m(Ku)$, as indicated by the dashed line in (a), respectively; (e) and (f) the vertical cross-section of the simulated $Z_e(Ka)$ and $Z_m(Ka)$, as indicated by the dashed line in (a), respectively.

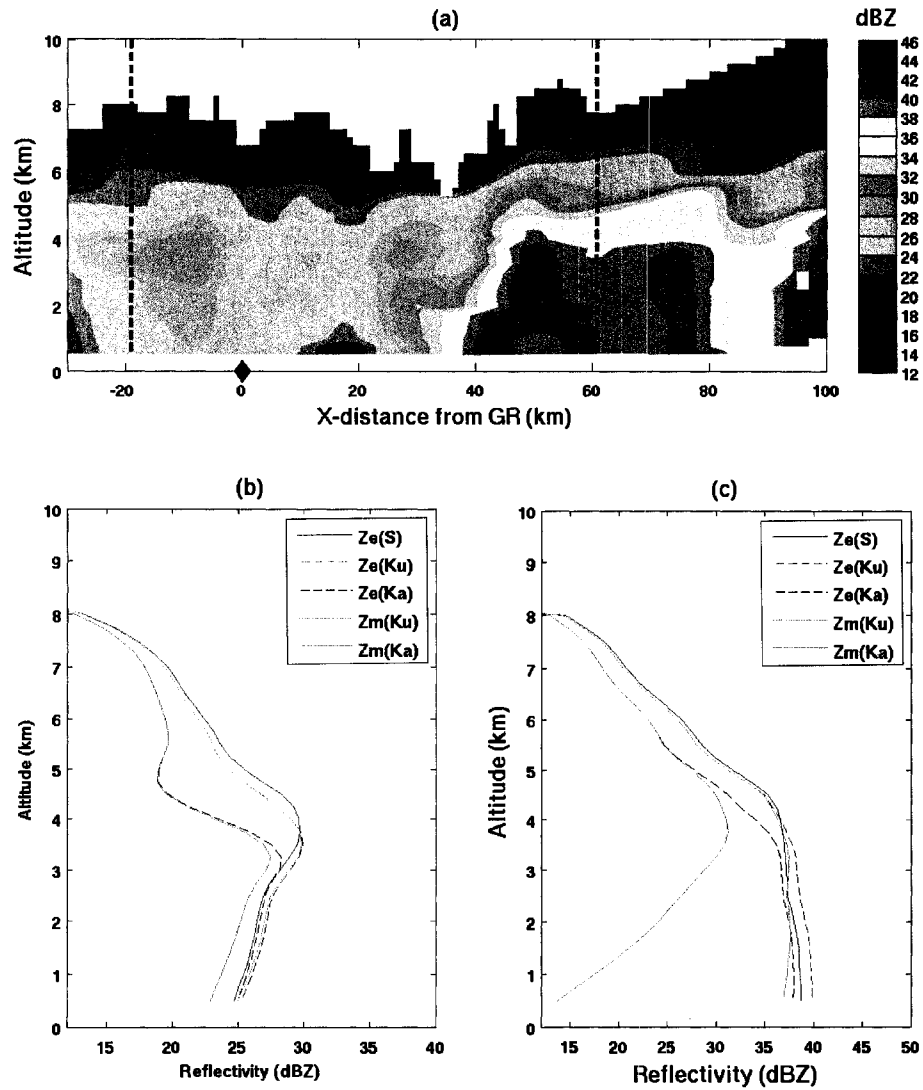


Figure 6.19: The vertical profiles of reflectivity: (a) a vertical cross-section of $Z_e(S)$ measurement from KMLB radar; (b) a vertical profile of the $Z_e(S)$, the simulated $Z_e(Ku)$, $Z_m(Ku)$, $Z_e(Ka)$, and $Z_m(Ka)$ for stratiform rain with a bright band, as indicated by the dashed line to the left of (a); (c) similar to (b) for the convective rain, as indicated by the dashed line to the right of (a).

Case II. Simulation using KTBW observations

A case of KTBW radar measurement on December 12, 2006, is used for this simulation. An intense radar echo of a squall line was observed on the day of measurement. Figures 6.20 and 6.21 shows horizontal cross-sections of simulated $Z_e(\text{Ku})$ and $Z_e(\text{Ka})$ using $Z_e(\text{S})$ KTBW measurements, respectively. As in the KMLB case, the horizontal cross-sections are shown at three different altitudes—2 km, 4.5 km, and 6 km. The sub figures (a), (c) and (e) show $Z_e(\text{S})$ at the three altitudes, and (b), (d) and (f) show the simulated $Z_e(\text{Ku})$ at the three altitudes. As seen in Fig. 6.20, the $Z_e(\text{S})$ and simulated $Z_e(\text{Ku})$ for all three altitude levels are very similar. This is because Rayleigh scattering dominantly occurs in both channels. On the other hand, the $Z_e(\text{Ka})$ are lower than $Z_e(\text{S})$ for all three altitudes. Again, this is caused by non-Rayleigh scattering in the Ka-band and Rayleigh scattering in the S-band. A very strong attenuation causes a complete extinction of the signal in the squall line at 1 km above the surface, as seen in Fig. 6.22 (e).

Vertical cross-sections of $Z_e(\text{S})$ and the simulated $Z_e(\text{Ku})$, $Z_m(\text{Ku})$, $Z_e(\text{Ka})$ and $Z_m(\text{Ka})$ are shown in Fig. 6.23. The dashed line in Fig. 6.23 (a) shows the location of the vertical cross-section. Figure 6.23 (b), (c), (d), and (e) show vertical cross-sections of $Z_e(\text{Ku})$, $Z_m(\text{Ku})$, $Z_e(\text{Ka})$ and $Z_m(\text{Ka})$, respectively. It is clear from Fig. 6.23 (f) that the attenuation causes the loss of signal in Ka-band at an altitude up to about 2 km above the surface. Two vertical profiles of reflectivity are shown in Fig. 6.24. The locations of the two profiles are marked as the dashed lines in Fig. 6.24 (a), and the plot of the profiles are shown in Fig. 6.24 (b) and (c), respectively. It is clear from the two profiles that the signal in the Ka-band channel is attenuated severely. In this case, the loss of signal occurs at about 2.5 and 3 km above the surface for the profile in (b) and (c), respectively. One implication drawn from this finding is that dual-frequency is inapplicable for this kind of profile; the retrieval method must rely on a single-frequency retrieval algorithm, such as a TRMM-like retrieval algorithm.

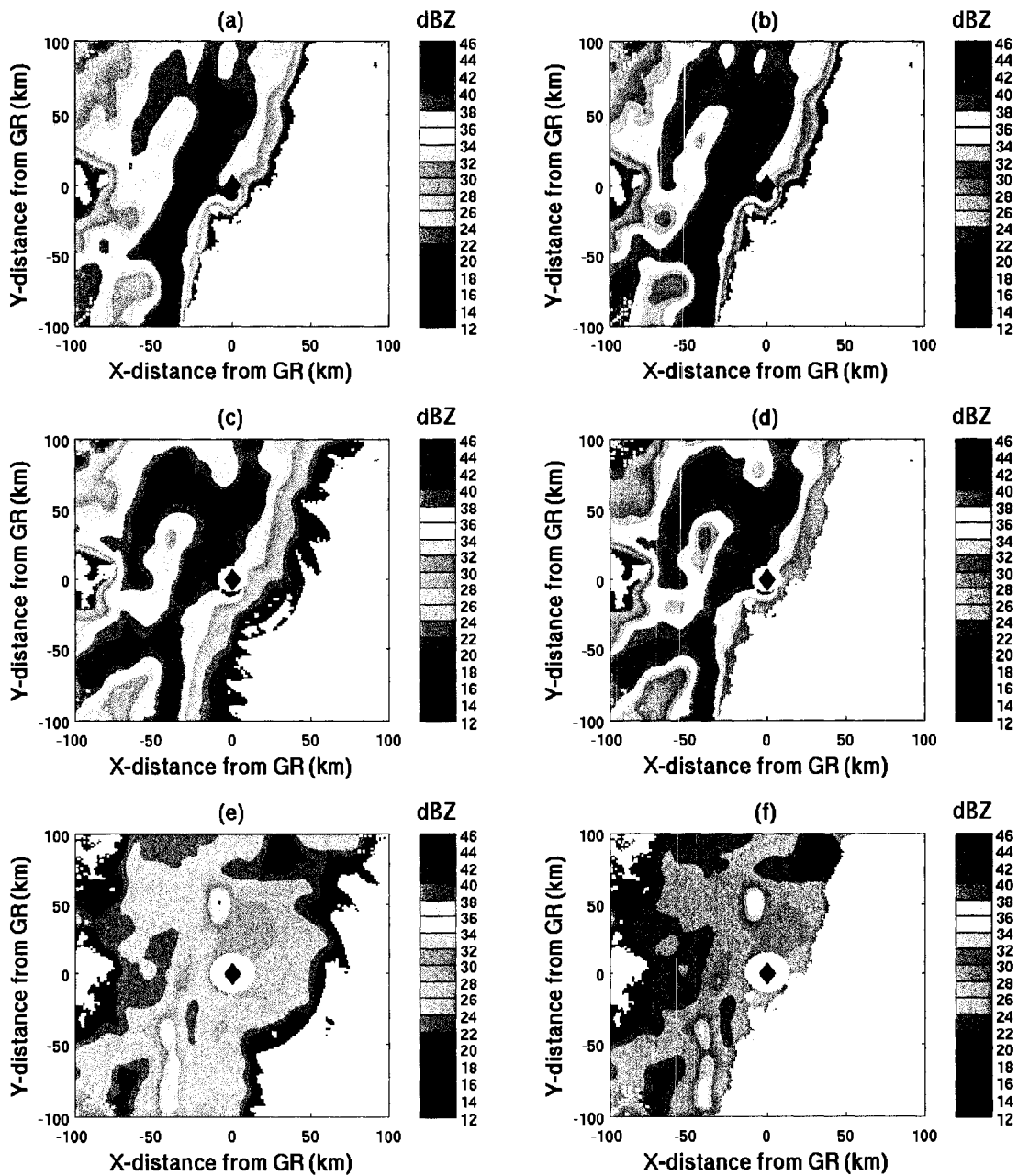


Figure 6.20: The simulation of $Z_e(Ku)$ using KTBW measurements ($Z_e(S)$) for three different height levels above the surface. In (a) and (b) $Z_e(S)$ and $Z_e(Ku)$ at 2 km, (c) and (d) $Z_e(S)$ and $Z_e(Ku)$ at 4.5 km, and (e) and (f) $Z_e(S)$ and $Z_e(Ku)$ at 6 km.

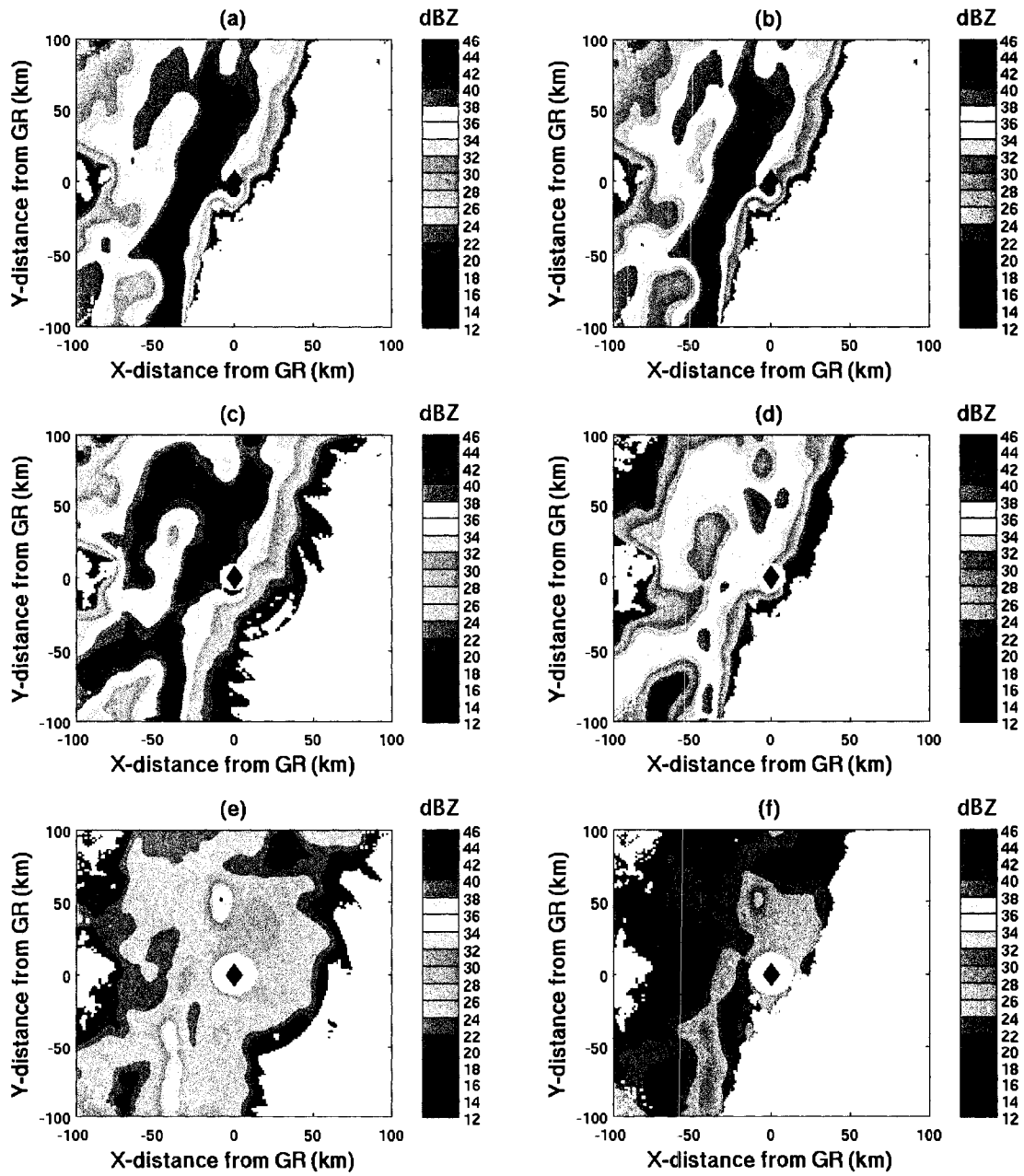


Figure 6.21: The same as Fig. 6.20 for Ka-band.

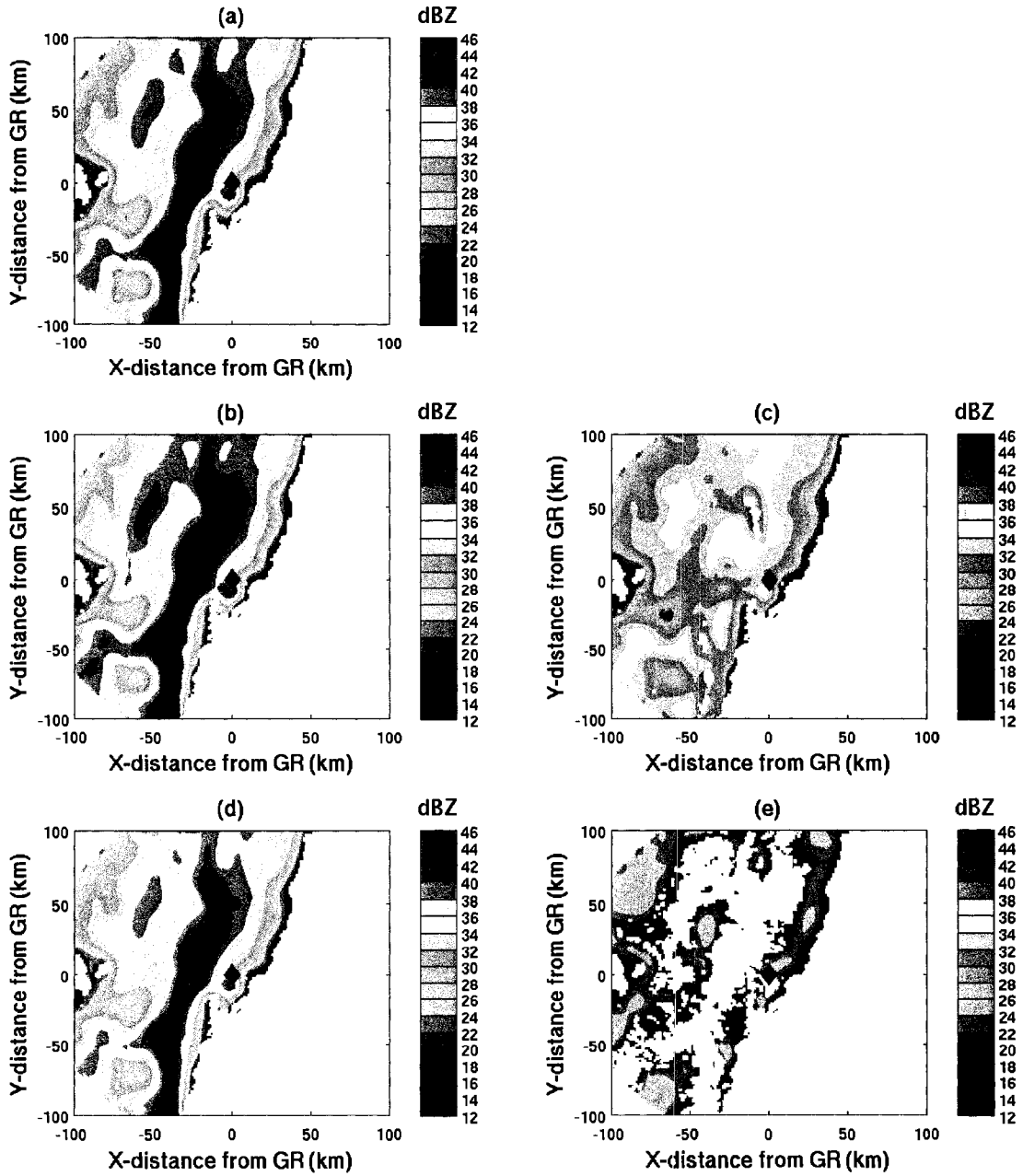


Figure 6.22: The horizontal cross-section of reflectivity at an altitude of 1 km above the surface: (a) the $Z_e(S)$ measurement from KTBW radar; (b) and (c) the simulated $Z_e(Ku)$ and $Z_m(Ku)$, respectively; (d) and (e) the simulated $Z_e(Ka)$ and $Z_m(Ka)$, respectively.

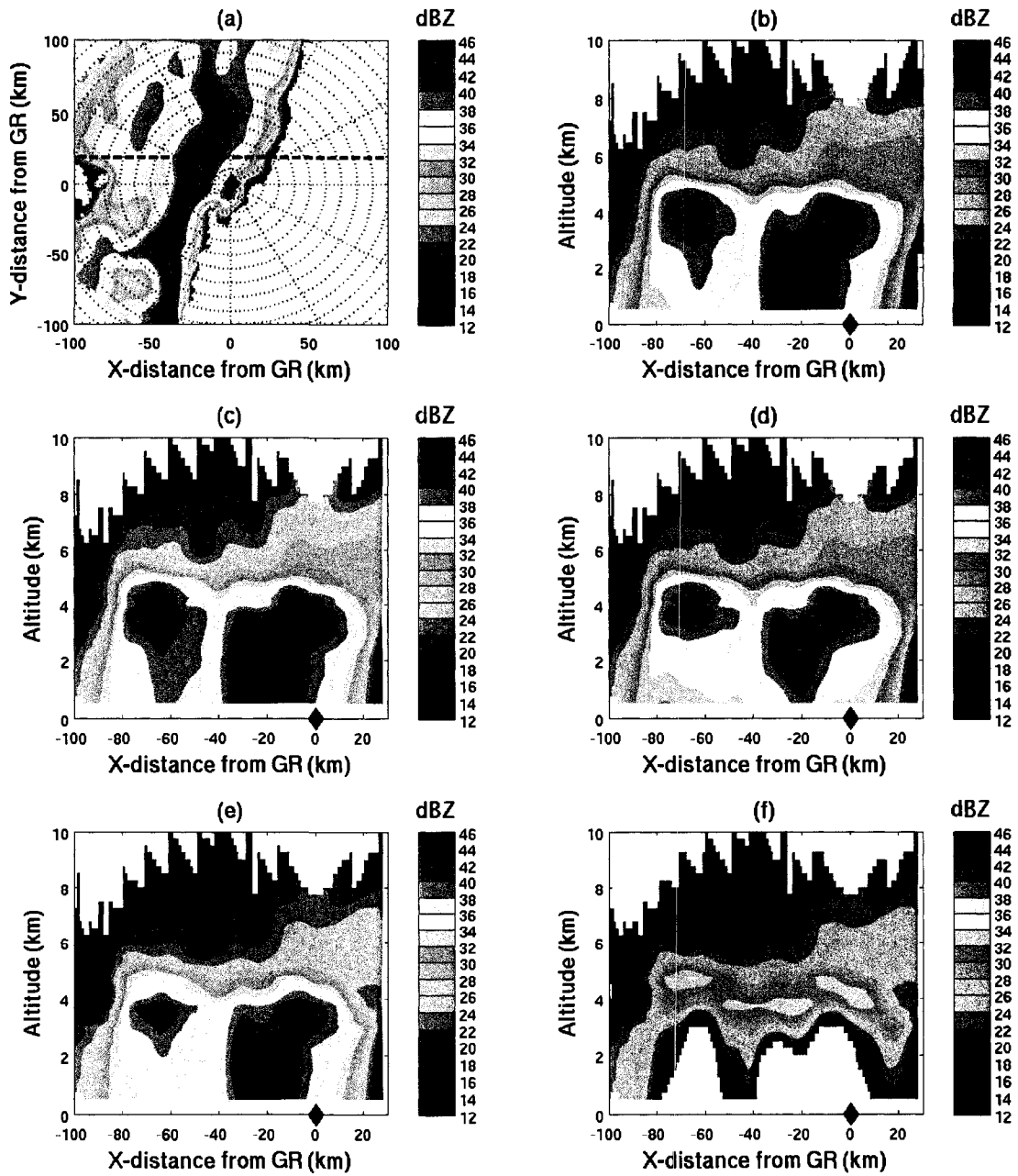


Figure 6.23: The vertical cross-section of reflectivity: (a) and (b) the horizontal and vertical cross-section of $Z_e(S)$ measurement from KTBW radar, respectively; (b) and (c) the vertical cross-section of the simulated $Z_e(Ku)$ and $Z_m(Ku)$, as indicated by the dashed line in (a), respectively; (d) and (e) the vertical cross-section the simulated $Z_e(Ka)$ and $Z_m(Ka)$, respectively, as indicated by the dashed line in (a), respectively.

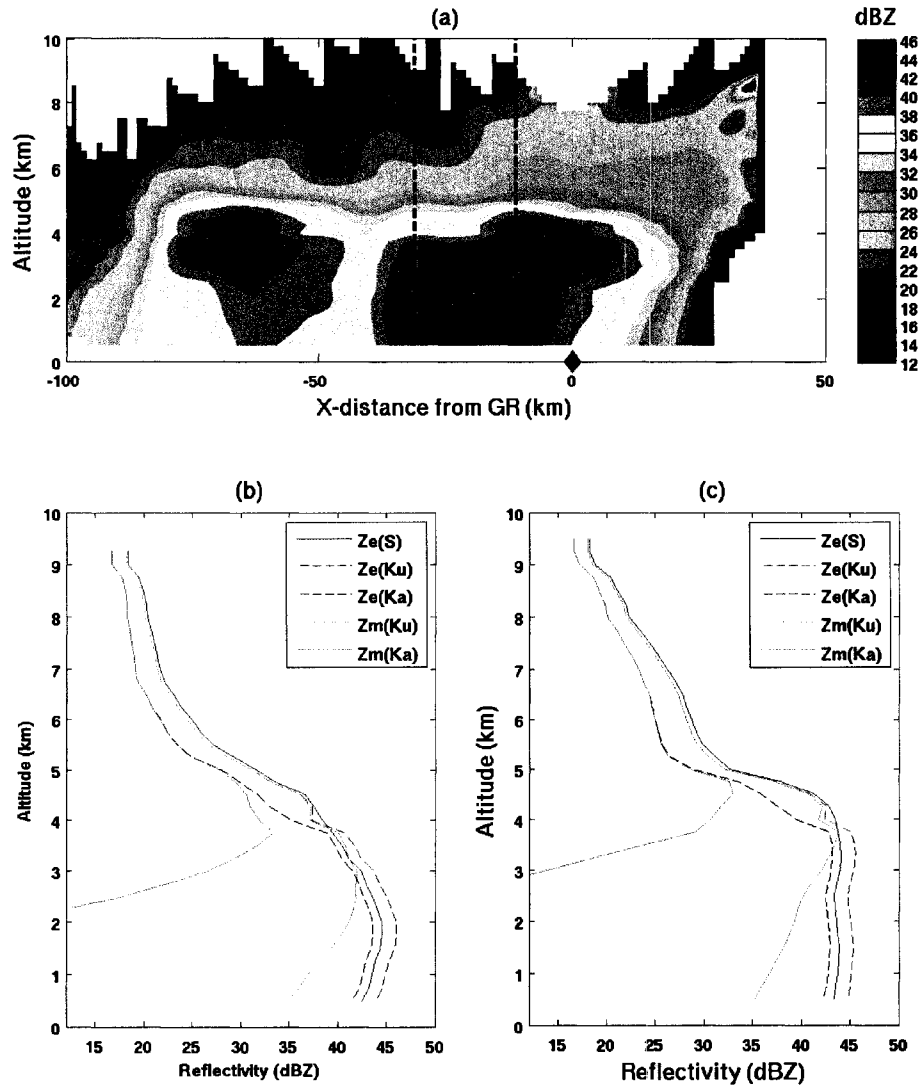


Figure 6.24: The vertical profiles of reflectivity: (a) a vertical cross-section of $Z_e(S)$ measurement from KTBW radar; (b) a vertical profile of the $Z_e(S)$, the simulated $Z_e(Ku)$, $Z_m(Ku)$, $Z_e(Ka)$, and $Z_m(Ka)$ for a stratiform rain with a bright band, as indicated by the dash line to the left of (a); (c) similar to (b) for the convective rain, as indicated by the dashed line to the right of (a).

6.3.2 Case Study: A simulation using dual-polarization ground-based radar measurements

In the GPM era, there will be a number of ground-based dual-polarization radars that will be observing precipitation around the globe. In addition, a major future implementation plan of the NEXRAD is polarization diversity (Crum et al., 1998; Serafin and Wilson, 2000). Therefore, in the future, there will be a greater number of ground-based radars with a dual-polarization capability, especially in the US, that will be measuring precipitation. The key feature of the simulation of DPR observations using dual-polarization ground-based radar measurements is that the phase-height transition (PHT) of precipitation particles, which is very important in the simulation, can be obtained via dual-polarimetric measurements.

In general, dual-polarization ground-based radar can provide five dual-polarization radar measurements, namely, horizontal reflectivity (Z_h), differential reflectivity (Z_{dr}), specific differential phase (K_{dp}), linear depolarization ratio (LDR), and correlation coefficient (ρ_{hv}). The definitions and expressions of these measurements are described in Appendix C. The dual-polarization measurements provide information about the PHT of precipitation particle—whether frozen or partially-melted or completely melted particles (raindrops). Such information is invaluable for the simulation process in that the transition of precipitation particles from the frozen to melted state and then to water drops can be determined more accurately. Lim and Chandrasekar (2005) have shown that the fuzzy logic technique using dual-polarimetric measurements provides a promising result for hydrometeor classification. Determining the PHT of the precipitation along the vertical profiles via the fuzzy logic classification is performed, and the $Z_e(Ku)$, $Z_m(Ku)$, $Z_e(Ka)$ and $Z_m(Ka)$ are simulated corresponding to the fuzzy logic classification results.

Case I. Simulation using CSU-CHILL radar measurements

The CSU-CHILL, a dual-polarization radar, operates at S-band (2.7 GHz). Dual-polarization radar measurements were obtained from the CSU-CHILL radar during a

severe thunderstorm electrification and precipitation study (STEPS) project in 2000. The detailed characteristics of the CSU-CHILL radar can be found in Brunkow et al. (2000). Figures 6.25 and 6.26 show the horizontal and vertical cross-sections of the five dual-polarimetric measurements, respectively.

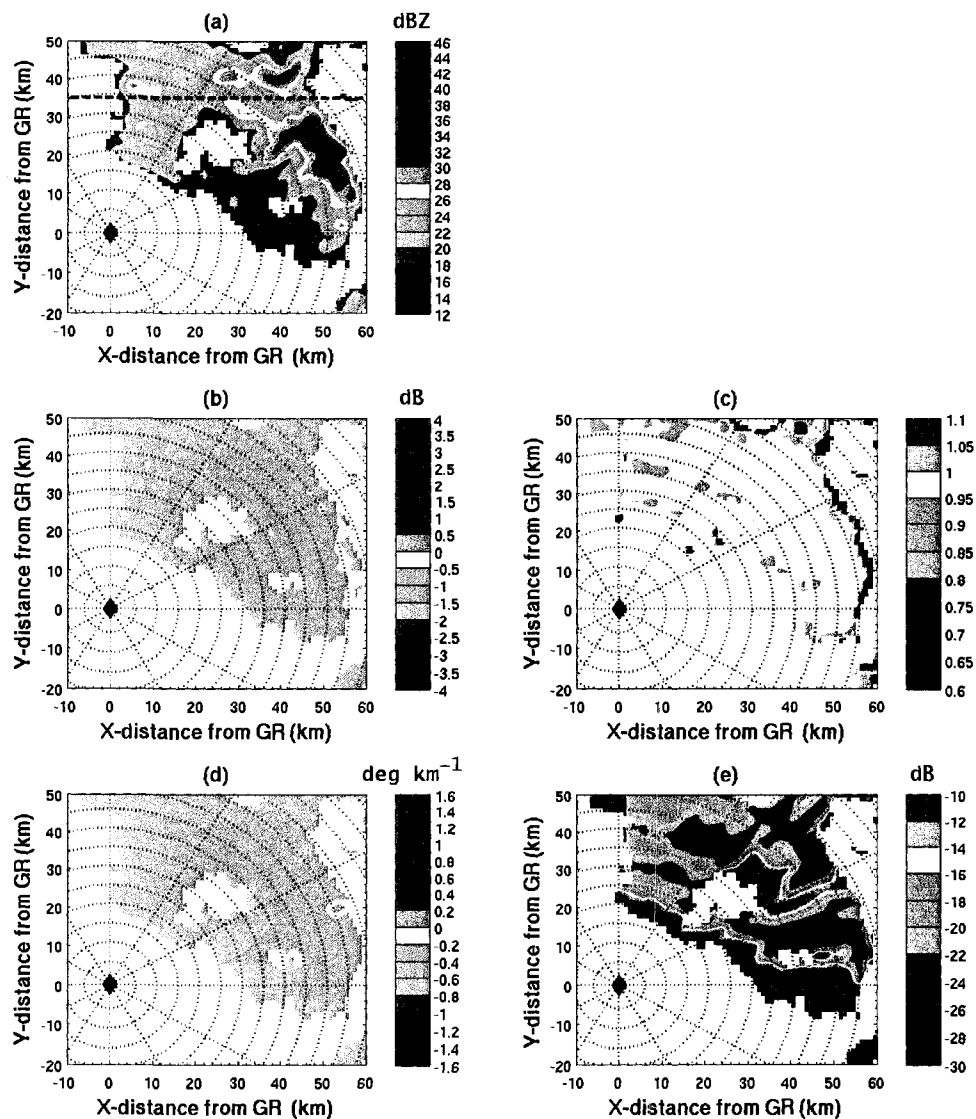


Figure 6.25: The horizontal cross-section of the five dual-polarimetric radar measurements: (a) horizontal reflectivity (Z_h); (b) differential reflectivity (Z_{dr}); (c) correlation coefficient (ρ_{hv}); (d) specific differential phase (K_{dp}), and (e) linear depolarization ratio (LDR).

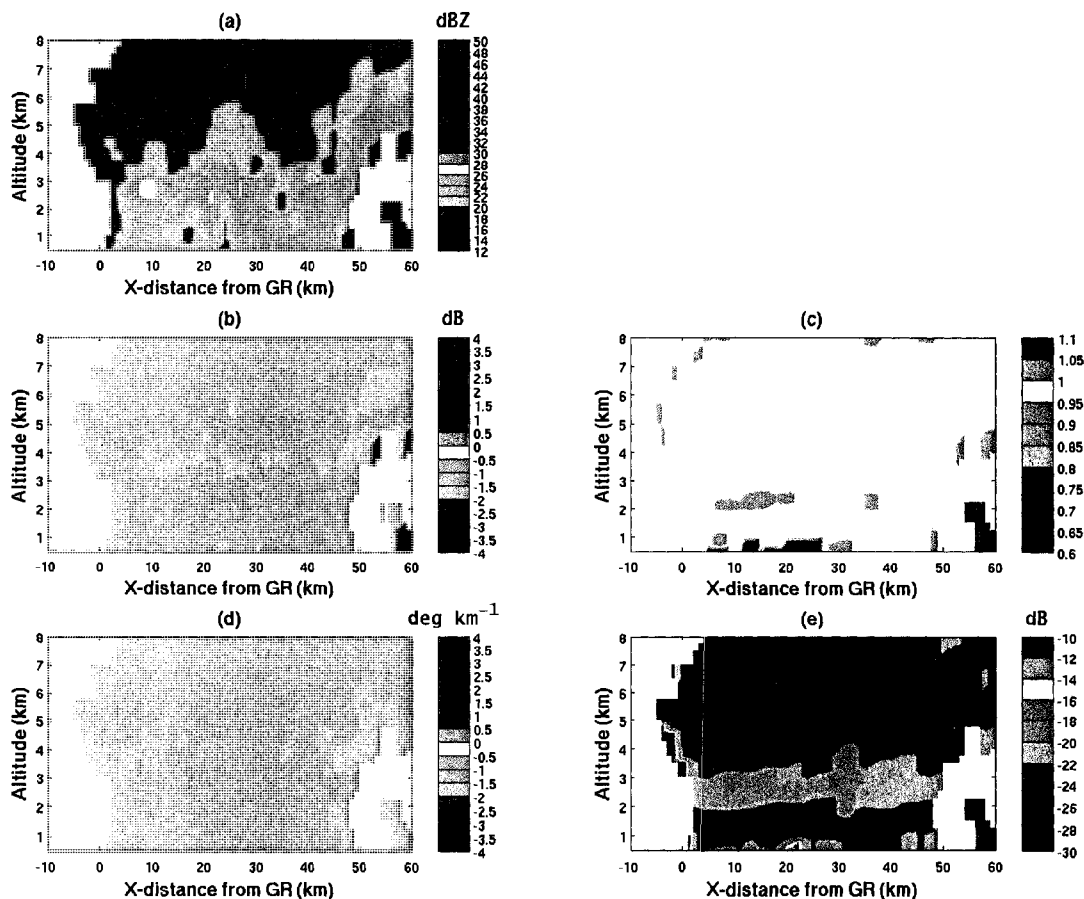


Figure 6.26: The vertical cross-section of the five dual-polarimetric radar measurements: (a) horizontal reflectivity (Z_h); (b) differential reflectivity (Z_{dr}); (c) correlation coefficient (ρ_{hv}); (d) specific differential phase (K_{dp}), and (e) linear depolarization ratio (LDR).

Figure 6.27 shows the horizontal and vertical cross-sections of the reflectivity and the fuzzy hydrometeor classification results. The phase-height transition (PHT) along the vertical profile is clearly defined, as seen in Figure 6.27 (d). Even though the rain types are mostly stratiform in this case, it can be seen that there is a wet graupel within and the top of the melting layer. This may seem to contradict to the model developed in chapter 5. However, as described in section 5.2.1, that graupel is actually snowflakes that are very dense and heavily rimed. Therefore, it is often difficult to make a complete distinction between the two.

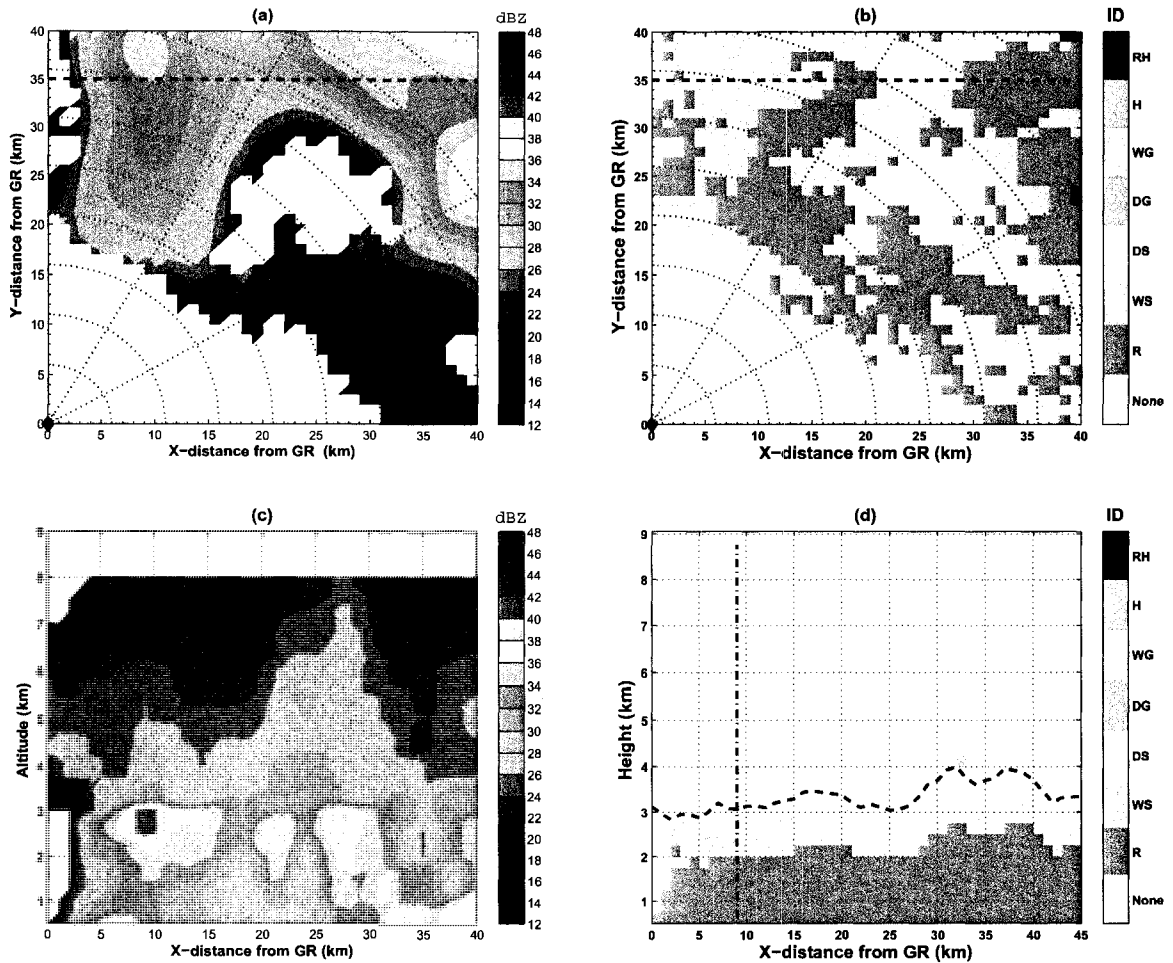


Figure 6.27: (a) The horizontal cross-section of reflectivity, (b) the horizontal cross-section of reflectivity particle type from fuzzy classification results, (c) the vertical cross-section of reflectivity, as indicated by the dashed line in (a), and (d) the vertical cross-section of particle type from fuzzy classification results, as indicated by the dashed line in (b).

The simulation are performed along the vertical profile corresponding to the results of hydrometeor classification. Figure 6.28 (a) shows a vertical cross-section of the hydrometeor classification results (same as 6.27 (d)). Three polarimetric measurements, LDR, ρ_{hv} , and Z_{dr} , are shown in the Fig. 6.28 (b). It can be seen that the melting layer signatures of LDR, ρ_{hv} , and the Z_{dr} measurements, as described in Appendix C are apparent. A vertical profile is selected, as indicated by the dashed line in Fig. 6.28 (a), for a demonstration of the simulation.

Fig. 6.28 (c) shows the vertical profiles of $Z_e(S)$, the simulated $Z_e(Ku)$, and the

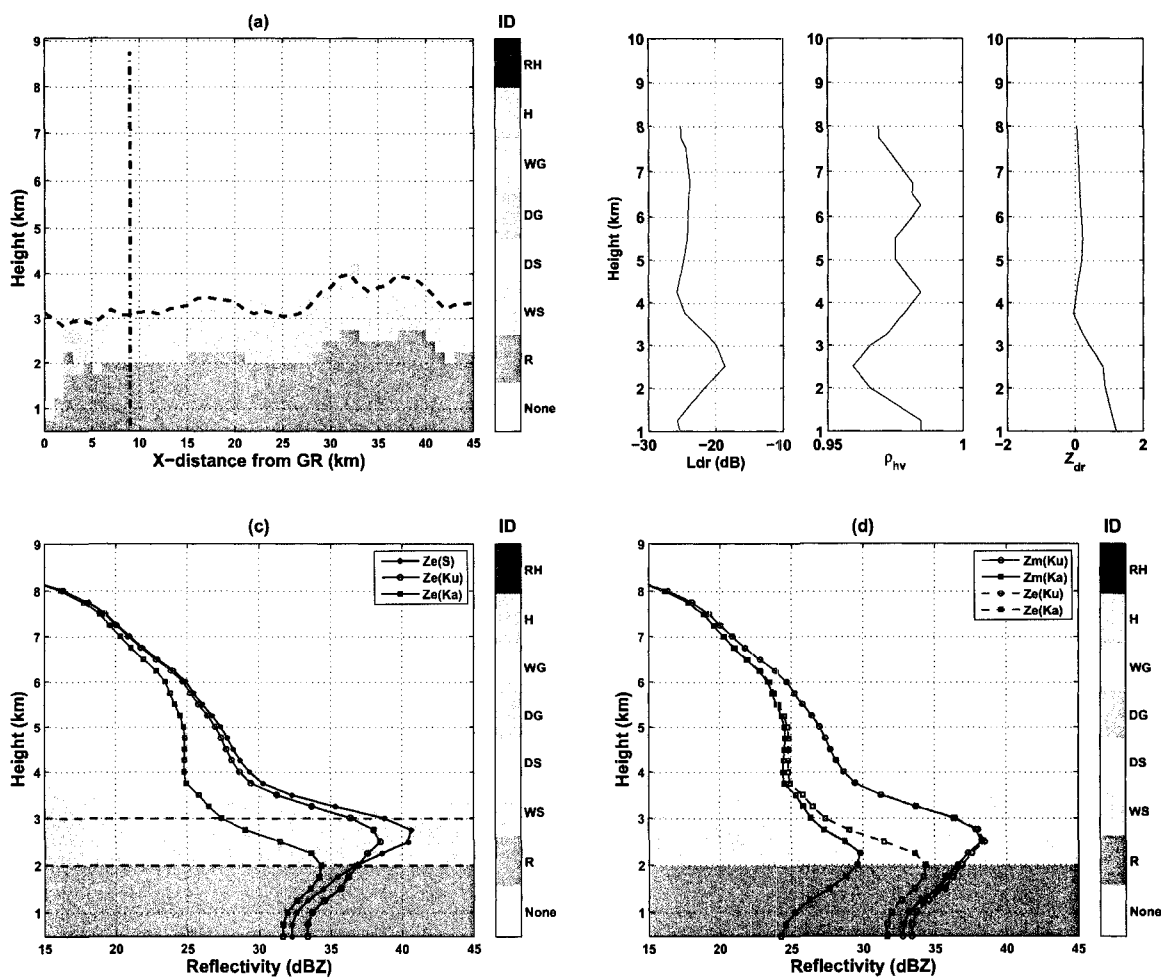


Figure 6.28: (a) The vertical cross-section of hydrometeor type, (b) the vertical profiles of three polarimetric measurements, namely, LDR, ρ_{hv} , and Z_{dr} , (c) the vertical profile of $Z_e(S)$, the simulated $Z_e(Ku)$, and $Z_e(Ka)$, as indicated by the dashed line in (a), and (d) the vertical profile of the simulated $Z_e(Ku)$, $Z_m(Ku)$, $Z_e(Ka)$, and $Z_m(Ka)$, as indicated by the dashed line in (a).

simulated $Z_e(Ka)$ along with the vertical profile of precipitation particles that reflect their phase-height transitions. In this case, the profile is stratiform rain with a bright band with a width of about 1 km. The height of the bright band from the ground and its thickness agree well with the three polarimetric measurements. Note that the bright band peak in this case is quite low when compared with the data from the NEXRAD radar. This is because the measurements were taken in Greeley, Colorado, a relatively high latitude precipitation regime, even though it was

in a summer. Figure 6.28 (d) shows the simulated $Z_e(\text{Ku})$, $Z_e(\text{Ka})$, $Z_m(\text{Ku})$, and $Z_m(\text{Ka})$. It can be seen from 6.28 (d) that there is no attenuation in dry snow region in Ku-band, whereas a small attenuation about 1 dB is observed in Ka-band. In the bright band the attenuation is found to be about 5 dB in Ka-band and a fraction of dB in Ku-band. Also, there is no sharp increase of reflectivity in the bright band for Ka-band channel. Since the rain region of the profile is only 2 km above the ground, even though there is an intense convective rain, a strong attenuation by raindrops is unlikely to cause an extinction of the signal. Therefore, dual-frequency retrieval algorithms are always applicable for this precipitation regime.

6.4 Summary and Conclusions

A simulation of Ku- and Ka-band radar observations using TRMM-PR observations and ground-based radar measurement has been presented. The microphysical models along the vertical profile of precipitation developed in Chapter 5 are used in the simulation. A methodology on generation of precipitation observations that would be “seen” by the Ka-band (35.6 GHz) using the TRMM-PR (Ku-band (13.6 GHz)) observation is demonstrated. The actual and the observed reflectivity in Ka-band are generated based on a precipitation event observed by the TRMM-PR. The horizontal and vertical cross-sections of the simulated Ka-band reflectivity are discussed and compared with those in the Ku-band. The simulation results show that the effect of attenuation along the vertical profiles are apparent in Ka-band when examining the simulation results. At some altitudes, because the attenuation in the rain region in Ka-band is very severe, there is a loss of signal. In this simulation, the loss of signal in Ka-band is observed at the altitude as high as 3 km. The simulation results also show that attenuation by precipitation medium above the melting layer is very small. However, in the melting layer the attenuation can be as high as 10 dB, given a melting layer thickness of 1 km. The attenuation in convective rain profiles appears to be more severe than that in stratiform rain.

Simulation of the Ku-and Ka-band observation using S-band ground-based radar measurement is also presented. The simulations are performed by using both single-polarization and dual-polarization measurements. Measurements of the single-polarization radar are obtained from NEXRAD radar measurements. Two precipitation events from two NEXRAD radar measurements are used in the simulation. The results of the simulation show that the simulated $Z_e(\text{Ku})$ are not much different from $Z_e(\text{S})$ because of the influence of the Rayleigh scattering in both channels. The simulated $Z_e(\text{Ka})$ are different from $Z_e(\text{S})$ and the simulated $Z_e(\text{Ku})$, resulting from dominant non-Rayleigh scattering in Ka-band and dominant Rayleigh scattering in S- and Ku-band. The simulated $Z_m(\text{Ku})$ and $Z_m(\text{Ka})$ are much different due to the attenuation effect.

Since the phase-height transition of the precipitation particle is very important when performing the volume simulation of the precipitation, availability of the PHT information enhances the accuracy of the simulation. The information of PHT along the vertical profiles was obtained via the particle type classification from dual-polarization radars. The simulation of Ku- and Ka-band observations using dual-polarization measurements obtained from the CSU-CHILL radar are performed. Since melting layer of this precipitation regime is quite low, rain column is shorter compared to the NEXRAD data shown here (data from Florida). The simulation results suggested that a strong attenuation from rain is unlikely to cause a loss of signal at the altitude close to the ground, even for an intense convective rain. Therefore, dual-frequency retrieval algorithms may mostly applicable in this precipitation regime.

CHAPTER 7

TROPICAL STORMS

7.1 Introduction

Until recently, the contribution of the earth-based radar systems, including ground-based and airborne radars, to the observation of precipitation over ocean has been quite rare, occurring only on a small, local scale. The observation of precipitation on a global scale by the TRMM-PR has enabled a large scale study of precipitation over ocean, especially tropical storms. The three-dimensional downward-looking observation characteristic of the TRMM-PR makes it possible to study the vertical structure of tropical storms. This chapter is dedicated to an extensive study of tropical storms in terms of the vertical structure of reflectivity, microphysics and rain rate relations, and the simulation of Ka-band radar observations.

Tropical storms, including hurricanes, typhoons, and cyclones, occur in the North Atlantic, Northwest Pacific, and South Indian Ocean, respectively. Data collected by TRMM-PR in three years (2000, 2002 and 2003) were used to study the vertical profile of reflectivity (VPR) of tropical storms. A total of 105 storms were studied. Data from 2001 were excluded because of orbit transition during that time. The SOM method was used to classify the vertical profile into a number of characteristic profiles. Convective rain type and the stratiform structure of storms were examined. The classification was used to build statistics of bright band profile characteristics in terms of bright band (BB) peak height, reflectivity at the peak of BB, the thickness

of BB, and BB sharpness index. A comparative study year-by-year of hurricanes, typhoons, cyclones, and generic ocean storms revealed similarities and systematic differences among them and those result are presented here. In addition, raindrop size distribution parameters were also estimated. A relation between rainfall rate and D_o and N_w are demonstrated and compared with relations reported in the literature. The chapter ends with a demonstration of a simulation of Ka-band radar observation of a tropical storm using TRMM-PR observations.

7.2 Result of VPR Classification of Storms

The reflectivity observation of the vertical rain profile from TRMM-PR is used as input data to the SOM classification technique. The data consist of vertical profiles of reflectivity (VPR) of hurricanes over the North Atlantic region, typhoons in the Northwestern Pacific region, and cyclones in the South Indian Ocean collected from the years 2000, 2002, and 2003. The three regions where vertical profiles were obtained are shown in Fig. 7.1. In total, 18 hurricanes, 41 typhoons, and 46 cyclones were studied. Each profile has 41 bins, which represent the TRMM-PR observation reflectivity for rain profiles from ground to heights up to 10 km with 250 m vertical resolution. All SOM algorithm maps were linearly initialized. A comparative study was performed by plotting the same storm type from different years side by side and discussing systematic similarities and differences. Comparison of vertical profiles for different storm types in the same year is also discussed.

7.2.1 Comparison of storms between years

A. Simple comparison

In order to demonstrate the application of the procedures developed in this work, a simple demonstration of the VPR classification of hurricanes, typhoons, and cyclones for the three years are presented in Figs. 7.2 to 7.4. The figures show the VPR classification for the hurricanes, typhoons, and cyclones, respectively. Of the four

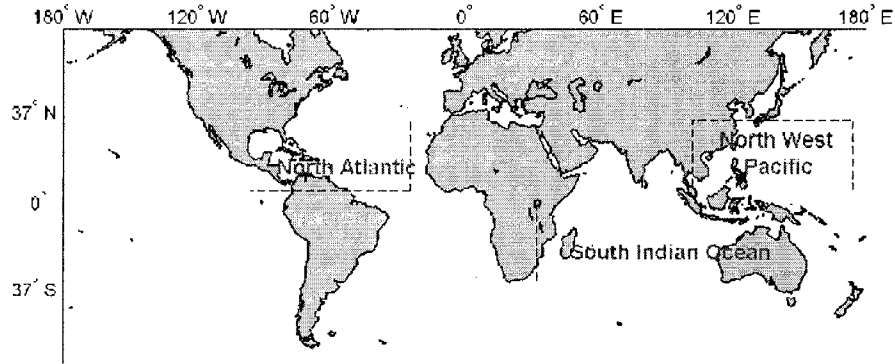


Figure 7.1: Illustrating the regions (North Atlantic, Northwestern Pacific, and South Indian Ocean) where vertical structure profiles of hurricanes, typhoons and cyclones, respectively, were collected.

classes of profiles, the strongest reflectivity vertical profile is class (1,2). In general, hurricanes in 2002 has strongest VPR, whereas cyclones have the strongest VPR in 2000, and the VPR of typhoons is of similar strength over the three years. A feature that is common for the three storm types of all years is that the percentage occurrence of the strongest VPR is smallest.

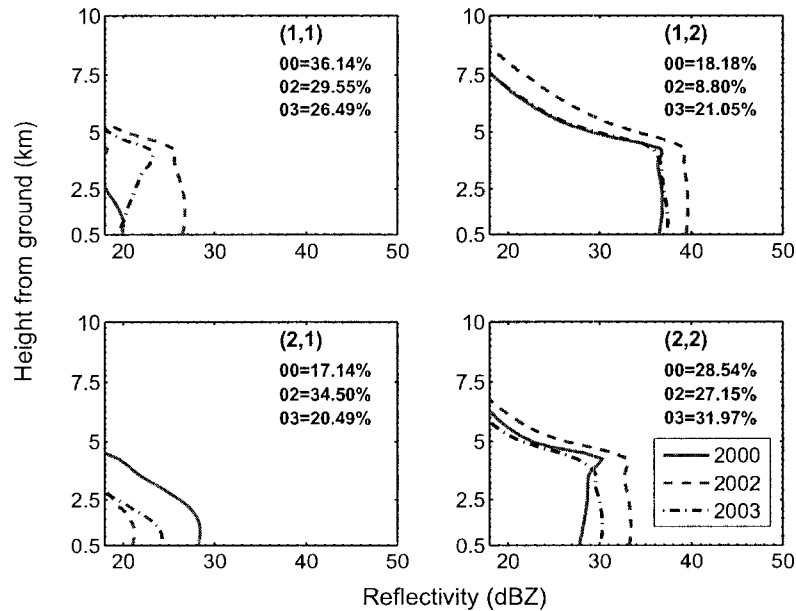


Figure 7.2: SOM (2x2) classification result of hurricanes. In each subfigure the solid line, dashed line, and dash-dot line represent the years 2000, 2002, and 2003, respectively. Percentage of occurrence for each class is also presented.

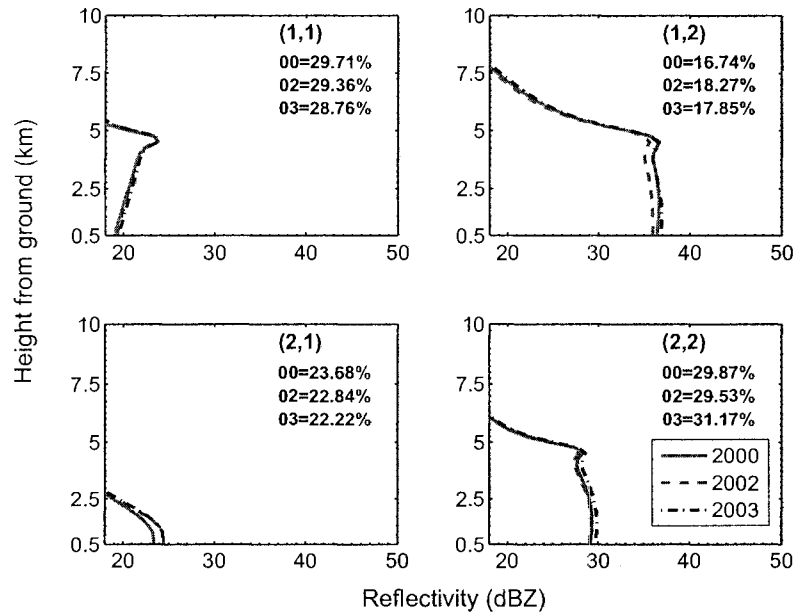


Figure 7.3: Same as Fig. 7.2 for typhoons.

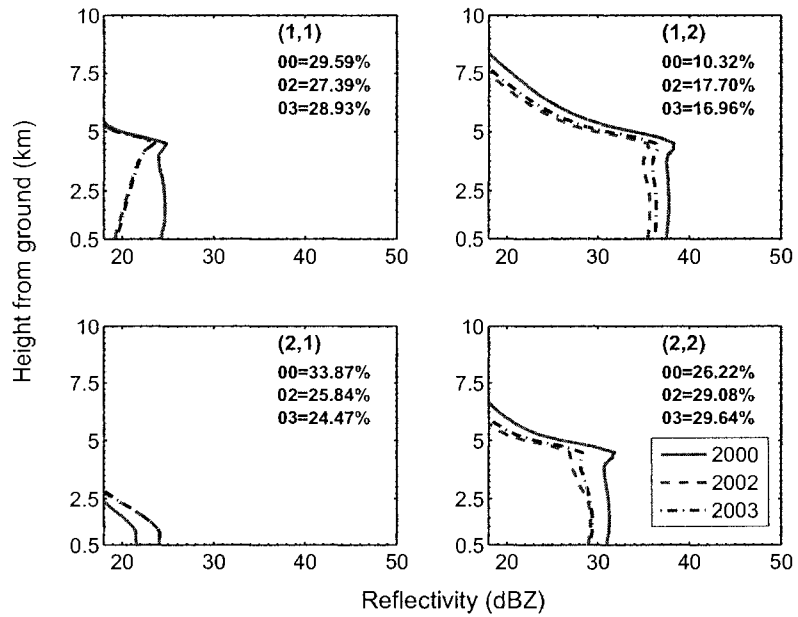


Figure 7.4: Same as Fig. 7.2 for cyclones.

B. Study of hurricane, cyclones, and typhoons with convective stratiform separation

In this analysis, all VPR samples are primarily categorized into two rain types—convective and stratiform. Then, a 2x2 SOM is applied to each rain type. It is well known that bright band (BB) occurs at various altitudes. Therefore, to accurately classify the vertical reflectivity structure of BB, the input of stratiform VPR is prepared as a function of height using the height of the BB peak as the reference—1.5 km above and below the height of the BB peak.

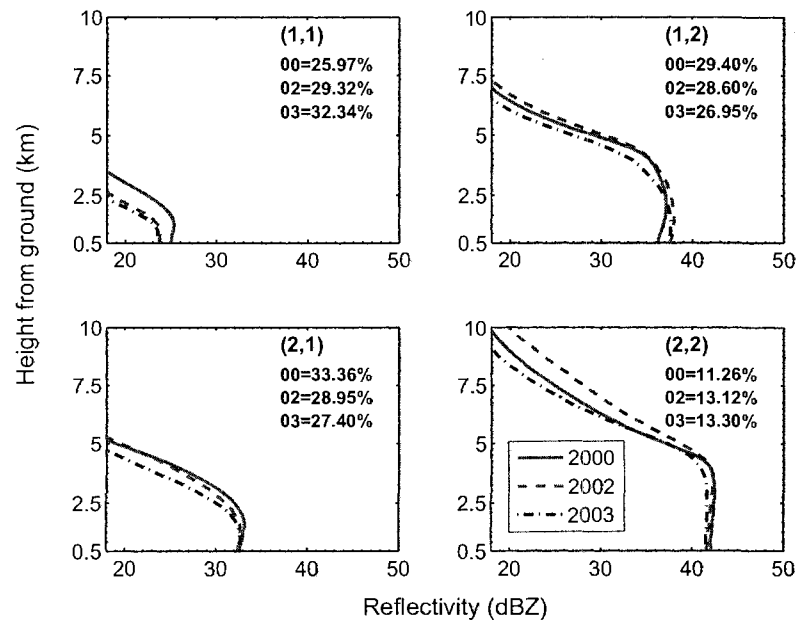


Figure 7.5: SOM (2x2) classification results of convective rain type of hurricanes. In each subfigure the solid line, dashed line, and dash-dot line represent the years 2000, 2002, and 2003, respectively. The percentage of occurrence for each class is also presented.

The resultant characteristic profiles of convective and stratiform rain type are shown in Figs. 7.5 to 7.7 and 7.8 to 7.10, respectively. From Fig. 7.5 to 7.7, it appears that the reflectivity of characteristic profiles in year 2000 (solid line) seem to be comparable to or stronger than other years (2002 in dashed line and 2003 in dash-dot line) for all classes. It is fairly obvious for convective rain profiles in the cyclone case, especially in class (2,2), that the VPR in 2000 is about 5 dBZ stronger than the

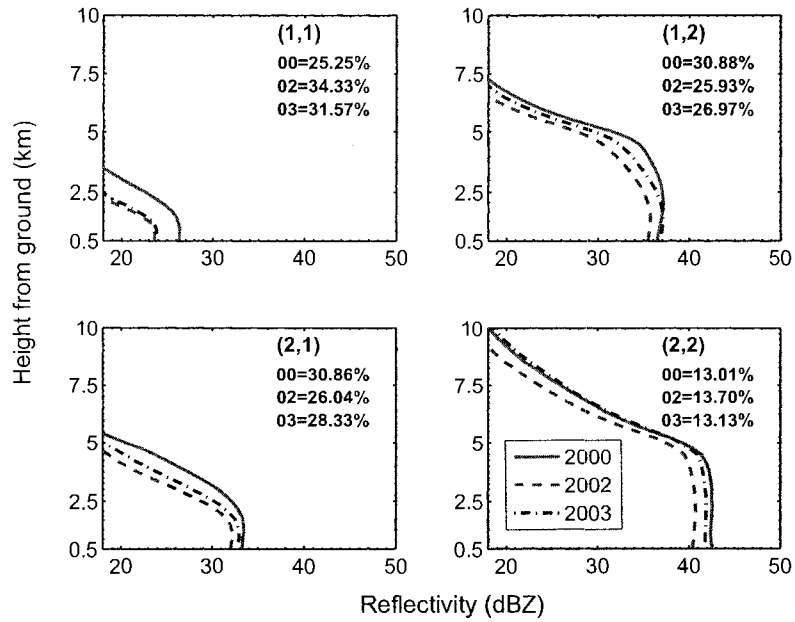


Figure 7.6: Same as Fig. 7.5 for typhoons.

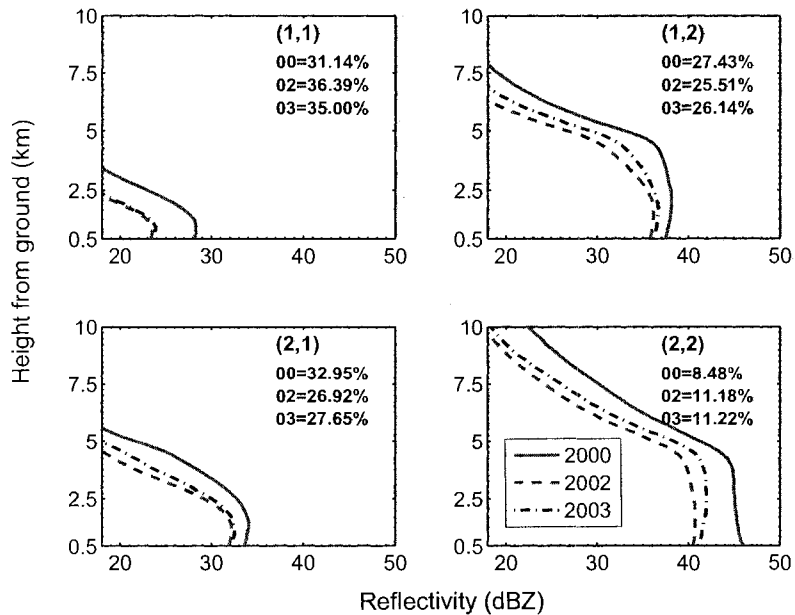


Figure 7.7: Same as Fig. 7.5 for cyclones.

others (see Fig. 7.7). Similarly to those in Figs. 7.2 to 7.4, regarding the frequency of occurrence, it can be seen that less-frequent occurrences happen in the class with the stronger reflectivity while the more frequent occurrences can be observed in the class with weaker reflectivity. For the stratiform rain type classification, shown in Figs.

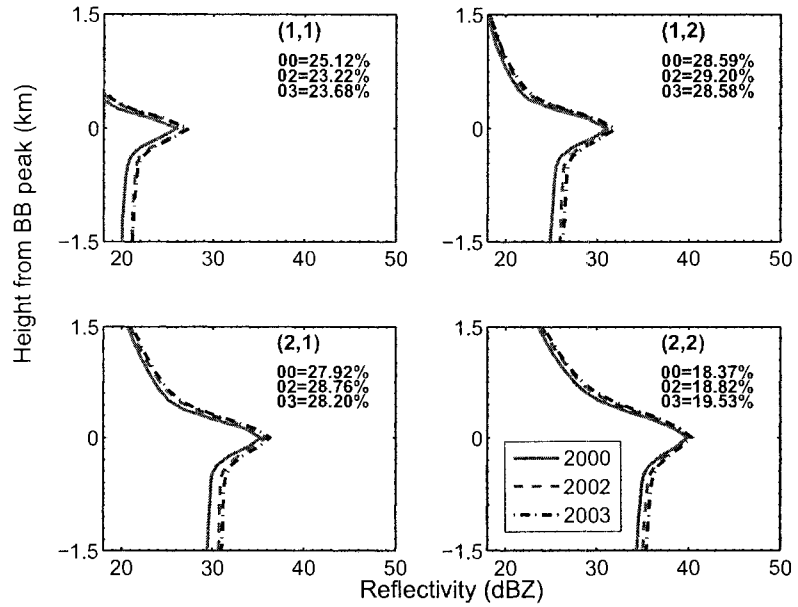


Figure 7.8: SOM (2x2) classification results of the stratiform rain type of hurricanes. In each subfigure the solid line, dashed-line and dash-dot line represent the years 2000, 2002 and 2003, respectively. The percentage of occurrence for each class is also presented.

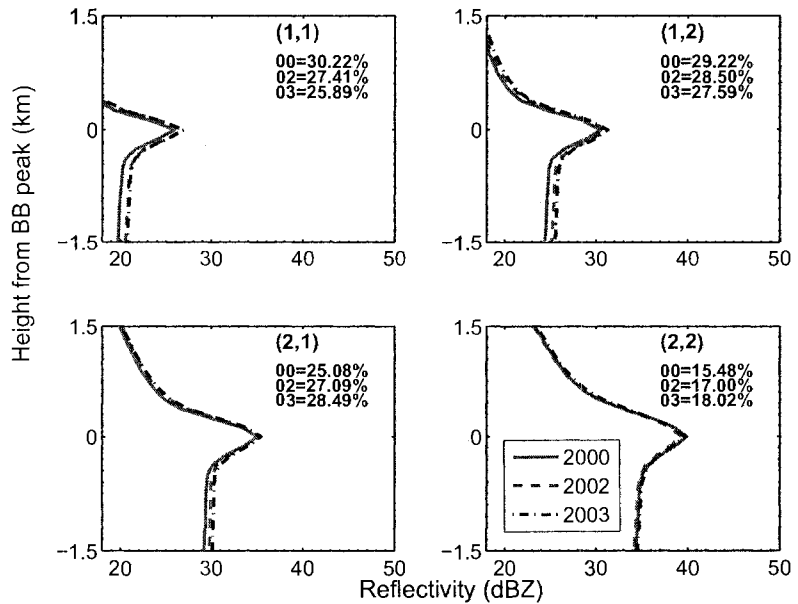


Figure 7.9: Same as Fig. 7.8 for typhoons.

7.8 to 7.10, the resultant VPR for all years and for all classes shows no significant difference.

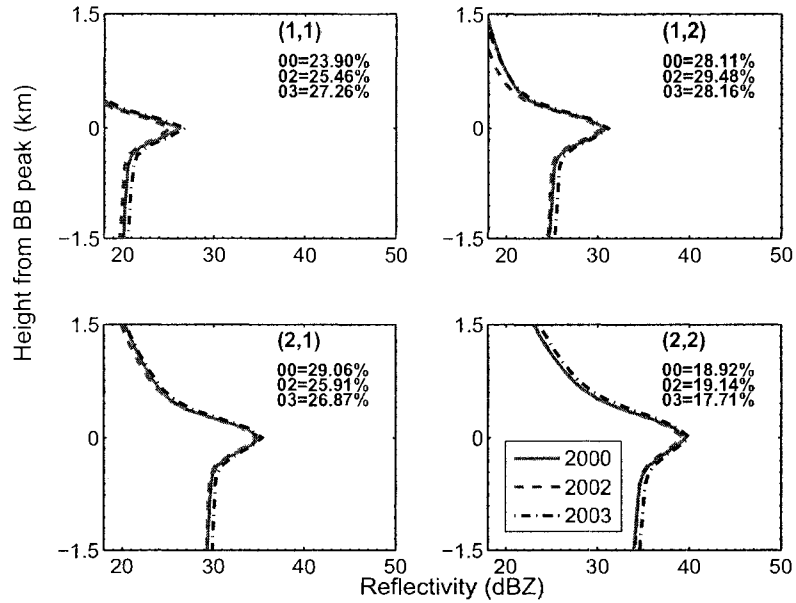


Figure 7.10: Same as Fig. 7.8 for cyclones.

7.2.2 Same-year storms comparison study

Hurricanes (H), typhoons (T), cyclones (C), and generic oceanic storm (O) in the same year are classified and resultant VPR characteristics are plotted together for the comparative study purpose of VPR for different storms in the same year. The classification result of profiles without rain type separation is only presented here in Figs. 7.11 to 7.13 .

The results show that in year 2000, the characteristic VPR of hurricanes, typhoons, and cyclones is slightly different in classes (1,2) and (2,2), whereas the differences become more noticeable in class (1,1), in which the strongest VPR comes from cyclones, as indicated by the dot-dash line; and in class (2,1) in which the strongest VPR comes from hurricanes, as indicated by the solid line. The year 2002 demonstrates different features from 2000. As seen in Fig. 7.12, hurricanes have noticeably stronger VPR than those of cyclones and typhoons in most classes. All characteristic VPRs of typhoons and cyclones are slightly different. In year 2003, VPR of all storms in all classes are comparable.

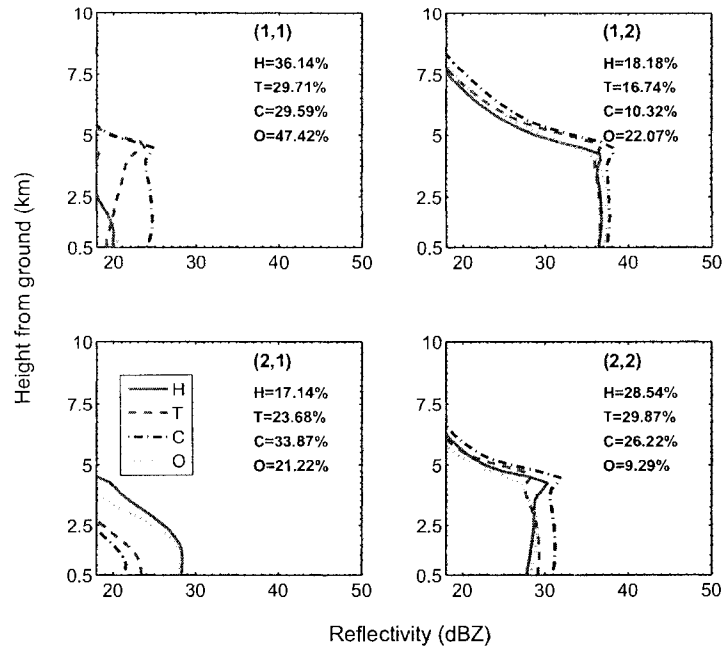


Figure 7.11: SOM (2x2) classification result without rain-type separation in year 2000. In each subfigure, the solid line, dashed line, and dash-dot line represent hurricanes (H), typhoons (T), and cyclones (C), respectively. H, T and C indicate percentage of occurrence in each class.

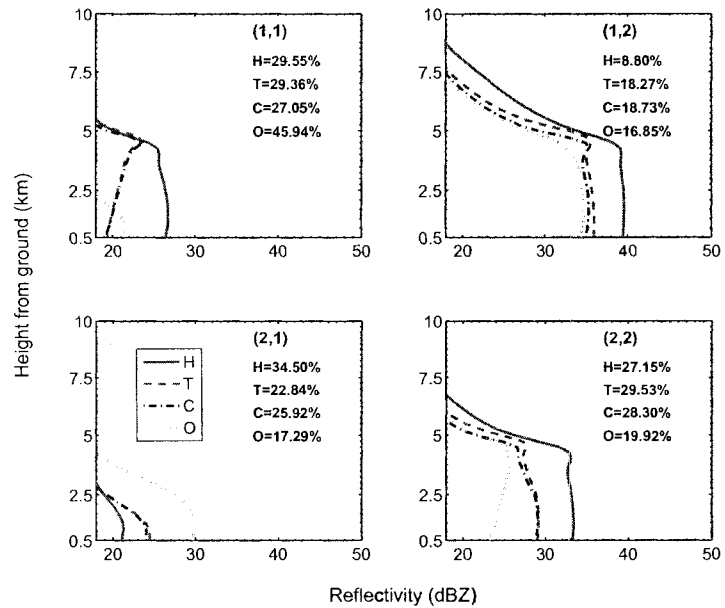


Figure 7.12: Same as Fig. 7.11 for year 2002.

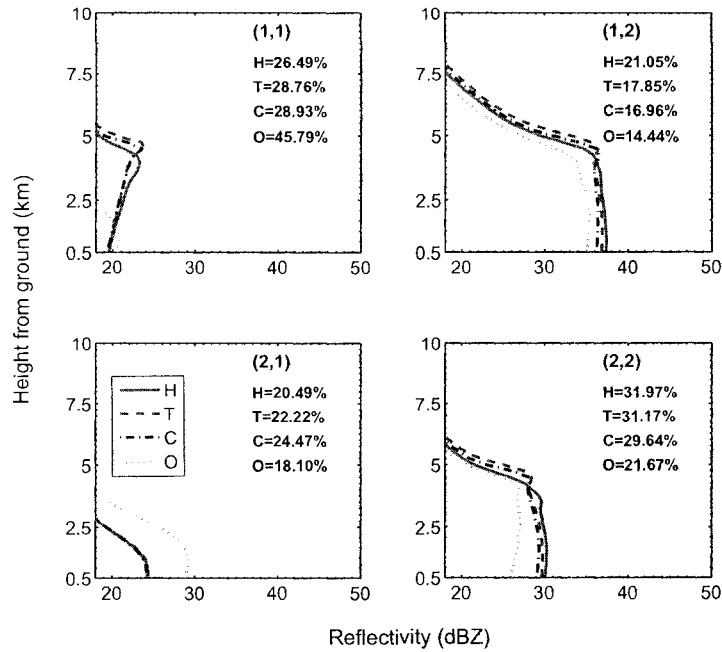


Figure 7.13: Same as Fig. 7.11 for year 2003.

7.3 Study of Bright Band (BB) Properties

An understanding of the bright band (BB) region in the vertical profile of reflectivity is essential for investigating the microphysical process of stratiform precipitation. Therefore, in addition to studying vertical structure, the properties of BB are also examined. Figures 7.14 to 7.16 show the results of studying three properties of bright band—height of BB peak from sea level, BB thickness, and reflectivity of BB peak. To prevent confusion concerning height of the BB peak, it should be noted that the vertical profiles of reflectivity in Fig. 7.8 to 7.10 use the peak of the BB as the reference; it is not the vertical profile from sea level.

Figure 7.14 shows the distribution of height of BB from sea level in hurricane, typhoon, cyclone, and generic oceanic storm in year 2002. From the figure, shapes of height of BB distribution are similar for all storms. However, the peaks occur at slightly different altitudes, with peaking at 4,336 m for hurricanes, and at 4690 m for typhoons. The BB peak of generic oceanic storms is the lowest, at about 3,980

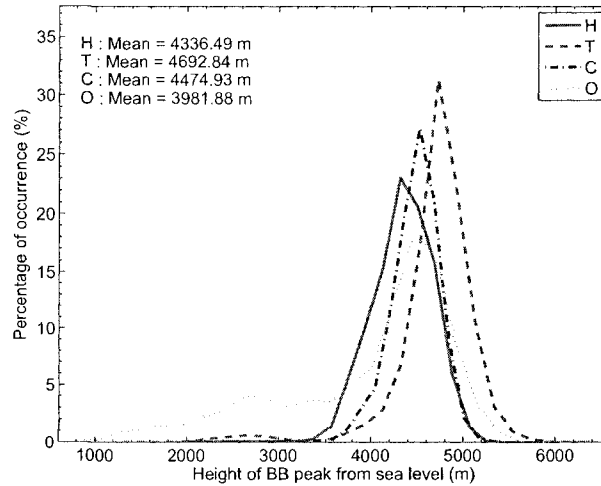


Figure 7.14: Distribution and averaged value of height of BB peak from sea level of hurricane (H), typhoon (T), cyclone (C) and generic oceanic storm (O).

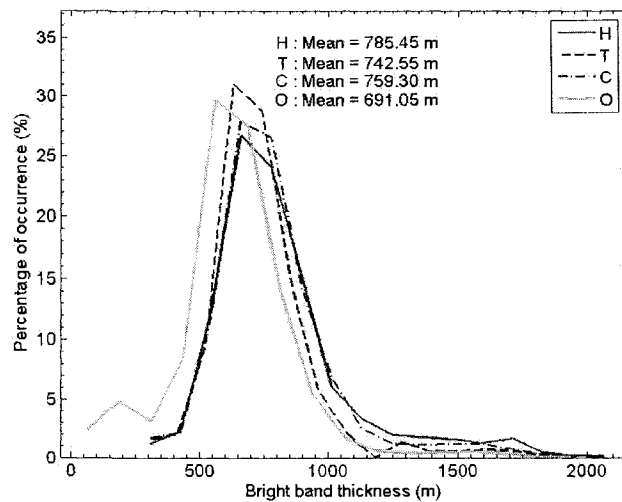


Figure 7.15: Distribution and averaged value of BB thickness of hurricane (H), typhoon (T), cyclone (C), and generic oceanic storm (O).

m from sea level. Figure 7.15 shows that hurricanes have a slightly thicker BB (785 m) than those of typhoons and cyclones; generic oceanic storms have the thinnest BB (690 m). However, the distribution of BB thickness takes a similar shape in all cases. Figure 7.16 shows that reflectivity at the BB peak of hurricanes is about 33 dBZ (about 1 dBZ higher than the other storms).

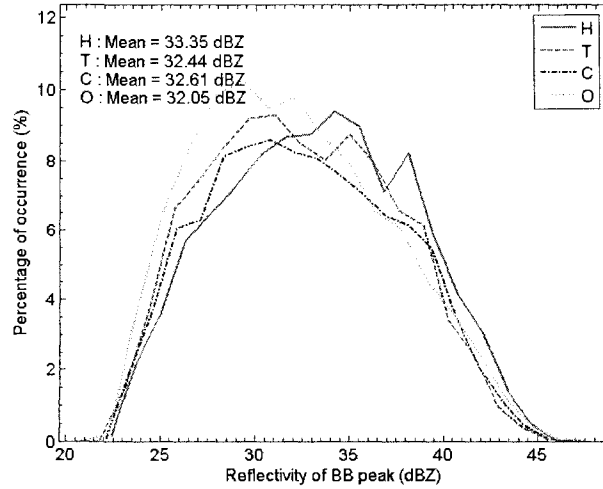


Figure 7.16: Distribution and averaged value of the reflectivity of BB peak of hurricane (H), typhoon (T), cyclone (C), and generic oceanic storm (O).

7.4 Drop Size Distribution Study

The particle size distribution (PSD), as outlined in section 2.2, plays an important role in defining the properties of precipitation (Bringi and Chandrasekar, 2001). The algorithm by Chandrasekar et al. (2005), as described in section 3.4, is used to estimate a vertical profile of drop size distribution (DSD) parameters— D_o and N_w — in the rain region of hurricanes, typhoons, and cyclones in year 2002. A relation between rain rate estimated by TRMM-PR algorithm, as described in section 3.2.2, and the retrieved D_o and N_w based on a gamma DSD are examined and compared with those reported in the literature. Sekhon and Srivastava (1971), hereafter SS, studied a thunderstorm using C-band Doppler radar and suggested relations based on exponential DSD as $D_o = 0.13R^{0.14} \text{ cm}^{-1}$ and $N_o = 0.07R^{0.37} \text{ cm}^{-4}$. Willis and Tattelman (1989), hereafter WT, studied tropical storm data collected by an imaging optical spectrometer and suggested relations based on a gamma DSD as $D_o = 0.097R^{0.158} \text{ cm}^{-1}$ and $N_w = 0.038R^{0.412} \text{ cm}^{-4}$. Note that N_w is the same N_o of an equivalent exponential DSD which has the same rainwater content and D_o as the gamma DSD (Bringi and Chandrasekar, 2001).

7.4.1 Result of D_o and N_w estimate

The distributions of the estimated D_o and N_w for various rain rate intervals for cyclones, typhoons, and hurricanes in year 2002 are shown in Figs. 7.17, 7.18, and 7.19, respectively. Several features common to the three storm types are observed as follows;

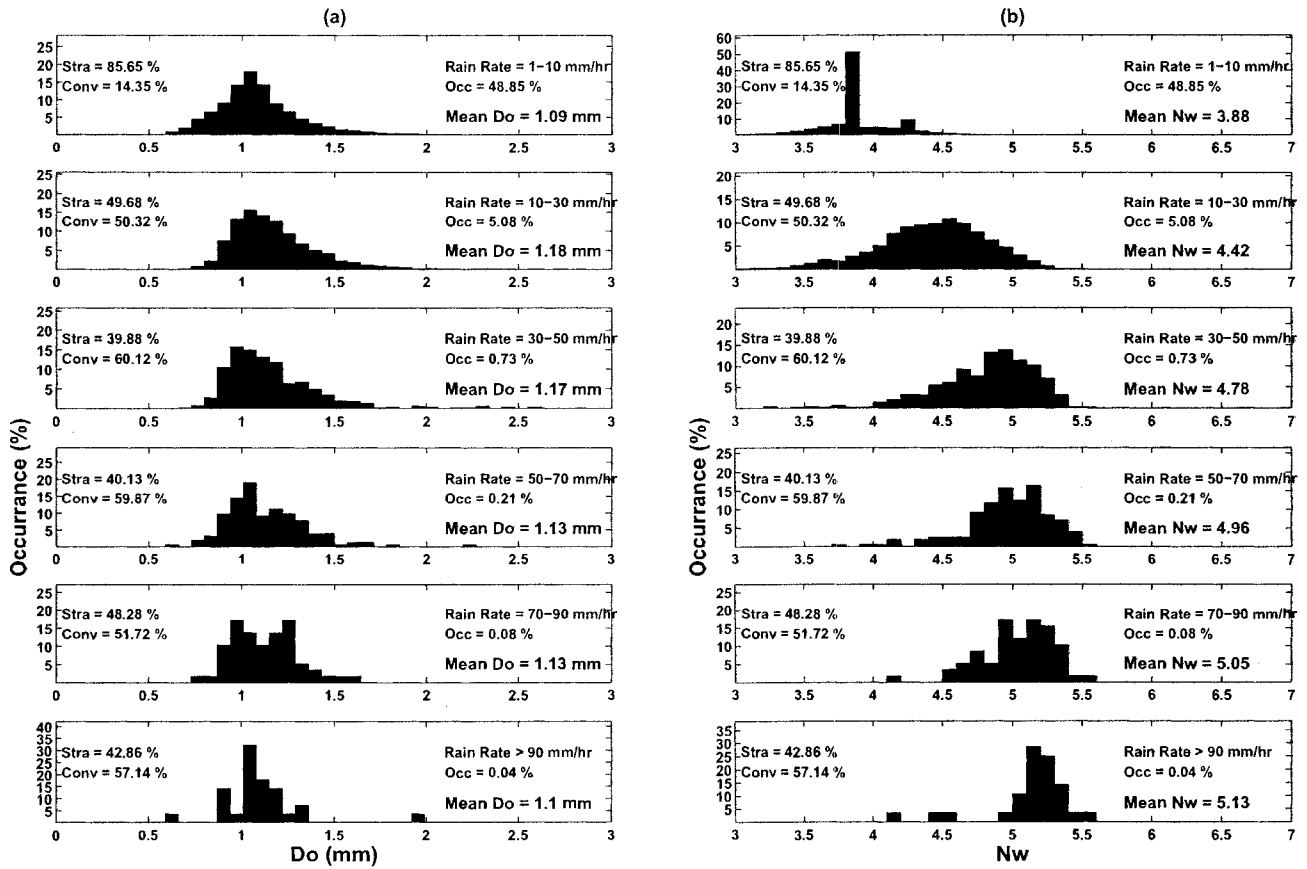


Figure 7.17: Distribution of (a) D_o and (b) $\log_{10}(N_w)$ for various rain rate intervals of cyclones in year 2002.

- The percentage of occurrence for rain rate between 1 - 10 mm hr⁻¹ is highest—about 48% for cyclones, 47% for typhoons, and 54% for hurricanes.
- The 1-10 mm hr⁻¹ are mainly from stratiform rain—about 85% for cyclones, 85% for typhoons, and 83% for hurricanes.

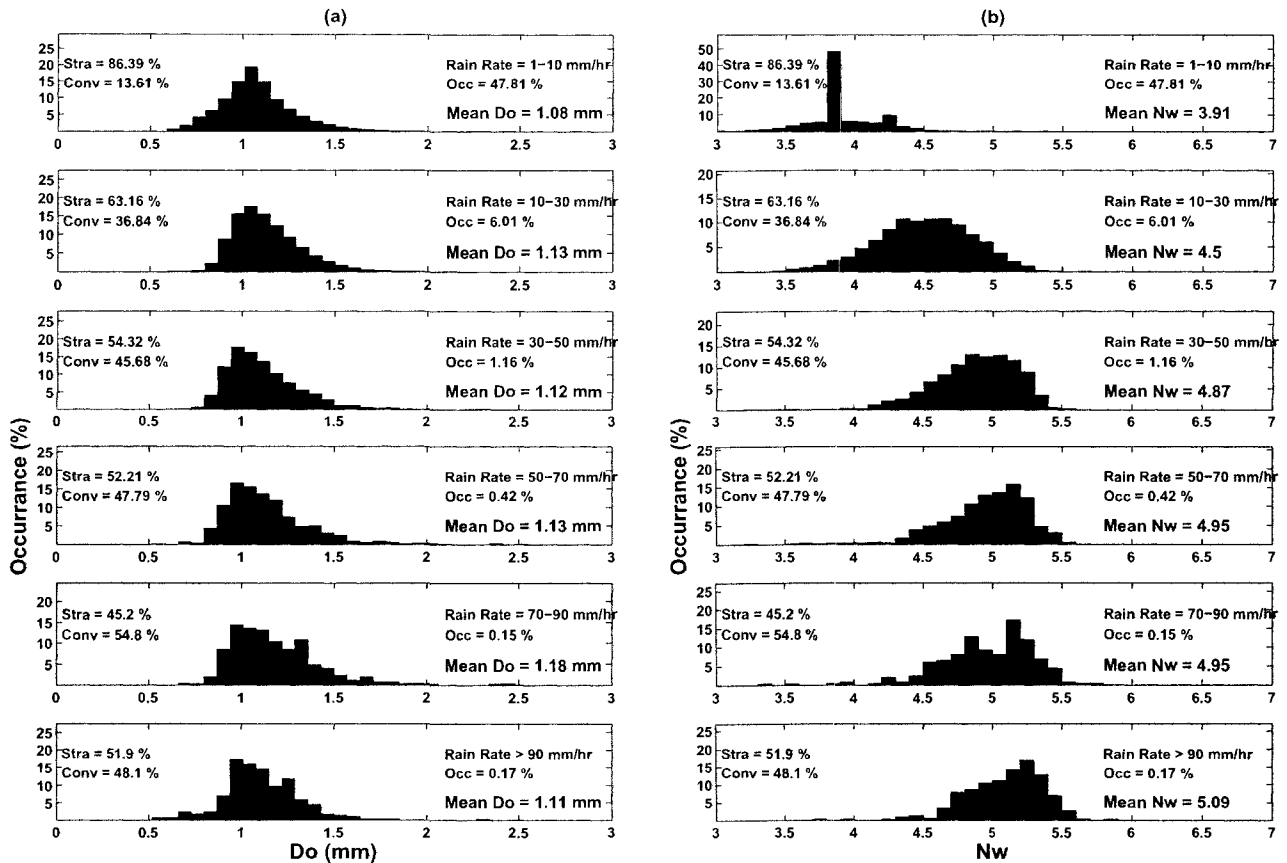


Figure 7.18: Same as Fig. 7.17 for typhoons.

- The percentage of occurrence of a rain rate higher than 90 mm hr^{-1} is less than 0.2% for the three storm types.
- For rain rate $1\text{-}10 \text{ mm hr}^{-1}$, the default values of $\log_{10}(N_w)$ —one for stratiform (about 3.9) and one for convective rain (about 4.2)—used in the TRMM-PR rain profiling algorithm are very apparent.
- When rain rate increases, the means of the distribution of $\log_{10}(N_w)$ tend to increase. The increase of $\log_{10}(N_w)$ is quite significant when rain rate increases from $1\text{-}10 \text{ mm hr}^{-1}$ to $10\text{-}30 \text{ mm hr}^{-1}$. However, the increase is mild when rain rate is high—say greater than 50 mm hr^{-1} .

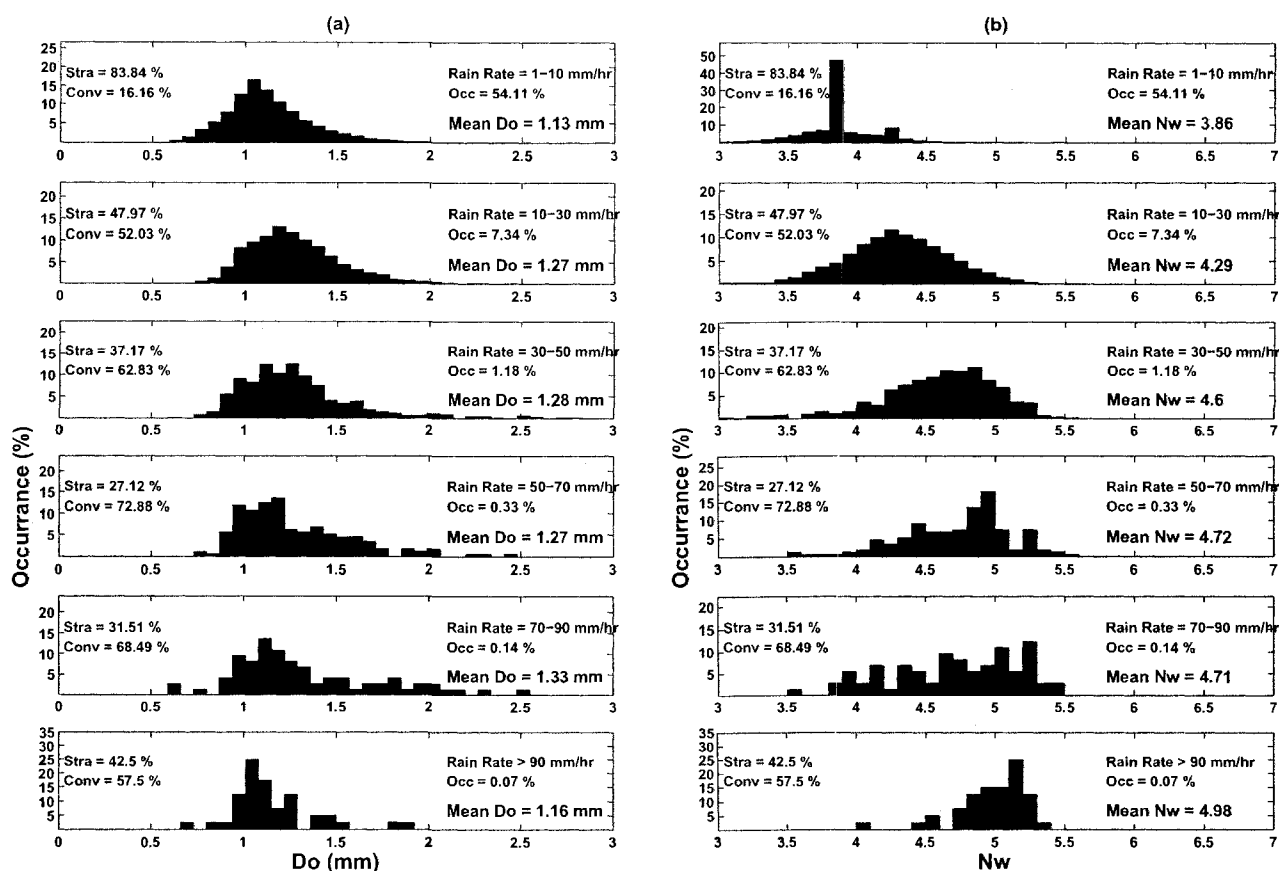


Figure 7.19: Same as Fig. 7.17 for hurricanes.

- When rain rate increases, the D_o increases slightly. At a very high rain rate, the D_o seems to have a mid decrease.
- At rain rate greater than 90 mm hr^{-1} , the percentage of convective rain is higher than stratiform for cyclones and hurricanes.

Figures. 7.20 to 7.21 show the scatter plots of the D_o vs. R and $\log_{10}(N_w)$ (denoted N_w for simplicity in notation) vs. R along with the fit of their corresponding mean values, averaged over 2 mm hr^{-1} rain rate interval, for convective and stratiform rain, respectively, for cyclones in year 2002. D_o - R and N_w - R relations by SS and WT are shown as a comparison. In each figure, the scatter plots are shown for three different altitudes—(a) and (b) for 0.5 km, (c) and (d) for 2 km, and (e) and (f) for

3 km—to demonstrate a variation of the D_o vs. R and $\log_{10}(N_w)$ vs. R along the height. The same demonstration of results is applied to typhoons, as shown in Figs. 7.22 to 7.23, and hurricanes, as shown in Figs. 7.24 to 7.25.

Several features common to the three storm types are as follows;

- When comparing the fit of the mean R vs. mean D_o , it is clear that for a given rain rate, the mean D_o is larger in stratiform than in convective rain for all storms.
- When comparing the fit of the mean R vs. mean D_o with SS and WT, the fits of mean R vs. mean D_o appear to agree well with WT at a rain rate between 1 and 10 mm hr⁻¹ at altitude of 2 and 3 km in stratiform rain. However, it is clear that is not the case in convective rain.
- In convective rain, the mean D_o tends to increase with the increase of mean R from 1 to 100 mm hr⁻¹. On the other hand, the mean D_o seems to decrease as the mean R increase beyond 10 mm hr⁻¹.
- The default values of the $\log_{10}(N_w)$, as mentioned in the preceding section, are apparent in the scatter plot of the mean R vs. $\log_{10}(N_w)$.

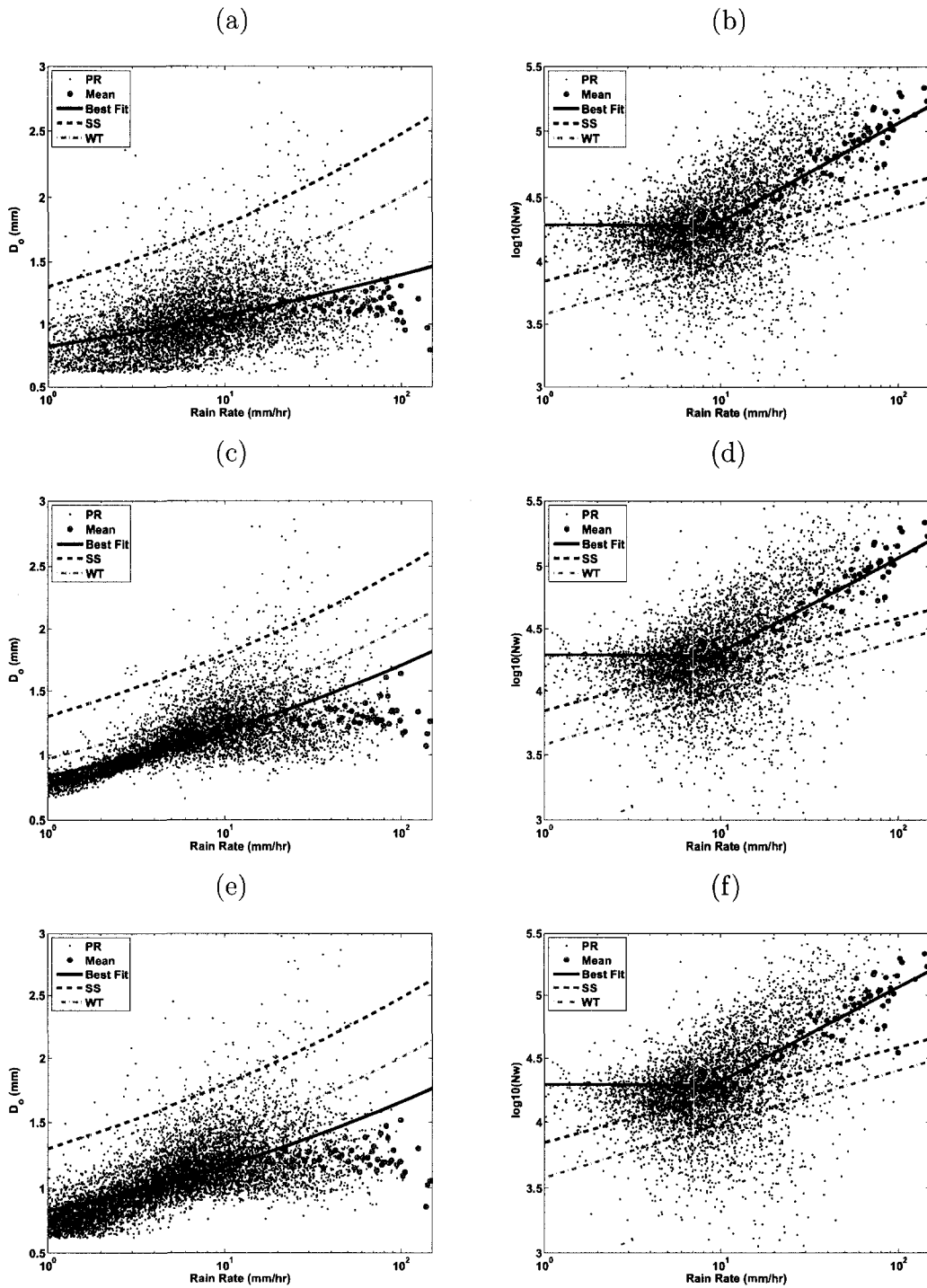


Figure 7.20: Illustration of scatter plots of D_o vs. R , and N_w vs. R , the best fit of the mean D_o vs. mean R , the best fit of the mean N_w vs. mean R , averaged over two mm hr^{-1} rain rate interval, and D_o - R and N_w - R relations by SS and WT for convective rain of cyclones in year 2002. The panels (a), (c), and (e) are for D_o vs. R at 0.5, 2, and 3 km altitude, respectively. The panels (b), (d), and (f) are for N_w vs. R for 0.5, 2, and 3 km altitude, respectively.

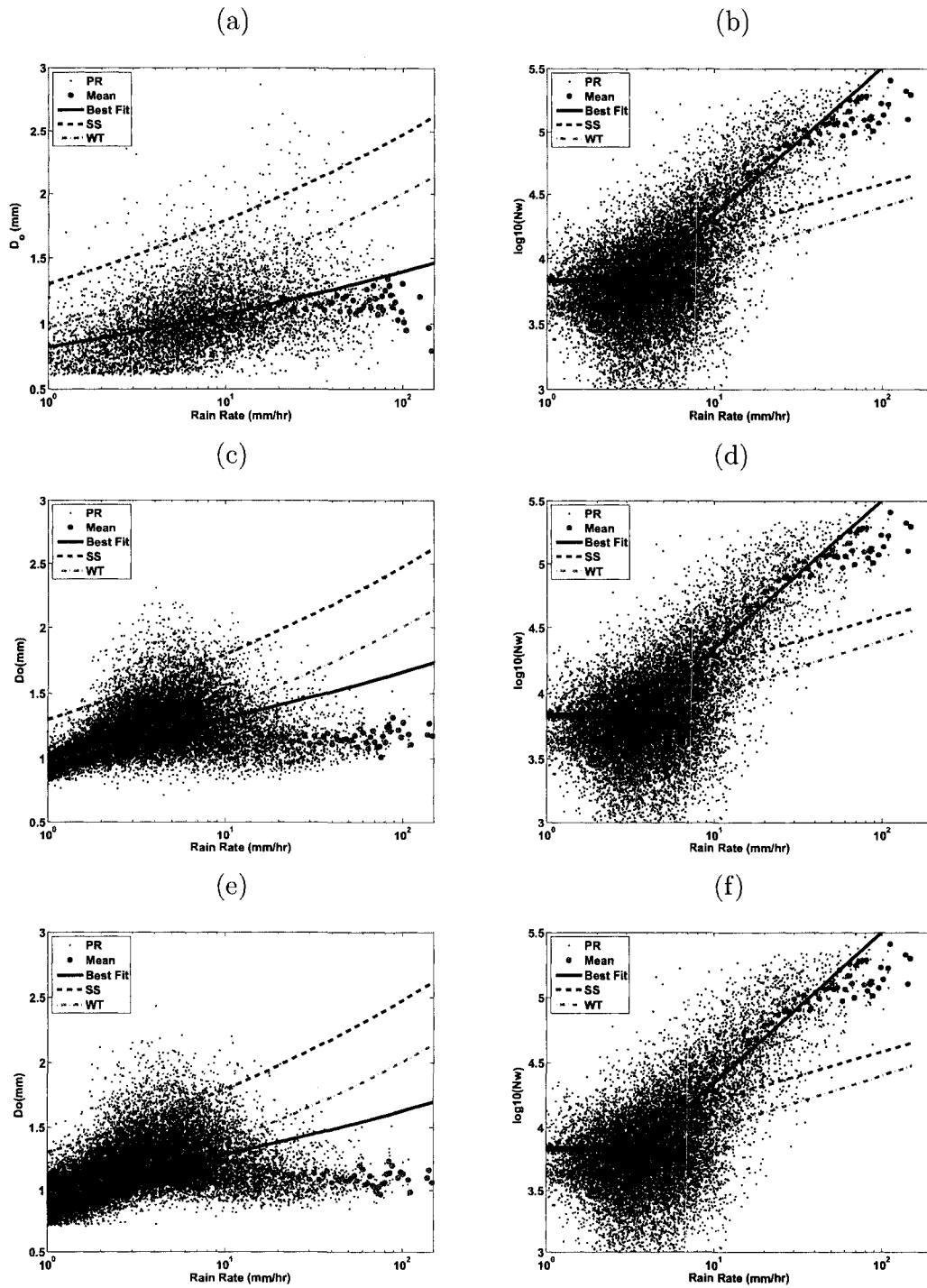


Figure 7.21: Same as Fig. 7.20 for stratiform rain.

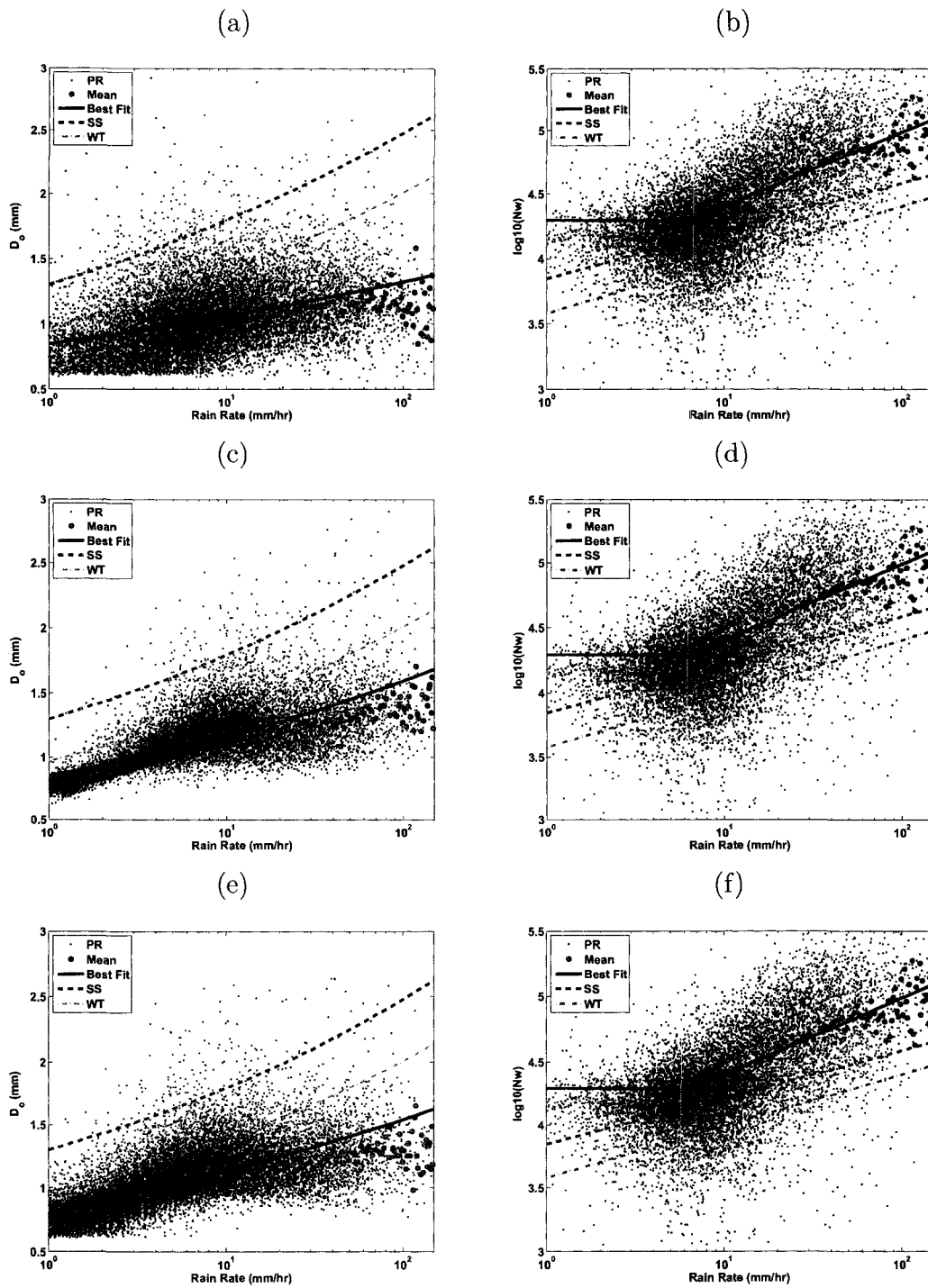


Figure 7.22: Illustration of scatter plots of D_o vs. R , and N_w vs. R , the best fit of the mean D_o vs. mean R , the best fit of the mean N_w vs. mean R , averaged over two mm hr^{-1} rain rate interval, and D_o - R and N_w - R relations by SS and WT for convective rain of typhoons in year 2002. The panels (a), (c), and (e) are for D_o vs. R at 0.5, 2, and 3 km altitude, respectively. The panels (b), (d), and (f) are for N_w vs. R for 0.5, 2, and 3 km altitude, respectively.

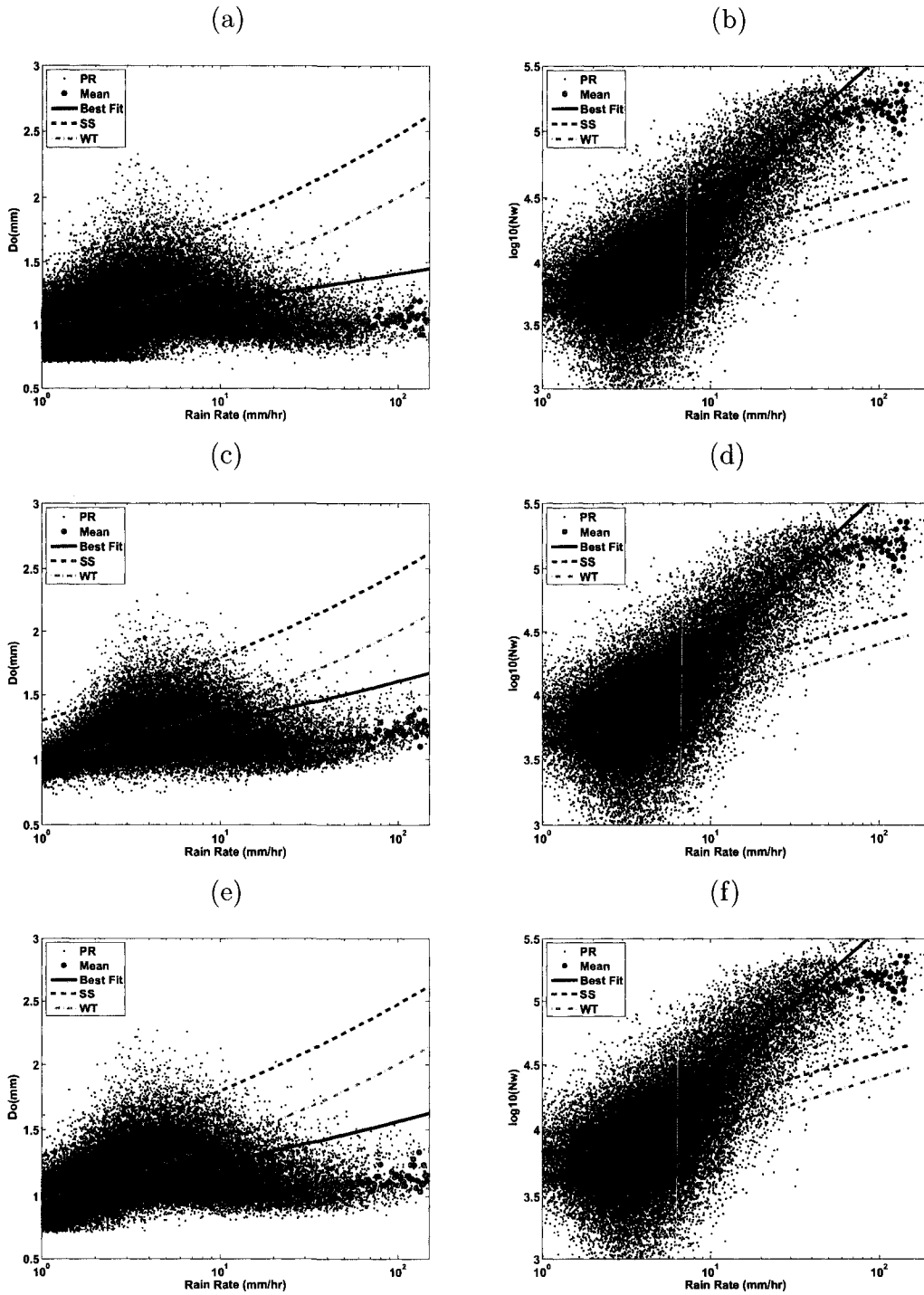


Figure 7.23: Same as Fig. 7.22 for stratiform rain.

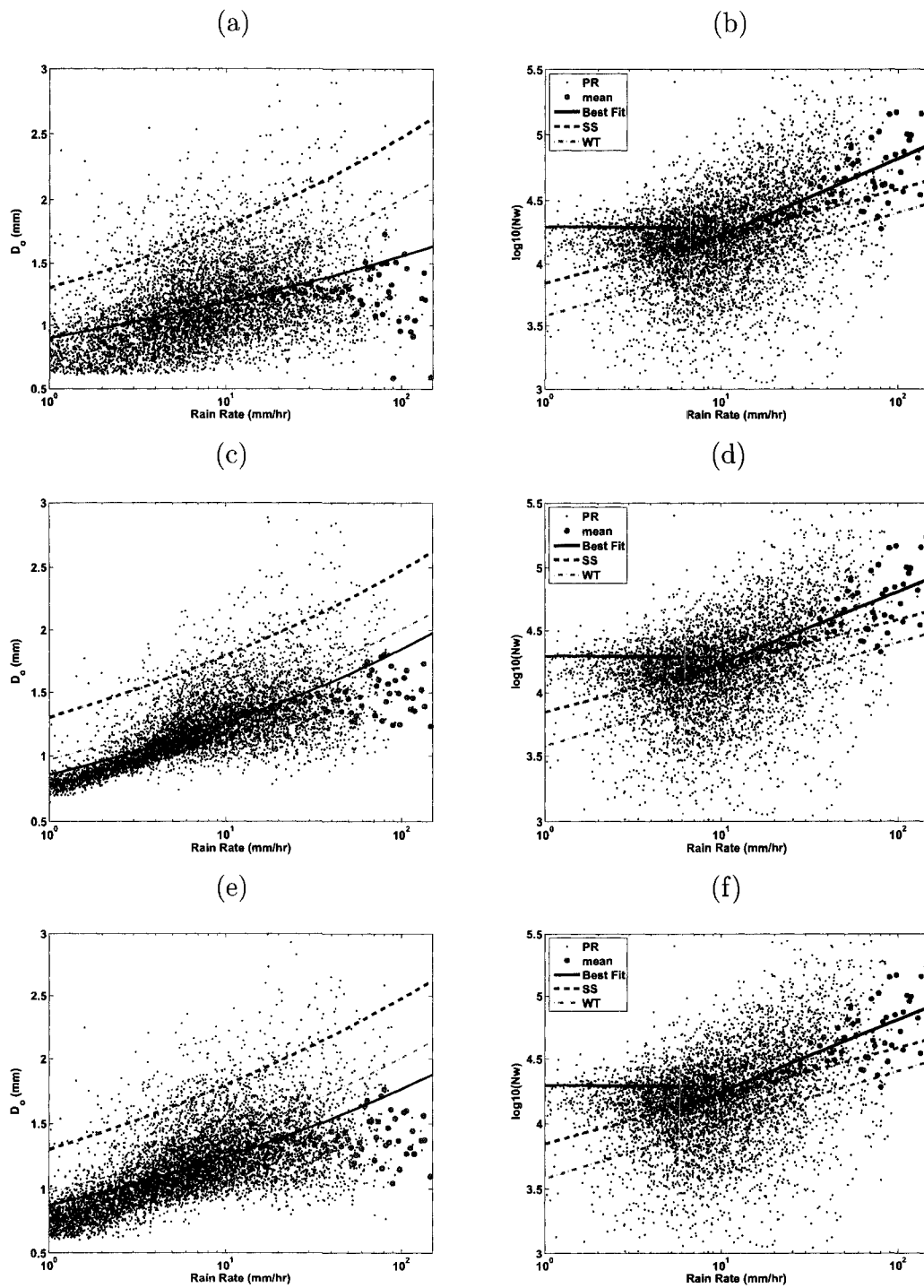


Figure 7.24: Illustration of scatter plots of D_o vs. R , and N_w vs. R , the best fit of the mean D_o vs. mean R , the best fit of the mean N_w vs. mean R , averaged over two mm hr^{-1} rain rate interval, and D_o - R and N_w - R relations by SS and WT for convective rain of hurricanes in year 2002. The panels (a), (c), and (e) are for D_o vs. R at 0.5, 2, and 3 km altitude, respectively. The panels (b), (d), and (f) are for N_w vs. R for 0.5, 2, and 3 km altitude, respectively.

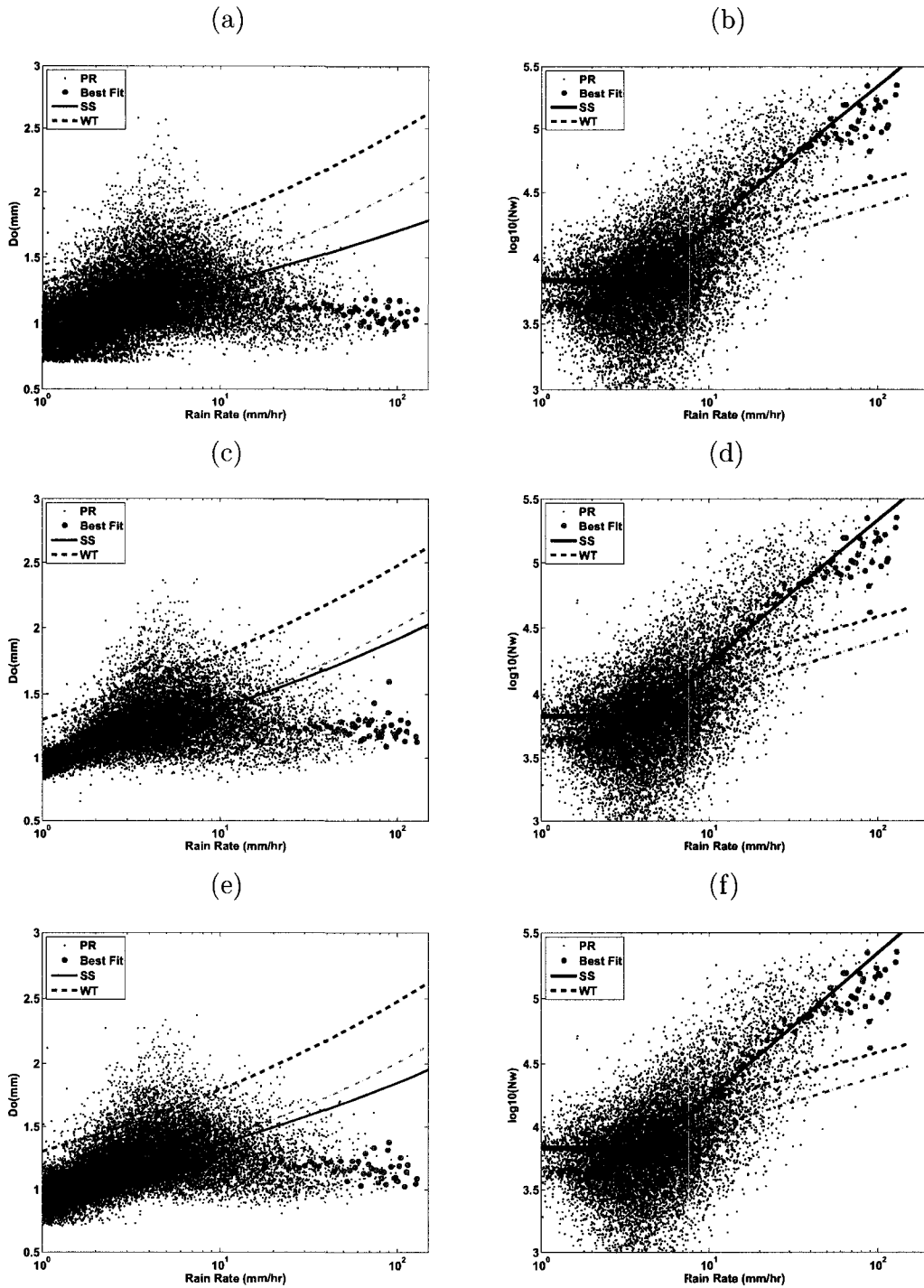


Figure 7.25: Same as Fig. 7.24 for stratiform rain.

7.5 Simulation of Ka-band Radar Observations of Tropical Storms

Cyclone Nargis, observed by the TRMM-PR on April 28, 2008, over the North Indian ocean, is used to simulate Ka-band radar observations. The simulation procedure developed in section 6.2 is used here. Figure 7.26 shows the three main rain types on the horizontal cross-section of the cyclone cell: (a) all rain types, (b) stratiform rain with a bright band, (c) convective rain, and (d) stratiform rain without a bright band. It is clear from Fig. 7.26 that the majority of this particular precipitation cell observed by TRMM-PR is stratiform with bright band, and only small fractions are convective and stratiform rain without bright band.

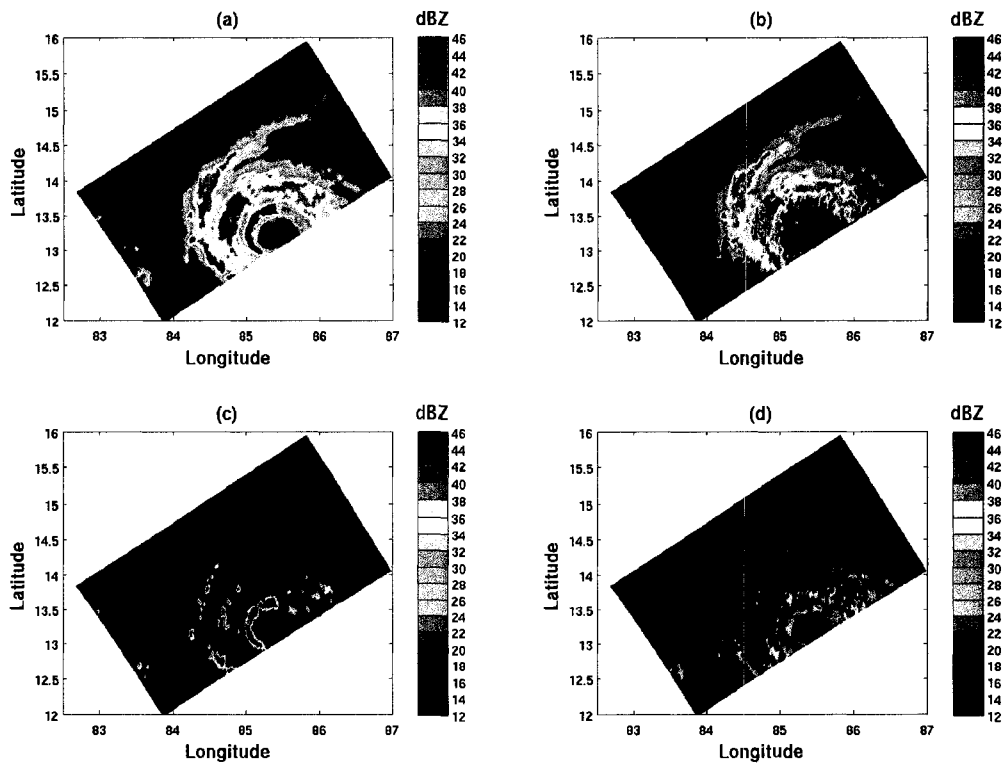


Figure 7.26: A horizontal cross-section of $Z_e(\text{Ku})$, separated based on the rain-type information of Cyclone Nargis, observed by the TRMM-PR in this case study: (a) all rain types (b) stratiform rain with bright band (c) convective rain, and (d) stratiform rain without bright band.

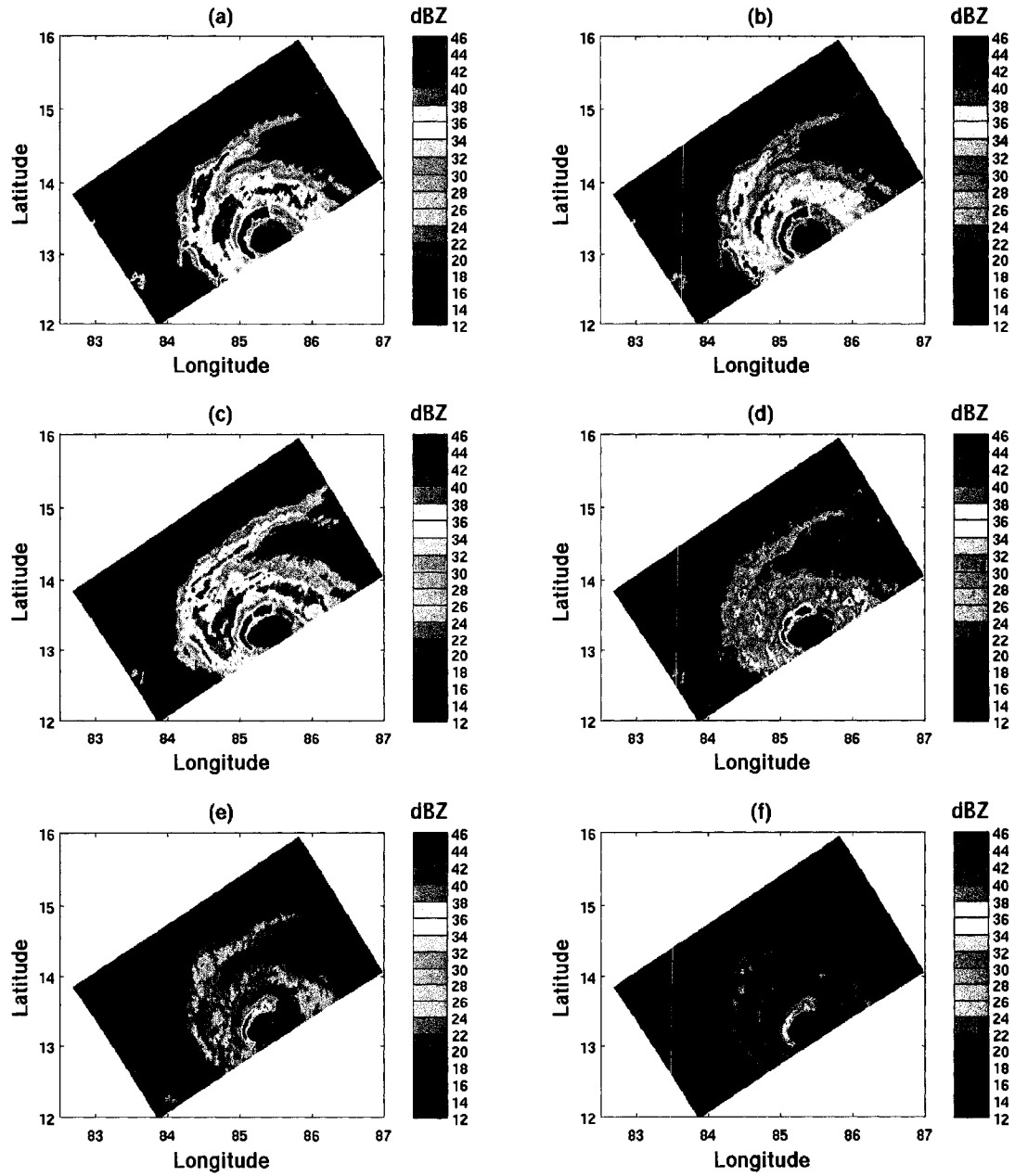


Figure 7.27: $Z_e(Ku)$ and simulated $Z_e(Ka)$ at three different horizontal cross-section heights above the surface: (a) and (b) at 2 km, (c) and (d) at 4.5 km, and (e) and (f) at 6 km.

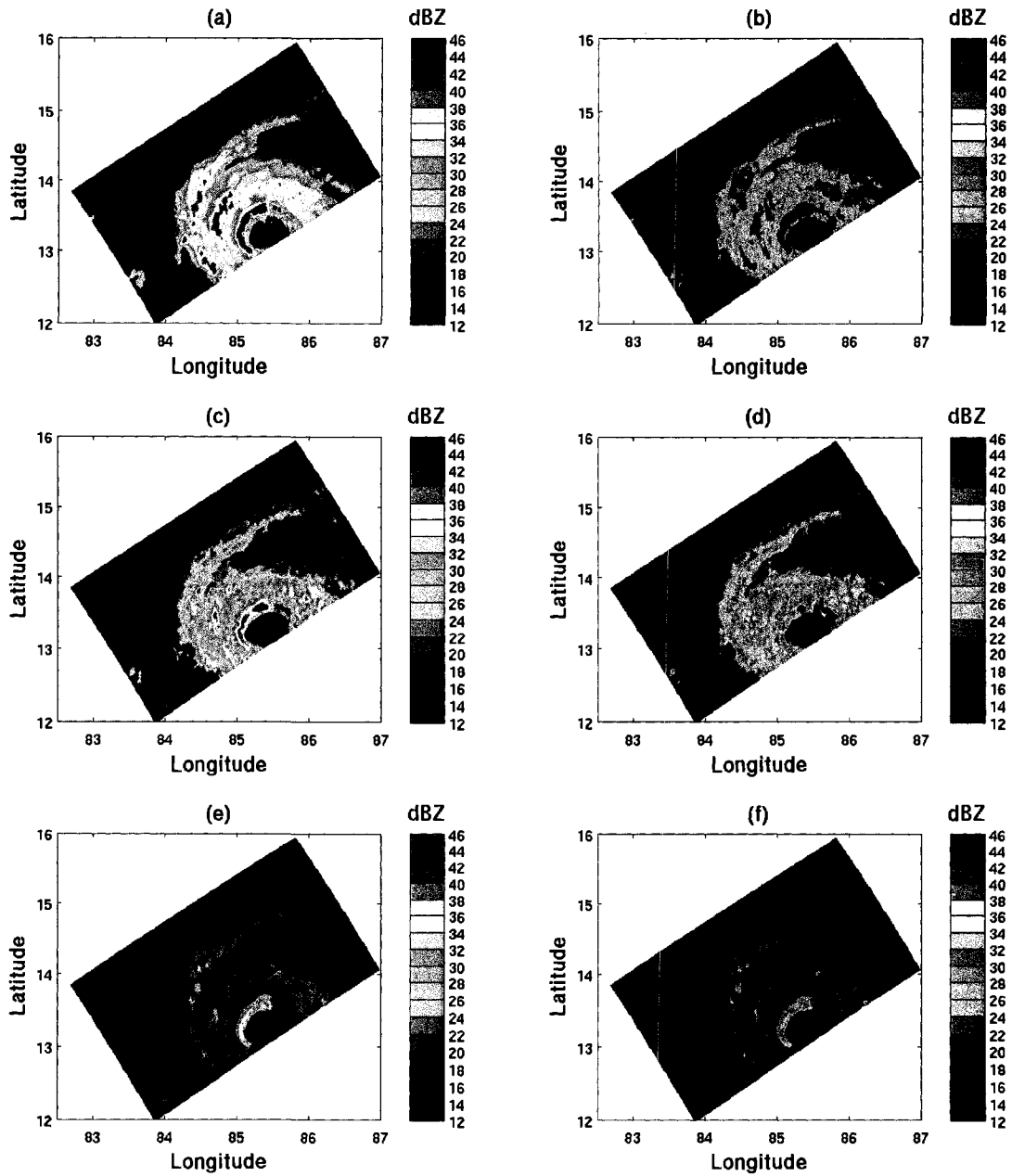


Figure 7.28: $Z_e(Ka)$ and simulated $Z_m(Ka)$ at 3 different horizontal cross-section heights above the surface. The (a) and (b) at 2 km, (c) and (d) region at 4.5 km, and (e) and (f) at 6 km.

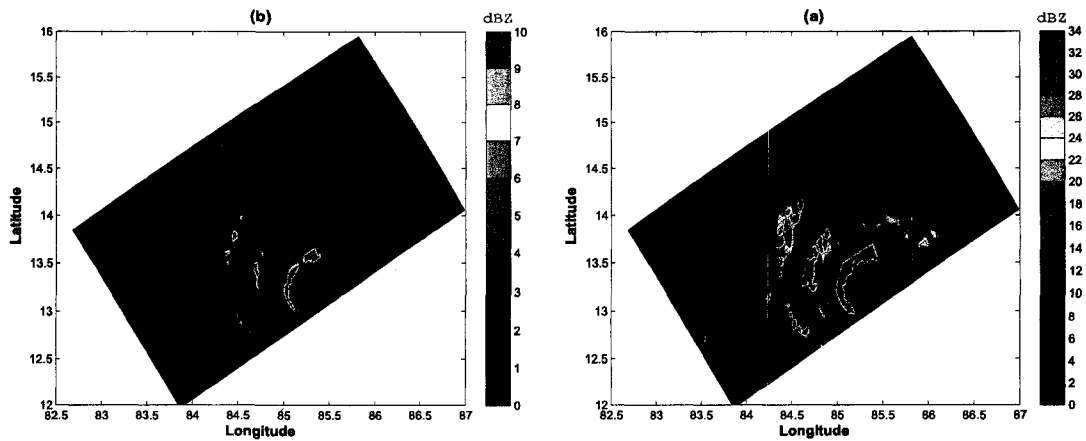


Figure 7.29: Simulated path-integrated attenuation: (a) Ku-band; (b) Ka-band.

Figure 7.27 shows a horizontal cross-section of the $Z_e(\text{Ku})$ and the simulated $Z_e(\text{Ka})$ at three different altitudes—2, 4.5, and 6 km, are shown in Fig. 7.27. From Fig. 7.27, the difference between $Z_e(\text{Ku})$ and $Z_e(\text{Ka})$ is caused by the non-Rayleigh scattering in one or both frequency bands. At near the cyclone center (the so-called “eye wall”), the intensity of reflectivity in the convective rain is as high as 50 dBZ. The simulated $Z_e(\text{Ka})$ of the convective rain band close to the eye wall, as shown in Fig. 7.28 (b), is significantly attenuated. The simulated two-way path integrated attenuation (PIA) in both channels is shown in Fig. 7.29. It is clear from Fig. 7.29 that the simulated PIA(Ka) is much higher than the simulated PIA(Ku), especially for strong reflectivity profiles near the eye wall, where the PIA(Ka) can be as high as 30 dB.

A vertical cross-section of $Z_e(\text{Ku})$, the simulated $Z_e(\text{Ka})$, the simulated $Z_m(\text{Ku})$, and the simulated $Z_m(\text{Ka})$ of the cyclone across the TRMM ground track are shown in Fig. 7.30 (a), (b), (c), and (d), respectively. It is clear from Fig. 7.30 (d) that at about 50 to 60 km across the TRMM ground track, the severe attenuation causes the extinction of the signal of the convective rain core at about 4 km altitude. The attenuation in stratiform rain, which is the largest portion of the storm cell, can also be as high as 20 dB. However, it is not strong enough to cause a loss of signal. This

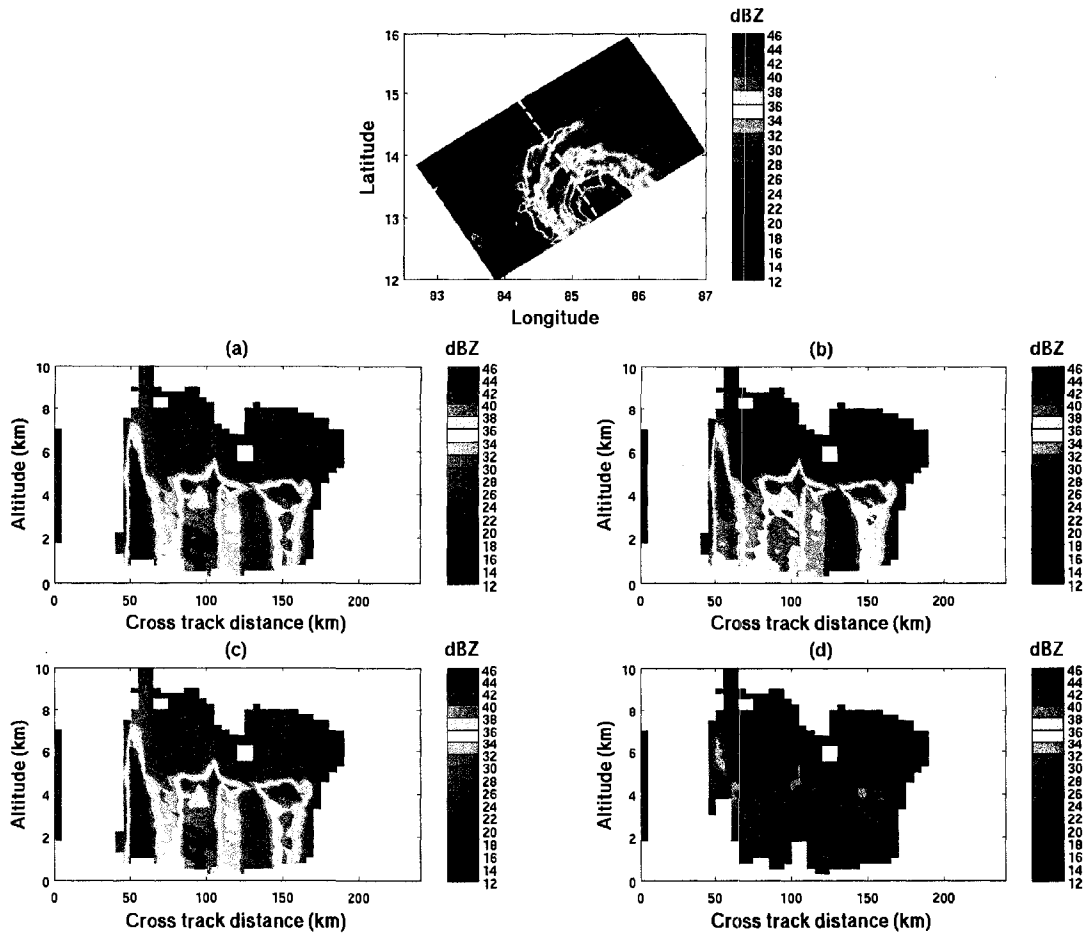


Figure 7.30: A vertical cross-section of cyclone Nargis, as indicated by the dashed line: (a) $Z_e(\text{Ku})$; (b) the simulated $Z_m(\text{Ku})$; (c) the simulated $Z_e(\text{Ka})$; and (d) the simulated $Z_m(\text{Ka})$.

suggests that dual-frequency retrieval techniques are applicable for most parts of the cyclone cell. The difference between $Z_e(\text{Ku})$ (Fig. 7.30 (a)) and $Z_e(\text{Ka})$ (Fig. 7.30 (c)) is shown in Fig. 7.31. It is clear that large differences occur in the bright band region. In this case, the difference can be observed to be as large as about 11 dBZ.

Two reflectivity profiles—one for convective rain and the other for stratiform with bright band, are shown in Fig. 7.32. It can be seen from Fig. 7.32 (a) that $Z_m(\text{Ka})$ of the convective rain profile, selected from the tall convective core near the eye wall, is below the minimum detectable reflectivity in Ka-band at about 3.8 km above the the

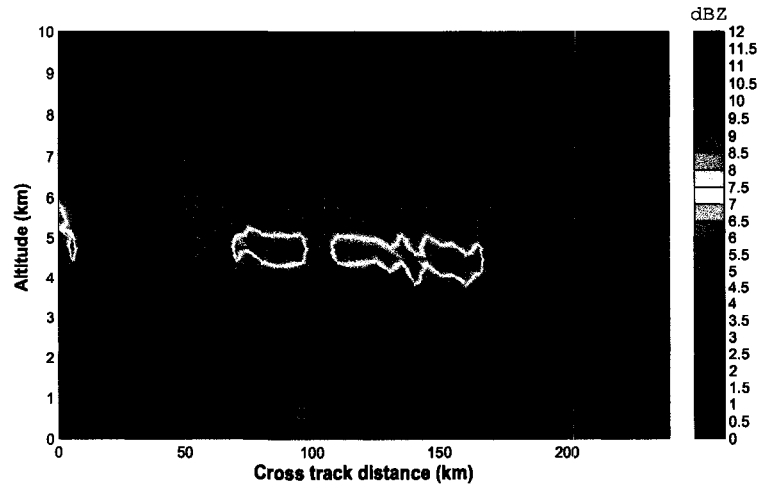


Figure 7.31: The difference between a vertical cross-section of $Z_e(\text{Ku})$ (Fig. 7.30 (a)) and the simulated $Z_e(\text{Ka})$ (Fig. 7.30 (c)) in stratiform rain.

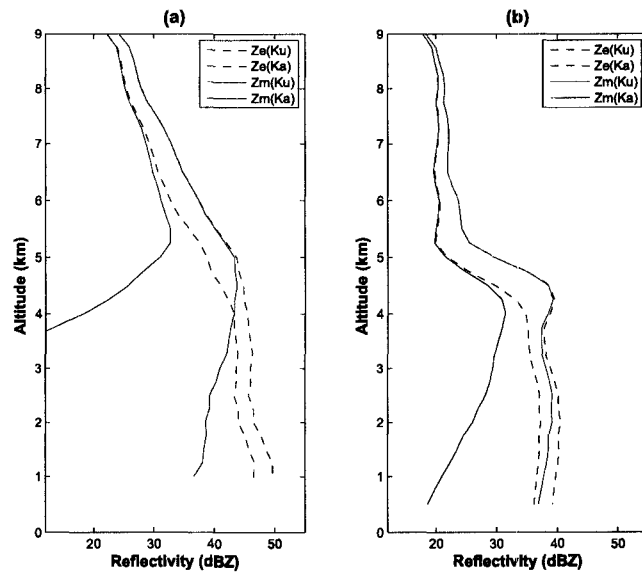


Figure 7.32: Two vertical profiles of reflectivity—one for convective rain, and the other for stratiform rain with a bright band. The dashed lines represent $Z_e(\text{Ku})$ and the simulated $Z_e(\text{Ka})$, while the solid lines represent the simulated $Z_m(\text{Ku})$ and $Z_m(\text{Ka})$.

surface. The simulated $Z_e(\text{Ka})$ stratiform rain with bright band is shown in Fig. 7.32 (b). The attenuation for this profile is about 20 dB in Ka-band.

7.6 Summary and Conclusion

Study of vertical profiles of reflectivity (VPR) of tropical storms observed by TRMM precipitation radar (PR) using the self-organizing (SOM) map technique is presented. A characterization of vertical reflectivity profiles of tropical storms—hurricanes in the North Atlantic, typhoons in the Northwest Pacific, and cyclones in the South Indian Ocean in the years 2000, 2002, and 2003—are performed and compared. The comparison is conducted both among the storms in the same year and the same storm type in different years. A comparative study is also performed with and without separating the storms into convective and stratiform type. Results show that, in general, the characteristic profiles that have stronger reflectivity occur less frequently than the ones with weaker reflectivity. Over 80% of the VPR of each storm type is stratiform. Bright band (BB) study shows that BB vertical structure of the storms is nearly the same for all three years. However, the height of the BB peak from sea level of hurricanes is lowest compared to those of typhoon and cyclone.

Estimation of gamma DSD parameters based on one year's data of the tropical storms is performed. The mean D_o of cyclones, typhoons, and hurricanes are about 1.13, 1.13 and 1.24 mm, respectively. This perhaps reflects the fact that hurricanes have the lowest BB peak. Stratifying D_o by a number of rain rate intervals, the mean D_o appears to slightly increase as rain rate increases, and tends to decrease when the rain rate reaches certain values. This characteristic is clearly seen when examining the scatter plot between rain rate vs. D_o . Following similar discussion, the mean N_w appears to increase as the rain rate increases. Comparing the best fit of the mean rain rate and the mean D_o with SS and WT shows that the best fits of the data appear to agree well with WT, especially in stratiform rain at 3 km altitude.

Simulation of cyclone Nargis observation at Ka-band radar using an observation from the TRMM-PR is performed. When examining the simulated PIA(Ka), it is clear that the extinction of signal occurs in convective rain. The path attenuation

of stratiform rain, which is the largest rain band of the storm cell, can be observed as high as 20 dB. However, the attenuation is not very strong to cause an extinction of the signal. This finding suggests that for most of the tropical storm cells, the dual-frequency retrieval algorithms can be used.

CHAPTER 8

SUMMARY, CONCLUSIONS, AND RECOMMENDATIONS FOR FUTURE WORK

8.1 Summary and Conclusions

The primary goal of this research is to study characteristics of precipitation observations from a dual-frequency space-based precipitation radar, and to provide procedures for simulating them. The key objective of this work is to have a direct impact on the evaluation and development of the dual-frequency precipitation radar (DPR) algorithms that is planned for the global precipitation measurement (GPM) mission. In this study, an array of relevant research results have been obtained towards this goal.

The theoretical framework for interpreting scattering and absorption of electromagnetic waves by precipitation particles and the microphysical model of precipitation were reviewed. The radar reflectivity factor (Z_e) and specific attenuation (k) for various types of precipitation particles—snow, graupel and raindrops—were computed based on a gamma particle size distribution (PSD) model. The relation between Z_e and k and a variation of Z_e with frequency were determined so that the precipitation measured in one radar frequency could be converted to another frequency. The computation was performed for three different frequency bands, namely, S-band (2.7 GHz), Ku-band (13.6 GHz), and Ka-band GHz, and for a wide variety of PSD parameters taken from those reported in the literature. For dry snow and graupel, various

snow and graupel densities were used in the computation. For partially melted particles, the computation was varied by different values of water fractions. It was found that the variation of Z_e with frequency is best represented by a simple linear function. The relation between Z_e and k was found to be well approximated by a power law form. These findings became very important to subsequent steps of the simulation. The coefficients of Z_e and k and variability of Z_e with frequency were determined. The simulation of the vertical profile of reflectivity as if it was observed from a space-based precipitation radar was demonstrated based on simple models for vertical storm microphysical structure.

In order to understand the general nature of spaceborne radar measurements of precipitation, an extensive analysis of TRMM-PR observations was conducted. Characterization of the vertical profile of reflectivity (VPR) observed on a global scale by the TRMM-PR using a self organizing map (SOM) technique was performed. By analyzing the TRMM observations this way, the wide spatial variation of VPR can be characterized by a number of distinctive VPRs, and the global statistics of VPR were generated. The analysis was performed separately on the data observed over land and over ocean as well as on stratiform and convective rain types. In addition, the correction factor (ϵ), used in the TRMM-PR attenuation algorithm, was used to stratify data into two sets—one with $\epsilon = 1$ and the other with $\epsilon \neq 1$. Stratification data by surface background—land and ocean—and by rain type—stratiform and convective—in a sense reflects a distinction in the underlying microphysical process. The data set with $\epsilon = 1$, which is the largest portion of data over land and over ocean, reflect the fact that the two-way path attenuation (PIA) in Ku-band for this data set is small, typically less than 3 dB. VPRs of convective rain over land with $\epsilon \neq 1$ are more intense than those over ocean, while they are similar for those with $\epsilon = 1$. The comparison of VPRs over land and over ocean for stratiform rain with bright band indicates no significant difference for both the $\epsilon = 1$ and $\epsilon \neq 1$ cases. However, when comparing the VPRs of stratiform rain with bright band with respect to the

ϵ value, it appears that the VPRs with $\epsilon \neq 1$ are much stronger than those with $\epsilon = 1$. Two parameters of a gamma DSD— D_o and N_w — were estimated according to the stratified data for one year’s TRMM data. The smaller ϵ is, the larger D_o are retrieved. In general, D_o over land is larger than that over ocean. On average, D_o over land is 1.54 mm and over ocean is 1.44 mm.

The characteristics of the GPM core satellite and the DPR and the overview of the mission were reviewed. By combining two independent observations at each range bin, the two parameters of PSD can be retrieved via dual-frequency retrieval algorithms. The forward method was found to give a promising estimation of D_o and N_w in the region of dry snow and graupel where the attenuation is almost negligible. The principle of the standard dual-frequency method is that a path-averaged rain rate (PAR) can be estimated from differential attenuation using the empirical relation between specific attenuation and rain rate, k - R . The differential attenuation is obtained by performing the frequency difference of the apparent reflectivity at specified r_1 and r_2 in each frequency, and then taking a difference of these differences. This leads to another name for this method, difference of attenuation difference (DAD). An extensive analysis of the DAD method was done. Although the DAD technique, in principle, relies on Rayleigh scattering and uniform rain assumptions, it is simple and can provide a robust path-averaged rain rate (PAR) estimate. The simulation results show that the DAD method maintains a high degree of accuracy of PAR estimate for dual-frequencies of 13.6 and 35.6 GHz despite non-Rayleigh scattering. The key factor that dictates the accuracy of the estimated PAR is the difference between D_o at r_1 and r_2 defined as $D_o(r_2) - D_o(r_1)$ (δD_o). Studying four different PAR values (5, 10, 15, and 20 mm hr⁻¹), it was found that the largest difference between the estimated PAR (Δ PAR) under the assumptions PAR_{DAD} and the “actual” PAR (PAR_{DADM}) is less than 1 mm hr⁻¹ when the maximum of δD_o is 0.2 mm, and it is slightly dependent on the PAR values. Δ PAR is approximately 5.2 times δD_o . This finding suggests that the DAD method can provide a robust estimation of path-averaged rain rate for

the dual-frequency precipitation radar (DPR) for the GPM mission. In this research, the DAD method is applied solely in the rain region.

A microphysical model of precipitation was developed based on airborne radar measurements from the NAMMA experiment conducted in 2006. The APR-2 is dual-frequency radar operating at the same frequency band as the DPR. A combination of dual-frequency retrieval algorithms were applied to the airborne data. The particle size distribution (PSD) along the vertical profile was generated for convective rain and stratiform rain. By examining the fall velocity characteristics of reflectivity profiles above the melting layer, particles above the melting layer of convective rain model and stratiform with bright band are assumed to be dry graupel and dry snow, respectively. Consequently, in the melting layer, the particles in the convective rain model and stratiform rain with bright band model were assumed to be wet graupel and wet snow. Below the melting layer, raindrops were assumed in both convective and stratiform rain models. Coefficients of the Z_e and k power law relation and a linear conversion of reflectivity between two frequency bands were calculated along the vertical profile for the two developed rain models, which were used quantitatively in the simulation of DPR observations.

The simulation of Ka-band radar observations using the TRMM-PR observations near the area of the NAMMA experiment was performed based on the developed microphysical models. The simulation results suggested that the surface reference technique (SRT), which is not applicable in the TRMM-PR retrieval algorithm because of a small $PIA(Ku)$, can be applied to VPRs when measured in Ka-band because $PIA(Ka)$ is almost 10 times $PIA(Ku)$. Such VPRs were associated with the $\epsilon = 1$, as discussed earlier. The shortcoming of a scaling relation between $PIA(Ku)$ and $PIA(Ka)$ is that when $PIA(Ku)$ is strong, a loss of signal or the radar echo being under the minimum detectable reflectivity in Ka-band channel occurs, hence preventing an application of dual-frequency retrieval algorithms. This finding is important for

designing a systematic retrieval scheme for GPM-DPR. Two case studies of simulation of DPR observations using NEXRAD radar measurement were performed. The precipitation regimes for two cases were close to the maritime precipitation regime. Strong attenuation in an intense squall line, observed in one of the two cases, typically causes an extinction of the signal at the height just below the melting layer. A simulation of DPR observations using dual-polarization ground radar measurement was performed. Phase-height transition (PHT) information along vertical profiles, an important factor of the simulation process, available through a particle classification using the dual-polarization measurements, yielded a realistic simulation results.

A study of tropical storms using long-term TRMM-PR observations was performed. Gamma DSD parameters of the tropical storms were estimated. The mean D_o of cyclones, typhoons, and hurricanes are about 1.13, 1.13 and 1.24 mm, respectively. This perhaps reflects the fact that hurricanes have the lowest BB peak. By stratification of D_o by a number of rain rate intervals; the mean D_o appears to slightly increase as rain rate increases, and tends to decrease when the rain rate reaches a certain value. This characteristic is clearly seen when examining the scatter plot between rain rate vs. D_o . Following the similar discussion, the mean N_w appears to increase as the rain rate increases. A comparison of the best fit of the mean rain rate and the mean D_o with SS and WT shows that the best fits of the data appear to agree well with WT, the study conducted by Willis and Tattelman (1989), especially in stratiform rain at 3 km altitude. A simulation of cyclone Nargis at the Ka-band radar using the observation from the TRMM-PR was also performed. When examining the simulated PIA(Ka), it was clear that the extinction of the signal occurs in such cyclone. The path attenuation of stratiform rain, which is the largest rain band of the storm cell, can be observed as high as 20 dB. However, the attenuation is not strong enough to cause an extinction of the signal. This finding suggests that for most parts of a storm cell, the dual-frequency retrieval algorithms can still be used.

8.2 Suggestion for Future Work

The following are suggestion for future work to carry the research further:

- The microphysical model in this research was developed based on a single data set from an airborne experiment over ocean. More data from a variety of precipitation regimes (maritime and continental) need to be analyzed so that microphysical model can be further generalized. This is likely to occur during the GPM program.
- A quantitative simulation of DPR observations using long-term observation of the TRMM-PR on a global scale should be performed so that a statistical characterization of a global diversity of DPR observations can be constructed.
- A quantitative testing of dual-frequency algorithms on the simulated observations of the DPR should be done so that their robustness and uncertainty can be statistically characterized.
- A simulation of DPR observations using measurements from the NEXRAD radar network should be done quantitatively so that a large data set of DPR observations for the High Plains precipitation regime can be extensively characterized.
- More simulation of DPR observations using ground-based radar dual-polarization measurements should be performed. In addition, the developed microphysical model for the simulation in this research does not account for snowfall on the ground or for hail. Therefore, to be able to perform the simulation of hail and snowfall on the ground, the microphysical model needs to be further implemented, based on dual-polarization radar observations.

APPENDIX A

SCATTERING OF ELECTROMAGNETIC WAVE BY DIELECTRIC SPHERE

A.1 Vector scattering amplitude and Scattering matrix

Incident plane wave with real amplitude E_0 propagating along the k_i -direction can be, in general, expressed in a form as,

$$\vec{E}^i = \hat{e}_i E_0 \exp(-jk_0 \hat{k}_i \cdot \vec{r}) \quad (\text{A.1})$$

where the complex unit vector \hat{e}_i defines the polarization state of the plane wave, At the origin, $\vec{E}^i(O) = \hat{e}_i E_0$, which is the plane wave amplitude (the spatial phase is at the origin). This vector amplitude is resolved into components as follow,

$$\vec{E}^i(O) = \hat{e}_i E_0 = \vec{E}_h^i \hat{h}_i + \vec{E}_v^i \hat{v}_i \quad (\text{A.2})$$

where $E_h^i = \hat{h}_i \cdot \hat{e}_i E_0$ and $E_v^i = \hat{v}_i \cdot \hat{e}_i E_0$

The far-field scattered wave (\vec{E}^s) is defined as,

$$\vec{E}^s = \vec{f}(\hat{s}, \hat{i}) \frac{e^{(-jk_0 r)}}{r} \quad (\text{A.3})$$

where $\vec{f}(\hat{s}, \hat{i})$ is vector scattering amplitude. In Rayleigh scattering, where diameter of sphere is small compared to radar wavelength, $\vec{f}(\hat{s}, \hat{i})$ is expressed as,

$$\vec{f}(\hat{s}, \hat{i}) = \frac{k_0^2 (\epsilon_r - 1)}{4\pi (\epsilon_r + 2)} 3V \left[\vec{E}^i - \hat{r}(\hat{r} \cdot \vec{E}^i) \right] \quad (\text{A.4})$$

and scattered wave is expressed as a function of incident wave as,

$$\vec{E}^s = \frac{k_0^2 (\varepsilon_r - 1)}{4\pi (\varepsilon_r + 2)} 3V \left[\vec{E}^i - \hat{r}(\hat{r} \cdot \vec{E}^i) \right] \frac{e^{-jk_0 r}}{r} \quad (\text{A.5})$$

Similar to \vec{E}^i , \vec{E}^s is resolved into components as

$$\vec{E}^s = E_h^s \hat{h}_s + E_v^s \hat{v}_s \quad (\text{A.6})$$

The 2 components of \vec{E}^s are related to the two component of \vec{E}^i via scattering matrix as follow,

$$\begin{bmatrix} E_h^s \\ E_v^s \end{bmatrix} = \frac{e^{-jk_0 r}}{r} \begin{bmatrix} S_{hh} & S_{hv} \\ S_{vh} & S_{vv} \end{bmatrix}_{\text{FSA}} \begin{bmatrix} E_h^i \\ E_v^i \end{bmatrix} \quad (\text{A.7})$$

where

$$\mathbf{S}_{\text{FSA}} \equiv \begin{bmatrix} S_{hh} & S_{hv} \\ S_{vh} & S_{vv} \end{bmatrix}_{\text{FSA}} \quad (\text{A.8})$$

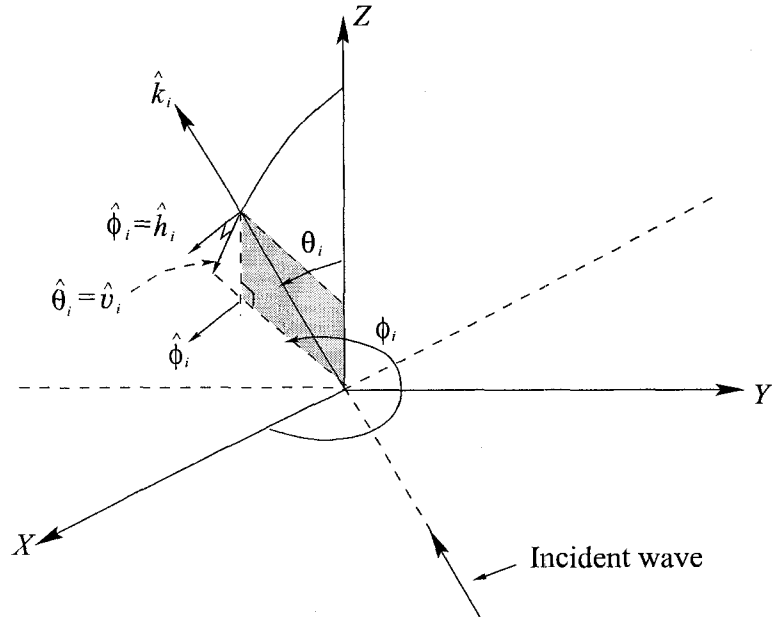
The 2x2 scattering matrix can be formulated in either forward scatter alignment (FSA) or back scatter alignment (BSA) convention (Bringi and Chandrasekar, 2001). Note that FSA convention is used in (A.7). In FSA convention, spherical triplet is $(\hat{k}_s, \hat{\theta}_s, \hat{\phi}_s)$ with $\hat{k}_s = \hat{\theta}_s \times \hat{\phi}_s$. Note that the subscript s denotes BSA convention. The horizontal and vertical unit vectors are defined as $\hat{h}_s = \hat{\phi}_s$ and $\hat{v}_s = \hat{\theta}_s$, so that the triplet becomes $(\hat{k}_s, \hat{v}_s, \hat{h}_s)$ with $\hat{k}_s = \hat{v}_s \times \hat{h}_s$. Fig. A.1 illustrates incident wave and scattered wave and the far-field scattered wave in spherical coordinate system. The complete representation of unit vectors of FSA are as follows,

$$\hat{\phi}_{i,s} = \hat{h}_{i,s} = -\sin \phi_{i,s} \hat{x} + \cos \phi_{i,s} \hat{y} \quad (\text{A.9a})$$

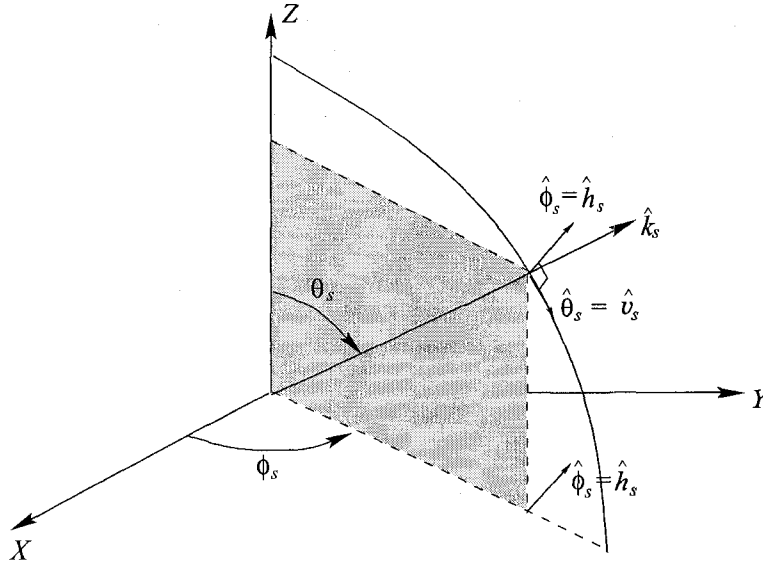
$$\hat{\theta}_{i,s} = \hat{v}_{i,s} = \cos \phi_{i,s} \cos \theta_{i,s} \hat{x} + \sin \phi_{i,s} \cos \theta_{i,s} \hat{y} - \sin \theta_{i,s} \hat{z} \quad (\text{A.9b})$$

$$\hat{k}_{i,s} = \cos \phi_{i,s} \sin \theta_{i,s} \hat{x} + \sin \phi_{i,s} \sin \theta_{i,s} \hat{y} + \sin \theta_{i,s} \hat{z} \quad (\text{A.9c})$$

In BSA convention, spherical triplet is $(\hat{k}_r, \hat{\theta}_r, \hat{\phi}_r)$ with $\hat{k}_r = \hat{\theta}_r \times \hat{\phi}_r$. Note that the subscript r denotes BSA convention. The horizontal and vertical unit vectors are defined as $\hat{h}_r = \hat{\phi}_r$ and $\hat{v}_r = \hat{\theta}_r$, so that the triplet becomes $(\hat{k}_r, \hat{v}_r, \hat{h}_r)$ with



(a)



(b)

Figure A.1: (a) Incident wave direction, specified by \hat{k}_i , with $\hat{k}_i = \hat{\theta}_i \times \phi_i$. ; and (b) the scattered wave direction in forward scatter alignment (FSA), specified by \hat{k}_s , with $\hat{k}_s = \hat{\theta}_s \times \phi_s$. (adopted from Bringi and Chandrasekar (2001))

$\hat{k}_r = \hat{v}_r \times \hat{h}_r$. Fig. A.2 illustrates incident wave and scattered wave and the far-field scattered wave in spherical coordinate system for BSA convention.

The scattered wave components in BSA relate to those in FSA as,

$$\begin{bmatrix} E_h^r \\ E_v^r \end{bmatrix} = \begin{bmatrix} -1 & 0 \\ 0 & 1 \end{bmatrix} \begin{bmatrix} E_h^s \\ E_v^s \end{bmatrix} \quad (\text{A.10})$$

Substitution of (A.10) in (A.7), scattered wave components in BSA become,

$$\begin{bmatrix} E_h^r \\ E_v^r \end{bmatrix} = \frac{e^{-jk_0 r}}{r} \begin{bmatrix} -1 & 0 \\ 0 & 1 \end{bmatrix} \begin{bmatrix} S_{hh} & S_{hv} \\ S_{vh} & S_{vv} \end{bmatrix}_{FSA} \begin{bmatrix} E_h^i \\ E_v^i \end{bmatrix} \quad (\text{A.11})$$

where,

$$\mathbf{S}_{BSA} = \begin{bmatrix} -1 & 0 \\ 0 & 1 \end{bmatrix} \mathbf{S}_{FSA} \quad (\text{A.12})$$

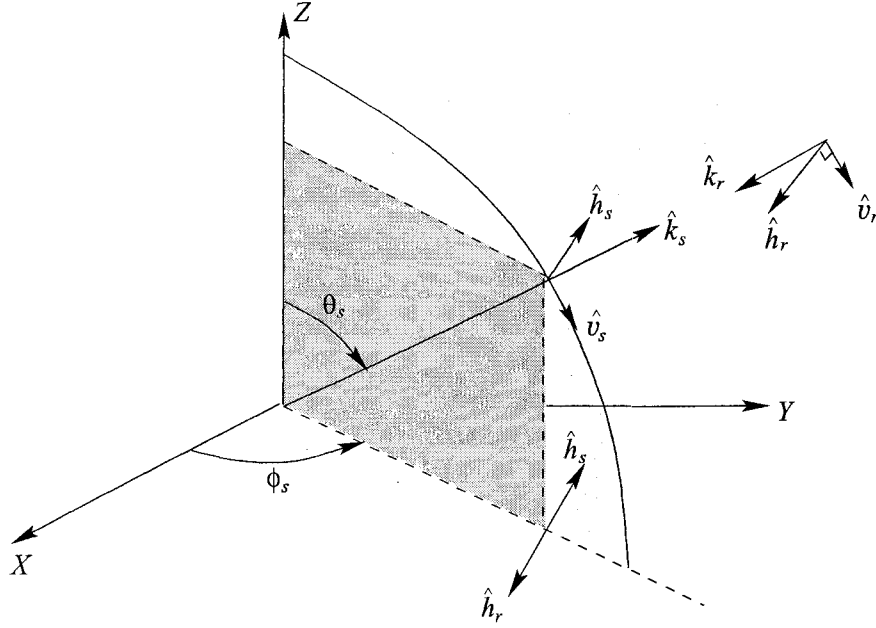


Figure A.2: Unit vectors $(\hat{k}_r, \hat{v}_r, \hat{h}_r)$ with $\hat{k}_r = \hat{v}_r \times \hat{h}_r$ for the back scatter alignment (BSA) convention. Note that $\hat{k}_r = -\hat{k}_s$, $\hat{v}_r = \hat{v}_s$ and $\hat{h}_r = -\hat{h}_s$. The scattered wave propagates along the \hat{k}_s direction. The scattered field is resolved as either $\vec{E}^s = E_h^s \hat{h}_s + E_v^s \hat{v}_s$ in the FSA, or as $\vec{E}^r = E_h^r \hat{h}_r + E_v^r \hat{v}_r$ in the BSA. (adopted from (Bringi and Chandrasekar, 2001))

For FSA, in the back scatter direction where $\hat{k}_s = -\hat{k}_i$, the angles (θ_s, ϕ_s) become $\theta_s = \pi - \theta_i$, $\phi_s = \phi_i + \pi$. Then $\hat{h}_s = -\hat{h}_i$ and $\hat{v}_s = \hat{v}_i$. In the BSA, $\hat{h}_r = \hat{h}_i$, $\hat{v}_r = \hat{v}_i$,

$\hat{k}_r = \hat{k}_i = -\hat{k}_s$ and the scattered wave triplet $(\hat{k}_r, \hat{v}_r, \hat{h}_r)$ with $\hat{k}_r = \hat{v}_r \times \hat{h}_r$ becomes identical to the incident wave triplet $(\hat{k}_i, \hat{v}_i, \hat{h}_i)$ with $\hat{k}_i = \hat{v}_i \times \hat{h}_i$. “In radar applications, this equivalence condition in the BSA is useful since the polarization state of an antenna, for example, is defined as the polarization of the wave radiated by the antenna, even when it is used as a receiving antenna” (Bringi and Chandrasekar, 2001).

A.2 Scattering matrix for dielectric sphere

A.2.1 Rayleigh Scattering

Let the incident wave direction be along the positive Z-axis, as shown in Fig. A.3. From (A.7), it follows that,

$$E_h^s = \frac{e^{(-jk_0r)}}{r} [S_{hh}E_h^i + S_{hv}E_v^i] \quad (\text{A.13a})$$

$$E_v^s = \frac{e^{(-jk_0r)}}{r} [S_{vh}E_h^i + S_{vv}E_v^i] \quad (\text{A.13b})$$

Let first the incident wave polarization be \hat{h}_i ; this means $E_v^i = 0$, and set $E_h^i = 1$, then

$$\vec{E}^s = \frac{e^{(-jk_0r)}}{r} [S_{hh}\hat{h}^s + S_{vh}\hat{v}^s] \quad (\text{A.14})$$

Consider (A.3) and (A.14), it appears that

$$\vec{f}(\hat{s}, \hat{i}) = S_{hh}\hat{h}^s + S_{vh}\hat{v}^s \quad (\text{A.15})$$

S_{hh} and S_{vh} elements of the scattering matrix can be determined as

$$\hat{h}^s \cdot (S_{hh}\hat{h}^s + S_{vh}\hat{v}^s) = \hat{h}^s \cdot (\vec{f}(\hat{s}, \hat{i})) \quad (\text{A.16a})$$

$$\hat{v}^s \cdot (S_{vh}\hat{h}^s + S_{vv}\hat{v}^s) = \hat{v}^s \cdot (\vec{f}(\hat{s}, \hat{i})) \quad (\text{A.16b})$$

Recall that $\vec{E}^i = E_h^i\hat{h}_i + E_v^i\hat{v}_i$, and for sphere $\hat{k}^s = \hat{r}$. Also from (A.9a) and (A.9b),

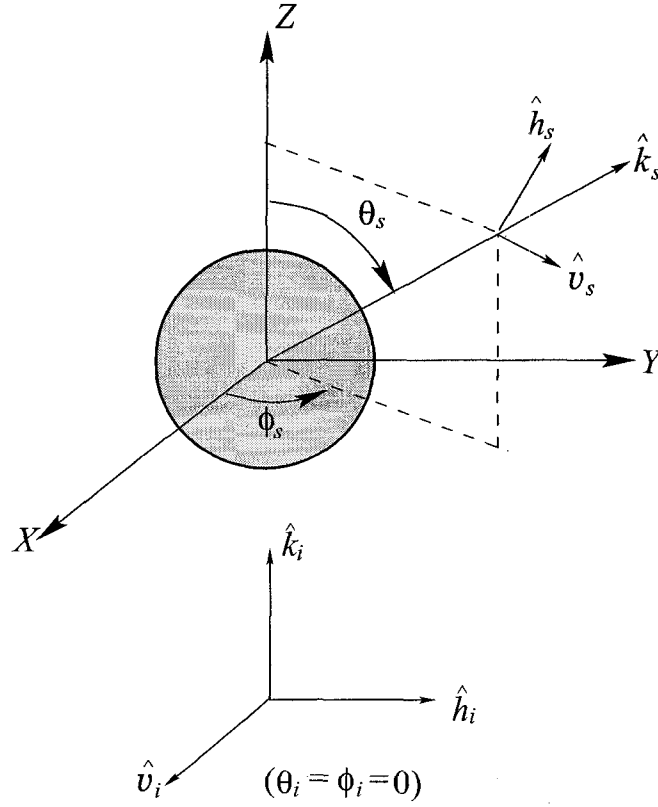


Figure A.3: Scattering direction and unit vectors of an incident plane wave in the FSA (adopted from Brongi and Chandrasekar (2001))

it is clear that when $\theta_i = \phi_i = 0^\circ$, then $\hat{h}_i = \hat{y}$ and $\hat{v}_i = \hat{x}$. Thus,

$$\begin{aligned}
 S_{hh} &= \frac{k_0^2 (\varepsilon_r - 1)}{4\pi (\varepsilon_r + 2)} 3V \left[\hat{h}_s \cdot (E_h^i \hat{h}_i + E_v^i \hat{v}_i) - \hat{h}_s \cdot \hat{k}_s (\hat{k}_s \cdot \vec{E}^i) \right] \\
 &= \frac{k_0^2 (\varepsilon_r - 1)}{4\pi (\varepsilon_r + 2)} 3V \left[(\hat{h}_s \cdot \hat{h}_i) \right] \\
 &= \frac{k_0^2 (\varepsilon_r - 1)}{4\pi (\varepsilon_r + 2)} 3V \left[(-\sin \phi_s \hat{x} + \cos \phi_s \hat{y}) \cdot \hat{y} \right] \\
 &= \frac{k_0^2 (\varepsilon_r - 1)}{4\pi (\varepsilon_r + 2)} 3V [\cos \phi_s] \tag{A.17}
 \end{aligned}$$

$$\begin{aligned}
S_{vh} &= \frac{k_0^2 (\varepsilon_r - 1)}{4\pi (\varepsilon_r + 2)} 3V \left[\hat{v}_s \cdot (E_h^i \hat{h}_i + E_v^i \hat{v}_i) - \hat{v}_s \cdot \hat{k}_s (\hat{k}_s \cdot \vec{E}^i) \right] \\
&= \frac{k_0^2 (\varepsilon_r - 1)}{4\pi (\varepsilon_r + 2)} 3V \left[(\hat{v}_s \cdot \hat{h}_i) \right] \\
&= \frac{k_0^2 (\varepsilon_r - 1)}{4\pi (\varepsilon_r + 2)} 3V \left[(\cos \phi_s \cos \theta_s \hat{x} + \sin \phi_s \cos \theta_s \hat{y} - \sin \theta_s \hat{z}) \cdot \hat{y} \right] \\
&= \frac{k_0^2 (\varepsilon_r - 1)}{4\pi (\varepsilon_r + 2)} 3V [\sin \phi_s \cos \theta_s] \tag{A.18}
\end{aligned}$$

Now, let the incident wave polarization be \hat{v}_i ; that means $E_h^i = 0$, and set $E_v^i = 1$, then

$$\vec{E}^s = \frac{e^{(-jk_0 r)}}{r} \left[S_{vv} \hat{h}_s + S_{hv} \hat{v}_s \right] \tag{A.19}$$

Consider again (A.3) and (A.19), it appears that

$$\vec{f}(\hat{s}, \hat{i}) = S_{vv} \hat{v}_s + S_{hv} \hat{h}_s \tag{A.20}$$

S_{vv} and S_{hv} elements of the scattering matrix can be determined as follows,

$$\hat{v}_s \cdot (S_{vv} \hat{v}_s + S_{hv} \hat{h}_s) = \hat{v}_s \cdot (\vec{f}(\hat{s}, \hat{i})) \tag{A.21a}$$

$$\hat{h}_s \cdot (S_{vv} \hat{v}_s + S_{hv} \hat{h}_s) = \hat{h}_s \cdot (\vec{f}(\hat{s}, \hat{i})) \tag{A.21b}$$

$$\begin{aligned}
S_{vv} &= \frac{k_0^2 (\varepsilon_r - 1)}{4\pi (\varepsilon_r + 2)} 3V \left[\hat{v}_s \cdot (E_h^i \hat{h}_i + E_v^i \hat{v}_i) - \hat{v}_s \cdot \hat{k}_s (\hat{k}_s \cdot \vec{E}^i) \right] \\
&= \frac{k_0^2 (\varepsilon_r - 1)}{4\pi (\varepsilon_r + 2)} 3V \left[(\hat{h}_s \cdot \hat{v}_i) \right] \\
&= \frac{k_0^2 (\varepsilon_r - 1)}{4\pi (\varepsilon_r + 2)} 3V \left[(\cos \phi_s \cos \theta_s \hat{x} + \sin \phi_s \cos \theta_s \hat{y} - \sin \theta_s \hat{z}) \cdot \hat{x} \right] \\
&= \frac{k_0^2 (\varepsilon_r - 1)}{4\pi (\varepsilon_r + 2)} 3V [\cos \theta_s \cos \phi_s] \tag{A.22}
\end{aligned}$$

$$\begin{aligned}
S_{hv} &= \frac{k_0^2 (\varepsilon_r - 1)}{4\pi (\varepsilon_r + 2)} 3V \left[\hat{h}_s \cdot (E_h^i \hat{h}_i + E_v^i \hat{v}_i) - \hat{h}_s \cdot \hat{k}_s (\hat{k}_s \cdot \vec{E}^i) \right] \\
&= \frac{k_0^2 (\varepsilon_r - 1)}{4\pi (\varepsilon_r + 2)} 3V \left[(\hat{h}_s \cdot \hat{v}_i) \right] \\
&= \frac{k_0^2 (\varepsilon_r - 1)}{4\pi (\varepsilon_r + 2)} 3V \left[(\cos \phi_s \cos \theta_s \hat{x} + \sin \phi_s \cos \theta_s \hat{y} - \sin \theta_s \hat{z}) \cdot \hat{x} \right] \\
&= \frac{k_0^2 (\varepsilon_r - 1)}{4\pi (\varepsilon_r + 2)} 3V [-\sin \phi_s] \tag{A.23}
\end{aligned}$$

Therefore, explicit expression for the scattering matrix for a dielectric sphere in the Rayleigh limit with incident plane wave along the positive Z -axis is,

$$\begin{bmatrix} E_h^s \\ E_v^s \end{bmatrix} = \frac{e^{-jk_0 r}}{r} \frac{k_0^2}{4\pi} \left(\frac{\epsilon_r - 1}{\epsilon_r + 2} \right) 3V \begin{bmatrix} \cos \phi_s & -\sin \phi_s \\ \cos \theta_s \sin \phi_s & \cos \theta_s \cos \phi_s \end{bmatrix}_{FSA} \begin{bmatrix} E_h^i \\ E_v^i \end{bmatrix} \quad (\text{A.24})$$

In the back scatter direction where $\theta_s = \pi - \theta_i = \pi$ and $\phi_s = \phi_i + \pi = \pi$, and suppressing the constant factors,

$$\mathbf{S}_{FSA} = \begin{bmatrix} -1 & 0 \\ 0 & 1 \end{bmatrix} \quad (\text{A.25a})$$

$$\mathbf{S}_{BSA} = \begin{bmatrix} 1 & 0 \\ 0 & 1 \end{bmatrix} \quad (\text{A.25b})$$

A.2.2 Mie Scattering

When the size of particle is no longer small relative to the radar wavelength, solving scattered wave is treated with non-Rayleigh scattering. Mie scattering yields solutions to four components of the scattering matrix for dielectric sphere as (Bringing and Chandrasekar, 2001),

$$(S_{hh})_{FSA} = \frac{i \cos \phi_s}{k_0} S_1(\theta_s) \quad (\text{A.26a})$$

$$(S_{vh})_{FSA} = \frac{i \sin \phi_s}{k_0} S_2(\theta_s) \quad (\text{A.26b})$$

$$(S_{hv})_{FSA} = \frac{-i \sin \phi_s}{k_0} S_1(\theta_s) \quad (\text{A.26c})$$

$$(S_{vv})_{FSA} = \frac{i \cos \phi_s}{k_0} S_2(\theta_s) \quad (\text{A.26d})$$

and thus,

$$\begin{bmatrix} E_h^s \\ E_v^s \end{bmatrix} = \frac{e^{-ik_0 r}}{r} \begin{bmatrix} \frac{i \cos \phi_s}{k_0} S_1(\theta_s) & \frac{-i \sin \phi_s}{k_0} S_1(\theta_s) \\ \frac{i \sin \phi_s}{k_0} S_2(\theta_s) & \frac{i \cos \phi_s}{k_0} S_2(\theta_s) \end{bmatrix}_{FSA} \begin{bmatrix} E_h^i \\ E_v^i \end{bmatrix} \quad (\text{A.27})$$

where

$$S_2(\theta_s) = \sum_{n=1}^{\infty} \frac{2n+1}{n(n+1)} \left\{ \alpha_{o1n} \frac{P_n^1(\cos \theta_s)}{\sin \theta_s} + \beta_{e1n} \frac{dP_n^1(\cos \theta_s)}{d\theta_s} \right\} \quad (\text{A.28a})$$

$$S_1(\theta_s) = \sum_{n=1}^{\infty} \frac{2n+1}{n(n+1)} \left\{ \alpha_{o1n} \frac{dP_n^1(\cos \theta_s)}{d\theta_s} + \beta_{e1n} \frac{P_n^1(\cos \theta_s)}{\sin \theta_s} \right\} \quad (\text{A.28b})$$

$$\alpha_{o1n} = \frac{\rho j_n(\rho)[\rho_o j_n(\rho_o)]' - \sqrt{\epsilon_r} \rho_o j_n(\rho_o)[\rho j_n(\rho)]'}{\sqrt{\epsilon_r} \rho_o h_n^{(2)}(\rho_o)[\rho j_n(\rho)]' - \rho j_n(\rho)[\rho_o h_n^{(2)}(\rho_o)]'} \quad (\text{A.29a})$$

$$\beta_{e1n} = \frac{\rho_o j_n(\rho_o)[\rho j_n(\rho)]' - \sqrt{\epsilon_r} \rho j_n(\rho)[\rho_o j_n(\rho_o)]'}{\sqrt{\epsilon_r} \rho j_n(\rho)[\rho_o h_n^{(2)}(\rho_o)]' - \rho_o h_n^{(2)}(\rho_o)[\rho j_n(\rho)]'} \quad (\text{A.29b})$$

and where

$$\rho_o = k_o a, \rho = \rho_o \sqrt{\epsilon_r}$$

$$[\rho j_n(\rho)]' = \rho j_{n-1}(\rho) - n j_n(\rho)$$

$$[\rho h_n^{(2)}(\rho)]' = \rho h_{n-1}^{(2)}(\rho) - n h_n^{(2)}(\rho)$$

The P_n^1 are the associated Legendre functions of the first kind.

The j_n are the spherical Bessel functions of the first kind.

The $h_n^{(2)}$ are the spherical Hankel functions of the second kind.

A.3 Extinction Cross-section and Backscatter Cross-section

A.3.1 Extinction Cross-section

The extinction cross-section is given as,

$$\sigma_{ext} = \frac{-4\pi}{k_o} \text{Im} \vec{f}(\hat{i}, \hat{i}) \cdot \hat{e}_i \quad (\text{A.30})$$

From (A.15) and using the fact, in forward scattered direction, that $\phi_s = \phi_i = 0$, $\hat{k}_s = \hat{r} = \hat{k}_i$, $\hat{h}_s = \hat{h}_i$, $\hat{v}_s = \hat{v}_i$, and that $\hat{e}_i = \hat{h}_i$ when setting $E_h^i = 1$ and $E_v^i = 0$,

$$\begin{aligned} \vec{f}(\hat{i}, \hat{i}) \cdot \hat{e}_i &= (S_{hh} \hat{h}^i + S_{vh} \hat{v}^i) \cdot \hat{h}_i \\ &= S_{hh} \\ &= \frac{k_0^2 (\epsilon_r - 1)}{4\pi (\epsilon_r + 2)} 3V [\cos \phi_s] \\ &= \frac{k_0^2 (\epsilon_r - 1)}{4\pi (\epsilon_r + 2)} 3V \end{aligned} \quad (\text{A.31})$$

Thus, in Rayleigh scattering, the extinction cross-section for dielectric sphere with...

complex $\varepsilon_r = \varepsilon_r' + j\varepsilon_r''$ has a simple form of

$$\begin{aligned}\sigma_{ext} &= \frac{-4\pi}{k_0} 3V \operatorname{Im} \left(\frac{k_0^2 (\varepsilon_r - 1)}{4\pi (\varepsilon_r + 2)} \right) \\ &= -k_0 3V \operatorname{Im} \left(\frac{(\varepsilon_r - 1)}{(\varepsilon_r + 2)} \right)\end{aligned}\quad (\text{A.32})$$

$$= 9k_0 V \frac{\varepsilon_r''}{|\varepsilon_r + 2|^2} \quad (\text{A.33})$$

Using (A.27) and (A.28), for $\theta_s = 0^\circ$, this yields,

$$\frac{dP_n^1(\cos \theta_s)}{d\theta_s} = \frac{P_n^1(\cos \theta_s)}{\sin \theta_s} = \frac{n(n+1)}{2} \quad (\text{A.34})$$

Mie solution to σ_{ext} of dielectric sphere is,

$$\sigma_{ext} = -\frac{2\pi}{k_0^2} \sum_{n=1}^{\infty} (2n+1) \operatorname{Re}(\alpha_{o1n} + \beta_{e1n}) \quad (\text{A.35})$$

where α_{o1n} and β_{e1n} are defined in (A.29).

A.3.2 Backscatter Cross-section

The backscatter or radar cross-section is defined as,

$$\sigma_b(-\hat{i}, \hat{i}) = 4\pi |\vec{f}(-\hat{i}, \hat{i})|^2 \quad (\text{A.36})$$

In Rayleigh scattering, from (A.15) and (A.17) with $\phi_s = \phi_i + \pi = \pi$,

$$\sigma_b(-\hat{i}, \hat{i}) = 4\pi \left| S_{hh} \hat{h}^s \right|^2 \quad (\text{A.37})$$

and, then

$$\sigma_b(-\hat{i}, \hat{i}) = 4\pi \left| \frac{k_0^2}{4\pi} 3V \frac{(\varepsilon_r - 1)}{(\varepsilon_r + 2)} \right|^2 \quad (\text{A.38})$$

$$= \frac{\pi^5}{\lambda^4} |K|^2 D^6 \quad (\text{A.39})$$

where $|k|^2 = \left| \frac{(\varepsilon_r - 1)}{(\varepsilon_r + 2)} \right|^2$ is dielectric factor and $D =$ is diameter of sphere.

In Mie scattering, from (A.28) with $\phi_s = \phi_i + \pi = \pi$, $\theta_s = \pi - \theta_i = \pi$ this results in,

$$\frac{dP_n^1(\cos \theta_s)}{d\theta_s} = (-1)^n \frac{n(n+1)}{2} = -\frac{P_n^1(\cos \theta_s)}{\sin \theta_s} \quad (\text{A.40})$$

By substitution above in (A.28) and substitution (A.28) in (A.26a) , and then substitution (A.26a) in (A.37) yields,

$$\sigma_b(-\hat{i}, \hat{i}) = \frac{\pi}{k_o^2} \left| \sum_{n=1}^{\infty} (-1)^n (2n+1) (\alpha_{o1n} - \beta_{e1n}) \right|^2 \quad (\text{A.41})$$

where α_{o1n} and β_{e1n} are defined in (A.29).

APPENDIX B

COEFFICIENTS OF THE k - Z_e RELATION AND VARIABILITY OF Z_e WITH FREQUENCY FOR SIMULATIONS

Table B.1: The coefficients of $Z_e(Ku) = a + bZ_e(S)$ and $k(Ku) = \alpha Z_e(Ku)^\beta$ relations for dry snow as a function of height above the bright band.

Height (km)	$Z_e(Ku) = a + bZ_e(S)$		$k(Ku) = \alpha Z_e(Ku)^\beta$	
	a	b	α	β
5	0.016636	0.99722	2.11e-05	0.8696
4.75	0.013105	0.99683	1.73e-05	0.88359
4.5	0.013954	0.99615	1.34e-05	0.90701
4.25	0.0076699	0.99599	1.09e-05	0.92415
4	0.003553	0.99526	9.1e-06	0.93895
3.75	-0.0006513	0.99457	7.8e-06	0.95144
3.5	-0.0062048	0.99384	7.1e-06	0.95817
3.25	-0.009727	0.99309	6.6e-06	0.96395
3	-0.0097367	0.99225	6.1e-06	0.96961
2.75	-0.024373	0.99132	5.5e-06	0.97921
2.5	-0.028435	0.99027	5.2e-06	0.98433
2.25	-0.027162	0.98867	4.8e-06	0.99035
2	0.0040484	0.98601	4.6e-06	0.99449
1.75	0.047648	0.98212	4.5e-06	0.99767
1.5	0.099835	0.97863	4.4e-06	1.001
1.25	0.11023	0.9757	4.1e-06	1.0071
1	0.1692	0.97026	4e-06	1.0112
0.75	0.25009	0.96383	3.9e-06	1.0159
0.5	0.32567	0.95756	3.7e-06	1.0231
0.25	0.36006	0.95131	3.6e-06	1.0301

Table B.2: The coefficients of $Z_e(Ka) = a + bZ_e(S)$ and $k(Ka) = \alpha Z_e(Ka)^\beta$ relations for dry snow as a function of height above the bright band.

Height (km)	$Z_e(Ka) = a + bZ_e(S)$		$k(Ka) = \alpha Z_e(Ka)^\beta$	
	a	b	α	β
5	0.10513	0.98083	0.0001699	1.0065
4.75	0.080618	0.97812	0.0001652	1.0117
4.5	0.086502	0.97347	0.000161	1.017
4.25	0.04333	0.97235	0.0001581	1.0214
4	0.014508	0.96729	0.0001566	1.0254
3.75	-0.014374	0.96259	0.0001525	1.0319
3.5	-0.052485	0.95754	0.0001605	1.0297
3.25	-0.077352	0.95251	0.0001414	1.0492
3	-0.077543	0.9468	0.0001328	1.0612
2.75	-0.17889	0.94061	0.0001397	1.0613
2.5	-0.20777	0.93364	0.0001359	1.0715
2.25	-0.20238	0.92315	0.0001304	1.0822
2	0.0002772	0.90592	0.0001221	1.0982
1.75	0.27269	0.88126	0.0001615	1.0765
1.5	0.58316	0.85994	0.0001279	1.1141
1.25	0.60136	0.84364	0.0001188	1.1343
1	0.848	0.81567	0.0001294	1.1399
0.75	1.0943	0.7863	0.0001362	1.1494
0.5	1.1634	0.76469	0.0001264	1.1789
0.25	0.8161	0.75056	0.0001453	1.1837

Table B.3: The coefficients of $Z_e(Ka) = a + bZ_e(Ku)$ relations for dry snow as a function of height above the bright band.

Height (km)	$Z_e(Ka) = a + bZ_e(Ku)$	
	a	b
5	0.088607	0.98357
4.75	0.0675	0.98125
4.5	0.072445	0.97725
4.25	0.035347	0.9763
4	0.010336	0.97194
3.75	-0.014642	0.96789
3.5	-0.047674	0.96355
3.25	-0.069519	0.95921
3	-0.070168	0.9543
2.75	-0.15822	0.94898
2.5	-0.18428	0.943
2.25	-0.18184	0.93396
2	-0.010835	0.91912
1.75	0.2184	0.89782
1.5	0.47705	0.87946
1.25	0.48295	0.8656
1	0.67568	0.84182
0.75	0.82335	0.81829
0.5	0.81024	0.80191
0.25	0.4178	0.79296

Table B.4: The coefficients of $Z_e(Ku) = a + bZ_e(S)$ and $k(Ku) = \alpha Z_e(Ku)^\beta$ relations for wet snow as a function of height above (+) and below (-) bright band peak.

Height (km)	$Z_e(Ku) = a + bZ_e(S)$		$k(Ku) = \alpha Z_e(Ku)^\beta$	
	a	b	α	β
0.5	-0.14968	0.93722	4.56e-05	0.89579
0.25	-0.30961	0.92431	3.32e-05	0.94013
0	0.68409	0.93198	2.51e-05	0.94419
-0.25	0.56841	0.97377	3.5e-05	0.91037
-0.5	-0.24068	0.99666	5.21e-05	0.91526

Table B.5: The coefficients of $Z_e(Ka) = a + bZ_e(S)$ and $k(Ka) = \alpha Z_e(Ka)^\beta$ relations for wet snow as a function of height above (+) and below (-) the bright band peak.

Height (km)	$Z_e(Ka) = a + bZ_e(S)$		$k(Ka) = \alpha Z_e(Ka)^\beta$	
	a	b	α	β
0.5	-3.6281	0.7782	0.0007851	1.1047
0.25	-6.1438	0.79994	0.0010333	1.1081
0	-2.9095	0.79132	0.0005788	1.1173
-0.25	3.7331	0.74158	0.0003707	1.1211
-0.5	3.8319	0.81709	0.0005536	1.0176

Table B.6: The coefficients of $Z_e(Ka) = a + bZ_e(Ku)$ relations for wet snow as a function of height above (+) and below (-) the bright band peak.

Height (km)	$Z_e(Ka) = a + bZ_e(Ku)$	
	a	b
0.5	-3.8229	0.84234
0.25	-6.3981	0.8816
0	-3.9816	0.86204
-0.25	3.1989	0.76426
-0.5	4.0653	0.81887

Table B.7: The coefficients of $Z_e(Ku) = a + b*Z_e(S)$ and $k(Ku) = \alpha*Z_e(Ku)^\beta$ relations for rain as a function of height below the bright band.

Height (km)	$Z_e(Ku) = a + b*Z_e(S)$		$k(Ku) = \alpha*Z_e(Ku)^\beta$	
	a	b	α	β
0	-1.0677	1.0667	0.0001163	0.85895
0.25	-1.1186	1.0678	0.0001218	0.85633
0.5	-1.0742	1.0676	0.000111	0.86456
0.75	-1.2202	1.07	0.0001126	0.86167
1	-1.0825	1.0672	0.0001042	0.86894
1.25	-1.1573	1.0693	9.76e-05	0.87499
1.5	-1.1448	1.0699	0.0001097	0.86267
1.75	-1.0612	1.0674	0.000111	0.86399
2	-1.1525	1.0699	8.79e-05	0.882
2.25	-1.0521	1.0676	9.62e-05	0.8747
2.5	-1.0547	1.0684	9.67e-05	0.87436
2.75	-1.0894	1.0685	0.0001205	0.85533
3	-1.0902	1.0687	0.0001108	0.86235
3.25	-1.079	1.0681	0.0001032	0.86808
3.5	-1.0994	1.0685	0.0001116	0.86134
3.75	-1.122	1.0699	8.07e-05	0.88907
4	-1.0896	1.0682	0.0001059	0.86611

Table B.8: The coefficients of $Z_e(Ka) = a + b*Z_e(S)$ and $k(Ka) = \alpha*Z_e(Ka)^\beta$ relations for rain as a function of height below the bright band.

Height (km)	$Z_e(Ka) = a + b*Z_e(S)$		$k(Ka) = \alpha*Z_e(Ka)^\beta$	
	a	b	α	β
0	3.859	0.86064	0.0005514	0.97657
0.25	3.9058	0.8604	0.0005439	0.97795
0.5	3.7792	0.86156	0.0005148	0.98309
0.75	4.3931	0.84757	0.0005226	0.98175
1	3.9339	0.85946	0.0005158	0.98287
1.25	4.057	0.85511	0.0005212	0.98189
1.5	4.0892	0.85115	0.0005111	0.98336
1.75	4.0027	0.85499	0.0005175	0.98259
2	4.0397	0.85348	0.0005325	0.97977
2.25	3.7807	0.86091	0.0005275	0.9806
2.5	3.8456	0.85744	0.0005228	0.98131
2.75	3.8815	0.85865	0.0005426	0.9778
3	3.895	0.85721	0.0005341	0.97953
3.25	4.094	0.85141	0.0005136	0.98296
3.5	3.9482	0.85573	0.0005267	0.98066
3.75	4.0002	0.85264	0.000511	0.9833
4	3.8994	0.85836	0.0005347	0.97928

Table B.9: The coefficients of $Z_e(Ka) = a + b*Z_e(Ku)$ relations for rain as a function of height below the bright band.

Height (km)	$Z_e(Ka) = a + b*Z_e(Ku)$	
	a	b
0	4.8022	0.80456
0.25	4.892	0.80342
0.5	4.7279	0.80467
0.75	5.4598	0.78936
1	4.8884	0.80302
1.25	5.0763	0.797
1.5	5.0823	0.79326
1.75	4.9505	0.79833
2	5.0609	0.79478
2.25	4.719	0.80383
2.5	4.7738	0.8002
2.75	4.8487	0.80099
3	4.8587	0.79951
3.25	5.0448	0.79463
3.5	4.9115	0.7985
3.75	4.9746	0.79467
4	4.8665	0.80094

Table B.10: The coefficients of $Z_e(Ku) = a + bZ_e(S)$ and $k(Ku) = \alpha Z_e(Ku)^\beta$ relations for dry graupel as a function of height above the melting layer.

Height (km)	$Z_e(Ku) = a + bZ_e(S)$		$k(Ku) = \alpha Z_e(Ku)^\beta$	
	a	b	α	β
5	-0.081476	0.99435	4.6e-06	0.98766
4.75	-0.081094	0.99386	4.5e-06	0.99103
4.5	-0.084101	0.99385	4.4e-06	0.99164
4.25	-0.087791	0.99359	4.4e-06	0.99293
4	-0.092415	0.99352	4.3e-06	0.99528
3.75	-0.088052	0.99288	4.4e-06	0.99431
3.5	-0.094002	0.99298	4.3e-06	0.9964
3.25	-0.10326	0.99244	4.3e-06	0.99836
3	-0.09854	0.99174	4.2e-06	0.9999
2.75	-0.093666	0.99096	4.1e-06	1.0022
2.5	-0.087433	0.98981	4.1e-06	1.0027
2.25	-0.075908	0.98931	4.1e-06	1.0046
2	-0.06931	0.98818	4.1e-06	1.0055
1.75	-0.04773	0.98608	4.1e-06	1.0044
1.5	-0.039978	0.98574	4e-06	1.008
1.25	-0.019644	0.98424	3.9e-06	1.0105
1	-0.0038071	0.98323	3.9e-06	1.0116
0.75	0.038208	0.98107	3.9e-06	1.0128
0.5	0.058474	0.97978	3.8e-06	1.0165
0.25	0.15986	0.97467	3.8e-06	1.0165

Table B.11: The coefficients of $Z_e(Ka) = a + bZ_e(S)$ and $k(Ka) = \alpha Z_e(Ka)^\beta$ relations for dry graupel as a function of height above the melting layer.

Height (km)	$Z_e(Ka) = a + bZ_e(S)$		$k(Ka) = \alpha Z_e(Ka)^\beta$	
	a	b	α	β
5	-0.63888	0.95642	0.0001684	1.055
4.75	-0.63716	0.95232	0.0001714	1.0528
4.5	-0.66096	0.95222	0.000161	1.0661
4.25	-0.69226	0.95008	0.0001608	1.0681
4	-0.72822	0.94957	0.0001561	1.0758
3.75	-0.69298	0.9444	0.000176	1.0577
3.5	-0.74014	0.94516	0.0001653	1.0698
3.25	-0.81616	0.94083	0.0001789	1.0611
3	-0.77529	0.93523	0.0001706	1.0708
2.75	-0.7375	0.92915	0.0001523	1.0903
2.5	-0.68585	0.92022	0.0001782	1.0705
2.25	-0.59295	0.91622	0.000151	1.0954
2	-0.54281	0.9078	0.0001587	1.0932
1.75	-0.3731	0.89199	0.0001917	1.07
1.5	-0.31791	0.89002	0.0001584	1.0985
1.25	-0.16833	0.87953	0.0001567	1.1047
1	-0.054556	0.87269	0.0001531	1.1081
0.75	0.2245	0.85918	0.0001512	1.1143
0.5	0.35858	0.85106	0.000134	1.132
0.25	0.94171	0.82141	0.0001764	1.1077

Table B.12: The coefficients of $Z_e(Ka) = a + bZ_e(Ku)$ relations for dry graupel as a function of height above the melting layer.

Height (km)	$Z_e(Ka) = a + bZ_e(Ku)$	
	a	b
5	-0.56078	0.96193
4.75	-0.55984	0.95828
4.5	-0.58088	0.9582
4.25	-0.60889	0.9563
4	-0.6404	0.95586
3.75	-0.6101	0.95129
3.5	-0.65167	0.95198
3.25	-0.71923	0.94814
3	-0.68397	0.94319
2.75	-0.65168	0.93781
2.5	-0.60687	0.92992
2.25	-0.52539	0.92636
2	-0.48361	0.91897
1.75	-0.33507	0.90491
1.5	-0.28809	0.90327
1.25	-0.15919	0.8941
1	-0.062269	0.88815
0.75	0.17591	0.87646
0.5	0.28945	0.86946
0.25	0.78238	0.84375

Table B.13: The coefficients of $Z_e(Ku) = a + bZ_e(S)$ and $k(Ku) = \alpha Z_e(Ku)^\beta$ relations for wet graupel as a function of height above (+) and below (-) the center of the melting layer.

Height (km)	$Z_e(Ku) = a + bZ_e(S)$		$k(Ku) = \alpha Z_e(Ku)^\beta$	
	a	b	α	β
0.5	-0.069727	0.98828	3.11e-05	0.85695
0.25	-0.047519	0.98771	6.23e-05	0.81931
0	-0.04097	0.98928	7.27e-05	0.8621
-0.25	0.061622	0.99274	8.21e-05	0.84676
-0.5	-1.7061	1.017	7.43e-05	0.89347

Table B.14: The coefficients of $Z_e(Ka) = a + b*Z_e(S)$ and $k(Ka) = \alpha*Z_e(Ka)^\beta$ relations for wet graupel as a function of height above (+) and below (-) the center of the melting layer.

Height (km)	$Z_e(Ka) = a + b*Z_e(S)$		$k(Ka) = \alpha*Z_e(Ka)^\beta$	
	a	b	α	β
0.5	-0.51908	0.90525	0.0002793	1.0476
0.25	-0.32865	0.89884	0.0003657	1.0333
0	-0.24758	0.87369	0.0006872	1.0119
-0.25	1.1982	0.84989	0.0006419	1.0422
-0.5	3.0445	0.83916	0.0005342	1.014

Table B.15: The coefficients of $Z_e(Ka) = a + b*Z_e(Ku)$ relations for wet graupel as a function of height above (+) and below (-) the center of the melting layer.

Height (km)	$Z_e(Ka) = a + b*Z_e(Ku)$	
	a	b
0.5	-0.45905	0.91626
0.25	-0.29038	0.91033
0	-0.21827	0.88352
-0.25	1.1356	0.85648
-0.5	4.5648	0.82229

Table B.16: The coefficients of $Z_e(Ku) = a + b*Z_e(S)$ and $k(Ku) = \alpha*Z_e(Ku)^\beta$ relations for rain as a function of height below the melting layer.

Height (km)	$Z_e(Ku) = a + b*Z_e(S)$		$k(Ku) = \alpha*Z_e(Ku)^\beta$	
	a	b	α	β
0.25	-0.74366	1.0497	0.0001645	0.85542
0.5	-0.85534	1.052	0.0001666	0.85304
0.75	-0.7614	1.05	0.0001449	0.86463
1	-0.74952	1.0493	0.0001512	0.86247
1.25	-0.81846	1.0517	0.000155	0.8603
1.5	-0.75944	1.0501	0.0001198	0.88143
1.75	-0.76781	1.0504	0.0001514	0.86103
2	-0.7179	1.0493	0.0001349	0.87198
2.25	-0.79386	1.0513	0.0001379	0.86896
2.5	-0.84385	1.0528	0.0001662	0.85255
2.75	-0.85484	1.0524	0.0001272	0.87239
3	-0.7993	1.0519	0.0001534	0.85822
3.25	-0.82464	1.0533	0.0001316	0.86955
3.5	-0.80773	1.0525	0.0001337	0.8676
3.75	-0.81402	1.0529	0.0001505	0.85876
4	-0.81231	1.0514	0.0001766	0.84625

Table B.17: The coefficients of $Z_e(Ka) = a + b*Z_e(S)$ and $k(Ka) = \alpha*Z_e(Ka)^\beta$ relations for rain as a function of height below the melting layer.

Height (km)	$Z_e(Ka) = a + b*Z_e(S)$		$k(Ka) = \alpha*Z_e(Ka)^\beta$	
	a	b	α	β
0.25	1.5666	0.94567	0.0006605	0.96426
0.5	1.8427	0.93823	0.0006673	0.96295
0.75	1.5662	0.94506	0.0006547	0.96459
1	1.4847	0.94764	0.0006717	0.96257
1.25	1.7935	0.93815	0.0006452	0.96615
1.5	1.5837	0.94465	0.0006423	0.96658
1.75	1.5942	0.9439	0.0006542	0.9649
2	1.3613	0.94903	0.0006263	0.96874
2.25	1.6659	0.94267	0.0006638	0.96363
2.5	1.906	0.93488	0.0006562	0.96428
2.75	1.9211	0.93637	0.0006436	0.9657
3	1.7887	0.93804	0.0006452	0.96567
3.25	1.8776	0.93183	0.000638	0.96632
3.5	1.8136	0.93717	0.0006218	0.96857
3.75	1.8315	0.93482	0.0006327	0.96717
4	1.7763	0.94081	0.0006644	0.9631

Table B.18: The coefficients of $Z_e(Ka) = a + b \cdot Z_e(Ku)$ relations for rain as a function of height below the melting layer.

Height (km)	$Z_e(Ka) = a + b \cdot Z_e(Ku)$	
	a	b
0.25	2.3016	0.89882
0.5	2.6746	0.88969
0.75	2.3124	0.89808
1	2.2227	0.90121
1.25	2.5931	0.88998
1.5	2.3332	0.89747
1.75	2.3482	0.89658
2	2.0688	0.90263
2.25	2.4494	0.89441
2.5	2.7248	0.88584
2.75	2.7621	0.88726
3	2.5688	0.88964
3.25	2.6762	0.88251
3.5	2.5972	0.88838
3.75	2.6234	0.88576
4	2.5741	0.89261

APPENDIX C

DUAL-POLARIZATION RADAR MEASUREMENTS

Five polarimetric radar measurements namely, horizontal reflectivity (Z_h), differential reflectivity (Z_{dr}), specific differential phase (K_{dp}), linear depolarization ratio (LDR), and correlation coefficient (ρ_{hv}) are useful to classify hydrometeor type.

C.1 Polarimetric Radar Measurements

C.1.1 Reflectivity (Z_h)

Z_h is proportional to the received power at h-port and related to the power of a horizontally polarized backscattered electric field from a radar resolution volume for a horizontally polarized transmitted wave. The equation is given by

$$Z_h = (4\lambda^4/\pi^4|K_w|^2) \langle |s_{hh}|^2 \rangle \quad (\text{C.1})$$

where λ is the wavelength of the radar, K_w is dielectric constant of water, and s_{hh} refers to an element of the backscattering matrix. For a particle of given size, ice produces lower Z_h than does liquid because of lower dielectric effects. Therefore, The reflectivity factor plays the important role to classify hydrometeor type.

C.1.2 Differential Reflectivity (Z_{dr})

Differential reflectivity is obtained from the ratio of horizontal reflectivity and vertical reflectivity and is given by

$$Z_{dr} = 10\log(Z_h/Z_v)(dB) \quad (\text{C.2})$$

Z_{dr} is a very reliable polarimetric parameter, which is a good discriminator between oblate rain and more spherical hail. The sharp change in Z_{dr} occurs near the 0°C isotherm and marks the transition between ice particles and water.

C.1.3 Specific Differential Phase (K_{dp})

K_{dp} is the difference between propagation consonants for horizontally and vertically polarized signals, which can be defined as,

$$\phi_{dp} = \phi_{hh} - \phi_{vv} \qquad K_{dp} = \frac{1}{2} \frac{d\phi_{dp}}{dr} \qquad (\text{C.3})$$

where ϕ_{hh} and ϕ_{vv} are the phase of the horizontally and vertically polarized waves, and r is the distance of measurements from a radar. Specific differential phase is independent of absolute calibration and it is not affected by attenuation and is dependent on hydrometeor number concentration. K_{dp} can be used to isolate the presence of rain from isotropic hydrometeors such as tumbling hail.

C.1.4 Linear Depolarization Ratio (LDR)

The ratio of the received cross-polar power to the transmitted co-polar power defines the linear depolarization ratio. LDR is can be expressed by

$$LDR = 10 \log(\langle |s_{vh}|^2 \rangle / \langle |s_{hh}|^2 \rangle) (\text{dB}) \qquad (\text{C.4})$$

The hydrometeor characteristics associated with depolarization of transmitted energy include hydrometeor shape, shape irregularity, thermodynamic phase, dielectric constant, and canting in the plane of polarization. Tumbling, wet nonspherical particles such as hail, melting aggregates, and wet graupel can be identified with large LDR values, whereas drizzle, and dry ice particles are associated with low LDR values. In CSU-CHILL radar, the lower limit of LDR measurement is about -34 dB.

C.1.5 Correlation Coefficient (ρ_{hv})

The correlation coefficient between horizontally and vertically polarized echoes is affected by the variability in the ratio of the vertical to horizontal size of individual hydrometeors. The correlation coefficient is defined by

$$\rho_{hv}(0) = \frac{\langle s_{vv}s_{hh}^* \rangle}{(\langle s_{hh}^2 \rangle^{1/2} \langle s_{vv}^2 \rangle^{1/2})} \quad (\text{C.5})$$

Values of ρ_{hv} are close to unity for rain and pure ice crystals. In the case of melting and mixed phase (rain and hail, wet graupel or wet snow) conditions, ρ_{hv} is smaller than unity. Low values of ρ_{hv} can be used for detecting hail and mixed phase precipitation.

BIBLIOGRAPHY

- Adam, W. J., 2002: Global Precipitation Measurement-Report 8. Tech. rep., NASA/TM-2002-211609.
- Atlas, D. and C. W. Ulbrich, 1977: Path- and area- integrated rainfall measurement by microwave attenuation in the 1-3 cm band. *J. Appl. Meteor.*, **16**, 1322–1331.
- Awaka, J., Y. Furuhashi, M. Hoshiyama, and A. Nishitsuji, 1985: Model calculations of scattering properties of spherical brightband particles made of composite dielectrics. *J. Radio Res. Lab*, **32**, 73–87.
- Awaka, J., T. Iguchi, H. Kumagai, and K. Okamoto, 1997: Rain type classification algorithm for TRMM precipitation radar. *Proc. IEEE IGARSS'97*, 317–319.
- Awaka, J., T. Iguchi, and K. Okamoto, 1998: Early results on rain type classification by the Tropical Rainfall Measurement Mission (TRMM) precipitation radar. *Proc. 8th URSI commission F Open Symp., Aveiro, Portugal*, 143–146.
- Beaver, J. D. and V. N. Bringi, 2003: The application of S-band polarimetric radar measurements to Ka band attenuation prediction. *IEEE Trans. Geosci. Remote Sens.*, **41**, 2153–2165.
- Beheng, K., 1978: Numerical simulation of graupel development. *J. Atmos. Sci.*, **35**, 683–689.
- Bolen, S. and V. Chandrasekar, 2000: Quantitative cross validation of space-based and ground-based radar observations. *J. Appl. Meteor.*, 2071–2079.

- , 2003: Methodology for aligning and comparing spaceborne radar and ground-based radar observations. *J. Atmos. Oceanic Technol.*, **20**, 647–659.
- Bringi, V. and V. Chandrasekar, 2001: *Doppler weather Radar-Principles and Applications*. Cambridge University Press.
- Bringi, V. N., V. Chandrasekar, and J. Hubbert, 2003: Raindrop size distribution in different climatic regimes from disdrometer and dual-polarized radar analysis. *J. Atmos. Sci.*, **60**, 354–365.
- Bringi, V. N., K. Knupp, A. Detwiler, L. Liu, I. Caylor, and R. Black, 1997: Evolution of a Florida thunderstorm during the convection and precipitation/electrification experiment: The case of 9 august 1991. *Mon. Weath. Rev.*, **125**, 2131–2160.
- Bringi, V. N., T. Tang, and V. Chandrasekar, 2004: Evaluation of a new polarimetrically based *Z-R* relation. *J. Atmos. Oceanic Technol.*, **21**, 612–623.
- Brunkow, D., V. N. Bringi, P. C. Kennedy, S. A. Rutledge, V. Chandrasekar, R. K. Bowie, and E. A. Mueller, 2000: A description of the CSU-CHILL national radar facility. *J. Atmos. Oceanic Technol.*, **17**, 1596–1608.
- Chandrasekar, V., S. Bolen, and E. Gorgucci, 2003a: Microphysical cross-validation of spaceborne radar and ground polarimetric radar observations. *IEEE Trans. Geosci. Remote Sens.*, **41**, 2153–2165.
- Chandrasekar, V., R. Meneghini, and I. Zawadzki, 2003b: Global and local precipitation measurements by radar. *Meteorological Monographs*, **30**, ISBN 1–878 220–57–8.
- Chandrasekar, V., L. Wanyu, and B. Zafar, 2005: Estimation of raindrop size distribution from spaceborne radar observations. *IEEE Trans. Geosci. Remote Sens.*, **43** (5), 1078–1086.

- Cherry, S. M., J. W. F. Goddard, and M. P. M. Hall, 1981: Use of dual-polarization radar data for evaluation of attenuation on a satellite-to-earth path. *Ann. Telecommun.*, **36**, 33–39.
- Cifelli, R., W. A. Peterson, L. D. Carey, S. A. Rutledge, and S. D. A. F. Maria, 2002: Radar observations of the kinematics, microphysical, and precipitation characteristics of two MCSs, in TRMM LBA. *J. Geophys. Res.*, **107 (D20)**, 8077.
- Cox, D., 1978: An overview of the bell laboratories 19 and 28 ghz comstar beacon propagation experiments. *J. Bell Syst. Tech.*, **57 (4)**, 1231–1240.
- Crum, D. T., R. E. Saffle, and J. W. Wilson, 1998: An update on the NEXRAD program and future WRS-88D support to operations. *J. Weather and Forecasting.*, **13**, 253–262.
- Fabry, F. and W. Szyrmer, 1999: Modeling of the melting layer, Part ii: Electromagnetic. *J. Atmos. Sci.*, **56**, 3593–3600.
- Fabry, F. and I. Zawadzki, 1995: Long-term radar observations of the melting layer of precipitation and their interpretation. *J. Atmos. Sci.*, **52 (7)**, 838–851.
- Fukatsu, H. and V. Chandrasekar, 2002: Global mapping of attenuation at X-band and higher frequencies. *Proc. IEEE IGARSS'02*, Vol. 1, 293–295.
- Goddard, J. W. F., J. D. Eastment, and M. Thurai, 1994: The chilbolton advanced meteorological radar: A tool for multidisciplinary atmospheric research. *J. Electron. and Commun. Eng.*, **6 (2)**, 77–86.
- Gorgucci, E., G. Scarchilli, V. Chandrasekar, and V. Bringi, 2002: Estimation of rain-drop size distribution parameters from polarimetric radar measurement. *J. Atmos. Sci.*, **59 (15)**, 2373–2384.

- GVS, 2007: *Global Precipitation Mission(GPM) Ground Validation System*. Goddard Space Flight Center, Greenbelt, Maryland, Draft ed.
- Hanado, H. and T. Ihara, 1992: Evaluation of surface clutter for design of the TRMM spaceborne radar. *IEEE Trans. Geosci. Remote Sens.*, **30**, 444–453.
- Haykin, S., 1998: *Neural networks a comprehensive foundation*. Prentice Hall.
- Hitschfeld, W. and J. Bordan, 1954: Errors inherent in the radar measurement of rainfall at attenuating wavelengths. *J. Meteor.*, **11**, 58–67.
- House, R. A., 1997: Stratiform precipitation in regions of convective: A meteorological paradox? *Bul. American Met. Soc.*, **78**, 2179–2196.
- Iguchi, T., 2003: Spaceborne precipitation radars in TRMM and GPM. *31st Conf. on Radar Meteorology*, Amer. Meteor. Soc., Seattle, WA, CD-ROM.
- , 2005: Possible algorithms for the dual-frequency precipitation radar (DPR) on the GPM core satellite. *32nd Conf. on Radar Meteorology*, Amer. Meteor. Soc., Albuquerque, NM, CD-ROM.
- Iguchi, T., H. Hanado, and T. Kozu, 2001: Accuracy of rain rate retrieval from dual-frequency precipitation radar data. *Proc. IEEE IGARSS'01*, Vol. 1, 317–319.
- Iguchi, T., T. Kozu, R. Meneghini, J. Awaka, and K. Okamoto, 2000: Rain-profiling algorithm for the TRMM precipitation radar. *J. Appl. Meteor*, **39**, 2038–2052.
- Iguchi, T. and R. Meneghini, 1994: Intercomparison of single-frequency methods for retrieving a vertical rain profile from airborne or spaceborne radar data. *J. Atmos. Oceanic Technol.*, **11**, 1507–1516.
- , 1995: Differential equations for dual-frequency radar returns. *27th Conf. on Radar Meteorology*, Amer. Meteor. Soc., Vail, CO, 190–193.

- Im, E., S. L. Durden, G. Sadowy, and L. Li, 2002: Rainfall observations by the airborne dual-frequency precipitation radar during CAMEX-4. *Proc. IEEE IGARSS'02*, 281–283.
- Ippolito, L. J., 1981: Radio-wave propagation for space communications systems. Tech. rep., National Aeronautics and Space Administration (NASA).
- Kohonen, T., 1990: The self-organizing map. *Proceeding of the IEEE*, Vol. 78, 1464–1480.
- Kozu, T., T. Kawanishi, and H. Kuroiwa, 2001: Development of precipitation radar onboard the tropical rainfall measuring mission (TRMM) satellite. *IEEE Trans. Geosci. Remote Sens.*, **39** (1), 102–116.
- Kummerow, C., W. Barnes, and T. Kozu, 1998: The tropical rainfall measuring mission (TRMM) sensor package. *J. Atmos. Oceanic Tech.*, **15**, 809–817.
- Kummerow, C., O. Simpson, and W. Thiele, 2000: The status of the tropical rainfall measuring mission (TRMM) after two years in orbit. *J. Appl. Meteor.*, **39**, 1965–1982.
- L'Ecuyer, T. S., C. Kummerow, and H. Masunaga, 2003: Relationships between the microphysics of precipitating cloud systems and their radar reflectivity patterns. *31st Conf. on Radar Meteorology*, Amer. Meteor. Soc., Seattle, WA, 399–402.
- Liao, L., R. Meneghini, T. Iguchi, and A. Detwiler, 2005: Use of dual-wavelength radar for snow parameter estimates. *J. Atmos. Oceanic Technol.*, **22**, 1494–1506.
- Lim, S. and V. Chandrasekar, 2005: Hydrometeor classification system using dual-polarization radar measurement: Model improvements and in situ verification. *IEEE Trans. Geosci. Remote Sens.*, **43** (4), 792–801.

- Mardiana, R., T. Iguchi, and N. Takahashi, 2004: A dual-frequency rain profiling method without the use of a surface reference technique. *IEEE Trans. Geosci. Remote Sens.*, **42**, 2214–2225.
- Marshall, T. S. and W. M. Palmer, 1948: The distribution of raindrops with size. *J. Meteorol*, **5** (4), 165–166.
- Matrosov, S. Y., 1992: Radar reflectivity in snowfall. *IEEE Trans. Geosci. Remote Sens.*, **30**, 454–461.
- , 1998: A dual-wavelength radar method to measure snowfall rate. *J. Appl. Meteor*, **7**, 1510–1521.
- Meneghini, R., T. Iguchi, T. Kozi, T. Kawanishi, H. Kuroiwa, H. Okamoto, and D. Atlas, 2001: The TRMM precipitation radar: opportunities and challenges. *29nd Conf. on Radar Meteorology*, Amer. Meteor. Soc., Montreal, Quebec, Canada, 621–624.
- Meneghini, R., T. Iguchi, T. Kozi, L. Liao, K. Okamoto, J. A. Jones, and J. Kwiatkowski, 2000: Use of the surface reference technique for path attenuation estimates from the TRMM precipitation radar. *J. Appl. Meteor*, **39**, 2053–2070.
- Meneghini, R. and T. Kozi, 1990: *Spaceborne Weather Radar*. Artech House, Inc.
- Meneghini, R., T. Kozi, H. Kumagai, and W. C. Boncyk, 1992: A study of rain estimation methods from space using dual-wavelength radar measurements at near-nadir incidence over ocean. *J. Atmos. Oceanic Technol.*, **9**, 364–382.
- Meneghini, R., H. Kumagai, J. R. Wang, T. Iguchi, and T. Kozi, 1997: Microphysical retrievals over stratiform rain using measurements from an airborne dual-wavelength radar-radiometer. *IEEE Trans. Geosci. Remote Sens.*, **35**, 487–506.

- Meneghini, R. and L. Liao, 1996: Comparison of cross sections for melting hydrometeors as derived from dielectric mixing formulas and numerical method. *J. Appl. Meteor*, **35**, 1658–1670.
- Meneghini, R., L. Liao, and T. Iguchi, 2002: Integral equations for a dual-wavelength radar. *Proc. IEEE IGARSS'02*, 272–274.
- Meneghini, R., K. Nakamura, C. W. Ulbrich, and D. Atlas, 1989: Experimental tests of methods for the measurement of rainfall rate using an airborne dual-wavelength radar. *J. Atmos. Oceanic Technol.*, **6**, 637–651.
- Oguchi, T., 1983: Electromagnetic wave propagation and scattering in rain and other hydrometeors. *IEEE Proc.*, **71**, 1029–1078.
- Passarelli, R. E., 1978: Theoretical and observation study of snow-size spectra and snowflake aggregation efficiencies. *J. Atmos. Sci.*, **35**, 882–889.
- Peterson, W. A. and S. A. Rutledge, 2001: Regional variability in tropical convection: Observations from TRMM. *J. of Climate*, **14** (17), 3566–3586.
- Pruppacher, H. R. and J. D. Klett, 1997: *Microphysics of Clouds and Precipitation*. 2d ed., Kluwer Academic.
- Rose, C. R. and V. Chandrasekar, 2004: System engineering of GPM dual-frequency retrieval algorithms. Ph.D. thesis, Colorado State University.
- , 2006a: Extension of GPM dual-frequency iterative retrieval method with DSD profile constraint. *IEEE Trans. Geosci. Remote Sens.*, **44** (2), 328–335.
- , 2006b: A GPM dual-frequency retrieval algorithm: DSD profile optimization method. *J. Atmos. Oceanic Technol.*, **23**, 1372–1383.
- Schumacher, C. and R. House, 2003: Stratiform rain in tropics as seen by the TRMM precipitation radar. *J. of Climate*, **16**, 1739–1756.

- Sekhon, R. and R. Srivastava, 1970: Snow size spectral and radar reflectivity. *J. Atmos. Sci.*, **27**, 299–307.
- , 1971: Doppler radar observations of drop size distributions in a thunderstorm. *J. Atmos. Sci.*, **6**, 983–994.
- Senbokuya, Y., S. Satoh, K. Furakuwa, M. Kojima, H. Hanado, N. Takahashi, T. Iguchi, and K. Nakamura, 2004: Development of the spaceborne dual frequency precipitation radar for the global precipitation measurement mission. *Proc. IEEE IGARSS'04*, 3365–3369.
- Serafin, R. J. and J. W. Wilson, 2000: Operational weather radar in the united states: progress and opportunity. *Bul. American Met. Soc.*, **81**, 501–518.
- Shin, D., N. G. R., and B. K. P., 2000: A summary of reflectivity profiles from the first year of TRMM radar data. *J. of Climate*, **13** (23), 4072–4086.
- Skolnik, M. I., 2001: *Introduction to radar systems*, chap. 2. 3rd ed., McGraw-Hill.
- Straka, J. M., D. Zrnić, and A. Ryzhkov, 2000: Bulk hydrometeor classification and quantification using polarimetric radar data: synthesis of relations. *J. Appl. Meteor*, **39**, 1341–1372.
- Tanelli, S., E. Im, L. Stephen, S. L. Durden, and P. M. Jonathan, 2004: Rainfall and snowfall observations by the airborne dual-frequency precipitation radar during the Wakasa Bay experiment. *Proc. IEEE IGARSS'04*, 3195–3198.
- Testud, J. E., S. Oury, P. Amayenc, and B. R. A., 2001: The concept of normalized distribution of describe raindrop spectra: A tool for cloud physics and cloud remote sensing. *J. Appl. Meteor*, **40**, 1118–1140.
- Thurai, M., H. Kumagai, T. Kozu, and J. Awaka, 2001: Effects of incorporating a brightband model in a downward-looking radar rainfall retrieval algorithm. *J. Atmos. Oceanic Technol*, **18**, 20–25.

- TRMM, 2001: *TRMM data users handbook*.
- , 2005: *TRMM instruction manual for version 6*.
- Ulbrich, C. W., 1983: Natural variation in the analytical form of drop size distribution. *J. Appl. Meteor*, **2**, 1764–1775.
- Wilheit, T. T., V. Chandrasekar, and L. Wanyu, 2007: Impact of uncertainty in the drop size distribution on oceanic rainfall retrievals from passive microwave observations. *IEEE Trans. Geosci. Remote Sens.*, **45** (10), 3160–3164.
- Willis, P. T. and P. Tattelman, 1989: Drop-size distribution associated with intense rainfall. *J. Appl. Meteor*, **28**, 3–15.
- Wolff, D. B., D. A. Marks, E. Amitai, S. D. S., F. B. L., A. Tokay, J. Wang, and P. J. L., 2005: Ground validation for the Tropical Rainfall Measuring Mission (TRMM). *J. Atmos. Oceanic Technol.*, **22**, 365–380.
- Zafar, B. and V. Chandrasekar, 2004: SOM of space borne precipitation radar rain profiles on global scale. *Proc. IEEE IGARSS'04*, Vol. 2, 925–928.
- Zawadzki, I., W. Szyrmer, C. Bell, and F. Fabry, 2005: Modeling of the melting layer. part III : The density effect. *J. Atmos. Sci.*, **62**, 3702–3723.